

**Material properties and toxicity of nanomaterials –  
investigation of the relevance of extrinsic properties for  
adverse biological effects**

**Inaugural-Dissertation**

to obtain the academic degree

Doctor rerum naturalium (Dr. rer. nat.)

submitted to the Department of Biology, Chemistry, Pharmacy  
of the Freie Universität Berlin

by

**JOHANNES GEORG KELLER**

Unterseen, Switzerland

**2020**

---

The work described here was performed from October 2017 until October 2020 at BASF SE in Ludwigshafen am Rhein. It was supervised by PD Dr. Robert Landsiedel at the Institute of Pharmacy of the Freie Universität Berlin and the Department of Experimental Toxicology and Ecology BASF SE, and Prof. Dr. Burkhard Kleuser at the Institute of Pharmacy of the Freie Universität Berlin.

I hereby declare that I have written the present thesis independently, without any assistance from third parties and without the use of resources other than those indicated. Ideas and statements taken directly or indirectly from external sources are cited and marked as such. The material, either in full or in part, has not been previously submitted for grading at this or any other academic institution.

Place, Date

Signature

1<sup>st</sup> Reviewer: PD Dr. Robert Landsiedel  
Institute of Pharmacy (Pharmacology and Toxicology)  
Freie Universität Berlin  
Königin-Luise-Straße 2+4  
14195 Berlin

2<sup>nd</sup> Reviewer: Prof. Dr. Burkhard Kleuser  
Institute of Pharmacy (Pharmacology and Toxicology)  
Freie Universität Berlin  
Königin-Luise-Straße 2+4  
14195 Berlin

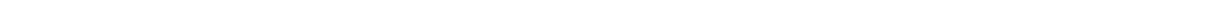
Date of disputation: 13.04.2021



---

*A work like this cannot be done in a solo attempt, only YOU, my bright supervisors, dearest colleagues, closest friends, and family made this work possible. Therefore, I want to express my gratitude towards all of you, who continuously supported me throughout this journey.*

***Thank you!***



---

## LIST OF ABBREVIATIONS

3R	Reduction, Refinement, and Replacement of animal testing
AOP	Adverse Outcome Pathway
ATSM	American Society for Testing and Materials International
AUC	Analytical Ultra Centrifugation
BET	Brunauer-Emmett-Teller theory
CFS	Continuous Flow-Through System
CNT	Carbon Nanotube
DMEM	Dulbecco's Modified Eagle's Medium
EC	European Commission
ECETOC	European Center for Ecotoxicology and Toxicology of Chemicals
ECHA	European Chemicals Agency
EFSA	European Food Safety Authority
ENMs	Engineered Nanomaterials
EU	European Union
FBS	Fetal Bovine Serum
GIF	Gastrointestinal Fluid
HARN	High Aspect Ratio Nanomaterial
HTS	High-Throughput Screening
IATA	Integrated Approaches for Testing and Assessment
ICP-MS	Inductively Coupled Plasma Mass Spectrometry
<i>In vitro</i>	performed without a living organism
<i>In vivo</i>	performed with a living organism
IOM	Institute for Occupational Medicine
IRMM	Institute for Reference Materials and Measurements
ISDD	<i>In vitro</i> Sedimentation, Diffusion and Dosimetry model
IUF	Leibniz Research Institute for Environmental Medicine
JRC	Joint Research Center
KETs	Key Enabling Technologies
KRISS	Korean Research Institute of Standards and Science
LSF	Lung lining Simulant Fluid
NM	Nanomaterial
OECD	Organization of Economic Cooperation and Development

PCP	Physicochemical Property
PSD	Particle Size Distribution
PSF	Phagolysosomal Simulant Fluid
REACH	Registration, Evaluation, Authorization, and Restriction of Chemicals
ROS	Reactive Oxygen Species
spICP-MS	Single Particle Inductively Coupled Plasma Mass Spectrometry
STIS	Short-Term Inhalation Studies
TEM	Transmission Electron Microscopy
MMVF	Man-Made Vitreous Fibers

---

## LIST OF PUBLICATIONS

### Main author publications:

1. Koltermann-Jülly J\*, **Keller JG\***, Vennemann A, Werle K, Müller P, Ma-Hock L, Landsiedel R, Wiemann M, Wohlleben W. *Abiotic dissolution rates of 24(nano)forms of 6 substances compared to macrophage-assisted dissolution and in vivo pulmonary clearance: Grouping by dissolution and transformation*. *NanoImpact* 2018 Okt, Volume 12, pp. 29-41. DOI: 10.1016/j.impact.2018.08.005.
2. Koltermann-Jülly J\*, **Keller JG\***, Vennemann A, Werle K, Müller P, Ma-Hock L, Landsiedel R, Wiemann M, Wohlleben W. Addendum to "Abiotic dissolution rates of 24(nano)forms of 6 substances compared to macrophage-assisted dissolution and in vivo pulmonary clearance: Grouping by dissolution and transformation". *NanoImpact* Feb 2019, Volume 14, pp. 100154. DOI: 10.1016/j.impact.2019.100154.
3. **Keller JG**, Graham UM, Koltermann-Jülly J, Gelein R, Ma-Hock L, Landsiedel R, Wiemann M, Oberdörster G, Elder A, Wohlleben W. *Predicting dissolution and transformation of inhaled nanoparticles in the lung using abiotic flow cells: The case of barium sulfate*. *Scientific Reports* 2020, 10. Jg., Nr. 1, S. 1-15. DOI: 10.1038/s41598-019-56872-3.
4. **Keller JG**, Peijnenburg, W., Werle, K., Landsiedel, R., & Wohlleben, W. *Understanding Dissolution Rates via Continuous Flow Systems with Physiologically Relevant Metal Ion Saturation in Lysosome*. *Nanomaterials* 2020, 10(2), 311. DOI: 10.3390/nano10020311.
5. **Keller JG\***, Quevedo DF\*, Faccani L, Costa AL, Landsiedel R, Werle K, Wohlleben W. *Dosimetry in vitro – exploring the sensitivity of deposited dose predictions vs. affinity, polydispersity, freeze-thawing, and analytical methods*. *Nanotoxicology* 2020. DOI: 10.1080/17435390.2020.1836281.
6. **Keller JG**, Persson M, Müller P, Werle K, Ma-Hock L, Landsiedel R, Wohlleben W. *Subtle differences between nanoforms of the same substance induce (dis)similarities of their dissolution and transformation behavior that suggest specific groupings for read-across of inhalation hazard assessment*. *NanoImpact*, submitted November 2020.
7. **Keller JG**, Wiemann M, Gröters S, Werle, K, Vennemann, A, Landsiedel R, Wohlleben W. *Which Aerogels are safe to use? A categorization approach of 17 organic and two inorganic aerogels based on biosolubility, oxidative potential, in vitro reactivity, and in vivo data*. To be submitted 2020.
8. **Keller JG\***, Di Cristo L\*, Ag Seleci D, Landsiedel R, Werle K, Sabella S, Wohlleben W. *Biodissolution in cascaded simulants of the gastro-intestinal tract: towards robust screening methods and nanomaterial grouping*. To be submitted 2020.

\*equal contributing authors

### Further collaboration publications:

1. Wiemann M, Sauer UG, Vennemann A, Bäcker S, **Keller JG**, Ma-Hock L, Wohlleben W, Landsiedel R. *In Vitro and In Vivo Short-Term Pulmonary Toxicity of Differently Sized Colloidal Amorphous SiO<sub>2</sub>*. *Nanomaterials* (Basel) 2018 Mar, Volume 8(3), pp.160. Doi: 10.3390/nano8030160.
2. Wohlleben W, Hellack B, Nickel C, Herrchen M, Hund-Rinke K, Kettler K, Riebeling C, Haase A, Funk B, Kühnel D, Göhler D, Stintz M, Schumacher C, Wiemann M, **Keller JG**, Landsiedel R, Broßell D, Pitzko S, Kuhlbusch TAJ. *The nanoGRAVUR framework to group (nano) materials for their occupational, consumer, environmental risks based on a harmonized set of material properties, applied to 34 case studies*. *Nanoscale* 2019, 11(38), 17637-17654. Doi: 10.1039/C9NR03306H.
3. Llewellyn SV, Kämpfer A, **Keller JG**, Schins R, Seleci DA, Vilsmeier K, Doak SH, Wohlleben W. *Designed exposure identity for in vitro testing: Concept and demonstration*. *Small*, accepted October 2020.
4. Ma-Hock L, Sauer UG, Ruggiero E, **Keller JG**, Wohlleben W, Landsiedel R. *Using Nanomaterial In Vivo Burden Data for In Vitro Dose Setting (OBIV)*. *Small*, submitted September 2020.
5. Yokel R, Wohlleben W, **Keller, JG**, Hancock ML, Unrine JM, Butterfield A, Grulke EA. *Nanoceria dissolution is greatly influenced by its physicochemical nature*. *Journal of Nanoparticle Research*, submitted December 2020.

---

## TABLE OF CONTENTS

LIST OF ABBREVIATIONS .....	V
LIST OF PUBLICATIONS .....	VI
TABLE OF CONTENTS .....	VII
1 INTRODUCTION.....	1
1.1 NANOTECHNOLOGY .....	2
1.2 NANOSAFETY .....	3
1.2.1 Inhalation Uptake .....	5
1.2.2 Oral.....	6
1.3 REGULATIONS AND REQUIREMENTS .....	7
1.4 NANOMATERIAL GROUPING AND RESEARCH NEEDS FOR SIMILAR NANOFORMS .....	8
2 MOTIVATION AND OBJECTIVES .....	11
2.1 DISSOLUTION AND TRANSFORMATION .....	12
2.2 DOSIMETRY.....	14
2.3 CHOICE OF MATERIALS .....	15
3 RESULTS.....	19
3.1 PUBLISHED RESULTS.....	20
3.1.1 The nanoGRAVUR framework to group (nano) materials for their occupational, consumer, environmental risks based on a harmonized set of material properties, applied to 34 case studies .....	20
3.1.2 Abiotic dissolution rates of 24 (nano)forms of 6 substances compared to macrophage-assisted dissolution and in vivo pulmonary clearance: Grouping by biodissolution and transformation .....	39
3.1.3 Addendum to “Abiotic dissolution rates of 24 (nano)forms of 6 substances compared to macrophage-assisted dissolution and in vivo pulmonary clearance: Grouping by biodissolution and transformation” [NanoImpact 12 (2018) 29-41] .....	53
3.1.4 Predicting dissolution and transformation of inhaled nanoparticles in the lung using abiotic flow cells: The case of barium sulfate .....	56
3.1.5 Understanding Dissolution Rates via Continuous Flow Systems with Physiologically Relevant Metal Ion Saturation in Lysosome .....	72
3.1.6 Dosimetry in vitro – exploring the sensitivity of deposited dose predictions vs. affinity, polydispersity, freeze-thawing, and analytical methods. ....	89
3.2 MANUSCRIPTS SUBMITTED OR UNDER PEER REVIEW .....	104

## TABLE OF CONTENTS

---

5	SUMMARY AND CONCLUSION.....	121
6	OUTLOOK.....	127
7	ZUSAMMENFASSUNG.....	129
8	REFERENCES.....	133

---

## **1 INTRODUCTION**

## 1.1 NANOTECHNOLOGY

*„There is plenty of room at the bottom. “*

On the 29<sup>th</sup> of December 1959, physicist Richard Feynman held his historical talk in front of a scientific audience at the California Institute of Technology. [1] It was not until then that people started to think about the endless possibilities of something so small. Feynman prospected that scientists in the future will be able to manipulate individual molecules and atoms for the construction of more advanced data storages or microscopic machines. It took another twenty years until the scanning tunneling microscope was developed, which finally allowed scientists to monitor individual atoms for the first time. [2] Norio Taniguchi finally coined the term nanotechnology in 1974. [3]

However, what is nanotechnology? The prefix originates from the Greek word nanós, which translates to dwarf and is nowadays used to describe, e.g., the billionth part of a meter ( $10^{-9}$  m). [4] A sheet of paper, for example, has a thickness of 100,000 nm, an ant is 5,000,000 nm long, and the human DNA strand has a diameter of 2.5 nm. [5] There are several, slightly different definitions by the International Organization for Standardization (ISO), [6] the Organization for Economic Co-Operation and Development (OECD), [7, 8] the European Commission (EC), [9] and the American Society for Testing and Materials International (ASTM) [10], but there is consensus that an object is considered to be in the nanoscale if one or more external dimensions (height, length, width) are in the size range between 1 and 100 nm. Thus, nanomaterials can exist as three-dimensional particles with three dimensions in the sub 100 nm range, tubes with two-dimensions within this range, or platelets with one dimension within this range. [6]

The term engineered nanomaterial (ENM) is used for intentionally produced nanomaterials. Nanotechnology engages with structures, shapes, or particles within the nanoscale, requiring a tight collaboration between material scientists, chemists, physicists, and biologists. Nanomaterials can also be naturally born through volcanic eruptions, dust from cosmic sources, or fires; for these materials, the term unintentionally nanomaterial is used within this thesis. [11] ENMs of the same chemical composition as their bulk counterparts have an increased surface to volume ratio, leading to a higher share of the atoms being exposed on the material's surface, where the crystalline structures need to have defects and thus more reactive sites. This can fundamentally alter the interaction between the particle and the surrounding environment, e.g., gold nanoparticles are effective catalysts, whereas bulk gold is one of the least reactive materials. Furthermore, the composition, surface functionalization, morphology, and the hydrophilic or hydrophobic nature of the particles can be designed to improve functionality. [12-14]

The interdisciplinary nature of nanotechnology has rapidly advanced into broad applications in the fields of chemistry, [15-18] construction, [19, 20] medicine, [12, 21-23] biotechnology, [24-26] electronics, [27, 28] automotive, [29, 30] personal care, [31, 32] food and packaging, [33, 34] as well as many more. [35] The European Union (EU) acknowledged the importance of nanotechnology as member of a group of six Key Enabling Technologies (KETs) additionally comprising micro and nanoelectronics, industrial biotechnology, advanced materials, photonics, and advanced manufacturing technologies. The KETs are thought to stimulate industrial innovation and address societal challenges and create advanced and sustainable economies in the



21<sup>st</sup> century. [36] These technologies are driving factors for economic growth as well as sustainability, eventually making our everyday lives more comfortable. With broad applications, there are nearly endless ENM compositions, surface functionalization, shapes, sizes, or structures. [37]

## 1.2 NANOSAFETY

With continually growing fields of applications for ENM and immense technological and economic potential, it needs to be kept in mind that nanotechnology also entails potential risks. [38, 39] due to their high surface to volume ratio, some nanomaterials are chemically more reactive. [40] Decreasing particle size will lead to increased reactivity for some ENM [41] and, furthermore, to the generation of reactive oxygen species (ROS) known to be one of the major causes of inflammation. [42-44] *ENM's* high reactivity [45] leading to *beneficial* intended uses, might *make* ENMs harmful for humans and the environment. [46, 47] All ENMs entering the market should be tested for their safety for human *and the* environment. Therefore, it is of greatest interest to *considerately* take the hazard potential into account while exploiting nanotechnologies' full potential. [48, 49] Exposure to dusts from handling powders of *ENMs* is mostly limited to manufacturers and production workers as well as scientists working with nanotechnology. [50, 51] Whereas consumers and the general population can be exposed to ENMs released into the environment or used in consumer products (e.g. other ENMs as sunscreens in cosmetics).[52]

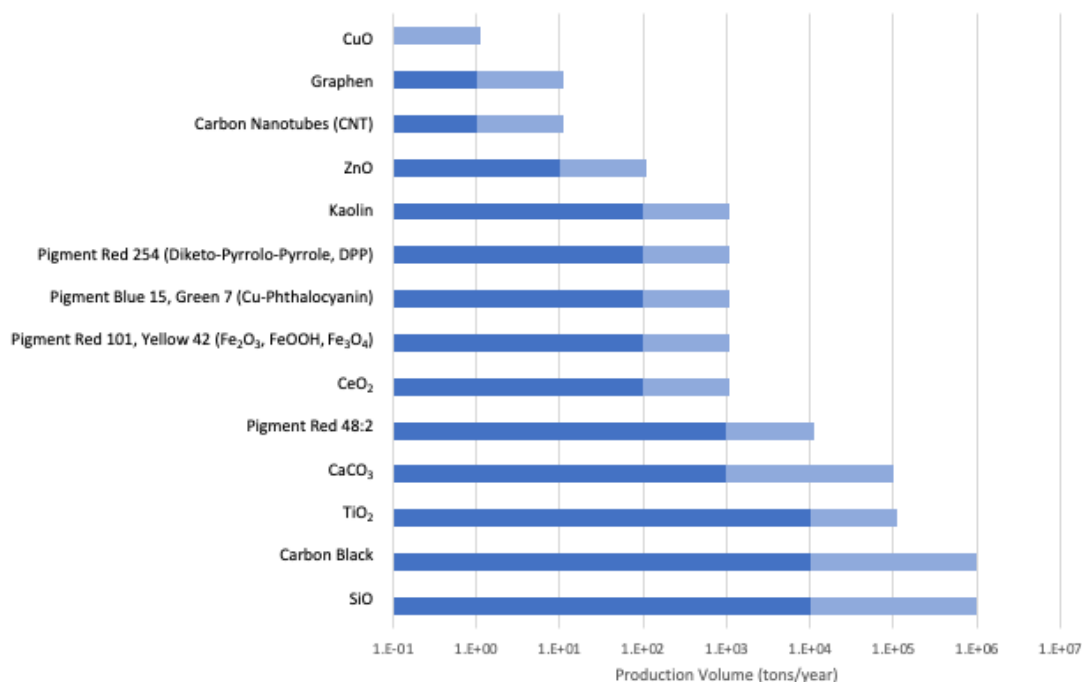


Figure 1: Production Volume of Nanomaterials in tons/year in France in 2019 [53]. Dark blue is marking the lower limit and light blue the upper limit of the production volume.

The European Union Observatory of Nanomaterials (EUON) currently lists 331 unique nanomaterial entries on their webpage. [54] Over 4400 consumer products are registered in the Danish database containing a „nano claim“. [55] **Figure 1** shows the production volume of some essential ENMs in the year 2019 in

## INTRODUCTION

---

France. [53]. SiO<sub>2</sub>, TiO<sub>2</sub>, CaCO<sub>3</sub>, Carbon Black are the most relevant materials, of which between 10,000 and 1,000,000 tons are produced as ENM. Various pigments and metal oxides with production quantities between 100 and 10,000 tons are the next most relevant substance class of ENMs.

The growth ENMs production volume and applications can lead to a higher exposure and diversified exposure pathways. When assessing the safety of ENMs, it is essential to understand their lifecycle and fate. Pioneering in the field of ultrafine particles, Oberdörster et al. and Seaton & Donaldson introduced in 2005 the term “nanotoxicology” while simultaneously pointing out the two elements to assess the potential risk of nanomaterials: the toxicity of ENMs and the expected exposure. [45, 56, 57] Several nanomaterials are embedded in a matrix, leading to a decreased probability of exposure. However, in other cases, nanomaterials might get taken up by humans through inhalation [58], ingestion [59] or skin contact [60, 61] or will end up in the environment. [62] ENMs, which lead to unexpected illnesses upon exposure, might be developed. [48] asbestos fibers are not a nanomaterial, but set precedence of a fatally long lag time between exposure and illness: Asbestos fibers have previously been used as inexpensive fillers in construction materials to function as anti-flaming agents but are nowadays known for their carcinogenic potential inducing the very specific mesothelioma cancer. [63] High aspect ratio nanomaterials (HARN) that are also similarly long and rigid as asbestos have similar toxic potential, leading equally to mesothelioma. [64-67] Among ENMs, only the “Mitsui NT7” type of Carbon Nanotubes (CNTs) fulfills these criteria and has been formally recognized as carcinogen. [68]

Most ENMs do not share these criteria, but nonetheless their hazards needs to be thoroughly assessed to facilitate risk management and prevent humans and the environment from being exposed to ENMs in quantities that cause adverse effects. [69] However, previously established guidelines to determine the hazard potential of bulk materials need adaptations to be applicable to ENM. Especially for inhalation studies the physicochemical properties (PCPs) of ENM must be assessed. The dispersibility, shape, particle size, dissolution, reactivity, and several more intrinsic and extrinsic PCPs are directly influencing the deposition within the lung, translocation to systemic sites, and inflammatory potential. [45]

The 3R principle calls for in vivo studies to be conducted with as little burden for the animals as possible (refinement), as little animals as possible (reduction) and wherever possible for a replacement by non-animal methods. [70-72] Hence there is a challenge to predict potential adverse effects of ENM based on their material properties (comparable to QSAR predictions for molecules) [73]. In a tiered approach, the intrinsic physicochemical properties (PCPs) of ENMs are addressed first, followed by the extrinsic properties (also termed “functionality” or interactions at the bio-nano interface), and in vitro toxicity testing to predict potential toxic effects in humans. In vivo testing in animals is the last resort to assessing the adverse effects. [70]

There is a tremendous amount of ENMs ranging in size, morphology, surface functionalization, and compositions. [69, 74] It is nearly impossible to test all PCPs that may eventually trigger biological responses. Therefore, the ISO published several essential characterization techniques relevant to the risk assessment in a tiered approach. The tiered testing methods should aim at the physicochemical characterization of the

ENMs with the surface area as calculated through the Brunauer-Emmett-Teller (BET) equation, [75] the bulk chemical composition, surface chemistry, particle size, particle size distribution (PSD), morphology/shape, surface charge, agglomeration/aggregation state, crystal structure, and solubility. [76-78]

There are several physiological ways how humans can take up both naturally occurring NMs as well as ENM either through inhalation, ingestion, or dermal uptake and injections for medical applications.

### 1.2.1 Inhalation Uptake

The most critical pathway for uptake of ENMs into the human body is by inhalation. [45] Ultrafine, airborne particles such as unintentionally produced soot from combustion engines or inorganic dust from volcanoes eruptions or dusts from handling ENM powders can remain suspended in the air for hours and can be transported over long distances. The inhalable fraction (below 10  $\mu\text{m}$  agglomerate size) can enter the human airways, and the respirable fraction (below 2.5  $\mu\text{m}$ ) can reach the lower airways and alveoli. Despite several allegations, [79] only a negligible fraction of ENM can cross biological barriers, resulting in systemic availability and internalization of cells other than by endocytosis.[80] Instead, ENMs mostly remain in the primary target organ, the lung, and are cleared by different processes, depending on where they are deposited: For the deposition in the upper airways a clearance through the mucociliary transport is rate-determining. Here particles deposit on the mucus blanket which covers the airways. The mucus blanket is then moved towards the pharynx by cilia.[81] Particles that reached the alveolar region are taken up by alveolar macrophages and are either digested or transported to the mucociliary escalator, the interstitium or the lung-associated lymph nodes. The alveolar clearance is slower than the mucociliary clearance. [58, 81]

ENMs taken-up by macrophages may partially or fully transform and or dissolve during these processes, and both the released ions and the remaining (transformed) particles may induce adverse effects. [82, 83] In standard inhalation models (i.e. OECD 413 and STI), groups of rats are exposed to defined (usually three) concentration of ENMs within an aerosol for a defined period (e.g., six hours per day, five days per week for 13 weeks in an OECD TG 413). [84, 85] After the exposure, the rats are examined for adverse effects induced by ENM inhalation; furthermore, lung and other organ burdens can be analyzed. However, these tests use animals and are time-consuming and expensive, making it impossible to test all ENMs by inhalation toxicity studies. This is calling for alternative approaches for nanotoxicological assessment for human exposure.

Immediately after deposition, ENMs interact with the lung lining fluid upon reaching the alveolar tract (Figure 2). PCPs of the ENMs such as surface functionalization, zeta-potential, and surface charge may alter their biological systems' behavior, eventually leading to different adverse effects. Uptake in cells and ensuing biokinetics confront the ENM with different physiological compartments, e.g., lysosomal fluids. Within STIS, a relationship between inflammation and surface-area dependent dose was found for carbon black. [86] Inhalation of ZnO ENM induced olfactory epithelium necrosis after 14- or 21- days in rats. Other ENMs are known to elicit concentration-dependent pulmonary inflammation. [87] Interspecies differences of e.g., the ventilation volume and the immune system need to be considered in extrapolating from animal (mostly rat and mice) inhalation studies to human effects. But very clearly, cohort studies on occupational exposure confirm that certain fine and ultrafine particles can be toxic even at low exposure concentrations. E.g.,

## INTRODUCTION

occupational exposure to crystalline SiO<sub>2</sub> resulted in an overall elevated standardized mortality ratio for renal disease, silicosis, lung cancer, and non-malignant respiratory disease. [68, 88, 89] And yet, puzzles remain. E.g., the substance of BaSO<sub>4</sub> was widely considered as inert and insoluble material. Surprisingly though, inhalation studies with nano-BaSO<sub>4</sub> in rats have shown rapid clearance from the lung with less than 10 days half-time. More than 30% of the Ba was found in the bones.[90] The abiotic and in vitro screening methods failed to predict such behavior.

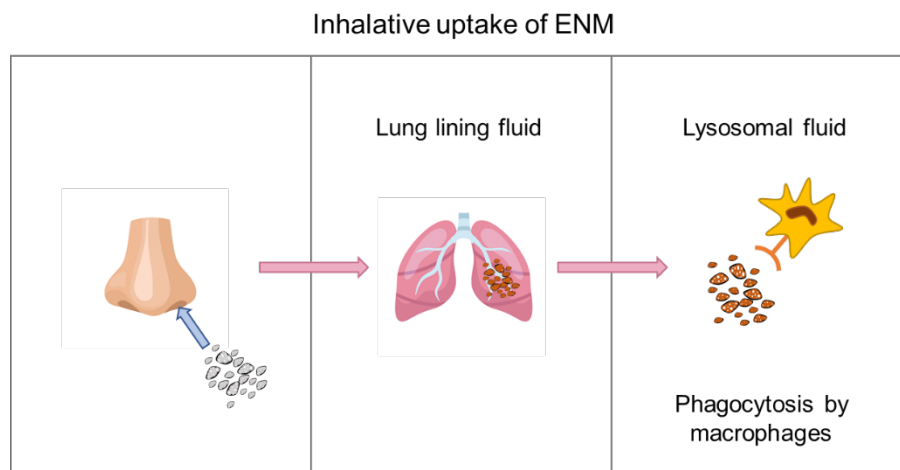


Figure 2: Schematic uptake of ENM through inhalation. After inhalation, particles are exposed to the lung lining fluid first, followed by the lysosomal fluid within the alveolar tract.

### 1.2.2 Oral

Oral uptake is another relevant pathway for the uptake of nanomaterials. ENMs can be taken up either via the ingestion of food (e.g., additives and formulated nutritional supplements), [91] or unintentional hand to mouth transfer, or swallowing particles cleared from the lung by the mucociliary escalator (Figure 3). [92] The toxicity of ENMs depends on their extrinsic properties upon exposure to the different relevant compartments, saliva, gastric juice, intestinal juice. [91] Even though the compartments within the gastrointestinal (GIT) tract contain enzymes, most inorganic ENMs will not be digested. However, some may partially or even fully dissolve. [93, 94] Persisting particles are excreted with the feces or absorbed – usually just a small fraction. Ingested ENM can also affect the commensal gut microbiota. [95] Bioavailability and toxicity are governed by particle size and aggregation and the surface reactivity and the release of toxic ions. [96] Studies have shown that ZnO nanoparticles, which are intentionally used for their antimicrobial property in packaging and could, therefore, accidentally leach into the food, could penetrate microbial cells where they induced cytotoxicity through reactive oxygen species (ROS) generation. [97] Zn uptake increased with decreasing particle size in rodents, leading to hepatic injury, kidney toxicity, and lung damage, [98] but the study did not conclusively demonstrate uptake as particles or as ions. The food-grade TiO<sub>2</sub>, E171, with only >36% of the particles being below the size of 100 nm (hence not an ENM by legal definitions) was found in some parts of the body.[99] Furthermore, only a little clearance within the tissues of mammals was found in a study with 16 rats[100] Sub chronic studies in rats with intragastrically administered TiO<sub>2</sub> at concentrations of up to 5000 mg/kg body-weight/day accumulated in liver, spleen, kidney, and lung tissue, adverse effects nephrotoxicity, hepatic injury, and myocardial damage were observed. [101] With an approximate uptake of

1.1 - 2.2 mg/kg body-weight/day by humans,  $\text{TiO}_2$  is one of the most relevant food additives. [99] For  $\text{SiO}_2$ , the European Food Safety Authority (EFSA) estimates an even higher daily intake of between 20 - 50 mg for a 60 kg person. [102] In a ten-week feeding study in mice with 30 nm  $\text{SiO}_2$  ENM and 30  $\mu\text{m}$   $\text{SiO}_2$  particles, Si content accumulated in similar concentrations in the liver whereas only the nano-sized particles caused adverse effects as usually observed in fatty livers. [103] EFSA requires producers to assess the safety of all purposely produced ENMs with a size between 1-100 nm, of materials larger than 100 nm with characteristic properties of the nanoscale, and materials not purposely engineered as an ENM but with fractions of particles with less than 50% in particle number in the range of 1-100 nm. [104] For the risk assessment the following extrinsic properties need to be determined: stability, solubility, degradation, dispersibility and reactivity. [104]

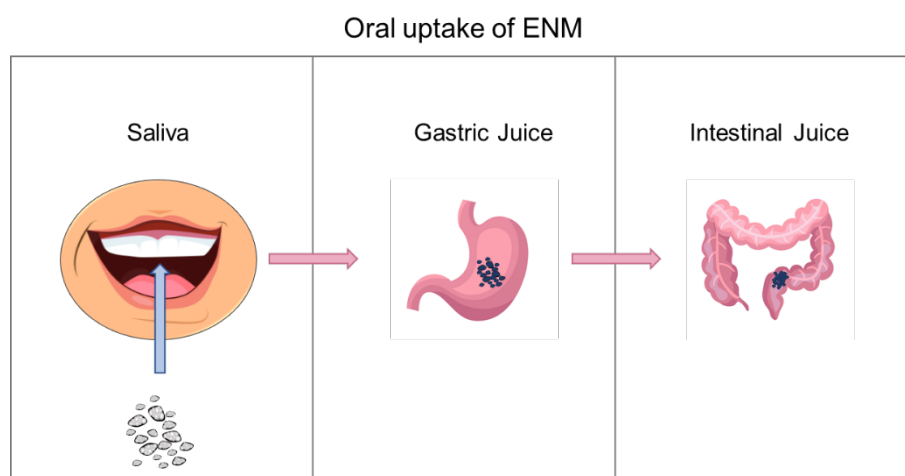


Figure 3: Schematic uptake of ENM through oral ingestion. After ingestion, particles are exposed to saliva first, followed by gastric juice within the stomach and intestinal juice within the intestine.

### 1.3 REGULATIONS AND REQUIREMENTS

Registration, Evaluation, Authorization, and Restriction of Chemicals (REACH) is the most important regulation of the European Union that is adopted to protect human health and the environment from the risks that can be posed by chemicals. [105] The REACH regulations also apply to all ENM produced or imported into the EU. [106] Therefore, hazard identification, hazard assessment, exposure assessment, and risk assessment must be conducted for chemicals manufactured or imported in the EU. [107] As of January 2020, manufacturers of nanomaterials have to provide information on ENMs, including the chemical safety assessment (ANNEX I), characterization of nanoforms, or set of nanoforms (ANNEX VI) and registration information requirements (Annexes III and VII-XI) including data on toxic effects. [106] Fulfilling the information requirements on nanoforms recently introduced by the new European Chemicals Agency (ECHA) guideline may entail extensive testing of each nanoform. [108] Testing requirements for each nanoform are derived from the yearly production volume of the substance. For production volumes above 1 ton/year, acute toxicity testing must be assessed through the oral route. Production volumes between 10-100 tons/year require, in addition to the acute toxicity studies, short-term repeated dose toxicity studies over 28 days if exposure of humans via inhalation is likely. Furthermore, the recovery period and lung clearance

shall be considered to assess nanoforms' toxicokinetics without high dissolution rate. And the degradation as well as transformation for non-soluble nanoforms. Additionally for nanoforms with a production volume above 100 tons/year, sub-chronic 90-days toxicity studies need to be conducted. [108] The ECHA guidelines require animal testing for each nanoform, unless if it can be shown by grouping and read-across that animal tests were previously examined on a similar nanoform. The perspective of an enormously increasing consumption of test animals intensified the development of alternative testing and non-testing (grouping) methods, such as those elaborated in this thesis. Physicochemical descriptors, as given in Table 1, are required to define a nanoform. Nanoforms with similar hazard profiles can be grouped in a “set of similar nanoforms” and only one nanoform needs to be tested in order to apply the test results to all nanoforms of a set. The similar compositions of nanoforms are not enough to justify the grouping of different nanoforms, because additional particle properties influence the hazard profile of a nanoform. Thus, defining sets of similar nanoforms has great potential to reduce animal testing. Identifying intrinsic and extrinsic material properties which are relevant for the hazard potential of nanoforms is critical to justify a set of similar nanoforms.

### 1.4 NANOMATERIAL GROUPING AND RESEARCH NEEDS FOR SIMILAR NANOFORMS

ENM can be produced in several nanoforms with different sizes, crystalline forms, shapes, and surface characteristics. The ECHA Guidance on nanoforms [108] defines nanoforms and sets of similar nanoforms. It notes that, in principle, toxicological data from a nanoform may be used for the safety assessment of another nanoform if it can be shown that they are similar enough. For other chemicals (molecules, not ENM), this approach is well-established and is termed grouping (identify sets of sufficiently similar chemicals) and read across (use the known toxicological properties of one chemical for the safety assessment of another chemical of this group). This approach helps to avoid case-by-case animal testing of all nanoforms of a given substance, but it does require testing by physical-chemical and alternative toxicological methods to substantiate the grouping. The ECHA provided guidance on read-across of chemicals as well as sets of similar nanoforms. [109, 110] While methods and read-across for chemicals have been developed during the last decade [111], specific methods and decision criteria to define groups of sets of similar nanoforms are not yet commonly accepted. The European Center for Ecotoxicology and Toxicology of Chemicals (ECETOC) proposed a decision-making framework for the grouping and testing nanomaterials (D4FnanoGrouping). [112] This framework highlighted the importance of assessing extrinsic properties to assign nanomaterials into four different main groups with additional sub-groups. The system-dependent properties – biopersistence, biophysical interactions, uptake, and biodistribution – were been chosen as relevant parameters for grouping purposes next to intrinsic properties and *in vitro* cellular next to apical toxic effects. [113] In the nanoGRAVUR project, a framework for the testing of ENM was established based on three Tiers. Starting with Tier 1, answering the question of “What they are” in terms of the ENMs' physical structure and chemical composition. Within Tier 2, the questions on “where they go” in terms of release and exposure and “where

they go” in relevant media are answered by assessing extrinsic properties. Furthermore, the “what they do” was assessed through reactivity studies abiotic and in vivo. Tier 3 then examined human toxicity and ecotoxicity (Figure 4). [114]

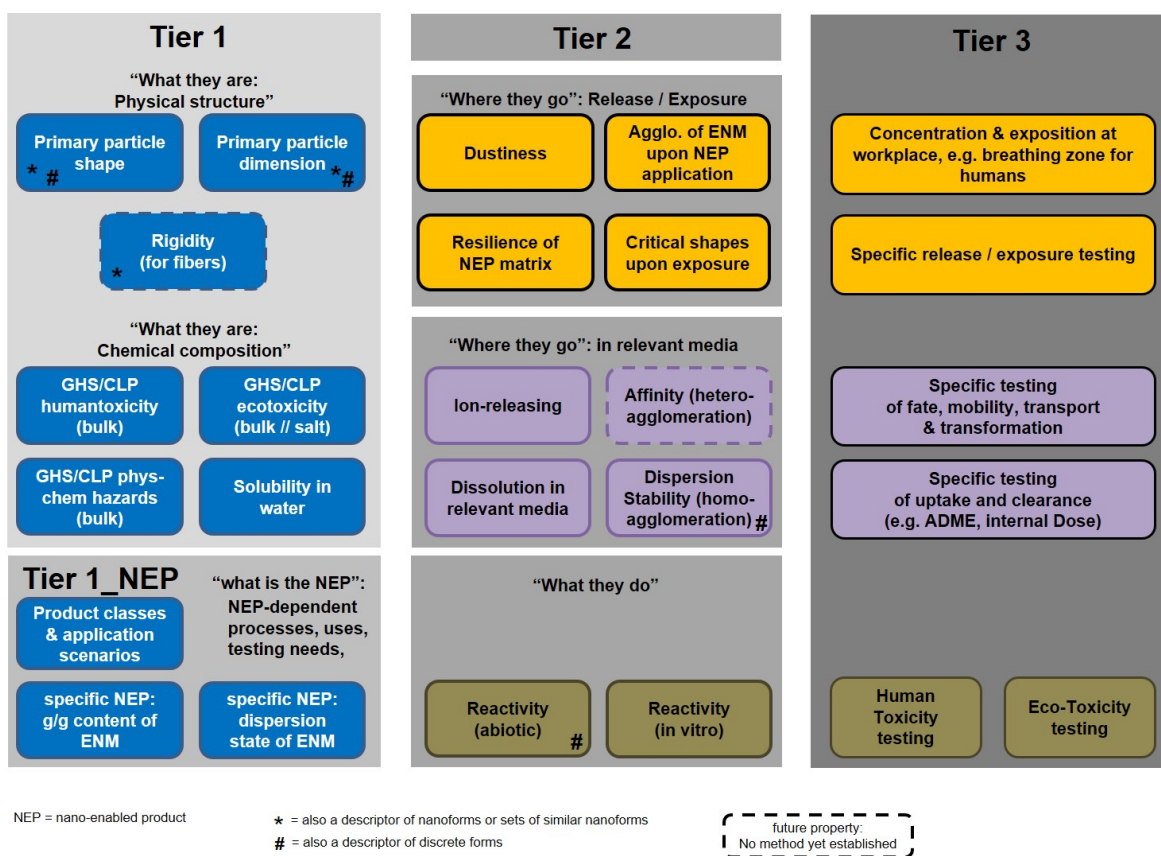


Figure 4: nanoGRAVUR grouping framework proposing a Tiered assessment of the risk. Figure reproduced from Wohlleben et al. 2019. [114]

There are several more grouping frameworks, e.g. Kuempel et al. proposed the assessment of basic parameters such as particle size, shape, density, surface area, reactivity, solubility, multiple exposures or dose groups, the biological significance of response, and target lung region surface area and volume. In animal tests. [115] Obviously, in-vitro testing and extrinsic (system-dependent) PCPs are very important for grouping frameworks, but so far, no OECD guidelines for their assessment exist. Furthermore, solely the determination of the system-dependent reactivity by electron spin resonance is described through an ISO norm; all other existing methods are not standardized. [116] On top of that, plenty of approaches assessing the *in vitro* toxicity are existing, but none of them are standardized, and none systematically considers in-vitro dosimetry.





---

## **2 MOTIVATION AND OBJECTIVES**

### 2.1 DISSOLUTION AND TRANSFORMATION

What happens to the nanomaterials after being taken up by humans? How can one explain, and properly predict for example the unexpectedly fast clearance of BaSO<sub>4</sub> from the lung, despite its insolubility in water? To determine the fate and the hazard potential of a nanomaterial within the human organism or the environment, it is mandatory to understand how an ENM interacts with physiological media. Essential for the understanding of the behavior is the determination of dissolution and the transformation of NM in relevant media. From mineral fibers, it is known that the Continuous Flow System (CFS) can be used to predict their persistence in the lung. For the testing of oral ingestion, several ways are presented in the literature.

The biopersistence of ENM is affecting their biological fate and hence their toxicity. The dissolution of ENM in biological media may be used to predict their biopersistence and can be useful to substantiate the similarity of nanoforms. Adopting and optimizing the CFS could provide a suitable method to understand their biological fate and substantiate sets of similar nanoforms. As many ENM are poorly soluble, such a method would require measuring trace amounts close to the detection (LoD) of the ENM's constituents released into the media. Apart from dissolution, ENM can undergo other transformations in biological media resulting in altered particles. Inductively coupled plasma mass spectrometry (ICP-MS) and transmission electron microscopy (TEM) were used to explore how these methods can be used to deliver the dissolution rate and structural information after exposure to physiological media. Most importantly, within this thesis, physicochemical parameters that are influencing particle dissolution were assessed. The results gained from these abiotic, dynamic dissolution tests were then compared to the particles actual biopersistence obtained from in vivo inhalation studies. According to the uptake through oral ingestion, a cascaded static dissolution setup needed to be developed to simulate the different compartments along the GI-tract with several pH changes. Both the particle dissolution as well as the transformation were to be investigated.

These processes are directly linked to both, the organ burden of (native and transformed) ENMs and the release of potentially toxic ions from ENMs in the human body. The aim of the work described here is, to develop and standardize methods to study the dissolution of ENMs in order to predict their fate in the human body. The data obtained from applying these methods can assist identifying sets of nanoforms with similar hazard profiles.

The following publications are related with this topic:

- Koltermann-Jüly J\*, **Keller JG\***, Vennemann A, Werle K, Müller P, Ma-Hock L, Landsiedel R, Wiemann M, Wohlleben W. *Abiotic dissolution rates of 24(nano)forms of 6 substances compared to macrophage-assisted dissolution and in vivo pulmonary clearance: Grouping by dissolution and transformation*. NanolImpact 2018 Okt, Volume 12, pp. 29-41. DOI: 10.1016/j.impact.2018.08.005.
- Koltermann-Jüly J\*, **Keller JG\***, Vennemann A, Werle K, Müller P, Ma-Hock L, Landsiedel R, Wiemann M, Wohlleben W. Addendum to "Abiotic dissolution rates of 24(nano)forms of 6 substances compared to macrophage-assisted dissolution and in vivo pulmonary clearance: Grouping by dissolution and transformation". NanolImpact Feb 2019, Volume 14, pp. 100154. DOI: 10.1016/j.impact.2019.100154.
- **Keller JG**, Graham UM, Koltermann-Jüly J, Gelein R, Ma-Hock L, Landsiedel R, Wiemann M, Oberdörster G, Elder A, Wohlleben W. *Predicting dissolution and transformation of inhaled nanoparticles in the lung using abiotic flow cells: The case of barium sulfate*. Scientific Reports 2020, 10. Jg., Nr. 1, S. 1-15. DOI: 10.1038/s41598-019-56872-3.

- **Keller JG**, Peijnenburg, W., Werle, K., Landsiedel, R., & Wohlleben, W. *Understanding Dissolution Rates via Continuous Flow Systems with Physiologically Relevant Metal Ion Saturation in Lysosome*. *Nanomaterials* 2020, 10(2), 311. DOI: 10.3390/nano10020311.
- Wohlleben W, Hellack B, Nickel C, Herrchen M, Hund-Rinke K, Kettler K, Riebeling C, Haase A, Funk B, Kühnel D, Göhler D, Stintz M, Schumacher C, Wiemann M, **Keller JG**, Landsiedel R, Broßell D, Pitzko S, Kuhlbusch TAJ. *The nanoGRAVUR framework to group (nano) materials for their occupational, consumer, environmental risks based on a harmonized set of material properties, applied to 34 case studies*. *Nanoscale* 2019, 11(38), 17637-17654. Doi: 10.1039/C9NR03306H.
- **Keller JG**, Persson M, Müller P, Werle K, Ma-Hock L, Landsiedel R, Wohlleben W. *Subtle differences between nanoforms of the same substance induce (dis)similarities of their dissolution and transformation behavior that suggest specific groupings for read-across of inhalation hazard assessment*. *NanoImpact*, submitted November 2020.
- **Keller JG\***, Di Cristo L\*, Ag Seleci D, Landsiedel R, Werle K, Sabella S, Wohlleben W. *Biodissolution in cascaded simulants of the gastro-intestinal tract: towards robust screening methods and nanomaterial grouping*. To be submitted 2020.
- **Keller JG**, Wiemann M, Gröters S, Werle, K, Vennemann, A, Landsiedel R, Wohlleben W. *Which Aerogels are safe to use? A categorization approach of 17 organic and two inorganic aerogels based on biosolubility, oxidative potential, in vitro reactivity, and in vivo data*. To be submitted 2020.
- Yokel R, Wohlleben W, **Keller, JG**, Hancock ML, Unrine JM, Butterfield A, Grulke EA. *Nanoceria dissolution is greatly influenced by its physicochemical nature*. *Journal of Nanoparticle Research* submitted December 2020.

### 2.2 DOSIMETRY

What and how much does the cell see?

When comparing results of ENM tested in *in vivo* toxicity studies with results from *in vitro* studies, a significant discrepancy is often observed [117]. These differences could result from varying effective doses present. For ENMs, the determination of the effective dose is challenging since most of ENMs do not ideally disperse as affected by particle-particle interactions, and the effective dose is determined by sedimentation and diffusion processes. State of the art *in vitro* testing methods with adherent cells or cells suspensions include, e.g., macrophages [118], endothelial cells [119], and pancreatic cancer cells [120]. To determine cellular effects of NMs *in vitro*, it is crucial to quantify the effective dose of NM to select doses relevant to the *in vivo* exposure scenario. Existing *in silico* techniques to model the dose are the In Vitro Sedimentation, Diffusion, and Dosimetry (ISDD) model [121], the Volumetric Centrifugation Method (VCM) [122], and the Distorted Grid (DG) model [123, 124]. These models face several challenges since the deposited dose is influenced by physicochemical parameters like particle size distribution (PSD), primary particle size, effective density, and user-chosen parameters.

Here the robustness of the DG model towards freeze-thawing protocols and a variation on user-chosen parameters such as particle affinity and estimations on polydispersity and their effect on dosimetry was tested. By measuring DLS, VCM, and AUC on a broad set of ENM, each differing in particle chemistry, size, shape, and surface coating, to identify ENMs and scenarios for which the actual deposited dose can be predicted.

Information on the effective dose is essential to establish dose-response relations and the toxic potency of ENMs. Moreover, avoiding excessively high test concentrations *in vitro* compared to the *in vivo* organ burdens, avoids irrelevant findings *in vitro*. The aim of the work described here is, to define limits and uncertainties of models for determining effective *in vitro* doses.

The following publications are related with this topic:

- **Keller JG\***, Quevedo DF\*, Faccani L, Costa AL, Landsiedel R, Werle K, Wohlleben W. *Dosimetry in vitro – exploring the sensitivity of deposited dose predictions vs. affinity, polydispersity, freeze-thawing, and analytical methods*. Nanotoxicology 2020. DOI: 10.1080/17435390.2020.1836281
- Wiemann M, Sauer UG, Vennemann A, Bäcker S, **Keller JG**, Ma-Hock L, Wohlleben W, Landsiedel R. *In Vitro and In Vivo Short-Term Pulmonary Toxicity of Differently Sized Colloidal Amorphous SiO<sub>2</sub>*. Nanomaterials (Basel) 2018 Mar, Volume 8(3), pp.160. Doi: 10.3390/nano8030160.
- Ma-Hock L, Sauer UG, Ruggiero E, **Keller JG**, Wohlleben W, Landsiedel R. *Using Nanomaterial In Vivo Burden Data for In Vitro Dose Setting (OBIV)*. Small, submitted September 2020.

## 2.3 CHOICE OF MATERIALS

The materials were chosen based on industrial relevance and available toxicity data, which will be exploited in the conclusion section of this thesis (obtained from *in vivo* toxicity studies; the references for the toxicity data are given in the list below). [125] Pharmaceutical preparations such as micelles and phospholipid vesicles were out of scope. This work aims to identify the relevance of physicochemical properties by systematic variation and testing of a broad set of materials. The chosen set varies in chemical composition, size, shape, crystallinity, and surface treatment. The test set of ENM covers a variety of metal oxide, metal, and organic nanomaterials (**Table 1**) and ranges in sizes between 7 and 500 nm. Identical materials were used both for dissolution and transformation, as well as for dosimetry studies. Most of the materials were sourced from the Joint Research Center (JRC) Nanomaterials Repository of the Organization for Economic Co-operation and Development (OECD) sponsorship program. [126]

These materials are sourced from large individual batches with significant industrial relevance. As provided by the ENM producer, the single batches are subsampled by JRC and procured as thoroughly characterized NMs for benchmarking, testing in research and development, and regulatory studies. The harmonization of test material within different labs furthermore allows the comparison and the reproduction of results. The most relevant ENM supplied by JRC are Ag NM300, BaSO<sub>4</sub> NM220, [127] Bentonite NM 600, CeO<sub>2</sub> NM211, CeO<sub>2</sub> NM212, [127-129] SiO<sub>2</sub> NM200, SiO<sub>2</sub> NM203, TiO<sub>2</sub> NM102, two UV active nanomaterials TiO<sub>2</sub> NM104 coated with Al<sub>2</sub>O<sub>3</sub>, and TiO<sub>2</sub> NM105, [43] ZnO NM110 and triethoxycapryl silane coated ZnO NM111. [43] Ag Sigma was purchased from Sigma-Aldrich. The non-nano sized reference material BaSO<sub>4</sub> IRMM381 was provided by the Institute for Reference Materials and Measurements (IRMM). [130, 131] Four additional silica ENMs with different sizes of untreated, colloidal silica: Levasil 50, Levasil 100, Levasil 200, and Levasil 300 were all commercially acquired from Akzo Nobel N. V.. [132] Two more nanoforms with surface coatings, which are based on Levasil 200, were tested: SiO<sub>2</sub>\_aminated and SiO<sub>2</sub>\_phosphonated. [133] Nouryon Pulp and Performance Chemicals AB provided Si\_Std, Si\_anis\_Std, Si\_Al, Si\_anis\_Al, and Si Silane. SiO<sub>2</sub> Amorphous IUF was provided by the Leibniz Research Institute for Environmental Medicine (IUF). The Institute for Occupational Medicine (IOM) procured SiO<sub>2</sub> DQ12 for the PATROLS project. The Korea Research Institute of Standards and Science (KRISS) produced and provided the food-grade TiO<sub>2</sub> E171. Additionally, a broad set of relevant pigments was investigated, including three different kinds of iron oxides, two CuPhthalocyanines, and three Diketopyrrolopyrrole. Cu\_Phthalocyanine\_nano Cu\_Phthalocyanine\_halogen, DPP\_nano, DPP\_non\_nano, DPP\_premixed, Fe<sub>2</sub>O<sub>3</sub>\_nano\_A, and the Fe<sub>2</sub>O<sub>3</sub>\_nano\_B were produced and provided by BASF SE. [134] The borderline-nano Fe<sub>2</sub>O<sub>3</sub>\_larger was provided by Rockwood Holdings Inc. [135] Powdered CuO was supplied by PlasmaChem GmbH. [136]

With this selection, the most important material categories shown in Figure 1 are covered. The methods developed within this thesis can, therefore, be applied to REACH registration of ENMs.

## MOTIVATION AND OBJECTIVES

Table 1 Overview of physicochemical parameters of materials used within this thesis.

Material	CAS Number	Minimum external dimension (TEM or * AUC)	Shape (TEM)	Specific Surface Area (BET)	Surface Treatment and Crystallinity
		[nm]	Descriptive	[m <sup>2</sup> /g]	
Ag NM300	7440-22-4	6.6	Spheroidal	Not applicable	Polymer Treatment; amorphous
Ag Sigma	7440-22-4	28	Spheroidal	6.4	PVP; crystalline
Amorphous SiO <sub>2</sub> IUF	7613-86-9	9	Spheroidal	192	Si; amorphous
BaSO <sub>4</sub> NM220	7727-43-7	32	Spheroidal	41	Ba; orthorombic
BaSO <sub>4</sub> IRMM381	7727-43-7	234	Spheroidal	2.5	Ba; orthorombic
Bentonite NM600	1302-78-9	1362	Platelets	52	
CeO <sub>2</sub> NM211	1306-38-3	15	Spheroidal	66	Ce; cubic, ceriantite
CeO <sub>2</sub> NM212	1306-38-3	40	Mixed spheroidal + platelets	27	Ba; orthorombic
CuO	1317-38-0	24	Spheroidal	34	Cu
Cu_Phthalo_halogen	1328-53-5	14	Platelet	69	Cu; 72% crystalline
Cu_Phthalo_nano	147-14-8	17	Spheroidal	53	Cu; 82% crystalline
DPP_nano	84632-65-5	36	Spheroidal	94	DPP; 65 % crystalline
DPP_non-nano	84632-65-5	233	Spheroidal	16	DPP; 75 % crystalline
DPP_premixed	84632-65-5	400	Spheroidal	17	Acrylic acid; monoclinic
Fe <sub>2</sub> O <sub>3</sub> _nano_A	1309-37-1	15-130 x 4-21	Rods	107	Fe; 95 % crystalline
Fe <sub>2</sub> O <sub>3</sub> _nano_B	52357-70-7	37	Spheroidal	30	Fe; 95 crystalline
Fe <sub>2</sub> O <sub>3</sub> _larger	1309-37-1	48		12	Fe
Levasil 50	7613-86-9		Spheroidal	50	Si; amorphous
Levasil 100	7613-86-9		Spheroidal	100	Si; amorphous

MOTIVATION AND OBJECTIVES

<b>Levasil 200</b>	<b>7613-86-9</b>	15	Spheroidal	200	Si; amorphous
<b>Levasil 300</b>	<b>7613-86-9</b>		Spheroidal	300	Si; amorphous
<b>SiO<sub>2</sub>_amino</b>	<b>7613-86-9</b>	15	Spheroidal	200	Amino; amorphous
<b>SiO<sub>2</sub> NM200</b>	<b>7613-86-9</b>	13	Spheroidal	190-220	Si; amorphous
<b>SiO<sub>2</sub> NM203</b>	<b>7613-86-9</b>	26	Spheroidal	213	Si; amorphous
<b>Silica_Al</b>	<b>7631-86-9</b>	13	Spheroidal	175	Al; amorphous
<b>Silica_anis_Al</b>	<b>7631-86-9</b>	5	Spheroidal	427	Al; amorphous
<b>Silica_silane</b>	<b>7631-86-9</b>	11	Spheroidal	216	Si; amorphous
<b>Silica_Std</b>	<b>7631-86-9</b>	11	Spheroidal	209	Si; amorphous
<b>Silica_anis_Std</b>	<b>7631-86-9</b>	11	Spheroidal	214	Si; amorphous
<b>SiO<sub>2</sub> DQ12</b>	<b>14808-60-7</b>	112	Spheroidal	11	Si; 87% crystalline
<b>SiO<sub>2</sub>_phosphonate</b>	<b>7613-86-9</b>	15	Spheroidal	200	Phosphonate, amorphous
<b>TiO<sub>2</sub> E171</b>	<b>13463-67-7</b>	169	Spheroidal	11	Ti, Anatase
<b>TiO<sub>2</sub> NM102</b>	<b>1317-70-7</b>	35	Spheroidal	80	Ti
<b>TiO<sub>2</sub> NM104</b>	<b>13463-67-7</b>	30	Spheroidal	60	Ti
<b>TiO<sub>2</sub> NM105</b>	<b>1317-80-2</b>	21	Spheroidal	51	Ti; anatase + rutile
<b>ZnO NM110</b>	<b>1314-13-2</b>	42	mixed spheroidal and rods	12	Zn; zincite
<b>ZnO NM111</b>	<b>1314-13-2</b>	80	Spheroidal	14	Triethoxycaprylsilane; zincite
<b>ZnO NM113</b>	<b>1314-13-2</b>	174	Spheroidal	11	Zn; zincite





---

### **3 RESULTS**

### 3.1 PUBLISHED RESULTS

#### 3.1.1 The nanoGRAVUR framework to group (nano) materials for their occupational, consumer, environmental risks based on a harmonized set of material properties, applied to 34 case studies

Wohlleben W, Hellack B, Nickel C, Herrchen M, Hund-Rinke K, Kettler K, Riebeling C, Haase A, Funk B, Kühnel D, Göhler D, Stintz M, Schumacher C, Wiemann M, **Keller JG**, Landsiedel R, Broßell D, Pitzko S, Kuhlbusch TAJ.

*Nanoscale*, 2019,11, 17637-17654  
<https://doi.org/10.1039/C9NR03306H>

**Author contribution:** In this work, the author was responsible for the data generation for several physchem parameters such as dissolution, transformation, and dosimetry for all case study materials as well as the interpretation of the results and illustration of data tables.

#### **Abstract:**

The project nanoGRAVUR (BMBF, 2015–2018) developed a framework for grouping of nanomaterials. Different groups may result for each of the three distinct perspectives of occupational, consumer and environmental safety. The properties, methods and descriptors are harmonized between the three perspectives and are based on: Tier 1 intrinsic physico-chemical properties (what they are) or GHS classification of the non-nano-form (human tox, ecotox, physical hazards); Tier 2 extrinsic physico-chemical properties, release from nano-enabled products, *in vitro* assays with cells (where they go; what they do); Tier 3 case-specific tests, potentially *in vivo* studies to substantiate the similarity within groups or application-specific exposure testing. Amongst all properties, dissolution and transformation are least modulated by different nanoforms within one substance, whereas dustiness, dispersion stability, abiotic and especially *in vitro* surface reactivity vary more often between different nanoforms. The methods developed or selected by nanoGRAVUR fill several gaps highlighted in the ProSafe reviews and are useful to implement (i) the concept of nanoforms of the European Chemicals Agency (ECHA) and (ii) the concept of discrete forms of the United States Environmental Protection Agency (EPA). One cannot assess the significance of a dissimilarity, if the dynamic range of that property is unknown. Benchmark materials span dynamic ranges that enable us to establish bands, often with order-of-magnitude ranges. In 34 case studies we observed high biological similarity within each substance when we compared different (nano)forms of SiO<sub>2</sub>, BaSO<sub>4</sub>, kaolin, CeO<sub>2</sub>, ZnO, organic pigments, especially when we compared forms that are all untreated on the surface. In contrast, different Fe<sub>2</sub>O<sub>3</sub> or TiO<sub>2</sub> (nano)forms differ more significantly. The same nanoforms were also integrated in nano-enabled products (NEPs) for automotive coatings, clinker-reduced cements, cosmetic sunscreen, and lightweight polymers.



Cite this: DOI: 10.1039/c9nr03306h

## The nanoGRAVUR framework to group (nano) materials for their occupational, consumer, environmental risks based on a harmonized set of material properties, applied to 34 case studies†

Wendel Wohlleben,<sup>a</sup> Bryan Hellack,<sup>b</sup> Carmen Nickel,<sup>b</sup> Monika Herrchen,<sup>c</sup> Kerstin Hund-Rinke,<sup>c</sup> Katja Kettler,<sup>d</sup> Christian Riebeling,<sup>d</sup> Andrea Haase,<sup>d</sup> Birgit Funk,<sup>e</sup> Dana Kühnel,<sup>f</sup> Daniel Göhler,<sup>g</sup> Michael Stintz,<sup>g</sup> Christian Schumacher,<sup>h</sup> Martin Wiemann,<sup>i</sup> Johannes Keller,<sup>a</sup> Robert Landsiedel,<sup>a</sup> Dirk Broßell,<sup>j</sup> Sabine Pitzko<sup>j</sup> and Thomas A. J. Kuhlbusch<sup>\*,j,k</sup>

The project nanoGRAVUR (BMBF, 2015–2018) developed a framework for grouping of nanomaterials. Different groups may result for each of the three distinct perspectives of occupational, consumer and environmental safety. The properties, methods and descriptors are harmonised between the three perspectives and are based on: Tier 1 intrinsic physico-chemical properties (what they are) or GHS classification of the non-nano-form (human tox, ecotox, physical hazards); Tier 2 extrinsic physico-chemical properties, release from nano-enabled products, *in vitro* assays with cells (where they go; what they do); Tier 3 case-specific tests, potentially *in vivo* studies to substantiate the similarity within groups or application-specific exposure testing. Amongst all properties, dissolution and transformation are least modulated by different nanoforms within one substance, whereas dustiness, dispersion stability, abiotic and especially *in vitro* surface reactivity vary more often between different nanoforms. The methods developed or selected by nanoGRAVUR fill several gaps highlighted in the ProSafe reviews, and are useful to implement (i) the concept of nanoforms of the European Chemicals Agency (ECHA) and (ii) the concept of discrete forms of the United States Environmental Protection Agency (EPA). One cannot assess the significance of a dissimilarity, if the dynamic range of that property is unknown. Benchmark materials span dynamic ranges that enable us to establish bands, often with order-of-magnitude ranges. In 34 case studies we observed high biological similarity within each substance when we compared different (nano) forms of SiO<sub>2</sub>, BaSO<sub>4</sub>, kaolin, CeO<sub>2</sub>, ZnO, organic pigments, especially when we compared forms that are all untreated on the surface. In contrast, different Fe<sub>2</sub>O<sub>3</sub> or TiO<sub>2</sub> (nano)forms differ more significantly. The same nanoforms were also integrated in nano-enabled products (NEPs) for automotive coatings, clinker-reduced cements, cosmetic sunscreen, and lightweight polymers.

Received 16th May 2019,  
Accepted 19th July 2019  
DOI: 10.1039/c9nr03306h  
rsc.li/nanoscale

## Introduction

Particles, *i.e.*, minute pieces of matter with defined physical boundaries,<sup>2</sup> are commercially available in a myriad of grades that are optimised in composition, size, shape and coating for

specific applications.<sup>3,4</sup> If the number metric median diameter of the constituent particles is below 100 nm, that grade is identified as nanomaterial for regulatory purposes by the definition that was recommended by the European Commission.<sup>5</sup> The identification as nanomaterial is explicitly

<sup>a</sup>BASF SE, Dept. of Material Physics and Dept. of Experimental Toxicology and Ecology, 67056 Ludwigshafen, Germany

<sup>b</sup>Institute of Energy and Environmental Technology e. V. – IUTA, 47229 Duisburg, Germany

<sup>c</sup>Fraunhofer Institute for Molecular Biology and Applied Ecology, 57392 Schmallenberg, Germany

<sup>d</sup>German Federal Institute for Risk Assessment (BfR), Department of Chemical and Product Safety, 10589 Berlin, Germany

<sup>e</sup>Zoz GmbH, 57482 Wenden, Germany

<sup>f</sup>Helmholtz Centre for Environmental Research GmbH - UFZ, Leipzig, Germany

<sup>g</sup>Research Group Mechanical Process Engineering, Institute of Process Engineering and Environmental Technology, Technische Universität Dresden, D-01062 Dresden, Germany

<sup>h</sup>German Social Accident Insurance e. V. -DGUV, 10117 Berlin, Germany

<sup>i</sup>IBE R&D Institute for Lung Health gGmbH, 48149 Münster, Germany

<sup>j</sup>Federal Institute for Occupational Safety and Health (BAuA), 44149 Dortmund, Germany. E-mail: Kuhlbusch.Thomas@baua.bund.de

<sup>k</sup>CENIDE, University Duisburg-Essen, Germany

† Electronic supplementary information (ESI) available. See DOI: 10.1039/c9nr03306h

intended to be without regard to hazard or risk,<sup>5</sup> but triggers additional or more specific testing requirements from 2020 on the revised REACH Annexes.<sup>6</sup> Several frameworks have been proposed that structure the risk assessment of nanomaterials in tiered testing strategies,<sup>7</sup> often supported by elements of grouping and read-across strategies,<sup>8,9</sup> often targeting a reduction of animal testing by alternative methods.<sup>10–12</sup> The tiered testing strategies serve two main purposes:

a. Industry has an interest to ensure the safe use of novel nanomaterials early during development, using a minimum amount (milligrams) of available material and without animal testing. If the safety testing feeds back to optimize the balance of performance, safety, costs and sustainability (or to stop the development), then the term “safer-by-design” is often used to describe this good industrial practice. The comparison of a novel nanomaterial to benchmark materials with a well-known (eco)toxicological profile can support the confidence in the assessment, but it is unknown which material properties should be used to make that comparison.

b. European regulators have established the concept of nanoforms (NF, nanomaterial form of a chemical which is characterised by ranges of morphology, particle size distribution, surface chemistry, specific surface area) to register forms of a substance that are identified as nanomaterial in the substance dossier.<sup>13</sup> The data requirements in the revised REACH Annexes VI to X have been amended accordingly.<sup>5</sup> Concepts of similarity and grouping are relevant since “sets of similar nanoforms” can be registered, with a justification.<sup>5</sup> Registrants can use concept of grouping for such justification and can use read-across to fill data gaps of one NF (or one set) by existing data of the non-nano-form or of another NF (or another set) of the same substance, if there is a specific hypothesis why “source” and “target” form should be similar.<sup>14</sup> Although the guidance proposes specific properties to substantiate the similarity, it does not mark them as mandatory and lists no methods, nor descriptors, nor benchmark materials.<sup>14</sup>

There are numerous deficiencies of the existing regulatory guidances and of the published frameworks:

Most of the grouping frameworks, including the seminal NIOSH proposal<sup>15</sup> and its implementation,<sup>16</sup> the DF4nanogrouping framework<sup>17</sup> and its implementations,<sup>18–20</sup> limit their scope to human safety, more specifically to inhalation hazards. Regarding the prediction of the environmental hazard of nanomaterials two approaches are pursued. Besides modelling and the development of structure–activity–relationships,<sup>21</sup> only a single framework assesses the environmental hazard from a grouping perspective with proposed trigger values for the identified physico-chemical properties to be relevant for ecotoxicity of metals and metal oxides.<sup>22,23</sup> Several frameworks recognize that the integration of nanomaterials into nano-enabled products (NEPs) determines the material properties of the fragments that may be released throughout the life cycle<sup>24</sup> and screening e-tools such as the LICARA nanoscan,<sup>25</sup> GuideNano,<sup>26</sup> SUN,<sup>27,28</sup> select some relevant NEP properties, but no grouping framework integrates the safety of consumer use of NEPs or the safety of professional handling of NEPs.<sup>7</sup>

The DF4nanogrouping<sup>17,18</sup> selects specific methods of analysis, quantitative cut-offs and benchmark materials.<sup>7</sup> In contrast, the ECHA nanomaterial grouping guidance refers to the generic physico-chemical guidance<sup>29</sup> that lists numerous optional methods, and refers also to the DF4nanogrouping method selection Tables S2 and S4.<sup>†14</sup> Often the frameworks used the same terminology and some select the same material properties to compare (nano)-forms,<sup>7</sup> but many properties may be determined by different analytical methods, and for some the reliability and standardisation is insufficient.<sup>30</sup> Additionally, there are numerous options of data reduction from the multidimensional raw data (images, spectra, distributions) to simple scalar descriptors (one numerical value) that can quantify the similarity between (nano)forms or the homogeneity of groups.

The project nanoGRAVUR (2015–2018) was funded by the German Federal Ministry of Research, and by industry and comprised partners from academia, regulatory agencies, insurance companies and industry. This paper presents the nanoGRAVUR grouping framework for nanomaterials and its implementation by selected methods of analysis and quantitative benchmark material values. Different groups may result for each of the three distinct perspectives of *Occupational*, *Consumer* and *Environmental safety (OCE)*, but rely on a harmonised set of material properties with specific methods of analysis, descriptors and ranges. The proof of concept is provided *via* quantitative data on 34 case studies.

## Framework and selection of properties

The nanoGRAVUR grouping framework (Fig. 1) consists of three tiers. Tier 1 determines intrinsic physicochemical properties (“what they are”) and/or the GHS classification of the non-nano form (human tox, ecotox, physical hazards). Tier 1 allows the user to describe concerns and accordingly a grouping hypothesis. Depending on the purpose of grouping (Table 1), Tier 2

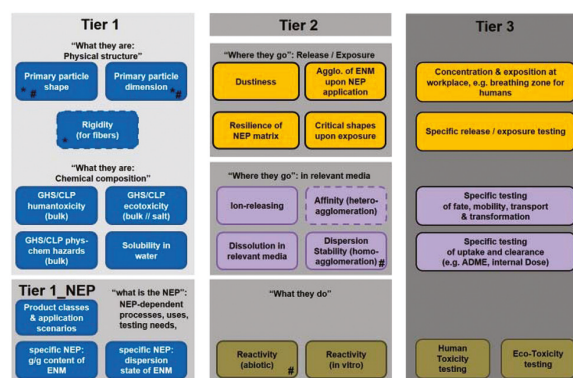


Fig. 1 nanoGRAVUR grouping framework. ENM: engineered nanomaterial; NEP: nano-enabled product; GHS: globally harmonised system; CLP: classification and Labelling of Products; \* denotes properties used by ECHA to differentiate nanoforms; # denotes properties used by EPA to differentiate discrete forms.<sup>†</sup> Dashed boxes denote properties with no sufficiently developed method.

**Table 1** nanoGRAVUR selection of material properties. The set is harmonised across the three purposes of grouping for (O) occupational, (C) consumer and (E) environmental risks, includes the risks in the value chain of nano-enabled products (NEP), and can be compared to regulatory guidance and previous frameworks that addressed selected purposes.<sup>1,13,14,17,22</sup> Proposed: property is not mandatory, but proposed for decision-making; criterion: property with quantitative cut-off for decision-making; supplementary: property without use in decision-making; qualifier: required to select appropriate conditions in further testing. The symbols for maturity of the methods are indicative of technology readiness level (TRL) 4 or lower (–), 5 to 7 (0), 8 or higher (+)

	Properties	nanoGRAVUR data in case studies	nanoGRAVUR (O) occupation (C) consumer (E) environment	nanoGRAVUR method TRL	EPA discrete forms (2017)	ECHA nanoform registration, best practice (2017)	ECHA grouping guidance (2017)	DF4nanogrouping framework (2015)	Environmental hazard grouping framework (2018)
What they are	Primary particle shape	✓	Criterion O,C,E	+	Criterion	Criterion	Proposed	Criterion O	Criterion E
	Primary particle dimension	✓	Criterion O,C,E	+	Criterion	Criterion	Proposed	Criterion O	Criterion E
	Composition + GHS (incl. impurities)	✓	Criterion O,C,E	+	Criterion	Criterion	Proposed	Criterion O	Criterion E
	Specific surface area (BET/VSSA)	✓		+	Criterion		Proposed	Suppl. O	
	Surface chemistry (descriptive)	✓		0	Criterion	Criterion	Proposed	Suppl. O	
	Surface charge (zeta-potential)	✓		+	Criterion		Proposed	Suppl. O	
	Hydrophobicity	✓		–			Proposed	Suppl. O	
	Rigidity (for fibers)			Proposed O	–				
	NEP classes & intended use scenarios	(✓)		Criterion (NEP) O,C					
	Specific NEP: g g <sup>-1</sup> content of ENM	✓		Criterion (NEP) O	+				
	Specific NEP: dispersion state of ENM	(✓)		Criterion (NEP) O,C	0				
	Where they go: release/exposure	Dustiness	✓	Criterion O	+			Proposed	Qualifier O
Critical shapes upon exposure		(✓)	Criterion (NEP) O,C	0					
Agglo. of ENM upon NEP application		(✓)	Criterion (NEP) O,C	0					
Where they go: in relevant media	Resilience of NEP Matrix	✓	Criterion (NEP) O,C	+					
	Dispersability (dispersion stability)	✓	Criterion O,C,E	+0			Proposed	Criterion O	
	Solubility in water (screening test)	✓	Criterion O,C,E	+			Proposed	Criterion O	
	Dissolution rate in relevant media	✓	Criterion O,C,E	0			Proposed	Criterion O	
	Ion releasing	(✓)	Criterion E	+0					Criterion E
	Transformation “change of what they are”	✓	Criterion E (Tier 3)	0–					
	Mobility (in soils)	✓	Criterion E (Tier 3)	+					
What they do	Mobility (systemic) by altern. Method		Criterion C	–					
	Affinity (heteroagglomeration)		Proposed E	0					
	Reactivity (abiotic)	✓	Criterion O,C,E	+0			Proposed	Criterion O	Criterion E
	Reactivity ( <i>in vitro</i> )	✓	Criterion O,C	+0				Criterion O	
	Reactivity (photo-)			–			Proposed		

determines extrinsic physicochemical properties, the release from nano-enabled products (NEPs, if in scope) and/or *in vitro* assays (“what is the NEP”; “where they go”; “what they do”). If the assessment remains inconclusive, Tier 3 deals with case-specific testing, potentially *in vivo* studies to substantiate the similarity within groups or application-specific exposure testing.

The nanoGRAVUR grouping framework serves three purposes of testing and grouping, that each require a different perspective: occupational safety, environmental safety, consumer safety. Aspects of both hazard and exposure are considered, and the intended use in NEPs is systematically integrated in the testing strategy. Depending on the purpose of grouping, only a sub-selection of the material properties is required. The assessment is guided by

- i. the purpose of grouping (Table 1)
- ii. tiers with increasing specificity of testing (Fig. 1).

Compared to the properties that are proposed (but not mandatory) by the ECHA guidance,<sup>14</sup> a core set of properties overlaps, some properties were added, and some were tested but not selected. Despite this difference, we view the nanoGRAVUR framework as an implementation of the ECHA guidance: if the purpose of grouping is to assess the risk of occupational handling of powders (“O” in Table 1), our choice of properties is a *selection* of the properties proposed by ECHA, without additions. The reason for *selecting* is that we do not group by *intrinsic* properties that are only a proxy of biological interactions. This concerns especially properties that describe surface chemistry including hydrophobicity and charge. Instead, we group by *extrinsic* properties (dispersibility, biological reactivity, dissolution in biological and environmental media), that assess the interactions more directly, and correlate to human and ecological hazard and fate results.<sup>31–33</sup> The additional properties decrease the uncertainty of risk estimation at limited additional efforts, as they are descriptive (e.g. NEP categories/intended uses), rely on simple methods of analysis (see next section), and widen the scope to NEPs as relevant for the value chains related to professionals, consumers and the environment. While the NEP does not need to be included in the assessment, at least the intended use of the engineered nanomaterial (ENM) needs to be known to select a “relevant medium” in Tier 2. This reasoning was already implemented in the DF4nanogrouping,<sup>17</sup> but is expanded here to environmental media.

In the stepwise methodology of the ECHA grouping guidance, the nanoGRAVUR Tier 1 data requirements of “Primary particle shape”, “Composition (incl. impurities)” with the corresponding “GHS/CLP human toxicity (bulk)”, “GHS/CLP ecotoxicity (bulk)” and “GHS/CLP physical hazards (bulk)” constitutes ECHA Step 1. We derive our hypothesis of most important hazards *via* the data reduction to quantitative property ranges as a simple implementation of ECHA steps 2 to 4. The only grouping decision that can be taken after Tier 1 is the grouping of a

highly soluble NF with their non-nano-form of the same substance, based on water solubility with a specific method of analysis and cut-off value (Table 2). All other cases will require testing by Tier 2 methods to substantiate the similarity of different NFs in a group. The testing in Tier 2 constitutes ECHA Steps 5 to 6, and the focus on extrinsic properties is supported explicitly by the ECHA guidance, reading “*It should be noted that differences in the physical parameters seen when characterising the nanoforms does not per se exclude the possibility to apply read-across. Indeed, similarities in the parameters related to the behaviour (e.g. solubility) or those relating to their reactivity may be more important to consider when building a read-across justification*”.<sup>14</sup> The Tier 1\_NEP data requirement of “NEP classes & intended use scenarios” adds a grouping hypothesis by relevant release and exposure pathways, and is essential to select relevant media in Tier 2. Of note, the same approach is taken by the US-Canada Regulatory Cooperation Council, where the prioritization of either of the human exposure pathways trigger dissolution testing in each different media, complemented by composition ionic toxicity, shape, and surface reactivity.<sup>34</sup>

The nanoGRAVUR scheme for ecological hazard grouping requires only Tier 2 results, and is consistent with the previous grouping developed on the basis of tests with algae, daphnia and fish embryo, that focused on ion release, reactivity, and shape<sup>22</sup> and its further development.<sup>23</sup> The additional property “surface affinity” was added, and further adaptations are not excluded. Grouping regarding environmental fate was based on a preliminary description of processes. Depending on the complexity of the studies, these are Tier 2 (e.g. dissolution in environmental media) or Tier 3 tests (e.g. mobility in soil and biological transformation). For the latter, no triggers were identified but these tests need to be performed to enable fate grouping.<sup>23</sup> The proposed methods of analysis and some quantitative cut-off values are listed in Table 2.

Analogously, if the validity of the hypothesis for grouping by occupational safety remains inconclusive after Tier 2, specific testing in Tier 3 is possible. This may involve exposure testing at specific workplaces and may involve *in vivo* animal studies.

In Tier 2, the assessment of exposure is approximated by dustiness and NEP properties that are most relevant for release or emission. This enables risk-based groupings, but still supports hazard-based groupings as prioritised in REACH. Thus, a grouping hypothesis might be that different NEPs that have similar matrices with different embedded ENMs are similar in the rate and form of released fragments, and thus also similar in the hazard by such fragments, as motivated by results on human hazard<sup>35–40</sup> and ecological hazard<sup>24,41</sup> of such fragments. Specific methods support the assessment of emission, fate and transport behaviour, as detailed in the following chapter, and thus expand from the groupings perspective of environmental hazard<sup>22</sup> and human hazard.<sup>17</sup>



**Table 2** Properties, harmonised methods of analysis, descriptors, and benchmark materials as proposed by the nanoGRAVUR grouping-framework for nanomaterials. Additional information on methods is provided in the ESI.† The optional scoring of the possible values of the descriptors implements a data reduction to indexed property bands

Properties	Methods	Descriptors, [metric]	Benchmark-materials	Optional: data reduction to indexed property bands
Primary particle shape	NanoDefine methodology (consistent with ECHA nanoforms)	Minimum external dimension [nm] + aspect ratio [unitless]	NanoDefine IRMM-repository NanoDefine IRMM-repository	Sphere 1, rod 2, platelet 3, fibre 4 Spherical and $\varnothing < 10$ nm 1; other 2
Primary particle dimension				
Rigidity (for fibres)	No valid method established yet	Modulus of elasticity [MPa] (for MWCNT: diameter [nm]) Consider impurities >1%	NM400 (10 nm, non-rigid)//NM401 (67 nm, rigid) Not required	Not established
GHS CLP (bulk) humantoxicity, ecotoxicity	Identify composition by XRF (or ICPMS, XRD), compare to CLP of Bulk if existent.			
Solubility in water	OECD TG draft: in 5 mM NaHCO <sub>3</sub> , pH7 at 10 mg L <sup>-1</sup> , 24 h	Document mg L <sup>-1</sup> of metal ion; the TG assesses % dissolved	TG specifies CuO (<50 nm, SA: 29 m <sup>2</sup> g <sup>-1</sup> , non-coated). On CuO (PlasmaChem): 0.32 mg L <sup>-1</sup> dissolved Not required	0 not significant/1 low (<1 mg L <sup>-1</sup> )/ 2 mid (<10 mg L <sup>-1</sup> )/3 high (<50 mg L <sup>-1</sup> )
Physico-chemical hazards (bulk)	Bulk GHS CLP	H-phrases		
Product classes and application scenarios	None (descriptive)		Sunscreen//plastics (solid polymers)//cement	Consumption by consumer//contained in consumer products//industrial or professional use
Specific application NEP: state of dispersion of ENM	Assignment to three fixed categories, which determine the disperse system as well as the type of embedding and agglomeration		Not required	Disperse system: 1 composites//2 suspensions//3 powder Embedding into a matrix: 1 complete embedding//2 partly embedding//3 attachment//4 isolated Agglomeration in matrix: 1 highly agglomerated//2 slightly agglomerated//3 individualised
Specific application in NEP: content (g g <sup>-1</sup> ) of ENM in NEP		Mass-% ENM in NEP	Not required	0 low/1 mid/2 high with low <5 wt%; mid: 5 to 50 wt%; high >50 wt%
Dustiness	EN 15051 methods (RD, CDD) and alternative methods with similar strain intensity (e.g. SRD, SHA, DEM) or FLU (esp. for fibres)	Dustiness coefficient dependent on mass and number [mg kg <sup>-1</sup> , # kg <sup>-1</sup> ] factor of emission in number metric	Fibre benchmarks in FLU method: NM400 (low dusting tendency: 150 mg <sup>-1</sup> h <sup>-1</sup> ), NM401 (high dusting tendency: 8000 mg <sup>-1</sup> h <sup>-1</sup> )	(0 low/1 mid/2 high) Particle ranges in DEM method: inhalable: low <4000 mg kg <sup>-1</sup> , moderate 4000–15 000 mg kg <sup>-1</sup> , high >15 000 mg kg <sup>-1</sup> Thoracic: low <1847 mg kg <sup>-1</sup> , moderate 1847–5000 mg kg <sup>-1</sup> , high >5000 mg kg <sup>-1</sup> Alveolar: low <70 mg kg <sup>-1</sup> , moderate 70 mg kg <sup>-1</sup> –300 mg kg <sup>-1</sup> , high >300 mg kg <sup>-1</sup> Fibre ranges <0.04 (low), 0.04–0.4 (medium), >0.4 (high)
Agglomeration of ENM upon application of NEP	For fibres: dustiness For sprays: intended application. Each with morphological analysis of the dust	Fibres: volumetric share of constituent fibres in agglomerates in relation to amount of single fibres within the dust (%) Tensile strength [MPa] or elongation at break [%]	Fibre benchmarks: ARIGM001 (X <sub>v</sub> = 0.003), NTX-3 (X <sub>v</sub> = 0.913)	
Resilience of NEP matrix	For mechanical stress: tensile elongation (ISO method)		Tensile strength (inverse to sanding release rates): • Low resilience (<10 N mm <sup>-2</sup> ): cement • Mid resilience (10–100 N mm <sup>-2</sup> ): epoxy, PA, acrylic • High resilience (>100 N mm <sup>-2</sup> ): steel, aluminium alloy	

Table 2 (Contd.)

Properties	Methods	Descriptors, [metric]	Benchmark-materials	Optional: data reduction to indexed property bands
Critical dimensions upon exposure	Dustiness + SEM analysis of aerosol sample: form	Amount of WHO-fiber-like objects from total number (%)	NM400: 0.4% NM401: 20.4%	Not established
Ion-releasing	OECD TG draft: screening method 10 mg L <sup>-1</sup> ENM in relevant medium	Dissolved ions [mg L <sup>-1</sup> ]	Ion releasing if >0.1 mg L <sup>-1</sup> metal ions. CuO in env. medium >0.8 mg L <sup>-1</sup> Cu <sup>2+</sup>	0: no/1: yes
Dissolution in relevant media	Flow-through dissolution: ICPMS quantification of ions	Rate <i>k</i> [ng cm <sup>-2</sup> h <sup>-1</sup> ]		
Transformation “changes of what they are”	Flow-through dissolution: TEM, (SAD, XPS) detection on remaining solids	Comparison of shape and size (optionally also crystallinity) before/after dissolution testing	For lysosomal dissolution: • Non-persistent, high dissol. (ZnO NM110) • Non-persistent, significant transformation (BaSO <sub>4</sub> NM220) • Low dissolution, significant transformation (SiO <sub>2</sub> NM203) • Low dissol., low transform. (CeO <sub>2</sub> NM212) For environmental transformation: BaSO <sub>4</sub> NM220 (particles dissolve but become more crystalline) TiO <sub>2</sub> NM105 10–90%, Ag NM300 >90% (from TG318) tbd.	For lysosomal dissolution: 1: non persistent high dissolution <i>k</i> > 100 ng cm <sup>-2</sup> h <sup>-1</sup> 2: non persistent significant transformation <i>k</i> = 1–100 ng cm <sup>-2</sup> h <sup>-1</sup> 3: low dissolution significant transformation <i>k</i> < 1 ng cm <sup>-2</sup> h <sup>-1</sup> 4: low dissolution, low transformation <i>k</i> < 1 ng cm <sup>-2</sup> h <sup>-1</sup> For environmental transformation: 0: non persistent, high transformation 1: no/low transformation <10% unstable (0)/intermediate (1)/>90% stable (2) (from TG318) No 0/yes 1
Homo-agglomeration	TG318 in relevant medium (instead of 3 × 3 Ca × NOM media)	Attachment efficiency ( <i>α</i> ) or fraction of attached particles		
Affinity (hetero-agglomeration)	tbd. possibly Geitner <i>et al.</i> ES&T 2016 or microscopic qualitative analysis relative to benchmark			
Mobility	Soil columns based on OECD TG 312	Transport distance [% of total length]	tbd	1: high or breakthrough (100%), 2: mobile in soil column, 3: no mobility
Reactivity (abiotic)	ESR (ecotoxicity), ESR + FRAS (human toxicity)	ESR: relative to LoD if 1.3 × negative control: mBOD (CPH) and mBOD(DMPO)	ESR: BaSO <sub>4</sub> (neg) vs. CuSO <sub>4</sub> (pos)	Additive scoring of ESR/FRAS: significant above LoD (+1/3 point), above 10% of positive control (+1 point)
Reactivity ( <i>in vitro</i> )	NR8383 dose response	FRAS: relative to LoD and positive benchmark: sBOD and mBOD • LDH (LOAEC) [μg mL <sup>-1</sup> ] • GLU (LOAEC) [μg mL <sup>-1</sup> ] • TNF (LOAEC) [μg mL <sup>-1</sup> ] • H <sub>2</sub> O <sub>2</sub> (LOEAC) [μg mL <sup>-1</sup> ]	FRAS positive benchmark: Mn <sub>2</sub> O <sub>3</sub> (sBOD = 2866 nmolTEU m <sup>-2</sup> ENM). No benchmark required	1: low, 2: mid-low, 3: mid-high, 4: high Score = number of vectors with significant effects at surface dose of 0.006 m <sup>2</sup> mL <sup>-1</sup>
	NRK-52E protein carbonylation	Carbonyl intensity rel. to positive control.	CuO (positive control)	Not established
<b>Additional properties that were tested in case studies but not selected for the nanoGRAVUR framework</b>				
Surface chemistry	Descriptive	Not required	Not required	1 untreated; 2 hydrophilic functionalization; 3 hydrophobic functionalization; 4 core-shell coating
Hydrophobicity	Water sessile drop	Contact angle (°)	Not required	F <sub>oil</sub> = hydrophilic, 0 to 90°; F <sub>ob</sub> = hydrophobic, >90°
Surface charge	Electrophoretic mobility	Zeta potential at pH7, mV	Not established	Not established
Reactivity (photo-)	Rhodamine-B-degradation	Photon efficiency (unitless, %)	Not established	Not established



## Framework concept in comparison to other approaches

There are fundamentally different grouping approaches. *E.g.*, one may group not by measurement of material properties but by hazard testing. NIOSH grouped by *in vivo* potency.<sup>16</sup> This is equivalent to skipping Tiers 1 and 2, and performing only Tier 3 *in vivo*. However, the resulting groups have no logical relationship, as is provided by the intrinsic and extrinsic properties, and thus also deviates from the seminal NIOSH proposal of four groups delimited by shape, solubility, and bulk toxicity<sup>42</sup> that was the basis of the AGS BekGS527<sup>43</sup> and of the DF4nanogrouping,<sup>17</sup> and is still recognisable in the nanoGRAVUR scheme. Another grouping by toxicity was performed *via* cytokine profiling,<sup>44</sup> but the experimental effort to generate such data may prevent a robust and pragmatic regulatory use, and may be more appropriate for mechanistic studies. However, it is interesting to note that both the grouping by *in vivo* potency and the grouping by cytokine profiling result in groups given primarily by the substance composition, *e.g.* grouping TiO<sub>2</sub> NFs, ZnO NFs and non-nano-forms, SiO<sub>2</sub> NFs.<sup>16,44</sup> Yet another complementary categorisation was proposed by the FutureNanoNeeds project, combining by “information multiplexing” the physico-chemical properties, descriptors of the adsorbed corona (in an unspecified medium), and a mapping of the biologically accessible epitopes,<sup>45</sup> and the chemical basis of nano-bio interactions was thought to enable structure–activity-relationships.<sup>46</sup> With the sparse data on corona and epitopes, these concepts may be true but remain speculative. If validated, the FutureNanoNeeds concept might be an approach to group especially pharmaceutical nano-formulations by their systemic transport, but the specificity would fall short of the Tier 3 requirements of specific uptake and clearance tests, and the experimental workload might not be justified against an *in vivo* study as valid option. We do not consider pharmaceutical purposes here.

## Recommended methods to determine material properties

The selection of specific methods of analysis or combinations of methods is an integral element of the nanoGRAVUR grouping-framework. Table 2 specifies the selected methods of analysis, the data reduction to descriptors as well as recommended metrics, and representative benchmark materials (OECD NMs). Additional details on the SOPs are provided in the ESI.†

We harmonised the selection of methods across all different purposes of grouping, aiming to simplify the practical implementation, to reduce costs, and to maximise the multiple use of data. The ProSafe review on the reliability of methods for the regulatory assessment of nanomaterials indicated for each property several “preferred methods”, but

also discussed their limitations and knowledge gaps.<sup>30</sup> The overlap between that ProSafe preference and the nanoGRAVUR selection is substantial, and supports the robustness of the nanoGRAVUR grouping framework. The nanoGRAVUR method selection deviates rarely from the ProSafe preference, and fills some essential knowledge gaps, as discussed in the following.

### Tier 1 Methods for “what they are” properties

The methods and descriptors for “what they are” properties concerning particle size distribution, shape, and specific surface area are implemented according to the recommendation of the project NanoDefine for methods (TEM and BET for powders, analytical centrifuges for suspensions), and descriptors (number metrics median).<sup>47,48</sup> The sample preparation is an essential element and was included in the NanoDefine validation.<sup>49</sup> For the chemical composition we agreed with ProSafe that ICPMS is suitable, but recommend XRF as digestion-free proxy for composition and all inorganic impurities. Properties that were not selected for the nanoGRAVUR framework were nonetheless determined for the case studies by methods recommended by ProSafe, *i.e.* crystalline phase by XRD, surface hydrophobicity by contact angle measurement, surface chemistry by XPS, surface charge *via* zeta potential by electrophoretic analyses.

### Tier 1\_NEP Methods for “what is the NEP” properties

Description of “what is the NEP” was beyond the scope of the ProSafe review but does not require methods other than the highly established elemental composition analysis (*e.g.* full digestion, then ICP-OES) and the morphological characterisation of a TEM cross-section to assess the dispersion state (examples in Fig. SI\_3,† criteria in Table 2). Producers of NEPs would not need to measure the composition if it is known from the production process.

### Tier 2 Methods for “where they go” properties

For the biodurability as central element of the “where they go” assessment we follow the advice of ProSafe to use the OECD draft TG on “solubility in aqueous media”, but restricted here to the “screening method”, which we use in Tier 1 to assess the solubility in water (documented as mg L<sup>-1</sup> value, assessed in the OECD draft TG as “% dissolved”) and in Tier 2 to assess the release of ions in a relevant medium (in mg L<sup>-1</sup> metric, since essential for ecotoxicity grouping). Once the intended use of the NEP is known, the release and the affected environmental compartment can be identified and in case of aquatic ecotoxicity the dissolution in the medium for the test organism can be determined.<sup>22</sup> We agreed with ProSafe that the “dissolution rate in physiological fluids [needs] to be further developed”, and showed on 24 (nano)forms of 7 substances that the flow-cell method as described by ISO/TR19057:2017 correctly predicts materials with low human *in vivo* and *in vitro* biodurability, and differentiates between nanoforms.<sup>50,51</sup> The detection of dissolved ions provides the ng cm<sup>-2</sup> h<sup>-1</sup> metric recommended by Oberdörster *et al.*,<sup>52</sup> is grouped by order of magnitude (*i.e.*, decadic ranges), and the group descriptors

include the assessment of transformation *via* the TEM analysis of remaining solids.<sup>51</sup> The “extended” test of the draft TG was not deemed useful in comparison.

Regarding the transport as another aspect of “where they go” properties, nanoGRAVUR does not endorse the full scope of OECD TG 318:2017, which requires to perform 54 measurements for 1 property per each NF, but instead we restricted the test to the specifically relevant medium to capture the dispersion stability by homoagglomeration. It is anyway not obvious how the multidimensional stability diagram over pH, NOM and Ca<sup>2+</sup> variation would be reduced to a simple descriptor to quantify the similarity of different NFs.<sup>33</sup> Reviews have considered methods to rank NEP matrix materials by their release rates during professional handling or consumer use. Our choice of tensile strength is highly standardised, but only relevant for mechanical stresses. For other release concerns we recommend to adhere to the stepwise decision-making process by the ISO draft TR of PG29, which would *e.g.* recommend the interlaboratory-tested NanoRelease protocol to assess and compare the form and rate of release by environmental weathering.<sup>53</sup>

There are numerous methods for the determination of dustiness data.<sup>54–56</sup> The most common methods (with conventional mg kg<sup>-1</sup> metric), which are standardised and also proposed by ECHA, are the rotating drum method (RD, EN 15051-2:2013) and the continuous drop-down method (CDD, EN 15051-3:2013). Since dustiness levels depend strongly on the used method,<sup>57,58</sup> different methods were tested concerning suitability, including the CDD method of EN 15051-3:2013, the small rotating drum method (ref. 54, CEN/TC 137; in # kg<sup>-1</sup> metric), the fluidizer method especially designed for fibres<sup>55,56</sup> (in # cm<sup>-3</sup>, # kg<sup>-1</sup> or # kg<sup>-1</sup> s<sup>-1</sup> metric), and a dustiness equivalent method (DEM, in mg kg<sup>-1</sup> metric) that is designed to mimic the CDD method by evaluating intrinsically measured size distributions (see ESI chapter 2.4.1†). Due to different assets and drawbacks of the methods and strongly limited comparability, no single method could be excluded or preferred, and it is recommended that for grouping purpose only data of one dustiness method should be used. For the case studies, results based on the DEM method were chosen, since DEM was able to provide dustiness data for most of the test substances in the metric proposed by ECHA (*i.e.*, in mg kg<sup>-1</sup> metric). For fibres, the average concentration was determined, in accordance with the metric of most exposure limit values.

### Tier 2 Methods for “what they do” properties

To assess “what they do” *via* surface reactivity, we combine the two abiotic assays of electron spin resonance (ESR, also known as electron paramagnetic resonance, with the DMPO and CPH spin traps as described by ISO/TS-18827:2017) and the very sensitive Ferric Reduction Ability of Serum (FRAS) assay<sup>59</sup> with the cell-based NR8383 macrophage assay. The NR8383 assay uses four standardised read-outs (LDH, ROS, GLU, TNF) and was pre-validated against *in vivo* inhalation studies.<sup>60</sup> We also found strong correlation between the abiotic assays and cell-based protein carbonylation, but did not see a necessity to

complicate the scheme by yet another redundant assay. (Bahl *et al.* in preparation) We slightly disagree with ProSafe on the strategy and terminology to assess surface reactivity. Redox potential and band gap are not synonyms as it seems to be suggested by Steinhäuser *et al.*<sup>30</sup> Instead, the LUMO band energy may be a more relevant parameter,<sup>19</sup> but even that remains a proxy for the actual biological oxidative damage. Hence, we do not define methods for any of the proxies, but group by the directly determined biological oxidative damage (sBOD).

For specific purposes, or when the evidence from Tier 2 remains inconclusive, the user is advised to overrule Tier 2 by a more specific testing in Tier 3. It is intended as backup with methods that are specific to a certain purpose of grouping, and that may be performed under conditions that are specific to a certain intended use with a scenario of emission or exposure. Human toxicity testing in Tier 3 may include *in vivo* studies, preferentially by OECD test guidelines, to support the similarity of different NFs and would overrule dissimilarity of screening methods in Tier 2. If exposure is relevant for the purpose of grouping, then Tier 3 may compare the similarity of personal exposure at specific workplaces. If environmental fate is central for the hypothesis of grouping, then Tier 3 might rely on environmental fate and transformation, for which OECD guidelines (*e.g.* TG312) exist but are not yet validated and standardised for nanomaterials. The Tier 3 is not fully detailed here, as the escalation to Tier 3 is anticipated to be the exception rather than the rule.

Two major method gaps remain: we believe that heteroagglomeration can be a predictive parameter for toxicity to environmental species such as algae. Therefore a screening method was developed that indicates the attachment efficiency to algae.<sup>23</sup> However, laboratory comparison tests and standardisation are still missing. It is also believed that the rigidity of fibres is predictive of adverse pulmonary effects,<sup>61</sup> but all methods are exploratory. An ongoing BAUA research project tests an approach based on curvature analysis and oscillatory measurement and may be one of the possible implementations.

Although the nanoGRAVUR framework can serve multiple purposes, it remains consistent with literature for the purpose of grouping by occupational hazard of handling nanomaterial powders: here the nanoGRAVUR framework and method selection coincide with the DF4nanogrouping, except that the Tier 2 dissolution is now assessed by an improved methodology of dissolution *rates* in a different metric (ng cm<sup>-2</sup> h<sup>-1</sup> instead of mg L<sup>-1</sup>).<sup>17,18</sup> Thus, *via* the recommendation of the DF4nanogrouping method selection in the ECHA guidance,<sup>14</sup> also the nanoGRAVUR method selection should be a defensible implementation of the ECHA grouping guideline. In comparison, the general ECHA physico-chemical guidance R7.1, that is also recommended by the ECHA grouping guidance,<sup>14</sup> allows many alternative methods. We concluded that similarity or dissimilarity can only be substantiated by identical methods, as supported also by the EPA guidance on the differentiation of “discrete forms”.<sup>1</sup>

We note that the determination of extrinsic properties by “functional assays” is as such not an innovation. Oomen *et al.* remarked that for molecular chemicals the partition coefficient  $\log k_{ow}$  is an example of a functional assay with very high regulatory acceptance, combining high predictivity and practical value.<sup>7</sup> We believe that for (nano)particles the assays for surface affinity, surface reactivity and dissolution rate will become just as important. Benchmark nanomaterials and benchmark nano-enabled products are essential to achieve reproducible groupings across different labs with slightly differing equipment (*e.g.* for dustiness, sanding, dispersion stability, reactivity).

#### Proof of concept (case studies, banding and calibration)

We applied the framework to 34 (nano)forms of 17 substances. Table 3 shows the numerical values of the material properties (Tier 1, Tier 1\_NEP and Tier 2 from Fig. 1), supplemented by representative SEM or TEM scans in Fig. SI\_1.† The case studies cover particles, platelets and fibrous shapes, with sizes from 10 nm to >1  $\mu\text{m}$ , BET surface areas from 1 to >500  $\text{m}^2 \text{g}^{-1}$ , surface chemistry: carbon from 4 to 99%, surface charge from  $-55$  to  $+36$  mV, and hydrophobicity determined as water contact angles from  $<10^\circ$  to  $163^\circ$ . This lends us to believe that the case studies explore a relevant portion of the NF design space.

Boundaries for the numerical ranges that define groups depend on the purpose (perspective) of grouping and may be universal or substance-specific. The nanoGRAVUR framework does not yet support a quantitative measure of similarity, nor criteria for sufficient similarity to substantiate read-across. But our diverse case studies allow an analysis how criteria of similarity impact the groups that result: one could consider the similarity between different NFs of the same substance as “ideal” if the different NFs are assigned to the same bands for *all* Tier 2 properties that are selected for the grouping purpose by Table 1. In a more pragmatic weight-of-evidence approach, one would jointly assess several properties that are relevant for the grouping purpose; such approach would implement the stepwise ECHA process of hypothesis formulation, data gathering and hypothesis substantiation for regulatory grouping.<sup>14</sup> In any case, Tier 3 can be used to overrule Tier 2, as exemplified in case studies.

In the following, we assess the similarity within substance families with the properties and descriptors given in Table 1 and Fig. 1 for the occupational and environmental grouping perspectives. We compare against *in vivo* and OECD guideline studies (Table 5) of human and environmental hazards, by well-established inhalation and relevant aquatic and soil organisms. We then perform *via* the rules given in Table 2 the data reduction to simple descriptors and order-of-magnitude (decadic) bands, resulting in Table 4, and again assess the similarity – this procedure calibrates the banding and grouping against regulatory testing. Below, we discuss which properties are very sensitive to different NFs, and how this might impact the conclusions on grouping of such NFs.

**BaSO<sub>4</sub>.** The NF and the non-nano-form of BaSO<sub>4</sub> share the same dissolution rate, and are similarly low reactive, both under abiotic and *in vitro* conditions. The NR8383 assay ranked the non-nano-form as being more reactive, but still not as “active”. The Tier 2 human perspective approach (Fig. 1) would thus recommend a common group for both forms. The *in vivo* STIS of NM220 BaSO<sub>4</sub> confirms low hazards at aerosol concentrations as high as 50  $\text{mg m}^{-3}$  (Table 5). The ECHA guideline, which requires a read-across process and, moreover, does not recommend a common group for nano- and non-nano-forms, appears to be overly conservative in this case study.

**Organic pigments.** The three DPP pigments form are another substance family with low abiotic reactivity. However, the non-nano-form showed two positive results in the macrophage assay (LOAECs below the surface area-based threshold of  $<6000 \text{ mm}^2 \text{ mL}^{-1}$ ), and was considered to be “active”.<sup>60</sup> The non-nano-form was, therefore, a candidate material for Tier 3 *in vivo* testing. However, at that stage of analysis a short-term inhalation study (STIS) had already shown that both forms of DPP elicit no adverse effects up to 30  $\text{mg m}^{-3}$ ,<sup>62</sup> (Table 5). Due to this similarity a joint assessment (grouping or read-across) of nano and non-nano DPP pigments appears justified.<sup>18</sup>

**TiO<sub>2</sub>.** Among the intrinsic properties of the four tested TiO<sub>2</sub> compounds we observed differences not only in particle size (21–204 nm) and surface area (15–80  $\text{m}^2 \text{g}^{-1}$ ) but also in surface coating. Here the UV-active TiO<sub>2</sub> NM102 and NM105 showed a slightly higher reactivity in the abiotic test (band 1) than the NM104\_coated and the non-nano-form. The *in vitro* assay dose-response is actually not very different between the three NFs (Table 3), but the scoring *via* specific surface area assigns band 3 (NM105, NM104) and band 0 (NM102), respectively, and is thus suggestive of dissimilarity in contrast to the similar abiotic reactivity in surface metric (FRAS sBOD, Table 3). The non-nano-form, which has an alumina coating, was similar to the NM104 coated NF in the absolute values of reactivity, and had no significant *in vitro* reactivity. The other extrinsic properties of TiO<sub>2</sub> materials were highly similar, with a dispersion stability  $<10\%$  after 24 h, and, furthermore, neither dissolution and nor transformation. As shown elsewhere,<sup>23</sup> the attachment efficiency varies significantly between different TiO<sub>2</sub> NFs. Moreover, in the NR8383 macrophage assay TiO<sub>2</sub> nanomaterials elicited divergent effects. In summary, neither the occupational nor the environmental perspective indicated enough similarity of the different TiO<sub>2</sub> NFs. This finding was attributed to the different crystallinities and coatings and does not rule out that more homogeneous selections of TiO<sub>2</sub> NFs may be sufficiently similar to justify groupings.

**SiO<sub>2</sub>.** In the Tier 2 environmental perspective, the different SiO<sub>2</sub> NFs are similar to each other in the relevant property bands of mobility in soils, dispersion stability, abiotic reactivity, and attachment to algae (Table 3). Because the dispersion stability ranges just around to 90% group cut-off suggested by TG318, the SiO<sub>2</sub>\_amino with 94% stability is not in the same band as the SiO<sub>2</sub>\_untreated with 74% or the NM203 with 48%,



# RESULTS

Published on 20 September 2019. Downloaded by Universitaet Duisburg Essen on 9/20/2019 2:55:04 PM.

Nanoscale

**Table 3** Numerical results of the case studies and OECD benchmark materials for both the ECHA recommended properties and the additional nanoGRAVUR harmonised properties. For each property, results were obtained for all materials by the same method (Table 2). For the properties that were selected for the nanoGRAVUR grouping framework (Table 1), the numerical values are assigned to bands in Table 4. Further measurements (e.g. transformation by TEM scans) provide images that are evaluated directly towards bands as shown in Table 4. "n.s." indicates that the result was not significant against the limit of detection. White cells are data gaps; the goal was to test grouping hypotheses, and not to fill all data gaps. Grey cells indicate that the method is not applicable. For each property and descriptor, the results are color-coded between the negative and positive benchmark materials (if defined in Table 2), and otherwise between the minimum and maximum values. For surface reactivity (*in vitro*), light color without numerical value documents that the property was determined, but that this descriptor was not significant up to a dose of 180  $\mu\text{g mL}^{-1}$

Paper

	descriptors	DPP_nano	DPP_non-nano	DPP_premixed	CuPhthalb_nano	CuPhthalb_biolagen	Fe2O3_nano_A	Fe2O3_nano_B	Fe2O3_larger	SiO2_untreated	SiO2_amino	SiO2_phosphonate	NM203_SiO2_h_pHil	GBS	GBS	HKP_GGBS_hr	CEM	NM211_CeO2	NM212_CeO2	NM110_ZnO	NM111_ZnO	CuO	NM105_TiO2_nano	NM102 - TiO2_active	NM104 - TiO2-coat.	TiO2_non-nano	NM400_CfNT	IRMM382_CfNT	Carbon Black	Graphene_monolayer	Graphen_multilayer	NM600_Bentonit	WS2	IRMM385_Kaolin	Kaolin	IRMM381_Bi5O4 non-nano	IRMM387_NM720_Bi5O4	Mn2O3				
Composition	CAS no.	84632-65-5			147-14-8	132-53-5	1309-37-1				7631-86-9				65996-09-2	65997-15-1, 68475-76-3		1306-58-3		1314-13-2		1317-38-0		1317-80-2	1317-70-0	13463-67-7		30868-56-6		1333-86-4	1034543-98-0		1302-78-9	12138-09-9	1332-58-7	1332-58-7	7727-43-7	7727-43-7	1317-34-6			
Primary particle dimension	median diameter, nm	43	233	400	17	39	12	37	48	15	15	15	26.2	206	333	1234	350	15	40	42	80	24	21	34.8	29.6	204	15.6	10				100	161	279	234	32	36					
Specific surface area (BET/VSSA)	BET, m <sup>2</sup> /g	94	16	17	53	69	107	30	12	200	200	200	213	1.1	2	2	1.8	66	27	12	14	34	51	80	60	15	254	234	56.5	559	17.6	52		16	24	2.5	41	20				
Surface Chemistry (measured)	% C	77.1	79.4	73.5	80.5	55.6	15.7	50.7	23.9	4		5						14.1	79.9	30	67.9	7	9	23.4	16.3	99												17				
	% O	10.9	19	9.5	9	0.8	54.2	33.7	49.6	66		66						57.2	17.7	38	24.3	47	63	50.7	63.5	1													52			
	% N	5.9	5.1	8.1	8.5	11.8																																		1		
	% metals	0.3	0.4	1.4	1.4	28.3	15.6	24.6	30			29						28.7	2.4	38	4.3	46	29	18.6	20.2	<1														13		
	% non metals	6.1	5.2	8.6	0.7	30.3	1.8												3	3.5																				17		
Surface charge (zeta-potential)	Zeta potential at pH7, mV	-16	-41	-30.4	-11	-38	-27	18	-55	-39	0	-43	-24					-24	15	30	-25	-34	-17	-33	26	36																
Hydrophobicity	water contact angle	135	136	103	138	163	10	10	10	0	0	0	44	10	10	10	10	10	60	10	152	10	60	10		10	140															
NEP class & intended use scenarios	lifecycle release tested	automotive coating										cement / concrete				sun screen		conc rete		sun scre.		coat ing		polymer for mobility				polymer for mobility														
Specific NEP: g/g content of ENM	% g/g	3	3	3	3	3	3	3	3	3			2	10	10	10	10			10	10			2	2	10	5	1	1	1	1	1								25		
Dustiness	g/kg inhalable	21	9	23	10	4	30	8	4				146	1	1	1	2						1	12		4														7		
	mg/kg thoracic	3064	428	1498	348	120	5273	358	155				19907	11	27	10	25						13	554		194															497	
	mg/kg respirable	51	0.6	6.6	0.4	0.1	220	0.4	0.1				1176	0.00	0.01	0.00	0.01							0.00	1.1		0.1														1	
	mean #/cm <sup>3</sup> (for fibres)																											179														
Critical shapes upon exposure (for fibres)	SEM of aerosol																																									
Agglo. of ENM upon NEP application	SEM of aerosol																																									
Dispersion stability (environ. homoaggl.)	% stable after 6 hours in ADaM				7	10	17	2	14	74	95	82	48					9	25	29	36	9	11	5													22		15	53		
Solubility in water	OECD screening LoD or value, metal ion, ppm				ns	ns	ns	ns	ns	27	13	12	56					0.1	0.1	3.6	3.3	97	ns	ns	ns	ns										0.1		0.8	6	0.2		
Ion releasing in relevant environ. media	OECD screening LoD or value, metal ion, ppm				ns	ns	ns	ns	51	27	55							ns	ns	2.3	2.4	0.8																				
Dissolution rate in relevant human media	lysosomal dissolution rate k [ng/cm <sup>2</sup> /h]				0.76	0.42	0.04	0.04	0.1	0.2	0.27	0.45	0.4					0.14	0.06	204	177	283	0.013	0	0.013	0							0.65				1.3	53	10	2		
Mobility (in soils)	% column transported				10		90	90										100	10																						100	
Reactivity (abiotic)	ESR_CPH: mBOD x-fold of D2O control	0.8	0.8	0.9	1.2	1	0.5	0.8	13.9	4	1	2.2	2.2				1	0.7	1	10.6	7.9	3.4	39.7	2.3	2.7	1.6	0.9	55												2	15.8	
	ESR_DMPO: mBOD x-fold of D2O control	0.8	0.8	0.8	1.6	7	1.1	0.8	4.3	11	21	19	19				1.3	1	0.9	1.3	1.4	2.8	14.1		0.9	0.9	1	1.1													2	2.3
	FRAS mBOD [nmolTEU/mg ENM]	2	1	2	3	2	5	1	1	3	4	8	4							4	6	43	25	326	5	13	0.7	2	23												0	78
	FRAS sBOD [nmolTEU/m <sup>2</sup> ENM]	3.4	2.4	0	12	18	44	15	34	14	18.9	8								14	8	151	20	9486	19	6.3	12	14													7	2866
Reactivity (in vitro) NR8383 cells	LDH (LOAEC) [ $\mu\text{g/mL}$ ]		90	180	90	180	90	180				22.2	45	90	90	180				90	90	2.8	5.6	2.8	90	180	90													45		
Reactivity (in vitro) NR8383 cells	GLU (LOAEC) [ $\mu\text{g/mL}$ ]		180		90	180		180				45	45	180	22.5	180	180	180	180	180	180	11.3	11.3	2.8	90	180	90		90												180	
Reactivity (in vitro) NR8383 cells	TNF (LOAEC) [ $\mu\text{g/mL}$ ]						180					22.5	22.5	90	180					22.5	22.5	11.3	22.5			90	180	90												90		
Reactivity (in vitro) NR8383 cells	H2O2 (LOAEC) [ $\mu\text{g/mL}$ ]							45				45	180	45						90	45	22.5																			22.5	
Reactivity (photo-)	photon efficiency [%]	0.49	1.1	0.82																1.97	16		10																			

This journal is © The Royal Society of Chemistry 2019

View Article Online  
Nanoscale

**Table 4** Data reduction of the case studies and OECD benchmark materials: each NF is assigned to a band, represented by a score 0 to 4. The scoring system is specified in Table 2. The similarity between different NFs of the same substance is assessed by the scores of those properties that are relevant for the grouping hypothesis, and as selected by Table 1 for the different purposes of grouping

	DPP_nano	DPP_non-nano	DPP_premixed	CuPhthalo_nano	CuPhthalo_halogen	Fe2O3_nano_A	Fe2O3_nano_B	Fe2O3_larger	SiO2_untreated	SiO2_amino	SiO2_phosphonate	NM203_SiO2_h'phil	GBS	GGBS	HKP_GGBS_hr	CEM	NM211_CeO2	NM212_CeO2	NM110_ZnO	NM111_ZnO	CuO	NM105_TiO2_nano	NM102 - TiO2_active	NM104 - TiO2-coat.	TiO2_non-nano	NM400_CNT	IRMM382_CNT	Carbon Black	Graphen_einlagig	Graphen_mehrlagig	NM600_Bentonit	WS2	IRMM385_Kaolin	Kaolin	IRMM381_BaSO4 non-nano	IRMM387_NM220_BaSO4	Mn2O3	
Primary particle shape	1	1	1	1	1	2	1	1	1	1	1	1	1	3	3	3	1	1	1	1	1	1	1	1	1	4	4	1	3	3	3	4	3	3	1	1	1	
median diameter, nm	2	2	2	2	2	2	2	2	2	2	2	2	2	2	2	2	2	2	2	2	2	2	2	2	2	2	1	2	2	2	2	2	2	2	2	2	2	2
Composition	.	.	.	.	.	315-319-335	315-319-335	315-319-335	.	.	.	.	.	.	.	302-315-318-335	.	.	410	410	302-410	.	.	.	.	319-335	.	351	319-335	319-335	330	315-319-335	.	.	.	.	302-332-315-319-335	
Surface Chemistry (descriptive)	1	1	2	1	1	1	1	1	1	2	2	1	1	1	1	1	1	1	3	1	1	1	3	3	1		1	1	1	1	1	1	1	1	1	1	1	1
water contact angle	1	1	1	1	1	0	0	0	0	0	0	0	0	0	0	0	0	0	0	1	0	0	0	0	1		1	1	1	0	0	0	0	0	0	0	0	0
lifecycle release tested	automotive coating										cement / concrete					sun screen					conc rete		sun scre.		coat ing		polymer for mobility					polymer for mobility						
Specific NEP: dispersion state of ENM	1	1	1	1	1	1	1	1				1	1	1	1	1			2	2	2			2	1	1	1	1	1	1	1	1	1	1	1	1		
	3	3	3	3	3	3	3	3				2	2	2	2	2			2	2	2			2	3	3	3	3	3	3	3	3	3	3	3	3		
% g/g	0	0	0	0	0	0	0	0				0	1	1	1	1			1	1		0	1		0		0	0	0	0	0	0	0	0	0	1		
mg/kg inhalable	2	1	2	1	0	2	1	0				2	0	0	0	0						0	1		1	0		1	1	2					1			
	1	0	0	0	0	2	0	0				2	0	0	0	0						0	0		0		0	0	1					0				
	0	0	0	0	0	1	0	0				2	0	0	0	0						0	0		0		0	0	0					0				
% stable after 6 hours in ADaM				1	0	1	1	1	2	2	1	1					1	1	1	1	1	0	0														1	
Mobility (in soils)				3		2	2										1	3				3												1			1	
Attachment to algae				0	0	1	1	0	0	0	0						1	1				1		1												1		2
OECD screening LoD or value, metal ion, ppm				0	0	0	0	0	2	2	2	3					0	0	2	1	3	0	0	0	0									0		1		2
OECD screening LoD or value, metal ion, ppm				1	1	0	0	0	1	1	1	1					0	0	1	1	1	0	0	0	0	0	0	0	0	0	0	0	1	0	1	1	1	1
Dissolution (environmental perspective)				1		0	0	0	0	0	0	0					1	1	0	0	0	1	1	1									1	0		0	0	
Transformation (environmental perspective)				1		0	0	0	0	0	0						1	1	0	0	0	1	1	1	1							1				1		
Dissolution & Transformation (human perspective)				3	3	4	4	4	3	3	3	3					4	4	1	1	1	4	4	4	4						3			3	2	2		
ESR_CPH: mBOD x-fold of D2O control	0	0	0	1	1	1	0	2	2	2	2	2					1	1	4	2	4	1	1	0	0						2		1	1	0	1	3	
Reactivity (in-vitro), human perspective	0	2	1	2	0	0	3	0	2	1	0	2	3	2	2	1	2	2	3	3	3	3	0	3	0	0		0	0	0	0	4	0	3	4	1	0	2

**Table 5** *In vivo* human toxicity and/or ecotoxicity testing on the case study ENM and benchmark materials. The existence of the data in this table was initially the reason for selecting the case studies and provided the basis to evaluate and discuss the validity of the framework. Inhalation hazards tested by short-term inhalation screening on rats (STIS, 5 d exposure at aerosol concentration indicated, 21 d recovery); results indicated the NOAEC or its lower limit by the highest dose tested without adverse effects.<sup>18,62–68</sup> Environmental hazards tested by Algae (OECD 201; *Raphidocelis subcapitata*), *Daphnia magna* (OECD 202), Zebrafish embryo (FET, OECD 236) and soil microflora (ISO 15655), with results given as EC50 or highest dose tested.<sup>22,23</sup> n.d. = not determined

	NOAEC (rat, STIS) mg m <sup>-3</sup>	EC50 (algae) mg L <sup>-1</sup>	EC50 (daphnids) mg L <sup>-1</sup>	EC50 (FET) mg L <sup>-1</sup>	EC50 (soil micro flora) mg L <sup>-1</sup>
DPP_nano	>30	n.d.	n.d.	n.d.	n.d.
DPP_non-nano	>30	n.d.	n.d.	n.d.	n.d.
CuPhthalo_nano	>30	>100	>100	>100	>1000
CuPhthalo_halogen		>100	>100	>100	>1000
Fe <sub>2</sub> O <sub>3</sub> _nano_A	30	3.6	>100	>100	>1000
Fe <sub>2</sub> O <sub>3</sub> _nano_B		2.4	>100	>100	>1000
Fe <sub>2</sub> O <sub>3</sub> _larger	30	111	>100	>100	>1000
SiO <sub>2</sub> _untreated	2.5	14	>100	>100	>1000
SiO <sub>2</sub> _amino	>50	29	>100	>100	>1000
SiO <sub>2</sub> _phosphonate	>50	46	>100	>100	>1000
NM203_SiO <sub>2</sub> _hydrophil	1.0	n.d.	n.d.	n.d.	n.d.
NM211_CeO <sub>2</sub>	<0.5	8.5	>100	>100	>1000
NM212_CeO <sub>2</sub>	<0.5	5.6	>100	>100	>1000
CuO (PlasmaChem)	0.6	1.4	0.3	≈30% effect at 100 mg L <sup>-1</sup>	~1000
NM110_ZnO	n.d.	0.1	3.4	>100	118
NM111_ZnO coated	0.5	0.1	8.3	>100	173
NM105_TiO <sub>2</sub> _nano	<2	4.7	n.d.	n.d.	n.d.
NM104	n.d.	63	n.d.	n.d.	n.d.
NM400_CNT	<0.5	n.d.	n.d.	n.d.	n.d.
NM220_BaSO <sub>4</sub>	50	n.d.	n.d.	n.d.	n.d.
Quartz DQ12	0.1	n.d.	n.d.	n.d.	n.d.

respectively. This does not need to prevent a grouping but would necessitate both aquatic and sediment testing in Tier 3 ecotoxicity. Hund-Rinke *et al.*<sup>22</sup> previously published the ecotox-scheme for the grouping of NMs, which was based on the properties “Ecotoxicity of bulk material”, “Ion release”, “Reactivity” and “Morphology/Size”. The EC50 results of aquatic species confirmed the similarity of SiO<sub>2</sub>\_untreated and SiO<sub>2</sub>\_amino, where algae as most sensitive species had EC50 of 14.1 and 29.2 mg L<sup>-1</sup> respectively.<sup>22</sup> In the Tier 2 human (occupational) perspective, the different SiO<sub>2</sub> NFs all share a slow (<1 ng cm<sup>-2</sup> h<sup>-1</sup>) dissolution and significant transformation by gel formation.<sup>51</sup> All are assigned to the same dissolution/transformation band (Table 4). However, their reactivity differs: the SiO<sub>2</sub>\_untreated has two LOAEC in the NR8383 assay below the surface area-based threshold of <6000 mm<sup>2</sup> mL<sup>-1</sup>. It is thus assigned two scores for reactivity (*in vitro*) and would be considered as “active” in the DF4nanogrouping, similarly to NM203. Other colloidal NFs have fewer LOAEC below that threshold, and are considered as “passive” in the DF4nanogrouping.<sup>60</sup> The abiotic reactivity is quite heterogeneous between the FRAS and EPR parameters in the numerical values (Table 3) but averages out to a combined band 2 for all tested silica NFs (Table 4). Overall, the differences in *in vitro* reactivity would prevent grouping in Tier 2 and would necessitate Tier 3 testing. *In vivo* studies (by STIS) confirmed that the NFs are different (Table 5) and would indicate SiO<sub>2</sub>\_untreated would be a suitable source for the SiO<sub>2</sub>\_amino and SiO<sub>2</sub>\_phosphonate as target NFs.<sup>69,70</sup>

**Aluminosilicates.** Comparing the SiO<sub>2</sub> (nano)forms with the aluminosilicates (kaolin, bentonite), we found simi-

larities in dissolution and transformation from both the environmental and human perspective, but differences in abiotic or *in vitro* reactivity (Table 3). Thus, platelet shaped aluminosilicate particles were more reactive in the *in vitro* reactivity (bands 2–4, Table 4) than their round shaped SiO<sub>2</sub> counterparts (bands 0–2), and even showed a higher cytotoxicity than our positive control Mn<sub>2</sub>O<sub>3</sub>. In contrast, the abiotic reactivity was lower for the aluminosilicates than for the SiO<sub>2</sub>. Comparing the two Kaolin NFs, IRMM385\_Kaolin (with BET of 16 m<sup>2</sup> g<sup>-1</sup>) has lower abiotic and *in vitro* reactivity *per BET* than the other Kaolin (with BET of 24 m<sup>2</sup> g<sup>-1</sup>), but is still similar. Both Kaolins are significantly less reactive than the Bentonite in the NR8383 dose response (Table 3). Nevertheless, the *in vitro* scoring system (compare ESI†) results in a band 4 for both Kaolin and Bentonite (Table 4). At present the high *in vitro* reactivity especially of bentonite is an unresolved issue. First *in vivo* studies show a high inflammatory potential of bentonite inside the rat lung (manuscript in preparation), thus confirming the NR8383 testing results. Possibly the layered structure of bentonite, rather than the platelet structure, interferes with the micro-milieu inside the phagolysosomal compartments, *e.g.* due to swelling, ion binding and/or osmotic challenges. However, the damage inferred by bentonite to the lung was transient, suggesting that the layered structure of bentonite transforms into a far less bioactive particulate. Understanding of the transformation processes *in vivo* may help. Studies on graphenes before/after reduction (thus comparing changes to composition at same shape) confirm that the chemical speciation is important to describe “where they go”.<sup>71</sup> Clearly,

nanofoms that share the shape of thin platelets can be very dissimilar.

**Cu-Compounds.** We also compared three copper containing materials with similar particle size but different CAS numbers (Tier 1, Fig. 1). CuO and two CuPhthalocyanines differed already with respect to their Tier 1 properties, e.g. by different elemental compositions (5–10% Cu for the pigments and 46% for CuO) and by the GHS classification of bulk CuO as compared to no GHS classification of CuPhthalocyanines. Furthermore, CuO is hydrophilic whereas the other two materials are hydrophobic with contact angles up to 163°. The sizes of the primary particles of the three materials did not vary much with 17 and 39 nm for the CuPhthalocyanines and 24 nm for CuO. Within CuPhthalocyanine the Cu is strongly bound to the complex, making it almost insoluble with dissolution rates around 0.5 ng cm<sup>-2</sup> h<sup>-1</sup> for both CuPhthalocyanines and 282 ng cm<sup>-2</sup> h<sup>-1</sup> for CuO.<sup>51</sup> Accordingly, CuPhthalocyanines showed only limited reactivity within the FRAS, ESR and NR8383 assay with bands of 1 in the abiotic assay and between 0–2 in the *in vitro* assay. Whereas CuO quickly dissolved, setting free Cu-ions. CuO was the material with the highest reactivity in the abiotic test and a band of 3 in the *in vitro* test. It furthermore dissolved the quickest, even quicker than the ZnO materials at lysosomal pH. The drastic differences are confirmed by STIS, showing complete dissolution of CuO with NOAEC at 0.6 mg m<sup>-3</sup> (ref. 67) vs. no adverse effects for CuPhthalo\_nano up to the highest dose tested of 30 mg m<sup>-3</sup> (ref. 18) (Table 5). The CuPhthalo\_nano gave most likely false positive result in the NR8383 assay, since STIS showed a low hazard potential.<sup>18</sup> Also, specific tests of ecotoxicity confirm the dramatic difference between Cu with an EC50 below 0.1 mg L<sup>-1</sup> for algae and daphnids, vs. a non-detectable EC50 above 100 mg L<sup>-1</sup> for the CuPhthalocyanines (Table 5).<sup>22,23</sup>

**Fe<sub>2</sub>O<sub>3</sub>.** For the three tested Fe<sub>2</sub>O<sub>3</sub> compounds, different values for the intrinsic properties were measured, such as a range in BET from 12 to 107 m<sup>2</sup> g<sup>-1</sup>, and furthermore the Zeta potential ranging from -18 to -55 mV for Fe<sub>2</sub>O<sub>3</sub>\_nano\_b and Fe<sub>2</sub>O<sub>3</sub>\_larger respectively (Table 3). Despite the significant differences in intrinsic properties, almost all extrinsic properties were found in the same bands in Table 4. E.g., all Fe<sub>2</sub>O<sub>3</sub> (nano)forms were similar in low dispersion stability <10% after 24 h. They also shared a very low dissolution below 0.1 ng cm<sup>-2</sup> h<sup>-1</sup> in lysosomal conditions, without transformation.<sup>51</sup> However their reactivity differed: the abiotic reactivity band ranged from mid-low (2) to mid-high (3), but remained below 10% the positive control for all forms, hence they were “passive” in the DF4nanogrouping terminology.<sup>17</sup> In the NR8383 assay, Fe<sub>2</sub>O<sub>3</sub>\_nano\_B was the only form with significant *in vitro* reactivity, whereas the other two materials were not reactive. Due to this disparity, Tier 3 comparison was applied and STIS indicated a similar outcome for the NF and non-nano-form of Fe<sub>2</sub>O<sub>3</sub> with respect to treatment-related microscopic findings after days 5 and 26 (Table 5).<sup>62</sup> Thus, grouping appears justified in the occupational perspective. The similarity of Fe<sub>2</sub>O<sub>3</sub> materials was even higher for the

environmental fate descriptors, which fall into the same bands for low dissolution, intermediate mobility in soils, intermediate dispersion stability, lacking transformation and ion release. Thus, the environmental fate of Fe<sub>2</sub>O<sub>3</sub> materials appears very similar. Spatial proximity (e.g. by attachment) is required for reactivity-induced ecotoxicity.<sup>31</sup> The environmental hazard was estimated to be similar for the two NFs, but the attachment to algae is more pronounced for the non-nano-form.<sup>23</sup> The EC50 results of aquatic species confirmed the similarity of Fe<sub>2</sub>O<sub>3</sub>\_nano\_A and Fe<sub>2</sub>O<sub>3</sub>\_nano\_B, where algae, as most sensitive species, had EC50 of 23.4 and 17.7 mg L<sup>-1</sup> (*Desmodesmus subspicatus*)<sup>22,23</sup> and of 3.6 and 2.4 mg L<sup>-1</sup> (*Raphidocelis subcapitata*)<sup>23</sup> respectively. In contrast, the EC50 for Fe<sub>2</sub>O<sub>3</sub>\_larger is extrapolated to be 111 mg L<sup>-1</sup> (*Raphidocelis subcapitata*)<sup>23</sup> (Table 5). Grouping the Fe<sub>2</sub>O<sub>3</sub> NFs for the purpose of demonstrating environmental safety is thus justified, but a discrepancy remains between the NFs and the non-nano-form.

**CeO<sub>2</sub>.** The assessment of the properties of CeO<sub>2</sub>\_NM211 and CeO<sub>2</sub>\_NM212 showed that they had hardly any intrinsic properties in common, such that particle sizes (15 and 40 nm), BET (66 and 27 m<sup>2</sup> g<sup>-1</sup>), contact angle (10° and 60°), and surface charge (-24 and 15 mV) were all different. Nevertheless, CeO<sub>2</sub>\_NM211 and CeO<sub>2</sub>\_NM212 behaved similar in many of the Tier 2 properties: both NF had a rather low dispersion stability with <10% stable particles after 24 h, no transformation (band 1), low dissolution (band 1). It was furthermore found that both materials share band 2 in the *in vitro* reactivity assay, and band 1 for the combined abiotic assays. The NF of smaller size, NM211, had higher reactivity FRAS sBOD per surface. This small disparity in Tier 2 is an interesting case for the calibration of “sufficient similarity”, as their similarity from the occupational perspective was confirmed by STIS in Tier 3 (Table 5), which furthermore revealed similar neutrophil influx at aerosol concentrations of 5 mg m<sup>-2</sup>.<sup>65</sup> Results of the two Ceria materials were even closer related if the surface area of the particles was used as a dose metrics for inflammatory responses.<sup>65</sup> However, their environmental transport in soils was significantly different and prevents grouping for all environmental endpoints. The strongly reduced mobility in soils of NM212 may be attributed to the hydrophobicity and positive charge of this material. On the other hand, properties relevant for environmental hazard (release of ions, reactivity/attachment, shape) were similar, indicated by EC50 values to algae which amounted to 8.5 and 5.6 mg L<sup>-1</sup> respectively (Table 5).<sup>22,23</sup> Thus, grouping the two (or more) NFs of CeO<sub>2</sub> might not be justified, but read-across for specific endpoints, as envisioned by ECHA,<sup>14</sup> is justifiable.

**ZnO.** The metal oxide particles ZnO\_NM110 and ZnO\_NM111 were largely different from CuO with respect to chemical composition and intrinsic properties (primary particle size 42–80 nm for both ZnO and 24 nm for CuO and BET 12–14 m<sup>2</sup> g<sup>-1</sup> and 34 m<sup>2</sup> g<sup>-1</sup> respectively). Nevertheless, all three materials shared bands with <10% dispersion stability, and the highest solubility, and were non-persistent/high transformation materials with high dissolution rates. STIS of ZnO



NM111<sup>66</sup> and CuO<sup>67</sup> confirmed the high solubility *in vivo* and indicated a fast clearance from the lung. Furthermore, ZnO and CuO exhibited a high abiotic (band 4) and *in vitro* reactivity (band 3). Although grouping across substances is not permitted by ECHA for regulatory purposes,<sup>14</sup> an industrial risk estimation based on these results would consider ZnO and CuO similar and would suggest the same measures for worker protection at production sites.<sup>66,67</sup> They are also the only materials with significant photon efficiency in the Rhodamine-based assay on photo-reactivity, which is proposed by the ECHA grouping but not incorporated in the nanoGRAVUR grouping scheme.<sup>14</sup> A large similarity of ZnO NM110 und ZnO NM111 was also suggested by the EC50 values for algae (0.1 mg L<sup>-1</sup>) and daphnids (3.4 to 8.3 mg L<sup>-1</sup>) (Table 5).<sup>22,23</sup> Within a substance, read-across from a soluble Zn salt to the ZnO NFs seems justified due to the biological similarity and high (>100 ng cm<sup>-2</sup> h<sup>-1</sup>) dissolution rates.

**NEPs.** The nanoGRAVUR scheme also offers a comparative risk estimation of NFs which were integrated in nano-enabled products (NEPs) for automotive coatings, clinker-reduced cements, cosmetic sunscreen and lightweight polymers. Representative photographs and cross-section SEM or TEM analyses of the NEPs are shown in Fig. SI\_2 and SI\_3.† The values of “matrix resilience” are not reported in Table 3 because they were not re-measured for each NEP, and because some NM were integrated in several different matrices, for release testing. As expected, incorporation into solid matrices dramatically changed the release probability for NM (Fig. SI\_4†). Although the different NFs differed significantly by their powder dustiness, the Tier 1\_NEP properties which predict their release potential from NEPs (Fig. 1) were the same for each NEP matrix and independent of the embedded NF, as confirmed experimentally by three independent laboratories (Fig. SI\_4†). As an exception CuO added to wood as a biocidal preservative differed from all other NEP case studies because CuO was attributed as “attached” only. We earlier showed that Cu ions have to be released for biocidal performance.<sup>72</sup> Fragments released from NEPs consisting of the same *solid* matrix but different *embedded* NFs have been shown to be similarly toxic for animals or humans,<sup>35–38,73</sup> We verified this grouping hypothesis on the case study of automotive coatings containing CuPhthalocyanine.<sup>40</sup> Fragments from NEPs consisting of the same *solid* matrix but different *embedded* NFs (characterised in Tier 1\_NEP) are also similar in their ecotoxicity.<sup>24</sup> Thus it appears that if the state of dispersion and content of a particular NF in the NEP, and also its intended use is the same, then the lifecycle-induced fragmentation is similar in form, rate, toxicity and ecotoxicity. In our case studies, all Tier 1\_NEP properties that could predict the rate and form of the release of fragments were the same for different nanoforms in the same solid matrix (see Fig. SI\_4†), supporting a grouping according to lifecycle issues primarily by the matrix material and the intended use of the NEP. Other accompanying studies confirmed this grouping hypothesis specifically for the automotive coatings with different embedded nano- and non-nano-pigments, and for the light-

weight materials with different embedded CNT, graphene, CB or Kaolin fillers.<sup>74–76</sup> Such a grouping is considered to be relevant by US-EPA and industrial downstream users but is not foreseen to be used in the context of European regulation *e.g.* REACH. ISO TC229 PG29 is currently working on the standardisation of this grouping in form of a decision tree. We found that the grouping by matrix and intended use only fails where the lifecycle process elicits catalytic activity, such as metal-based NFs during NEP incineration,<sup>77</sup> or where the NEP formation itself is a reactive process such as cement hydration, where the “matrix” crystallinity and porosity is controlled by the NFs, and whose formation consumes the NFs, which is the very purpose of the slag (GGBS) to replace CO<sub>2</sub>-intensive clinker<sup>78</sup> or of nano SiO<sub>2</sub> in a “pozzolanic reaction”.

Several of the case studies have been evaluated by other grouping frameworks before and focussed especially on OECD NM and on some of the pigments. Comparing *e.g.* the grouping by occupational (inhalation) safety of ZnO NM111, both the nanoGRAVUR framework and the DF4nanogrouping framework categorize NM111 in Tier 2 as “biosoluble” in the relevant medium and read across to the non-nano form. In contrast, pigment blue 15 : 1 (Cu-phthalocyanine) was a false positive in the binary decision logic of the DF4nanogrouping framework, being “active” in Tier 2, but “*in vivo* passive” in a Tier 3 calibration. In the risk matrix of nanoGRAVUR<sup>79</sup> several criteria are combined and result in a “green” risk group, consistent with the “*in vivo* passive” Tier 3 calibration. Of note, the risk matrices that build on the current framework are only intended for non-regulatory use. In the current framework, fibres are still recognised as a specific group already in Tier 1, triggering adapted tests such as descriptors of the form that is released during the intended use. In future, benchmark materials (*e.g.* Mitsui NT7) and methods for rigidity are foreseen to enhance the robustness of the HARN category. In this context it has to be mentioned that the trigger values for fibres regarding human toxicity and ecotoxicity presumably differ and still need to be defined for ecotoxicity.<sup>23</sup>

We did not test polymer particles among our case studies, but the tested pigments (DPP NFs and CuPhthalocyanine NFs) represent hydrophobic organic particles with low human toxicity<sup>62</sup> and low ecotoxicity.<sup>23</sup> No unique ecotoxicity<sup>80,81</sup> or human toxicity<sup>82</sup> of polymer NFs was discovered, and hence properties beyond those of our framework should not be required to assess the similarity between polymer particles. There may be limits if the polymer NF is significantly soluble or swelling, such as hydrogels, for which not enough data exists to draw conclusion.

As noted by Gao & Lowry, extrinsic properties result from a more or less complex interplay of the surrounding medium and one or more intrinsic properties,<sup>83</sup> but some extrinsic properties are less sensitive than others towards variations of size, shape *etc.* of different NFs of the same substance. The assessment of dissolution and transformation by either the environmental or the human perspective typically assigns different NFs of the same substance to the same band, with rare exceptions. This property is determined more by the substance than



by size or shape or crystallinity or organic surface treatment (we did not test true core-shell systems, which would certainly modulate the dissolution behavior).

We observed that, when different NFs of the same substance are evaluated by harmonized methods, they are *often* assigned to different bands of dustiness, *sometimes* to different bands in the dispersion stability and mobility in soils, *sometimes* to different bands in abiotic reactivity, but *very often* to different bands of the by descriptor of *in vitro* (NR8383) reactivity, which is constructed from several read-outs. The sensitivity of dustiness to different NFs is supported by literature, which furthermore supports the order-of-magnitude (decadic) bands.<sup>55,56,84</sup>

Not only for reactivity, our construction of descriptors and bands may in fact exaggerate dissimilarity: *e.g.* for CeO<sub>2</sub> reactivity, TiO<sub>2</sub> reactivity, GGBS reactivity or SiO<sub>2</sub> dispersion stability, the numerical values are similar (Table 3), but fall on different bands of the universally fixed order-of-magnitude (decadic) cutoffs. Instead of the risk-screening purpose, for which fixed bands are appropriate, the grouping purpose may be better served by floating band center values with a fixed order-of-magnitude (decadic) span. The floating bands would focus on similarity within a given candidate group of NFs but would still keep the evaluation transparent with independent assessment of each property. We may also have to reconsider the normalization of the NR8383 NOAEC by specific surface areas,<sup>60</sup> and the indexing by it, because – apart from partico-kinetics, cell contact and particle uptake into cells – there is no simple and apparent reason why the non-nano-form of BaSO<sub>4</sub> should be more reactive than the NF, or why the non-nano-form of DPP should be significantly more reactive than the NF. Possibly the NR8383 evaluation can be adapted to the same concept of order-of-magnitude (decadic) bands as used for most other descriptors. However, this demands careful and quantitative studies on particle uptake, especially for well dispersed (*i.e.* diffusing, not sedimenting) particles.

Any property descriptors that are constructed from several redundant assays need data reduction strategies. On the example of “biological reactivity”, we combined abiotic reactivity (two assays, four read-outs) and one *in vitro* assay (another four read-outs), but our addition of “points” (Table 2) is not optimal and triggers numerous cases of “false positive dissimilarity”. False positives in Tier 2 require the user who wishes to use grouping to escalate to Tier 3 testing, only to find there that the NFs are similar, such that animal testing should have been prevented by a more efficient Tier 2.

In summary of the case study calibration by the *in vivo* studies and ecotox OECD studies, “ideal” similarity (*i.e.* different NFs are assigned to the same bands for *all* Tier 2 properties that are relevant for the grouping purpose by Table 1) resulted in false positives (apparent dissimilarity) in too many cases and would have triggered extensive animal testing. The more pragmatic weight-of-evidence approach (*i.e.*, joint assessment of properties that are relevant for the grouping purpose by Table 1) is more appropriate to implement the stepwise

ECHA process of hypothesis formulation, data gathering and hypothesis substantiation for regulatory grouping.<sup>14</sup>

In this perspective, the outstanding importance of benchmark materials becomes evident: we cannot assess the significance of any dissimilarity, if we do not know the dynamic range of that particular property. Benchmark materials span the dynamic range. We observe that for many properties the dynamic range spans about three to four orders of magnitude between the positive and negative controls (*i.e.* benchmark materials). This applies to size, aspect ratio, solubility, reactivity, dissolution rate, dustiness, ENM content, resilience of matrix, but not to homo-agglomeration or *in vitro*-reactivity. Thus, order-of-magnitude (decadic) band ranges are appropriate for NFs based on experimental evidence, and this is fully in line with the GHS, where such a factor of 10 is often applied in the assessment of non-nano chemical substances. As discussed above, floating band center values would be the next step from risk-screening perspective towards a grouping by similarity (instead of categorization and banding). But, alternatively to bands, one may develop algorithms that compare the pairwise distance of materials in a multidimensional space spanned by the relevant properties (Table 1, Fig. 1), and compare it to the distance of benchmark materials (Tables 2 and 5). Such concepts are explored in follow-up projects such as GRACIOUS (H2020) and InnoMat.Life (BMBF).

## Conclusions

The methods developed or selected by nanoGRAVUR fill several gaps highlighted in the Steinhäuser & Sayre (2017)<sup>28</sup> reviews and are useful to implement both the ECHA concept of grouping of *nanofoms* or sets thereof, as well as the EPA concept of *discrete forms*. Previous frameworks had a narrower focus on occupational or ecological hazard. The nanoGRAVUR framework serves three purposes of grouping for occupational, environmental and consumer safety. Depending on the purpose, different properties become relevant to assess the similarity. Grouping decisions can be made in the Tier 2 mostly based on extrinsic properties with quantitative bands that are order-of-magnitude (decadic) for many properties. Benchmark materials span the dynamic range, which in general crosses about three to four orders of magnitude.

Case studies include families of Fe<sub>2</sub>O<sub>3</sub>, SiO<sub>2</sub>, Aluminosilicates, BaSO<sub>4</sub>, CeO<sub>2</sub>, organic pigment, ZnO, TiO<sub>2</sub> (nano)forms. We find that for some substances the biological similarities were high when (nano)forms only differed in morphology and particle size, specifically for NFs and non-nano-forms of SiO<sub>2</sub>, BaSO<sub>4</sub>, Kaolin, CeO<sub>2</sub>, ZnO, organic pigments. In contrast, different Fe<sub>2</sub>O<sub>3</sub> or TiO<sub>2</sub> (nano)forms differ more significantly. Surface treatments in the sense of the ECHA guidance<sup>13</sup> were tested on ZnO, TiO<sub>2</sub>, SiO<sub>2</sub>, and were found to modulate to a significant extent the dispersion stability and the reactivity, but only had transient influence on dissolution rates in the presented cases.<sup>51</sup>

We further observed that, when different NFs of the same substance are evaluated by harmonised methods, they are often assigned to different bands of dustiness, sometimes to different bands in the dispersion stability and mobility in soils, sometimes to different bands in abiotic reactivity, and very often to different bands by the descriptors of *in vitro* and abiotic reactivity. In contrast, the dissolution and transformation behaviour, measured by several approaches, was primarily determined by the substance.

The NFs were also integrated in nano-enabled products (NEPs) for automotive coatings, clinker-reduced cements, cosmetic sunscreen, lightweight polymers. Once incorporated into a certain NEP with solid matrix, all relevant properties that could predict and assess the rate and form of release were within an order-of-magnitude (decadic) band for different NFs in the same solid matrix; together with the state-of-the-art on (eco)toxicity of NEP fragments, our findings support a grouping of lifecycle issues primarily by intended use and NEP matrix.

The evaluation of the developed framework with a diverse set of case studies clearly showed its usability for grouping for different purposes – but also the limits: we still need to develop rules for read-across, to explore measures that quantify similarity across multiple descriptors. The nanoGRAVUR case studies, thoroughly tested by ISO standards and OECD guidelines, will be essential to validate any future frameworks.

## Conflicts of interest

WW, JK, RL, BF are employees of companies producing and marketing nanomaterials.

## Acknowledgements

This work was partially funded by the BMBF (German Federal Ministry of Education and Research) project nanoGRAVUR - Nanostructured materials – Grouping in view of worker, consumer and environmental safety and risk minimization (FKZ 03XP0002X). We gratefully acknowledge the work and contribution of the entire consortium to materials, data and concepts namely by Axel Horster (General Reinsurance); Nicole Neubauer, Emmanuel Ruggiero, Patrick Fiedler (BASF SE); Bianca Oeffling, Carsten Möhlmann (Institut für Arbeitsschutz der DGUV); Michael Kirchner (Institut für Gefahrstoff-Forschung der BGRCl); Jürgen Schnekenburger (Westfälische Wilhelms-Universität Münster); Burkhard Stahlmecke (IUTA); Frederic Krabigell, Bernd Staubach (HDI Global SE); Tobias Teckentrup (Universität Duisburg-Essen); and by Umweltbundesamt (Dessau).

## References

- 1 E. P. A. (EPA), *Fed. Regist.*, 2017, **82**, 22088.
- 2 T. C. Iso, *ISO/AWI TS 80004-4*, 2010.

- 3 W. Wohlleben, C. Punckt, J. Aghassi-Hagmann, F. Siebers, F. Menzel, D. Esken, C.-P. Drexel, H. Zoz, H. U. Benz, A. Weier, M. Hitzler, A. I. Schäfer, L. D. Cola and E. A. Prasetyanto, in *Metrology and Standardization for Nanotechnology: Protocols and Industrial Innovations*, ed. E. Mansfield, D. L. Kaiser, D. Fujita and M. Van de Voorde, John Wiley & Sons, 2017, pp. 411–464.
- 4 W. Stark, P. Stoessel, W. Wohlleben and A. Hafner, *Chem. Soc. Rev.*, 2015, **44**, 5793–5805.
- 5 EC, Commission recommendation of 18 October 2011 on the definition of nanomaterial, *Official Journal of the European Union*, 2011.
- 6 K. Aschberger, H. Rauscher, H. Crutzen, K. Rasmussen, F. M. Christensen, B. Sokull-Klütgen and H. Stamm, *JRC Science and Policy Reports*, 2017, DOI: 10.2788/3044.
- 7 A. G. Oomen, K. G. Steinhäuser, E. A. J. Bleeker, F. van Broekhuizen, A. Sips, S. Dekkers, S. W. P. Wijnhoven and P. G. Sayre, *NanoImpact*, 2018, **9**, 1–13.
- 8 J. H. Arts, M. Hadi, A. M. Keene, R. Kreiling, D. Lyon, M. Maier, K. Michel, T. Petry, U. G. Sauer, D. Warheit, K. Wiench and R. Landsiedel, *Regul. Toxicol. Pharmacol.*, 2014, **70**, 492–506.
- 9 A. G. Oomen, E. A. Bleeker, P. M. Bos, F. van Broekhuizen, S. Gottardo, M. Groenewold, D. Hristozov, K. Hund-Rinke, M.-A. Irfan, A. Marcomini, W. J. Peijnenburg, K. RASMUSSEN, A. Sanchez Jimenez, J. Scott-Fordsmand, M. Van Tongeren, K. Wiench, W. Wohlleben and R. Landsiedel, *Int. J. Environ. Res. Public Health*, 2015, **12**, 13415–13434.
- 10 N. Burden, K. Aschberger, Q. Chaudhry, M. J. Clift, S. H. Doak, P. Fowler, H. Johnston, R. Landsiedel, J. Rowland and V. Stone, *Nano Today*, 2017, **12**, 10–13.
- 11 H. Godwin, C. Nameth, D. Avery, L. L. Bergeson, D. Bernard, E. Beryt, W. Boyes, S. Brown, A. J. Clippinger, Y. Cohen, M. Doa, C. O. Hendren, P. Holden, K. Houck, A. B. Kane, F. Klaessig, T. Kodas, R. Landsiedel, I. Lynch, T. Malloy, M. B. Miller, J. Muller, G. Oberdorster, E. J. Petersen, R. C. Pleus, P. Sayre, V. Stone, K. M. Sullivan, J. Tentschert, P. Wallis and A. E. Nel, *ACS Nano*, 2015, **9**, 3409–3417.
- 12 A. E. Nel, E. Nasser, H. Godwin, D. Avery, T. Bahadori, L. Bergeson, E. Beryt, J. C. Bonner, D. Boverhof, J. Carter, V. Castranova, J. R. Deshazo, S. M. Hussain, A. B. Kane, F. Klaessig, E. Kuempel, M. Lafranceschi, R. Landsiedel, T. Malloy, M. B. Miller, J. Morris, K. Moss, G. Oberdorster, K. Pinkerton, R. C. Pleus, J. A. Shatkin, R. Thomas, T. Tolaymat, A. Wang and J. Wong, *ACS Nano*, 2013, **7**, 6422–6433.
- 13 ECHA, *How to prepare registration dossiers that cover nanomaterials: best practices*, 2017, DOI: 10.2823/128306.
- 14 ECHA, *Appendix R.6-1 for nanomaterials applicable to the Guidance on QSARs and Grouping of Chemicals*, 2017, DOI: 10.2823/884050.
- 15 E. D. Kuempel, V. Castranova, C. L. Geraci and P. A. Schulte, *J. Nanopart. Res.*, 2012, **14**, 1029.

- 16 N. M. Drew, E. D. Kuempel, Y. Pei and F. Yang, *Regul. Toxicol. Pharmacol.*, 2017, **89**, 253–267.
- 17 J. H. E. Arts, M. Hadi, M.-A. Irfan, A. M. Keene, R. Kreiling, D. Lyon, M. Maier, K. Michel, T. Petry, U. G. Sauer, D. Warheit, K. Wiench, W. Wohlleben and R. Landsiedel, *Regul. Toxicol. Pharmacol.*, 2015, **71**, S1–S27.
- 18 J. H. E. Arts, M.-A. Irfan, A. M. Keene, R. Kreiling, D. Lyon, M. Maier, K. Michel, N. Neubauer, T. Petry, U. G. Sauer, D. Warheit, K. Wiench, W. Wohlleben and R. Landsiedel, *Regul. Toxicol. Pharmacol.*, 2016, **76**, 234–261.
- 19 A. Gajewicz, *Environ. Sci.: Nano*, 2018, **5**, 408–421.
- 20 R. Landsiedel, L. Ma-Hock, K. Wiench, W. Wohlleben and U. G. Sauer, *J. Nanopart. Res.*, 2017, **19**, 171.
- 21 Z. Wang, M. G. Vijver and W. J. Peijnenburg, *Environ. Sci. Technol.*, 2018, **52**(14), 7598–7600.
- 22 K. Hund-Rinke, K. Schlich, D. Kühnel, B. Hellack, H. Kaminski and C. Nickel, *NanoImpact*, 2018, **9**, 52–60.
- 23 D. Kühnel, C. Nickel, B. Hellack, E. van der Zalm, C. Kussatz, M. Herrchen, B. Meisterjahn and K. Hund-Rinke, *NanoImpact*, 2019, **15**, 100173.
- 24 M. J. B. Amorim, S. Lin, K. Schlich, J. M. Navas, A. Brunelli, N. Neubauer, K. Vilsmeier, A. L. Costa, A. Gondikas, T. Xia, L. Galbis, E. Badetti, A. Marcomini, D. Hristozov, F. v. d. Kammer, K. Hund-Rinke, J. J. Scott-Fordsmand, A. Nel and W. Wohlleben, *Environ. Sci. Technol.*, 2018, **52**, 1514–1524.
- 25 T. van Harmelen, E. K. Zondervan-van den Beuken, D. H. Brouwer, E. Kuijpers, W. Fransman, H. B. Buist, T. N. Ligthart, I. Hincapié, R. Hirschier, I. Linkov, B. Nowack, J. Studer, L. Hilty and C. Som, *Environ. Int.*, 2016, **91**, 150–160.
- 26 M. L. Fernandez-Cruz, D. Hernandez-Moreno, J. Catalan, R. K. Cross, H. Stockmann-Juvala, J. Cabellos, V. R. Lopes, M. Matzke, N. Ferraz, J. J. Izquierdo, J. M. Navas, M. Park, C. Svendsen and G. Janer, *Environ. Sci.: Nano*, 2018, **5**, 381–397.
- 27 L. Pizzol, D. Hristozov, A. Zabeo, G. Basei, W. Wohlleben, A. J. Koivisto, K. A. Jensen, W. Fransman, V. Stone and A. Marcomini, *NanoImpact*, 2019, **13**, 26–36.
- 28 D. Hristozov, S. Gottardo, E. Semenzin, A. Oomen, P. Bos, W. Peijnenburg, M. van Tongeren, B. Nowack, N. Hunt and A. Brunelli, *Environ. Int.*, 2016, **95**, 36–53.
- 29 ECHA, *Guidance on information requirements and chemical safety assessment*, 2012.
- 30 K. G. Steinhäuser and P. G. Sayre, *NanoImpact*, 2017, **7**, 66–74.
- 31 C. O. Hendren, G. V. Lowry, J. M. Unrine and M. R. Wiesner, *Sci. Total Environ.*, 2015, **536**, 1029–1037.
- 32 H. Zhang, Z. Ji, T. Xia, H. Meng, C. Low-Kam, R. Liu, S. Pokhrel, S. Lin, X. Wang, Y. P. Liao, M. Wang, L. Li, R. Rallo, R. Damoiseaux, D. Telesca, L. Mädler, Y. Cohen, J. I. Zink and A. E. Nel, *ACS Nano*, 2012, **6**, 4349–4368.
- 33 F. Abdolapur Monikh, A. Praetorius, A. Schmid, P. Kozin, B. Meisterjahn, E. Makarova, T. Hofmann and F. von der Kammer, *NanoImpact*, 2018, **11**, 42–50.
- 34 R. C.-o. C. N. I. (RCC), *Work Area 3: Risk Assessment-Risk Management*, 2014.
- 35 W. Wohlleben, S. Brill, M. Meier, M. Mertler, G. Cox, S. Hirth, B. von Vacano, V. Strauss, S. Treumann, K. Wiench, L. Ma-Hock and R. Landsiedel, *Small*, 2011, **7**, 2384–2395.
- 36 W. Wohlleben, M. W. Meier, S. Vogel, R. Landsiedel, G. Cox, S. Hirth and Ž. Tomović, *Nanoscale*, 2013, **5**, 369–380.
- 37 A. T. Saber, A. Mortensen, J. Szarek, I. K. Koponen, M. Levin, N. R. Jacobsen, M. E. Pozzebbon, S. P. Mucelli, D. G. Rickerby, K. Kling, R. Atluri, A. M. Madsen, P. Jackson, Z. O. Kyjovska, U. Vogel, K. A. Jensen and H. Wallin, *Part. Fibre Toxicol.*, 2016, **13**, 1–20.
- 38 A. Saber, N. Jacobsen, A. Mortensen, J. Szarek, P. Jackson, A. Madsen, K. Jensen, I. Koponen, G. Brunborg, K. Gutzkow, U. Vogel and H. Wallin, *Part. Fibre Toxicol.*, 2012, **9**, 4.
- 39 A. Saber, I. Koponen, K. Jensen, N. Jacobsen, L. Mikkelsen, P. Moller, S. Loft, U. Vogel and H. Wallin, *Nanotoxicology*, 2012, **6**, 776–788.
- 40 C. Pang, N. Neubauer, M. Boyles, D. Brown, N. Kanase, D. Hristozov, T. Fernandes, V. Stone, W. Wohlleben and A. Marcomini, *NanoImpact*, 2017, **7**, 75–83.
- 41 J. J. Scott-Fordsmand, J. M. Navas, K. Hund-Rinke, B. Nowack and M. J. B. Amorim, *Nano Today*, 2017, **17**, 7–10.
- 42 E. Kuempel, V. Castranova, C. Geraci and P. Schulte, *J. Nanopart. Res.*, 2012, **14**, 1029.
- 43 AGS, *Committee on Hazardous Substances*, 2013, p. 527.
- 44 K. Bhattacharya, G. Kiliç, P. M. Costa and B. Fadeel, *Nanotoxicology*, 2017, **11**, 809–826.
- 45 V. Castagnola, J. Cookman, J. M. de Araujo, E. Polo, Q. Cai, C. P. Silveira, Z. Krpetic, Y. Yan, L. Boselli and K. A. Dawson, *Nanoscale Horiz.*, 2017, **2**, 187–198.
- 46 Q. Mu, G. Jiang, L. Chen, H. Zhou, D. Fourches, A. Tropsha and B. Yan, *Chem. Rev.*, 2014, **114**, 7740–7781.
- 47 F. Babick, J. Mielke, W. Wohlleben, S. Weigel and V.-D. Hodoroba, *J. Nanopart. Res.*, 2016, **18**, 1–40.
- 48 W. Wohlleben, J. Mielke, A. Bianchin, A. Ghanem, H. Freiberger, H. Rauscher, M. Gemeinert and V.-D. Hodoroba, *J. Nanopart. Res.*, 2017, **19**, 61.
- 49 D. Mehn, I. M. Rio-Echevarria, D. Gilliland, M. Kaiser, K. Vilsmeier, P. Schuck and W. Wohlleben, *NanoImpact*, 2018, **10**, 87–96.
- 50 OECD, *ISO/TR 19057:2017*, 2017.
- 51 J. Koltermann-Jully, J. G. Keller, A. Vennemann, K. Werle, P. Müller, L. Ma-Hock, R. Landsiedel, M. Wiemann and W. Wohlleben, *NanoImpact*, 2018, **12**, 29–41.
- 52 G. Oberdörster and T. A. J. Kuhlbusch, *NanoImpact*, 2018, **10**, 38–60.
- 53 W. Wohlleben, C. Kingston, J. Carter, E. Sahle-Demessie, S. Vázquez-Campos, B. Acrey, C.-Y. Chen, E. Walton, H. Egenolf, P. Müller and R. Zepp, *Carbon*, 2017, **113**, 346–360.

- 54 T. Schneider and K. A. Jensen, *Ann. Occup. Hyg.*, 2007, **52**, 23–34.
- 55 D. Broßell, E. Heunisch, A. Meyer-Plath, D. Bäger, V. Bachmann, K. Kämpf, N. Dziurowitz, C. Thim, D. Wenzlaff and J. Schumann, *Powder Technol.*, 2019, **342**, 491–508.
- 56 C. Dazon, O. Witschger, S. Bau, R. Payet, K. Beugnon, G. Petit, T. Garin and L. Martinon, *J. Phys. Conf. Ser.*, 2015, **838**, 012005.
- 57 I. Pensis, J. Mareels, D. Dahmann and D. Mark, *Ann. Occup. Hyg.*, 2009, **54**, 204–216.
- 58 D. Göhler and M. Stintz, *J. Phys.: Conf. Ser.*, 2015, **617**, 012029.
- 59 B. Hellack, C. Nickel, C. Albrecht, T. A. J. Kuhlbusch, S. Boland, A. Baeza-Squiban, W. Wohlleben and R. P. F. Schins, *Environ. Sci.: Nano*, 2017, **4**, 1920–1934.
- 60 M. Wiemann, A. Vennemann, U. G. Sauer, K. Wiench, L. Ma-Hock and R. Landsiedel, *J. Nanobiotechnol.*, 2016, **14**, 1–27.
- 61 A. B. Kane, R. H. Hurt and H. Gao, *Toxicol. Appl. Pharmacol.*, 2018, **361**, 68–80.
- 62 T. Hofmann, L. Ma-Hock, V. Strauss, S. Treumann, M. Rey Moreno, N. Neubauer, W. Wohlleben, S. Gröters, K. Wiench, U. Veith, W. Teubner, B. van Ravenzwaay and R. Landsiedel, *Inhalation Toxicol.*, 2016, **28**, 463–479.
- 63 R. Landsiedel, L. Ma-Hock, T. Hofmann, M. Wiemann, V. Strauss, S. Treumann, W. Wohlleben, S. Groeters, K. Wiench and B. Ravenzwaay, *Part. Fibre Toxicol.*, 2014, **11**, 16.
- 64 L. Ma-Hock, V. Strauss, S. Treumann, K. Kuttler, W. Wohlleben, T. Hofmann, S. Groeters, K. Wiench, R. B. van and R. Landsiedel, *Part. Fibre Toxicol.*, 2013, **10**, 23.
- 65 J. Keller, W. Wohlleben, L. Ma-Hock, V. Strauss, S. Gröters, K. Kuttler, K. Wiench, C. Herden, G. Oberdörster and B. van Ravenzwaay, *Arch. Toxicol.*, 2014, **88**, 2033–2059.
- 66 R. Landsiedel, L. Ma-Hock, A. Kroll, D. Hahn, J. Schnekenburger, K. Wiench and W. Wohlleben, *Adv. Mater.*, 2010, **22**, 2601–2627.
- 67 I. Gosens, F. R. Cassee, M. Zanella, L. Manodori, A. Brunelli, A. L. Costa, B. G. H. Bokkers, W. H. de Jong, D. Brown, D. Hristozov and V. Stone, *Nanotoxicology*, 2016, **10**, 1084–1095.
- 68 J. H. E. Arts, H. Muijser, E. Duistermaat, K. Junker and C. F. Kuper, *Food Chem. Toxicol.*, 2007, **45**, 1856–1867.
- 69 R. Landsiedel, J. Schnekenburger, F. Alessandrini, A. Haase, A. Luch, L. Ma-Hock and M. Wiemann, nanoGEM final project report (Gemeinsamer Abschlussbericht nanoGEM), *Work package 4 (AP4): Nanoparticle toxicology: Material properties and effects*, 2014, ch. 6, pp. 105–144, DOI: 10.2314/GBV:82774322X (project report in German).
- 70 W. Wohlleben, M. D. Driessen, S. Raesch, U. F. Schaefer, C. Schulze, B. V. Vacano, A. Vennemann, M. Wiemann, C. A. Ruge, H. Platsch, S. Mues, R. Ossig, J. M. Tomm, J. Schnekenburger, T. A. J. Kuhlbusch, A. Luch, C.-M. Lehr and A. Haase, *Nanotoxicology*, 2016, 1–11, DOI: 10.3109/17435390.2016.1155671.
- 71 L. Chen, C. Wang, S. Yang, X. Guan, Q. Zhang, M. Shi, S.-T. Yang, C. Chen and X.-L. Chang, *Environ. Sci.: Nano*, 2019, **6**, 1077–1088.
- 72 D. Pantano, N. Neubauer, J. Navratilova, L. Scifo, C. Civardi, V. Stone, F. von der Kammer, P. Müller, M. S. Sobrido, B. Angeletti, J. Rose and W. Wohlleben, *Environ. Sci. Technol.*, 2018, **52**(3), 1128–1138.
- 73 J. P. Kaiser, M. Roesslein, L. Diener and P. Wick, *PLoS One*, 2013, **8**, e83215.
- 74 E. Ruggiero, K. Vilsmeier, P. Mueller, S. Pulbere and W. Wohlleben, 2019, *Environ. Sci.: Nano*, 2019, DOI: 10.1039/c9en00227h.
- 75 R. S. Lankone, E. Ruggiero, D. G. Goodwin, Jr., K. Vilsmeier, P. Mueller, S. Pulbere, K. Challis, Y. Bi, P. Westerhoff, J. Ranville, D. H. Fairbrother, L.-P. Sung and W. Wohlleben, 2019, Manuscript submitted.
- 76 R. Zepp, E. Ruggiero, B. Acrey, M. J. B. Davis, C. Han, H.-S. Hsieh, K. Vilsmeier, W. Wohlleben and S. D. Endalkachew, 2019, submitted.
- 77 D. Singh, W. Wohlleben, R. D. L. T. Roche, J. C. White and P. Demokritou, *NanoImpact*, 2019, **13**, 44–55.
- 78 B. Funk, D. Göhler, B. Sachsenhauser, M. Stintz, B. Stahlmecke, B. A. Johnson and W. Wohlleben, *Environ. Sci.: Nano*, 2019, **6**, 1443–1456.
- 79 T. A. J. Kuhlbusch, S. W. P. Wijnhoven and A. Haase, *NanoImpact*, 2018, **10**, 11–25.
- 80 V. Adam, T. Yang and B. Nowack, *Environ. Toxicol. Chem.*, 2019, **38**, 436–447.
- 81 M. Hauser, G. Li and B. Nowack, *J. Nanobiotechnol.*, 2019, **17**, 56.
- 82 R. Lehner, C. Weder, A. Petri-Fink and B. Rothen-Rutishauser, *Environ. Sci. Technol.*, 2019, **53**, 1748–1765.
- 83 X. Gao and G. V. Lowry, *NanoImpact*, 2018, **9**, 14–30.
- 84 T. Schneider and K. A. Jensen, *Ann. Occup. Hyg.*, 2008, **52**, 23–34.

### 3.1.2 Abiotic dissolution rates of 24 (nano)forms of 6 substances compared to macrophage-assisted dissolution and in vivo pulmonary clearance: Grouping by biodissolution and transformation

Koltermann-Jüly\*, **Keller JG\***, Vennemann A, Werle K, Müller P, Ma-Hock L, Landsiedel R, Wiemann M, Wohlleben W.

\*Equal contribution

NanoImpact Volume 12, October 2018, Pages 29-41

<https://doi.org/10.1016/j.impact.2018.08.005>

#### **Abstract:**

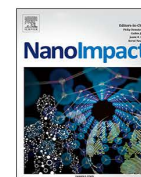
Numerous recent reviews have highlighted the urgent need for methods to determine the biodissolution of nanomaterials in relevant lung fluids, and to validate the results against the bioprocessing *in vivo*. Moreover, it is largely unknown to what extent (nano)forms of a substance that differ in size, shape, or coating also differ in biodissolution. Here we apply a previously optimized abiotic flow-through method to 24 (nano)forms of 6 substances and compare the results with alveolar macrophage-assisted biodissolution of a subset of these nanomaterials *in vitro* and short-term inhalation results *in vivo*. As a main result we found that the results obtained with the flow-through method for the lung were consistent to the results of *in vivo* studies and were not improved by measuring alveolar macrophage-assisted biodissolution for up to 48 h. Based on selected benchmark materials we propose four groups of materials according to quantitative biodissolution rates (1 ng/cm<sup>2</sup>/h to 100 ng/cm<sup>2</sup>/h cutoffs) and qualitative transformation parameters, as detected by TEM analysis. These groups were also reflected by different lung clearance rates, as previously determined in short term inhalation studies. Biodissolution was similar within substance (nano)forms of Fe<sub>2</sub>O<sub>3</sub>, SiO<sub>2</sub>, CeO<sub>2</sub>, ZnO, though slightly varied upon surface area/coating. But the difference of biodissolution between the substances was in some cases more than 1000-fold. In contrast, Cu-containing nanoforms behaved heterogeneously and require case-by-case testing of dissolution and transformation. Different production routes and/or surface coatings significantly modulated biodissolution, whereas effects of shape or size were limited. In summary, we refined a protocol for the abiotic determination of biodissolution along with an integrated assessment of nanomaterial transformation. The protocol is suggested as tier 2 methodology for grouping and read-across purposes.





Contents lists available at ScienceDirect

NanoImpact

journal homepage: [www.elsevier.com/locate/nanoimpact](http://www.elsevier.com/locate/nanoimpact)

## Abiotic dissolution rates of 24 (nano)forms of 6 substances compared to macrophage-assisted dissolution and *in vivo* pulmonary clearance: Grouping by biodissolution and transformation



Johanna Koltermann-Jüly<sup>a,c,1</sup>, Johannes G. Keller<sup>a,b,1</sup>, Antje Vennemann<sup>d</sup>, Kai Werle<sup>b</sup>, Philipp Müller<sup>b</sup>, Lan Ma-Hock<sup>a</sup>, Robert Landsiedel<sup>a</sup>, Martin Wiemann<sup>d,\*</sup>, Wendel Wohlleben<sup>a,b,\*\*</sup>

<sup>a</sup> BASF SE, Dept. of Experimental Toxicology and Ecology, 67056 Ludwigshafen, Germany

<sup>b</sup> BASF SE, Dept. of Material Physics, 67056 Ludwigshafen, Germany

<sup>c</sup> Biopharmaceutics and Pharmaceutical Technology, Saarland University, 66123 Saarbrücken, Germany

<sup>d</sup> IBE R&D Institute for Lung Health gGmbH, 48149 Münster, Germany

### ARTICLE INFO

#### Keywords:

Dissolution

Transformation

Grouping

Read-across

Alveolar macrophages

### ABSTRACT

Numerous recent reviews have highlighted the urgent need for methods to determine the biodissolution of nanomaterials in relevant lung fluids, and to validate the results against the bioprocessing *in vivo*. Moreover, it is largely unknown to what extent (nano)forms of a substance that differ in size, shape, or coating also differ in biodissolution. Here we apply a previously optimized abiotic flow-through method to 24 (nano)forms of 6 substances and compare the results with alveolar macrophage-assisted biodissolution of a subset of these nanomaterials *in vitro* and short-term inhalation results *in vivo*. As a main result we found that the results obtained with the flow-through method for the lung were consistent to the results of *in vivo* studies and were not improved by measuring alveolar macrophage-assisted biodissolution for up to 48 h. Based on selected benchmark materials we propose four groups of materials according to quantitative biodissolution rates (1 ng/cm<sup>2</sup>/h to 100 ng/cm<sup>2</sup>/h cutoffs) and qualitative transformation parameters, as detected by TEM analysis. These groups were also reflected by different lung clearance rates, as previously determined in short term inhalation studies. Biodissolution was similar within substance (nano)forms of Fe<sub>2</sub>O<sub>3</sub>, SiO<sub>2</sub>, CeO<sub>2</sub>, ZnO, though slightly varied upon surface area/coating. But the difference of biodissolution between the substances was in some cases > 1000-fold. Among the Cu-containing materials, the behavior of the two CuPhthalocyanin nanoforms was similar with each other, but completely different than the dissolution and transformation of Cu salts. Different production routes and/or surface coatings significantly modulated biodissolution, whereas effects of shape or size were limited. In summary, we refined a protocol for the abiotic determination of biodissolution along with an integrated assessment of nanomaterial transformation. The protocol is suggested as tier 2 methodology for grouping and read-across purposes.

### 1. Introduction

Engineered nanomaterials (ENM) are produced in numerous grades, which are each optimized for specific applications and differ in properties such as composition, size, shape, surface treatments. Especially fillers and pigments represent established materials that are produced in megaton quantities in many different (nano)forms (Wohlleben et al.,

2017a; Ministère de l'Environnement, 2015). For a given material composition, the properties size, shape, and surface chemistry describe the “nanoform” for regulatory purposes (ECHA, 2017a), but none of these properties is sufficient to predict the extent to which human or environmental hazards differ from the non-nanoform of the same composition (Godwin et al., 2015; Landsiedel et al., 2017; Donaldson and Poland, 2013). Assessing similarity to known benchmark materials

\* Correspondence to: M. Wiemann, IBE R&D Institute for Lung Health gGmbH, 48149 Münster, Germany.

\*\* Correspondence to: W. Wohlleben, BASF SE, Dept. of Material Physics and Dept. of Experimental Toxicology and Ecology, 67056 Ludwigshafen, Germany.

E-mail addresses: [johanna.koltermann-juelly@basf.com](mailto:johanna.koltermann-juelly@basf.com) (J. Koltermann-Jüly), [johannes-georg.keller@basf.com](mailto:johannes-georg.keller@basf.com) (J.G. Keller), [vennemann@ibe-ms.de](mailto:vennemann@ibe-ms.de) (A. Vennemann), [kai.werle@basf.com](mailto:kai.werle@basf.com) (K. Werle), [lan.ma-hock@basf.com](mailto:lan.ma-hock@basf.com) (L. Ma-Hock), [robert.landsiedel@basf.com](mailto:robert.landsiedel@basf.com) (R. Landsiedel), [martin.wiemann@ibe-ms.de](mailto:martin.wiemann@ibe-ms.de) (M. Wiemann), [wendel.wohlleben@basf.com](mailto:wendel.wohlleben@basf.com) (W. Wohlleben).

<sup>1</sup> Equal contribution.

<https://doi.org/10.1016/j.impact.2018.08.005>

Received 26 April 2018; Received in revised form 6 August 2018; Accepted 22 August 2018

Available online 25 August 2018

2452-0748/ © 2018 The Authors. Published by Elsevier B.V. This is an open access article under the CC BY-NC-ND license (<http://creativecommons.org/licenses/by-nc-nd/4.0/>).

can be a powerful approach to reduce the uncertainty related to the risks of innovative (nano)materials, and to revisit the safety of established materials. Especially the rate of dissolution under simulated physiological conditions (biodissolution) is an important criterion to assess similarity between (nano)forms of the same substance in several frameworks of grouping and read-across (Collier et al., 2015; Nel et al., 2013; Kuempel et al., 2012; Braakhuis et al., 2014; Oomen et al., 2017; Arts et al., 2015, 2016). However, Steinhäuser and Sayre have stressed that most frameworks do not propose a specific method, often confound solubility with the dissolution rate or transformation, and rarely propose quantitative group limits (Steinhäuser and Sayre, 2017). One has to differentiate:

- “solubility” is measured in equilibrium saturated suspensions, with appropriate descriptors of mg/L ion, identical with the conventional solubility limit. Implicitly, it often means solubility in water at neutral pH and was proposed as Tier 1 screening for soluble ENM, (Arts et al., 2015) to be refined to the solubility in relevant medium as Tier 2 method (Arts et al., 2015; Avramescu et al., 2016). Plakhova et al. demonstrated that “% dissolved” is not an equivalent metric, and probably not appropriate (Plakhova et al., 2016).
- “dissolution rate” is measured out of equilibrium conditions and below the saturation in the relevant medium, with appropriate descriptors in units of ion mass per solid mass per time (=%/h) or ion mass per solid particle surface per time (=ng/cm<sup>2</sup>/h). It is considered an extrinsic property.
- “transformation” describes the propensity of the non-dissolved remaining solids to “change what they are” in the relevant medium, regarding their physical shape, or size, or chemical identity, and has no clearly defined descriptors. It is also considered as extrinsic property and has implications for hazard assessment, e.g. if the aspect ratio or crystalline phase changes.

Accordingly, a recent review by Oberdörster and Kuhlbusch found that “because the *in vivo* dissolution rates of ENM can differ widely, it is too simplistic to group ENM just into soluble and poorly soluble materials.” (Oberdörster and Kuhlbusch, 2018), and the appropriate differentiation of (nano)materials by static solubility values has been questioned (Klaessig, 2018). To measure instead dissolution rates, flow cells (Nti, 2017) mimic the non-equilibrium physiological conditions, where ions can be transported away from the lungs. Variants of flow cells have been used recently for environmental dissolution (Kent and Vikesland, 2016) and for oral dissolution of nanomaterials (Bove et al., 2017a). For mineral fibers, flow-through cell dissolution rates correlate strongly with *in vivo* pulmonary clearance (Guldberg et al., 1995; IARC, 2002). Simulant media need to be sufficiently complex to offer oxidative, reductive and pH-driven dissolution pathways (Wang et al., 2016). Specifically for pulmonary biodissolution, phagolysosomal simulant media with a low pH value (4.5) are appropriate because alveolar macrophages (AMs) collect and engulf the vast majority of inhaled ENM from the alveolar surface, and rapidly transfer them into acidic phagolysosomes (Stefaniak et al., 2005; Marques et al., 2011).

Here we apply the abiotic flow-through method with a phagolysosomal simulant to a wide range of (nano)materials with different substance, size, shape, coating. Following the dissolution rate quantification we prepare the remaining solids on transmission electron microscopy (TEM) grids and assess the transformation of nanoparticles by electron microscopy.

However, abiotic dissolution at phagolysosomal conditions remains a simplistic approximation and may underestimate the more complex macrophage-assisted physical (mobility) and chemical (dissolution) clearance (Kass, 1964; Geiser, 2010). Oberdörster and Kuhlbusch concluded that “Results from [Alveolar Macrophage] *in vitro* assays with microparticles show good agreement with *in vivo* kinetics; yet further studies using MNs/ENM of different solubilities are required to validate this *in vitro* AM assay for nanomaterials.” (Oberdörster and Kuhlbusch,

2018) Here we hypothesize that AMs might accelerate dissolution, especially of pH sensitive nanomaterials, and explore to which extent the dissolution rates are compatible between abiotic and macrophage-assisted dissolution, using BaSO<sub>4</sub>, ZnO and SrCO<sub>3</sub> as test cases. ZnO was proposed earlier as benchmark material, because it is poorly soluble in water, but becomes soluble under phagolysosomal conditions (Arts et al., 2015; Avramescu et al., 2016). Further, it is known that SrCO<sub>3</sub> is poorly soluble in water but readily soluble under acidic conditions. In contrast to an earlier approach based on human and dog AMs (Kreyling et al., 1979) whose isolation demands human volunteers or animal experiments, we used an AM cell line (NR8383) from rat lung lavage cells (Helmke et al., 1987, 1989). It was shown, that NR8383 cells maintain their typical AM-like size, appearance, and phagocytic properties over many passages. In addition, they maintain their immunological properties, thus reacting to test material exposure by the formation and release of different pro-inflammatory and fibrogenic cytokines and chemokines, including TNF- $\alpha$ , IL-1, TGF- $\beta$  and PDFG (Helmke et al., 1987, 1989; Koslowski et al., 2003; Albrecht et al., 2007; Scherbart et al., 2011; Bhattacharjee et al., 2012). Furthermore, the cells are capable of producing H<sub>2</sub>O<sub>2</sub> e.g. via the NADPH oxidase reaction process (also known as “respiratory burst”) which is an inherent part of the macrophages’ armament and may contribute to the processing or dissolution of ENM.

NR8383 cells have been used for the *in vitro* testing of a variety of ENM including functionalized amorphous silicates, indium tin oxide, alumina, ultrafine titania, (multi-walled) carbon nanotubes (mWCNTs), various copolymers and also heparin nanoparticles (Scherbart et al., 2011; Bhattacharjee et al., 2012; Lison et al., 2008, 2009; Pulskamp et al., 2007; Wagner et al., 2007; Eidi et al., 2010, 2012; Bhattacharjee et al., 2013). Most specifically, the *in vitro* potency screening by NR8383 cells correlates excellently with *in vivo* inflammatory short-term inhalation study (STIS) results for the purposes of Tier 2 grouping of ENM in the DF4nanoGrouping framework (Arts et al., 2015; Wiemann et al., 2016), such that cell-assisted biodissolution with NR8383 macrophages would seamlessly integrate in a grouping framework, if necessary.

## 2. Materials and methods

### 2.1. Materials

To obtain results which are representative for the broad field of ENM applications, six substances with 24 different (nano)forms were selected with prioritization by availability of *in vivo* studies (cited for each material in the following) and industrial relevance (Ministère de l’Environnement, 2015). The (nano)forms vary in size, crystallinity/shape and coating. Both, CeO<sub>2</sub> NM-211 and CeO<sub>2</sub> NM-212 were provided by the JRC repository of the Organization for Economic Co-operation and Development (OECD) sponsorship program, they differ in size and form (Keller et al., 2014; Molina et al., 2014). The test set also includes two kinds of BaSO<sub>4</sub> whereas the nanosized BaSO<sub>4</sub> NM-220 was provided by the OECD sponsorship program (via Fraunhofer Institute) and the non-nano-sized BaSO<sub>4</sub> IRMM381 is a reference material, provided by the Institute for Reference Materials and Measurement (IRMM, Geel, with kind permission by Solvay) (Babick et al., 2016; Wohlleben et al., 2017b). Seven different silica materials were investigated. Four different sizes of untreated, colloidal silica: Levasil 50, Levasil 100, Levasil 200 and Levasil 300 were all commercially acquired from Akzo Nobel N. V. (Wiemann et al., 2018). Based on Levasil 200, we synthesized two nanoforms with surface coatings: SiO<sub>2</sub>aminated and SiO<sub>2</sub>phosphonated (Landsiedel et al., 2014). The powdered silica NM-203 was provided by the JRC repository of the OECD sponsorship program. In addition, the test set includes three different kinds of Iron Oxides (Pigment Red 101), the rod shaped Fe<sub>2</sub>O<sub>3</sub>\_nano\_A and the spherical Fe<sub>2</sub>O<sub>3</sub>\_nano\_B were both provided by BASF SE and the cubic Fe<sub>2</sub>O<sub>3</sub>\_larger (borderline non-nano) was provided by Rockwood



Holdings Inc. (Hofmann et al., 2016). Two UV-active TiO<sub>2</sub> materials were compared: TiO<sub>2</sub> NM-104 with an Al<sub>2</sub>O<sub>3</sub> coating and TiO<sub>2</sub> NM-105, both supplied by the JRC repository of the OECD sponsorship program and extensively tested by inhalation (Landsiedel et al., 2010). Both ZnO materials NM-110 and NM-111 are supplied by the JRC repository of the OECD sponsorship program and differ in their coating. ZnO NM-111 has a hydrophobic silicone coating, and is a benchmark “biosoluble” material in the DF4nanogrouping framework (Arts et al., 2016; Landsiedel et al., 2010). Furthermore, the test set consists of four copper-containing materials: The powdered nanoform CuO, provided by PlasmaChem GmbH (Gosens et al., 2016), and the suspension-micronized nanoform Cu<sub>2</sub>(OH)<sub>2</sub>CO<sub>3</sub>, were previously studied for environmental transformations (Pantano et al., 2018), and we added two nanoforms of metal-organic pigments Cu\_Phthalocyanine\_nano (Pigment Blue 15) and Cu\_Phthalocyanine\_halogen (Pigment Green 7), which were provided by BASF SE (Arts et al., 2016). Hydrophilic SrCO<sub>3</sub> was donated by Solvay and was characterized previously in the course of the NanoCare project (Kroll et al., 2011).

## 2.2. Abiotic flow-through testing of dissolution and transformation

The setup (Fig. 1) implements a “continuous flow system” described in ISO 19057:2017 (Nti, 2017). It is essentially a replication of the established flow-through testing of the dissolution kinetics of mineral fibers (Guldberg et al., 1995; IARC, 2002), was described for this purpose (Wohlleben et al., 2017c), and was used here with minor adaptations to match the specifics of ENM: The ENM mass of 1 mg was weighed onto a membrane (cellulose triacetate, Sartorius Stedim Biotech GmbH, Goettingen, Germany): 47 mm diameter, 5 kDa pore size, topped by another membrane, and enclosed in flow-through cells. Standard conditions are 1 mg initial solid mass in the flow-through cell, and 2 mL/h flow. The phagolysosomal simulant fluid (PSF), an acidic buffer simulating the phagolysosomal compartment of macrophages (Stefaniak et al., 2005; Wohlleben et al., 2017c), which was previously validated for the purpose of inhaled beryllium dissolution by NIST laboratories (Stefaniak et al., 2005), was employed at 37 ± 0.5 °C. The PSF composition is reproduced in the supplementary information (SI). In contrast to the larger volume flow cells used by Bove et al. for oral dissolution testing (Bove et al., 2017a), in our setup the ENM are in direct contact with the ultrafiltration membrane. In contrast to the flow cells used by Kent et al., our cells hold industrially produced ENM, not lab-grown arrays of same chemical composition (Kent and Vikesland,

2016). The core idea of separating ions from remaining solids is shared by all three setups.

The programmable sampler drew 4–10 mL of the eluate once per day for seven days. For shorter sampling times at the beginning of the dissolution, the samples were drawn for only 2–3 h instead of 5 h. The rest of the eluate was collected in a container. The ion concentrations of the eluates from different time points were determined by inductively coupled plasma-optical emission spectrometry (ICP-OES Agilent 5100 and Varian 725 ES) with a limit of detection of 0.1 mg/L, alternatively by inductively coupled plasma-mass spectrometry (ICP-MS Perkin Elmer Nexion 2000b) with a limit of detection of 0.1 ppb. Prior to taking the measurement, the instrument was optimized in accordance with the manufacturer's specification. Duplicate measurements are taken and averaged. We measured with 10 s integration time, and the dilution factors were between 1 and 10. External calibration used concentrations of 0/1/5 mg/L with matrix-matched standards. The nebulizer (Meinhard 1 mL) had a flow of 0.7 L/min at a pump rate of 15 rpm. For ICP-MS duplicate measurements were taken and averaged. The eluate was diluted with a factor between 100 to 1000 and the external calibration used concentrations of 0.1/1/10 ppb. The nebulizer had a flow of 0.92 L/min at a pump rate of 35 rpm.

After the experiment, the remaining solids were rinsed off the membrane as shown in the photo-protocol in Fig. SI\_S3 documenting specifically developed accessories. The resulting suspension was then pelleted onto a TEM grid held at the bottom of a centrifuge vial within 30 min, then dried, so that the remaining solids morphology can be inspected without interference from drying artifacts of PSF salts, which are removed by this preparation. The remaining solids were analyzed by TEM with a Tecnai G2-F20ST or Tecnai Osiris Microscope (FEI Company, Hillsboro, USA) at an acceleration voltage of 200 keV under bright-field conditions. For the automated image analysis the pre-validated NanoDefine SEM/TEM software packages were used (Ullmann and Müller, 2017; Mielke et al., 2016; Muller et al., 2015).

We multiplied the measured ion concentration of each eluate with the eluted volume to obtain a mass of dissolved ions, and corrected for the molar mass  $m$  of the pristine ENM and of the detectable metal ion, to obtain the mass of ENM solids  $M_{dissolved}(t)$  that were dissolved during the sampling interval  $\Delta t_i$ . Interim calculations are detailed in the SI. Cumulated from all samplings with concentration  $c_i$ , flow  $V_i$  and sampling interval  $\Delta t_i$ , the dissolved mass at the final time  $T$  is

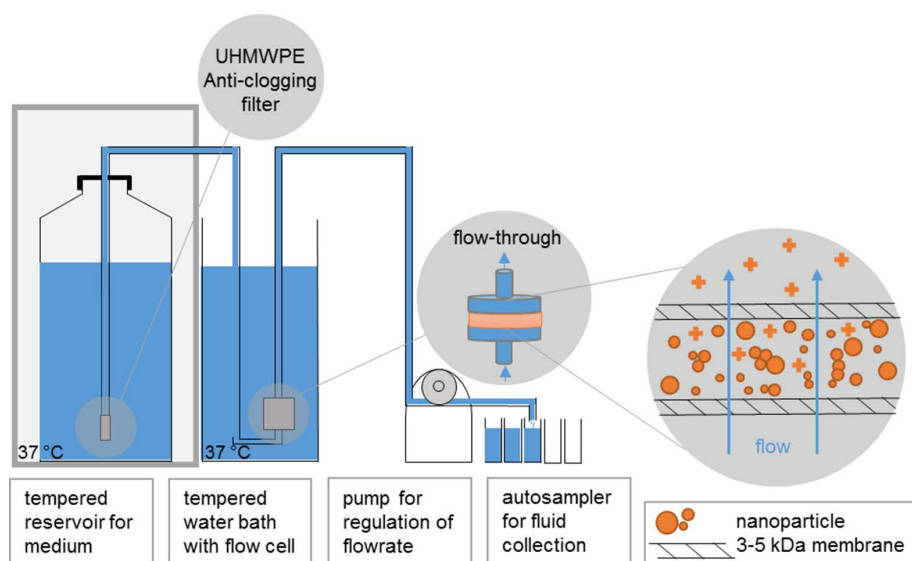


**Fig. 1.** Dissolution setup. The reservoir for the physiological fluid is controlled at 37 °C, as well as the flow-through cells. The peristaltic pump regulates the flow-rate of up to 8 cells in parallel, with a programmable autosampler for fluid collection. The flow-through cell is equipped with 5 kDa membranes to hold back particles and only allow the flow of ions. The meniscus of the reservoir is elevated approx. 0.5 m above the cells such that the hydrostatic pressure balances the pressure drop by the 5 kDa membrane.



$$M_{\text{dissolved}}(T) = \frac{m(\text{ENM})}{m(\text{metal\_ion})} * \sum_{i=0}^T c_i(\text{ion}) * V_i * \Delta t_i \quad (1)$$

The dissolution rate  $k$  is then obtained via  $M_{\text{solids}}(T) = M_0 - M_{\text{dissolved}}(T)$  with the relation:

$$k = \ln \{M_0/M_{\text{solids}}(T)\}/(\text{SSA}(T)*T) \quad (2)$$

This calculation is consistent with the first order modeling of ISO 19057:2017 (Nti, 2017), but gives  $k$  in units of  $\text{ng}/\text{cm}^2/\text{h}$  as recommended by Oberdörster and Kuhlbusch (2018).  $\text{SSA}(T)$  is the specific surface area at time  $T$ , equal to BET at time zero;  $k$  can be converted to a half-time  $t_{1/2}$  by Eq. SI.1. The alternative metric “% dissolved” is given by  $M_{\text{dissolved}}(T)/M_0$ .

### 2.3. Preparation of nanoparticle suspensions for in vitro testing

BaSO<sub>4</sub> NM-220, SrCO<sub>3</sub>, ZnO NM-110, or ZnO NM-111 ENM were suspended in double distilled H<sub>2</sub>O at a concentration of 1 mg/mL. Suspensions were ultrasonicated on ice for 10 × 10 s using a 3 mm probe adjusted to 50 W (Vibra Cell™, Sonics & Materials, USA). To remove larger aggregates (typical for the spray dried BaSO<sub>4</sub> ENM) which cannot be engulfed by macrophages, the BaSO<sub>4</sub> and SrCO<sub>3</sub> suspensions were filtered through a depth-type filter with 2.7 μm pore size (Whatman™ GD/X 25 syringe filter with 2.7 μm GF/D Glass Microfiber Membrane). The filtrate was dried and the particle content was measured gravimetrically, resulting in a concentration of 500 μg/mL. Aqueous suspensions of SrCO<sub>3</sub> and BaSO<sub>4</sub> were then adjusted to 90 μg/mL. Suspensions of ZnO NM-110 and ZnO NM-111 were diluted to 11.25 μg/mL. All aqueous suspensions were then mixed with an equal volume of double-concentrated (2×) F-12K cell culture medium prepared from powder medium (Sigma-Aldrich GmbH, Munich, Germany), supplemented with glutamine (4 mM) and penicillin (200 U), streptomycin (200 mg/ml), and 10% (v/v) fetal bovine serum (FBS) (PAN Biotech GmbH, Aidenbach, Germany), or with double-concentrated phagolysosomal simulant fluid (PSF) adjusted to pH 4.5 with 1 M NaOH. The final suspension, as used for dissolution experiments, therefore contained all F-12K components and supplements, 5% FBS and 45 μg/mL (SrCO<sub>3</sub>, BaSO<sub>4</sub>) or 5.6 μg/mL (ZnO) of the ENM, respectively. Equal concentrations of ENM were prepared in PSF. All ENM suspensions were prepared shortly before use and vortexed immediately before *in vitro* application. Based on previous cytotoxicity data for BaSO<sub>4</sub> and ZnO (Wiemann et al., 2016) the concentrations were maximized up to values where cytotoxic effects were absent or minimal. For SrCO<sub>3</sub>, a no adverse effect level larger than 90 μg/mL was found under the same conditions. This strategy was chosen to increase the yield of dissolved ions and also to avoid early cell death.

### 2.4. Preparation of the NR8383 test system

The rat AM cell line NR8383 (Helmke et al., 1987, 1989) was purchased from ATCC (Manassas, VA, USA) and used for *in vitro* experiments. Cells were grown in F-12K medium (Sigma-Aldrich GmbH, Munich, Germany) supplemented with 15% FBS, glutamine, and penicillin (100 U), streptomycin (100 μg/ml) under standard cell culture conditions (37 °C, 5% CO<sub>2</sub>) as described (Wiemann et al., 2016). For dissolution tests, the macrophages were detached from the substrate by mechanical agitation, fully dispersed by pipetting, seeded into 96-well flat-bottom plates (Primaria™, Corning, NY, USA) at a density of 3 × 10<sup>5</sup> live cells per well, and pre-incubated in F-12K supplemented with 5% FBS for 24 h. Then the medium was completely replaced by ENM suspensions (see above). Cell-free experiments were conducted side-by-side, i.e. on the same plates, using F-12K medium with 5% FBS and PSF as dispersants. For each single experiment 8 identical wells were run in parallel. To accelerate sedimentation of particles and unify the onset of exposure of cells to ENM, plates were centrifuged at 100 ×g (37 °C) for 10 min and incubated under cell culture conditions for 3 h,

6 h, 12 h, 24 h, and 48 h with SrCO<sub>3</sub> or BaSO<sub>4</sub>, or 24 h to ZnO NM-110 or NM-111, respectively. Phase contrast micrographs were taken to monitor gravitational settling, uptake of larger particles or cell lysis using a Zeiss Axiovert C40 microscope equipped with an AxioCam C3 camera.

Following incubation with ENM, cells were completely lysed by adding 20 μl of a concentrated mixture of Triton X-100 and proteinase K (final concentration: 0.1% and 0.1 mg/mL, respectively) for 45 min, as controlled by phase contrast microscopy. Non-lysed ENM were separated by ultrafiltration. Therefore lysates were pooled, loaded onto 100 kDa filter devices (Amicon 100k ultra-0.5, Merck KGaA, Darmstadt, Germany) and centrifuged at 14,000 ×g for 15 min. Filtrates were then forced through a 3 kDa filter (Amicon 3k ultra-0.5, Merck KGaA, Darmstadt, Germany) by centrifugation (14,000 ×g, 20 min) and used for chemical analysis.

The ionic Ba, Sr, or Zn concentration was assessed by ICP-MS (ICP-MS 8800, Agilent Technologies, Santa Clara, CA, US) and corrected for the molar mass of the pristine ENM and the detectable metal ion, to obtain the mass of dissolved ENM solids. Results are shown as mean ± standard deviation (SD). To test for statistical significance, test values were compared to control values using Welch's unequal variances *t*-test. Test results with  $p \leq 0.05$  were assessed as significant (\*). All experiments were performed in triplicates.

### 2.5. Determination of cytotoxicity

Cytotoxic effects of ENM were monitored by measuring the lactate dehydrogenase (LDH) activity in the cell culture supernatant as an indicator for membrane damage and/or cell necrosis. Measurements were carried out as described (Wiemann et al., 2016) using the Roche Cytotoxicity Kit (Roche, Germany). In brief, cell culture supernatants were centrifuged (10 min, 200g) to remove larger particles and cell debris. A volume of 50 μL was incubated with LDH reaction mix (Roche Cytotoxicity Kit; Roche, Germany) and evaluated as described by the manufacturer. Optical density (OD) was measured at 490 and 620 nm in a plate photometer (Tecan 200Pro, Tecan, Germany). Measurements were routinely corrected for cell free-adsorption (to erase effects of particles on the optical signal) and normalized to the positive control value (set to 100%) obtained from NR8383 cells lysed with 0.1% Triton X-100 (Sigma, Aldrich, Germany). Particles investigated in this study had no influence on the LDH signals.

## 3. Results

### 3.1. Abiotic dissolution and transformation

The dissolution kinetics of 24 ENM was investigated in pH 4.5 PSF (Fig. 2A–E). For some materials, e.g. both nanoforms of CeO<sub>2</sub>, the ion concentration in the eluate remains below the limit of detection (LoD) at any sampling time. In this case a virtual value was calculated from the number of consecutive measurements multiplied by LoD, however no plot was generated for this data. With ICP-OES as analysis technique, dissolution remained below LoD for all nanoforms of CeO<sub>2</sub> and Fe<sub>2</sub>O<sub>3</sub>. With ICP-MS as analysis technique that is sufficiently sensitive on the ppb ion level that is to be expected, (Plakhova et al., 2016) quantitative values could be generated also by the flow cells, but would not change the assignment to the group of materials with low dissolution rate. The dissolution of the barely soluble material BaSO<sub>4</sub> NM-220 (Fig. 2B) has been identified elsewhere as a combination of dissolution and Ostwald ripening, highlighted by an unexpected growth of particle size (re-produced in Fig. SI.56) (Keller et al., 2018). Here we compare the non-nanoform by the same supplier BaSO<sub>4</sub> IRMM381, and find that by matching the initial surface area of the two forms (testing BaSO<sub>4</sub> NM-220 at  $M_0 = 0.17$  mg), both the nanoform and the non-nanoform have nearly identical  $k_{\text{app}}$  and  $M_{\text{ion}}/T$  (Table 1). In this manner, the maximum ion concentration is different but remains for both below the

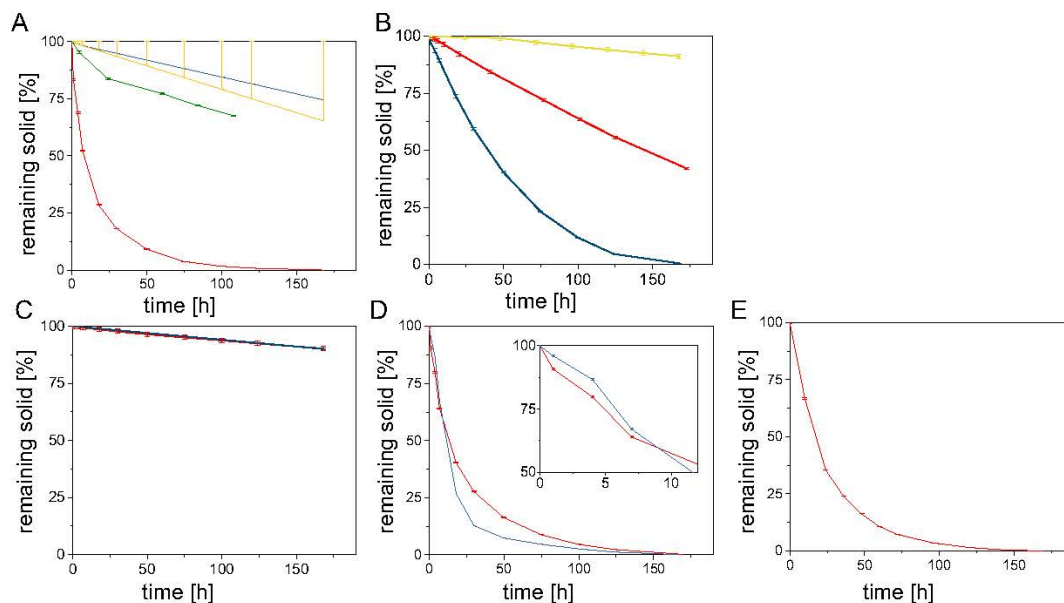


**Fig. 2.** Dissolution kinetics. A: Cu (red CuO, blue CuPhthalo\_nano, yellow CuPhthalo\_halogen, green  $\text{Cu}_2(\text{OH})_2\text{CO}_3$ ); B:  $\text{BaSO}_4$  (red NM-220 1.05 mg, blue NM-220 0.17 mg, yellow IRMM381), C:  $\text{SiO}_2$  (red NM-203, blue  $\text{SiO}_2$ \_amino), D: ZnO (red NM-110, blue NM-111), with inset enlarging the initial effects. E:  $\text{SrCO}_3$ . The error bars displayed here equal the duplicate uncertainty of the ICP-OES measurements.

pH 4.5 solubility limit, such that reprecipitation and Ostwald ripening are suppressed. The matching of dissolution rates from nano- and non-nanoform confirms the validity of the surface-based  $k$  metric.

For all six forms of  $\text{SiO}_2$  (Table 1 and Fig. 2C) the dissolution is rather limited in the acidic PSF medium, as expected. However, we do observe a higher dissolution for  $\text{SiO}_2$  NM-203, which is produced by a different process (precipitation, then drying) than the colloidal nanoforms of  $\text{SiO}_2$  ( $\text{SiO}_2$ \_untreated\_50 to  $\text{SiO}_2$ \_untreated\_300). Knowing that soluble forms of  $\text{SiO}_x$  tend to polymerize, we stored the elution samples from NM-203 alternately with or without addition of 10% of 1 M HCl, but the resulting kinetics superimposed completely, confirming sufficient stability of dissolved Si-species before detection. Additionally, we measured another  $\text{SiO}_2$  powder (NM-200) and found similar dissolution rates. While there is a trend to release more ions from smaller particles (in the  $\text{SiO}_2$ \_untreated\_50 to  $\text{SiO}_2$ \_untreated\_300 family (Wiemann et al., 2018)), the surface increase is larger so that the nominal dissolution rate  $k$  is lower for the smaller forms. Considering that especially in acidic medium  $\text{SiO}_2$  tends to undergo polymerization and gel formation, a lower initial concentration of solids might help to demonstrate a stronger relationship with size, but would underscore the detection limit of our ICP-MS. Interestingly, surface functionalization ( $\text{SiO}_2$ \_amino\_200,  $\text{SiO}_2$ \_phosphonate\_200) can increase dissolution threefold compared to the core particle ( $\text{SiO}_2$ \_untreated\_200).

The four Cu-containing nanoforms show a very diverse dissolution as seen in Fig. 2A. CuO dissolves completely after 7 days under standard conditions, whereas  $\text{Cu}_2(\text{OH})_2\text{CO}_3$  dissolves moderately (32% after 7 days) and both Cu Phthalocyanin nanoforms shed only negligible amounts of ions. The difference is evident by the comparison of daily Cu release of  $456 \mu\text{g}$  from CuO compared to  $0.66 \mu\text{g}$  from Cu Phthalocyanin\_nano (Pigment Blue 15). These traces of Cu from Pigment Blue 15 are not necessarily attributed to particle dissolution but rather to remaining Cu from the complexation synthesis of the technical materials.

Very interestingly, Fig. 2D demonstrates a small retardation (from day 2 to 5) of the dissolution kinetic for the ZnO nanoform with coating, ZnO NM-111. However, after this retardation, attributed to the dissolution of the coating, the overall dissolution of ZnO NM-111 is accelerated (Table 2).

Transformation is frequently observed for zero-valent Ag- or Cu-particles with numerous studies showing re-crystallization, re-speciation (changing the chemical composition) especially in environmental media (Gao and Lowry, 2018; Vencalek et al., 2016; Dale et al., 2015; Mitrano and Nowack, 2017; Mitrano et al., 2015). Here we apply a standardized protocol of aging and sample preparation (Fig. S1S3), with representative results shown in Fig. 3. Comparing the first pair of images (Fig. 3a), the TEM results support the complete dissolution of ZnO NM-110 incurred from the addition of all ions in the eluates, observations made for with the dissolution setup, as no particles could be found. In contrast,  $\text{Fe}_2\text{O}_3$ \_nano.B (Fig. 3b) showed no significant difference between the pristine material and the material after a week of exposure to PSF. Cu Phthalocyanin\_nano tended to form aggregates, as no smaller particles remained (Fig. 3c). TEM images of  $\text{SiO}_2$ \_untreated nanoparticles (Fig. 3d) revealed a moderate shrinkage. Furthermore, the homogeneous electron density of the particles transformed into an electron dense core and a less electron dense surface layer, which may be interpreted as gel-like and is not unexpected for  $\text{SiO}_2$  under acidic conditions (Iler, 1979).

In addition to the representative cases (potential benchmark materials) in Fig. 3, more ENM have been analyzed with TEM of initial solids vs. remaining solids (Fig. 4). For Cu Phthalocyanin\_halogenated we observed the same behavior as for Cu Phthalocyanin\_nano, because the remaining particles were strongly aggregated. When comparing the TEM image of the pristine particles of  $\text{Cu}_2(\text{OH})_2\text{CO}_3$  with the TEM after the treatment with PSF, we observed that pristine particles had disappeared, while very few secondary particles were visible which consisted mainly of Si, but were devoid of Cu.  $\text{SiO}_2$  NM-203 was found to dissolve faster than colloidal silica of roughly the same constituent particle size ( $\text{SiO}_2$ \_untreated\_200), and forms different intermediate structures (Fig. 4c). This may be due to the aggregate structure with negative radii of curvature (necks between primary particles) (Iler, 1979). As CuO and ZnO underwent complete dissolution within 7 days, an “infinite dilution” approach was employed to study transformation processes: we repeatedly dipped the grids into PSF and successively imaged the same spot of a TEM grid. The results on ZnO nicely demonstrate how its dissolution behavior is completely different from



**Table 1**  
Nanoform physical-chemical descriptors of the 24 test materials.

	Minimum external dimension (TEM or AUC <sup>a</sup> )	Shape (TEM)	Specific surface area (BET)	Composition/crystallinity/impurities (XRD, ICP-MS, XPS)	Surface modification
	[nm]	Descriptive	[m <sup>2</sup> /g]	[%]	Descriptive
BaSO <sub>4</sub> NM-220	32	Spheroidal	41	Purity > 93.8%; Na, Ca, Sr, F, Cl, organic compounds	None
BaSO <sub>4</sub> IRMM381	253	Spheroidal	2.5	Ba 58.8% O 27.4% S 13.7%	None
CeO <sub>2</sub> NM-211	4–15	Spheroidal	66	Purity > 95%	None
CeO <sub>2</sub> NM-212	40	Mixed spheroidal + platelets	27	Purity > 99.5%, 0.7% organic contaminations	None
Cu <sub>2</sub> (OH) <sub>2</sub> CO <sub>3</sub>	34 <sup>a</sup>	Platelets	19	Cu 57%	None
Cu_Phthalo_halogen	14	Platelets	61	Cu 5%	None
Cu_Phthalo_nano	17	Spheroidal	58	Cu 10.4%	None
CuO	40	Spheroidal	34	Purity > 99%, Al, Si 0.1–1%	None
Fe <sub>2</sub> O <sub>3</sub> _larger	48 ± 27	Spheroidal	12	Predominantly Fe <sub>2</sub> O <sub>3</sub> , hematite; traces of magnetite (cubic) Fe <sub>3</sub> O <sub>4</sub>	None
Fe <sub>2</sub> O <sub>3</sub> _nano_A	15–130 × 4–21	Rod shaped	107	Fe <sub>2</sub> O <sub>3</sub> , hematite	None
Fe <sub>2</sub> O <sub>3</sub> _nano_B	37	Spheroidal	30	Fe <sub>2</sub> O <sub>3</sub> , hematite	None
SiO <sub>2</sub> NM-203	20	Spheroidal	200–226	Purity > 99%, Al 0.43%	None
SiO <sub>2</sub> _aminated	15 <sup>a</sup>	Spheroidal	200	SiO <sub>2</sub> amorphous	covalent surface functionalization with low-molar-mass silane having a pos. charged amino end group
SiO <sub>2</sub> _phosphonated	15 <sup>a</sup>	Spheroidal	200	SiO <sub>2</sub> amorphous	covalent surface functionalization with low-molar-mass silane having a neg. charged phosphonate end group
SiO <sub>2</sub> _untreated_50	55 <sup>a</sup>	Spheroidal	50	SiO <sub>2</sub> amorphous	None
SiO <sub>2</sub> _untreated_100	30 <sup>a</sup>	Spheroidal	100	SiO <sub>2</sub> amorphous	None
SiO <sub>2</sub> _untreated_200	15 <sup>a</sup>	Spheroidal	200	SiO <sub>2</sub> amorphous	None
SiO <sub>2</sub> _untreated_300	9 <sup>a</sup>	Spheroidal	300	SiO <sub>2</sub> amorphous	None
SrCO <sub>3</sub>	13–19	Rod shaped	33	Sr: 21.1%; C 27.1%; O: 51.3%	None
TiO <sub>2</sub> NM-104	21	Spheroidal	57	TiO <sub>2</sub> rutile	Al <sub>2</sub> O <sub>3</sub> coating + 2% Polydimethylsiloxan
TiO <sub>2</sub> NM-105	25	Spheroidal	51	TiO <sub>2</sub> mix rutile/anatase	None
ZnO NM-110	42	Mixed spheroidal and rod shaped	12	ZnO > 99%	None
ZnO NM-111	34	Mixed spheroidal and rod shaped	14	ZnO > 97%	Triethoxycaprylsilane silicone coating

<sup>a</sup> Following the NanoDefine e-tool (<http://www.nanodefine.eu/index.php/nanodefiner-e-tool>), materials that are originally produced as colloidal suspensions were characterized by Analytical Ultracentrifugation (AUC) (Mehn et al., 2018), and powders by Transmission Electron Microscopy (TEM).

BaSO<sub>4</sub> NM-220 (Keller et al., 2018), as ZnO reduces the radii of curvature until complete disappearance (Fig. SI\_S4). No dissolution was quantified with our ICP-OES limit of detection for TiO<sub>2</sub> NM-104, CeO<sub>2</sub> NM-212 or Fe<sub>2</sub>O<sub>3</sub>\_nano\_A. The absence of major dissolution or transformation was also confirmed through the analyzation of the crystal structure through selected area electron diffraction (SAD, Fig. SI\_S7). The SAD graph showed unique Cerianite (CeO<sub>2</sub>) signals and thus confirmed that transformation remained limited, although especially Ce<sup>III</sup>-rich surface layers may have undergone transformations. In contrast to the case of BaSO<sub>4</sub> NM-220 (Fig. SI\_S6 reproduced from (Keller et al., 2018)) no Ostwald ripening has occurred for BaSO<sub>4</sub> non-nano (Fig. SI\_S7).

### 3.2. Uptake of nanomaterials by NR8383 cells and cell-assisted dissolution

In the next step we explored in as much macrophage-assisted dissolution differs from the abiotic flow-through dissolution. In contrast to former experiments with AMs (Kreyling et al., 1979), we used cultivated NR8383 rat AMs to avoid animal consumption necessary for the use of primary cells. NR8383 cells are actively moving phagocytic cells which gather particles from the bottom of the cell culture vessels. The cells can be transiently cultivated under low serum-conditions. However, as NR8383 cells are not firmly attached to the substrate, a change of medium may lead to cell loss, such that their incubation with SrCO<sub>3</sub> and BaSO<sub>4</sub> in wells of a 96 well plate was limited to 1–2 days. To increase the yield of dissolved ions under these conditions, a comparatively high concentration of 45 µg/mL was used which, in case of

BaSO<sub>4</sub>, were found to be non-toxic under the conditions of the macrophage assay ((Wiemann et al., 2016), see Supplement Table SI 1 for SrCO<sub>3</sub>). Exposure of the cells to the particle was accelerated by brief centrifugation of ENM onto the bottom of the 96-well plate (Fig. 5a). This procedure had no obvious influence on cell shape or motility but circumvented the phase of gravitational settling and, therefore, provided a common starting point for the time-lapse study of particle dissolution. Under these conditions AMs had entirely engulfed microscopically visible SrCO<sub>3</sub> agglomerates from the bottom of the wells after ≥ 3 h and this situation persisted until the end of incubation (Fig. 5b).

To measure the total amount of intra- and extracellular Sr ions by ICP-MS analysis, cells within each well were completely lysed with Triton X-100 and proteinase K after 3, 6, 12, 24 and 48 h and the homogenates were separated from any particulate constituents by passing through a 3 kDa filter unit. Incubation of SrCO<sub>3</sub> with NR8383 cells significantly increased the concentration of dissolved material in the medium compared to cell-free control at any point in time. For example, after 24 h concentrations of 21.87 ± 0 mg/kg (49% of total mass) and 6.71 ± 0 mg/kg (15% of total mass, n = 3) were measured for the macrophage-mediated dissolution and the cell-free medium control, respectively. Of note, the macrophage-mediated increase in dissolved SrCO<sub>3</sub> developed progressively up to 48 h, indicating ongoing cellular activity. In contrast, the incubation of SrCO<sub>3</sub> ENM in acidic PSF for 24 h led to a rapid dissolution of 97% of the total SrCO<sub>3</sub> mass (43.79 ± 0 mg/kg) and these high values remained fairly constant over time (Fig. 6, Table SI S1a). To analyze cytotoxic effects during SrCO<sub>3</sub> incubation, the activity of LDH was monitored in the cell culture

Table 2

Cumulative evaluation of biodissolution of ENM in flow cells with pH 4.5 media at 2 mL/h flow-through. For many materials, the ion concentration remained below the limit of detection (LoD), but could be improved by using dedicated ICP-MS instruments. **Significant dissolution** is marked bold.

Unit	M <sub>0</sub> [mg]	Max. ion concentration [mg/L]	Dissolved per 7 days [%]	k [ng/cm <sup>2</sup> /h]	M <sub>ion</sub> /T [µg/day]
BaSO <sub>4</sub> NM-220 (nano)	1.05	<b>1.3</b>	<b>58</b>	<b>10</b>	<b>51</b>
BaSO <sub>4</sub> NM-220 (nano)	0.17	<b>0.8</b>	<b>100</b>	<b>45</b>	<b>18</b>
BaSO <sub>4</sub> IRMM381 (non-nano)	1.78	<b>0.49</b>	<b>9</b>	<b>53</b>	<b>16</b>
CeO <sub>2</sub> NM-211	1.1	< 0.1 (LoD)	< 3	< 0.28 (LoD)	< 3.9 (LoD)
CeO <sub>2</sub> NM-212	1.02	< 0.1 (LoD)	< 3	< 0.73 (LoD)	< 3.6 (LoD)
Cu <sub>2</sub> (OH) <sub>2</sub> CO <sub>3</sub>	1.07	<b>3.0</b>	<b>32</b>	<b>172</b>	<b>24</b>
Cu_Phthalohalogen	1	< 0.1 (LoD)	< 35 (LoD)	< 3.7 (LoD)	< 2.4 (LoD)
Cu_Phthalohalogen_nano	0.98	<b>0.05</b>	<b>0.4</b>	<b>0.531</b>	<b>0.66</b>
CuO	1.56	<b>37</b>	<b>100</b>	<b>283</b>	<b>456</b>
Fe <sub>2</sub> O <sub>3</sub> _larger	1.09	< 0.1 (LoD)	< 3 (LoD)	< 1.56 (LoD)	< 3.7 (LoD)
Fe <sub>2</sub> O <sub>3</sub> _nano_A	1.07	< 0.1 (LoD)	< 3 (LoD)	< 0.17 (LoD)	< 3.2 (LoD)
Fe <sub>2</sub> O <sub>3</sub> _nano_B	0.99	< 0.1 (LoD)	< 3 (LoD)	< 0.65 (LoD)	< 3.6 (LoD)
SiO <sub>2</sub> NM-203	1.12	<b>0.3</b>	<b>8</b>	<b>0.23</b>	<b>11</b>
SiO <sub>2</sub> NM-200	1.01	<b>0.45</b>	<b>11</b>	<b>0.383</b>	<b>7.76</b>
SiO <sub>2</sub> _amino_200	1.06	<b>0.28</b>	<b>7</b>	<b>0.216</b>	<b>4.83</b>
SiO <sub>2</sub> _phosphonate_200	1.01	<b>0.18</b>	<b>8</b>	<b>0.275</b>	<b>5.76</b>
SiO <sub>2</sub> _untreated_50	1.17	<b>0.03</b>	<b>0.5</b>	<b>0.088</b>	<b>1.6</b>
SiO <sub>2</sub> _untreated_100	1.08	<b>0.04</b>	<b>0.9</b>	<b>0.066</b>	<b>1.7</b>
SiO <sub>2</sub> _untreated_200	1.0	<b>0.05</b>	<b>1.2</b>	<b>0.044</b>	<b>2.1</b>
SiO <sub>2</sub> _untreated_300	1.05	<b>0.06</b>	<b>1.4</b>	<b>0.034</b>	<b>2.6</b>
SrCO <sub>3</sub>	1.08	<b>12.7</b>	<b>100</b>	<b>108</b>	<b>240</b>
TiO <sub>2</sub> NM-104	1.09	< 0.1 (LoD)	< 0.03 (LoD)	< 0.031 (LoD)	< 2.4 (LoD)
TiO <sub>2</sub> NM-105	1.04	< 0.01 (LoD)	< 0.1 (LoD)	< 0.013 (LoD)	< 0.1 (LoD)
ZnO NM-110	1.12	<b>18</b>	<b>100</b>	<b>204</b>	<b>217</b>
ZnO NM-111	1.12	<b>17</b>	<b>100</b>	<b>177</b>	<b>150</b>

supernatants. LDH activity was low after 3 h and 24 h ( $9.8 \pm 6.5\%$  of Triton X-100 control), but increased to  $81.0 \pm 38.1\%$  of positive control at 48 h. At this point in time light microscopic inspection revealed cells with many pseudopodia and smooth surface, devoid of any signs of cell deterioration (Fig. 5b). In summary, SrCO<sub>3</sub>, whose solubility is known to be pH-dependent, showed an enhanced and progressive dissolution upon uptake and digestion by live macrophages *in vitro*.

In the next step we analyzed whether the dissolution of BaSO<sub>4</sub>, a material with a low solubility at neutral pH, might be also enhanced after uptake by macrophages. Following the same procedure as described for SrCO<sub>3</sub>, 45 µg/mL BaSO<sub>4</sub> ENM suspension was applied to NR8383 AMs. Phase contrast micrographs confirmed the settling of BaSO<sub>4</sub> to the bottom of the wells after centrifugation (Fig. 7a). No BaSO<sub>4</sub> agglomerates remained visible between the cells at all timepoints  $\geq 3$  h (Fig. 7b). ICP-MS analysis of the filtrated cell homogenates and respective controls revealed that, after 24 h incubation of BaSO<sub>4</sub> with NR8383 cells,  $1.88 \pm 0.38$  mg/kg material had dissolved, compared to  $1.33 \pm 0.37$  mg/kg in the cell-free medium control, which corresponds to 4.18% and 2.95% of applied material, respectively. Exposure of BaSO<sub>4</sub> ENM to acidic PSF for 24 h led to dissolved material fractions of  $2.4 \pm 0.08$  mg/kg, which corresponds to a dissolution of 5.34% (Figs. 8 and SI S1b). In accord with the well-known poor solubility of BaSO<sub>4</sub>, we found low amounts of dissolved material in F-12K medium for all time points investigated, namely 2.98% of applied material in average. Although very subtle, NR8383 AM increased the dissolved material portion up to 6.13% at the 48 h timepoint. Similarly, PSF accelerated the dissolution up to 5.34% after 48 h.

The release of LDH 3, 6, 12, and 24 h post administration was very moderate ( $9.53 \pm 4.05\%$  of positive control) but raised to  $48.86 \pm 10.22\%$  of positive control values after 48 h. Again, the microscopic inspection of BaSO<sub>4</sub>-treated cells showed no signs of cell deterioration.

We finally assessed the macrophage-assisted dissolution of uncoated ZnO (NM-110) and surface-coated ZnO (NM-111). Both materials show a high solubility under *in vivo* conditions, i.e. at near neutral pH. NR8383 cells were exposed to only 5.6 µg/mL ZnO NM-110 and ZnO

NM-111. At this concentration, cytotoxic effects of both ENM were moderate after 24 h (ZnO NM-110: 33.59%; ZnO NM-111: 33.69%) and were not influenced by stimulation with lipopolysaccharide (data not shown). ZnO agglomerates of either quality were not visible on the bottom of the cell culture vessel between the cells (not shown) after 24 h. At this timepoint  $2.86 \pm 0.1$  mg/kg (51% dissolution) and  $2.7 \pm 0.12$  mg/kg ZnO NM-110 (48% dissolution) were detected in the supernatant in the presence and absence of NR8383 cells, respectively. Compared to the medium control a significantly higher amount of ZnO NM-110 ( $p = 0.005$ ) was dissolved in PSF ( $3.78 \pm 0.06$  mg/kg, 67% dissolution). Likewise, concentrations of ZnO NM-111 amounted to  $2.2 \pm 0.06$  mg/kg in the NR8383 sample (39%),  $2.2 \pm 0.38$  mg/kg in the medium control (39%), and  $2.86 \pm 0.35$  mg/kg in PSF (51%). Due to these results we abstained from measuring after 48 h.

In summary, while the high solubility of both ZnO ENM was confirmed and shown to be increased in acidic PSF, phagolysosomal processes of live macrophages had no major influence on the solubilization of Zn ions (Fig. SI S1c and d).

## 4. Discussion

### 4.1. Discussion of macrophage-assisted mechanisms

As previously shown for the dissolution of poorly soluble, radiolabeled <sup>57</sup>Co<sub>3</sub>O<sub>4</sub> by primary alveolar macrophages (AMs) from humans and dogs (Kreyling et al., 1979), we found that also cultured AMs can accelerate the biodissolution of particulate matter. This was most obvious for SrCO<sub>3</sub>, which is known to be soluble only under acidic conditions. Whereas SrCO<sub>3</sub> was readily soluble in PSF after 3 h incubation, only a minor fraction was dissolved after 3 h incubation with NR8383 macrophages. However, with longer incubation periods the dissolved fraction increased continuously. This might be due to the gradual acidification of the macrophage's phagolysosomes. In contrast, no significant dissolution occurred in the control experiment of medium without macrophages.

BaSO<sub>4</sub> was tested in comparable static (beaker) super-saturation condition in acidic PSF and in pH neutral medium. In this static



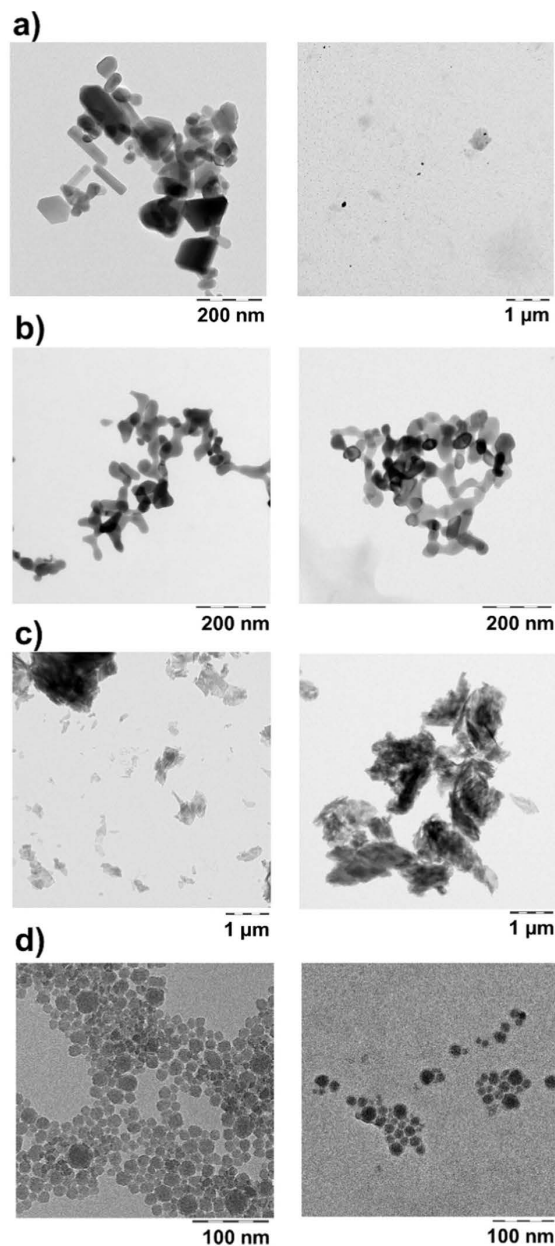


**Fig. 3.** Electron microscopic analysis of representative cases of ENM transformation. Comparison between TEM images of the pristine state (left column) and after the recovery from the flow-through cell after 7 days of treatment (right column). a) ZnO NM-110 (complete dissolution), b)  $\text{Fe}_2\text{O}_3\cdot\text{nano.B}$  (no dissolution, no transformation), c)  $\text{Cu\_Phtalo.nano}$  (no dissolution, aggregating transformation), d)  $\text{SiO}_2\text{\_untreated\_200}$  (low dissolution, reprecipitation transformation).

experiment, Ba ion concentration was slightly higher in acidic PSF than in pH neutral medium control. Interestingly, the total dissolved fraction was considerably higher in the flow-through system (Keller et al., 2018). However, a trend of acceleration was hardly discernible after incubation with NR8383 cells. Because of the trace concentrations of Ba to be measured the analytical uncertainty might mask subtle cellular effects. In addition, the incubation time was limited to 48 h (to prevent a change of medium), and this is a major difference to the study of

Kreyling and co-workers on the *in vitro* dissolution of  $^{57}\text{Co}_3\text{O}_4$ , who exposed AMs for 14 days and measured dissolved Co ions by gamma counting.

To compare the dissolution efficiency of AMs *in vivo*, we approximate the deposited dose per AM for an inhalation exposure of rats to  $50\text{ mg/m}^3$   $\text{BaSO}_4$  for 5 days, resulting in a lung burden of  $1055.7\text{ }\mu\text{g/lung}$ . After a post-exposure period of 21 days the lung burden decreased to  $239.7\text{ }\mu\text{g/lung}$  (difference  $816\text{ }\mu\text{g}$ ) (Landsiedel et al., 2014). The average AM cell count of female Wistar rats is approximately  $1 \times 10^7$  (Rehn et al., 1992). Assuming a stable AM number throughout the post-exposure period, each macrophage engulfed/cleared  $3.9 \times 10^{-6}\text{ }\mu\text{g}$   $\text{BaSO}_4$  per day, partially by dissolution. In the present study,  $3 \times 10^5$  NR8383 cells were exposed to  $9\text{ }\mu\text{g}$   $\text{BaSO}_4$  ( $45\text{ }\mu\text{g/mL}$ ). After 24 h each macrophage dissolved  $1.3 \times 10^{-6}\text{ }\mu\text{g}$   $\text{BaSO}_4$ . Hence, the *in vivo* dissolution was augmented approximately by a factor of 3 compared to the *in vitro* situation. The *in vivo* clearance of particulate matter from the alveolar surface is primarily triggered by AMs, as particles are known to be phagocytosed within a few hours. Besides AM-associated mucociliary clearance, dissolution may contribute significantly to the clearance *in vivo*, which is obviously dependent on additional factors like surfactant turnover, lymphatic flow, and lung perfusion. This complex process cannot be mimicked *in vitro*. We conclude that for materials with a low solubility limit, an increase of biological complexity e.g. using macrophages of the testing method, compared to the abiotic dissolution system, is not beneficial.

This is also true for the ZnO ENM investigated. The dynamic *in vivo* situation which leads to a fast ZnO clearance from rat lungs could not be simulated in the static cell culture approach. It should be noted, that LDH activity was increased after 48 h incubation with  $\text{SrCO}_3$  and  $\text{BaSO}_4$  possibly pointing at beginning cytotoxicity although there were no visible signs of reduced viability or deteriorated cells. Apart from Sr, Ba, or Zn ions high LDH activity or membrane leakage may be caused by the comparatively high cell density under static culture conditions. Moreover, the AM approach suffers from unknown effective doses. Even if dissolution in phagolysosome occurs, reprecipitation and low-dose effects may occur, as shown for Ni-containing particles (Latvala et al., 2016). The dose uncertainties are especially relevant for materials that are partially soluble in the medium (ZnO) and/or well dispersed nanoparticles (such as colloidal silica) whose gravitational settling cannot be monitored by light microscopy (Wiemann et al., 2018). Complete transformation (by dissolution) during the *in vitro* incubation was confirmed for CuO and ZnO using advanced characterization with a synchrotron X-ray source (Ivask et al., 2017).

#### 4.2. Discussion of abiotic dissolution vs. macrophage-assisted dissolution vs. *in vivo* pulmonary clearance

For the three cases of direct abiotic-vs-*in vitro* comparison,  $\text{BaSO}_4$  NM-220,  $\text{SrCO}_3$  and ZnO NM-111, the differentiation of dissolution rates from abiotic flow-through testing was consistent with differentiation by the *in vitro* AM method, and quantitative rates were within a factor 2.4, 1.8 and 1.5, respectively (Table 3). Time-resolved *in vivo* clearance kinetics are available for  $\text{CeO}_2$  NM-212 and  $\text{BaSO}_4$  NM-220 (from radio-activated intratracheal instillation), and are plotted against the dissolution rates of flow-through testing (Fig. 9) (Keller et al., 2014; Konduru et al., 2014). For all other materials, the percentage of remaining solid after 7 days in abiotic flow-through testing is compared in Table 3 to the remaining lung burden after 21 days of recovery *in vivo*, because only this value is available from the standardized STIS inhalation results. Thus our comparison in Table 3 targets consistency, not quantitative predictivity, and avoids modeling that would require several assumptions, such as mono-exponential decay, spherical shape etc. Assuming first-order kinetics (mono-exponential decay), the dissolution rate can be converted to half-times by Eq. SI\_1, with the results given in Table 3. Assuming monodisperse size and spherical shape, Eqs. SI\_4 to SI\_5b reproduce the modeling of shrinking spheres from ISO

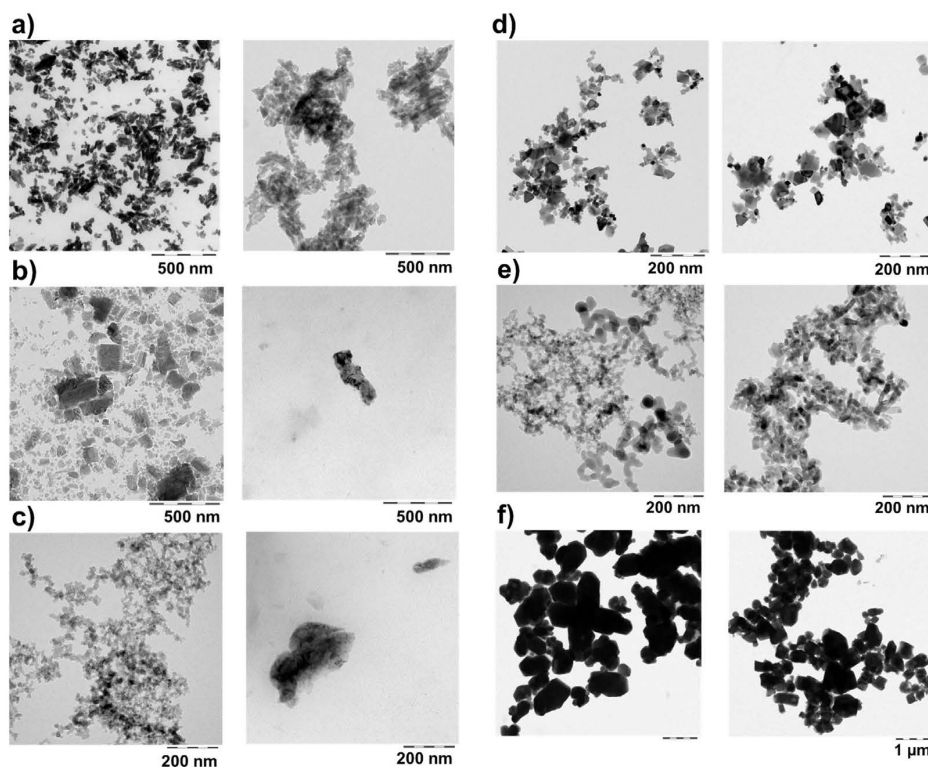


**Fig. 4.** Transformation analysis of additional materials: TEM images of the pristine materials (left) and after 7 days dissolution under standard conditions in PSF (right). a) CuPhthalocyanin halogenated, b) Cu(OH)<sub>2</sub>CO<sub>3</sub>, c) SiO<sub>2</sub> NM-203, d) CeO<sub>2</sub> NM-212, e) TiO<sub>2</sub> NM-104, f) non-nano BaSO<sub>4</sub>\_IRMM381. By additional EDX, the structure in b) was found to contain mainly Si, not Cu, and is thus not assigned to the test material.

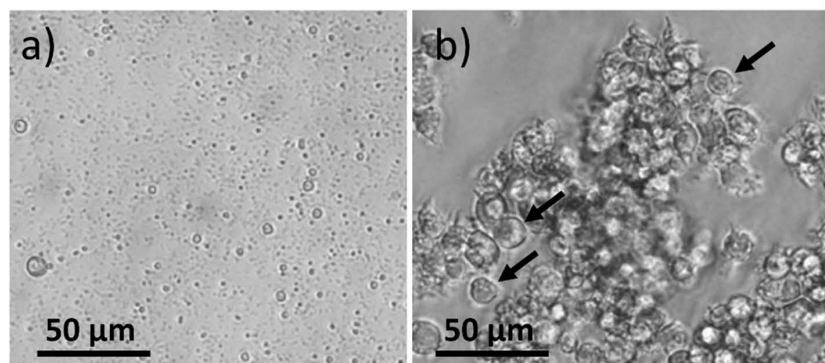


**Fig. 5.** Exposure of NR8383 alveolar macrophages to SrCO<sub>3</sub> ENM. Contrast-enhanced phase contrast micrograph showing (a) numerous SrCO<sub>3</sub> ENM agglomerates settled onto the bottom of the culture vessel post centrifugation under cell-free conditions, and (b) NR8383 cells after a 48 h incubation period with SrCO<sub>3</sub> ENM. Note that cells appear healthy with smooth outer contours (arrows). The space between cells is devoid of visible particles.

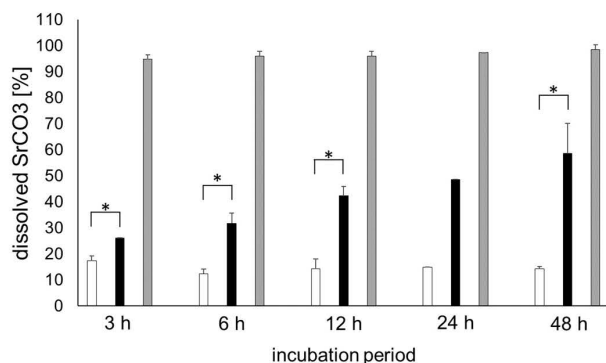


**Fig. 6.** Dissolution of SrCO<sub>3</sub> subjected to neutral and acidic pH conditions over time. F-12K cell culture medium control without cells (white bars); NR8383 rat AM (black bars); PSF pH 4.5 (grey bars); n = 3; \* means p ≤ 0.05.

TR19057:2017. With polydispersity, however, the time course of mass and surface area may result in multiphase kinetics, such as observed for ZnO (Fig. 2D); the *in situ* TEM (Fig. SI\_4) confirms that this material is initially polydisperse in size and shape, and deviates even stronger from spherical shape during dissolution and transformation.

The measured reduction of lung burden was available for CuO (Gosens et al., 2016), ZnO NM-111 and TiO<sub>2</sub> NM-105 (Landsiedel et al., 2010), CeO<sub>2</sub> NM-212, NM-211 (Keller et al., 2014), SiO<sub>2</sub> untreated, and SiO<sub>2</sub> amino (Landsiedel et al., 2014). Most of these studies were also summarized as case studies of the DF4nanogrouping framework (Arts et al., 2016).

For all materials, the abiotic dissolution is consistent with *in vivo* observations, considering that both physical clearance and chemical dissolution contribute. For TiO<sub>2</sub> NM-105 and both nanoforms of SiO<sub>2</sub>, dissolution means a marginal contribution to clearance, indicating that *in vivo* clearance is dominated by macrophage-mediated transport. However, for BaSO<sub>4</sub> NM-220, CuO, ZnO NM-110 and ZnO NM-111 lung



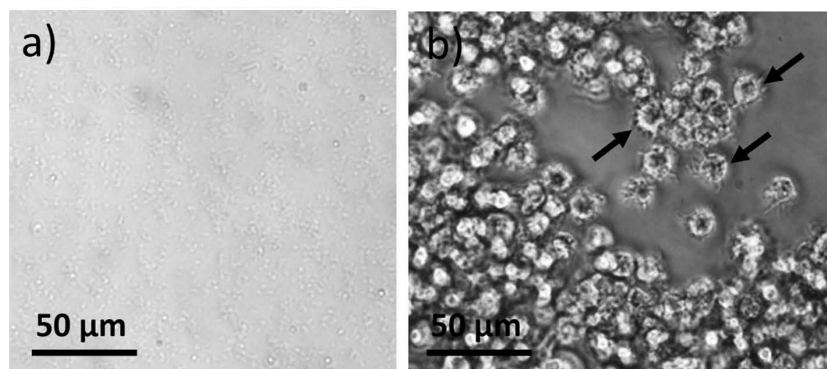


**Fig. 7.** Exposure of NR8383 alveolar macrophages to BaSO<sub>4</sub> ENM. Contrast-enhanced phase contrast micrographs showing (a) numerous BaSO<sub>4</sub> ENM agglomerates settled onto the bottom of the culture vessel post centrifugation under cell-free conditions and (b) NR8383 cells after a 48 h incubation period with BaSO<sub>4</sub> ENM. Note that cells have numerous pseudopodia (arrows). The space between cells is devoid of particles.

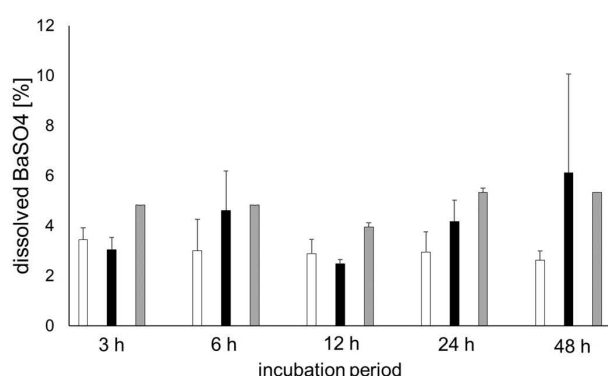


**Fig. 8.** Dissolution of BaSO<sub>4</sub> subjected to neutral and acidic pH conditions over time. F-12K cell culture medium control without cells (white bars); NR8383 rat AM (black bars); PSF pH 4.5 (grey bars); n = 3.

clearance is dominated by dissolution. The dynamic dissolution flow-through system is the method of choice to predict the contribution of dissolution for *in vivo* clearance. Materials that were identified as of low dissolution rate in this system (e.g. TiO<sub>2</sub> NM-105) will be removed *in vivo* from the lungs mainly by AM-assisted mucociliary clearance. The physical clearance as well as the mobility of particles within the rat lungs may also be influenced by agglomeration *in situ*, whose mechanisms are beyond the scope of this discussion. For a read-across on low dissolution ENM (see group ranges proposed below), extrinsic properties such as dispersion stability, heteroagglomeration, affinity need to be considered to appropriately frame the mobility in the body. E.g., affinity to phospholipids is higher for SiO<sub>2</sub>-amino than for SiO<sub>2</sub>-untreated (Wohlleben et al., 2016), and may contribute to the slightly lower clearance despite faster dissolution rates. Chemical

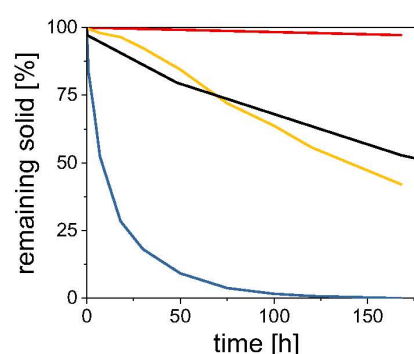


**Fig. 9.** Comparison of *in vivo* clearance vs. abiotic flow-through dissolution in PSF on BaSO<sub>4</sub> NM-220, CuO and CeO<sub>2</sub> NM-212. Red: CeO<sub>2</sub> NM-212 *in vivo* (Molina et al., 2014), yellow: BaSO<sub>4</sub> NM-220 abiotic flow-through, black: BaSO<sub>4</sub> NM-220 *in vivo* (Konduru et al., 2014), blue: CuO abiotic flow-through. After 504 h, the *in vivo* remaining CuO solids are zero or maximally 15% (LoD *in vivo*), consistent with the abiotic results (Gosens et al., 2016). Throughout the abiotic test from 0 h to 168 h, the dissolved CeO<sub>2</sub> is < 3% (LoD abiotic), consistent with the *in vivo* result.

transformation has been observed also *in vivo* (Graham et al., 2017a,b), and specifically for the case of BaSO<sub>4</sub> we showed that the Ostwald ripening is consistently observed in the flow-through setup and *in vivo* (Keller et al., 2018). In principle, the remaining solids that we recover by the centrifugation procedure could be administered to cell cultures to test the response to the transformed material, as was done for static transformation in stomach/intestine simulants (DeLoid et al., 2017). However, our system cannot currently predict reprecipitation after systemic circulation, as has been observed on some ceria species (Graham et al., 2014).

It should be noted that the recommended conditions of (M<sub>0</sub> = 1 mg,

**Table 3**  
Comparison of 7-day abiotic dissolution (standard conditions) with 1-day alveolar macrophage-assisted dissolution and 28-day clearance *in vivo* STIS.

	Dissolution rate macrophage-assisted (24 h) [ng/cm <sup>2</sup> /h]	Dissolution rate Abiotic flow-through, pH 4.5 [ng/cm <sup>2</sup> /h]	Half-time calculated from k [days]	Dissolution rate Abiotic flow-through, pH 4.5 [% per 7 days]	<i>In vivo</i> pulmonary clearance in STIS recovery [% per 21 days]
BaSO <sub>4</sub> NM-220	4.2	10	7	58%	52%
CeO <sub>2</sub> NM-211		< 0.28 (LoD)	> 156	< 3% (LoD)	7%
CeO <sub>2</sub> NM-212		< 0.73 (LoD)	> 146	< 3% (LoD)	5%
CuO		283	0.7	100%	> 85% (LoD)
SiO <sub>2</sub> -amino		0.216	66	7%	34%
SiO <sub>2</sub> -untreated		0.044	328	1.2%	39%
TiO <sub>2</sub> NM-105		< 0.013 (LoD)	> 4356	< 0.1% (LoD)	26%
ZnO NM-111	117	177	1.2	100%	93%
SrCO <sub>3</sub>	61	108	1.9	100%	

LoD: level of detection. STIS: short term inhalation study.

$V = 2 \text{ mL/h}$ ) are appropriate for many materials, but no universal optimum. As a quality control, it is recommended to check that measurement at two different SA/V leads to the same grouping. If SA/V was lower, then for several materials in our test set (e.g. the Cu-Phthalocyanines, the  $\text{SiO}_2$  materials), the ion concentration in the eluate drops below the limit of detection of ICP-OES as a method that is highly established and robust against the high matrix concentrations of physiological buffers. ICP-MS and more optimization would allow to measure at lower SA/V. In contrast, for higher SA/V more materials may be limited by saturation. The specific SA/V conditions are selected to reproduce on the critical test case of  $\text{BaSO}_4$  the *in vivo* transformation and dissolution behavior (Fig. 9) (Keller et al., 2018).

Flow-through systems are described by ISO 19057:2017 as “seen to be the best method of measuring durability *in vitro*” (Nti, 2017). Recently, flow-systems have been used to study gastro-intestinal dissolution of nanomaterials (without the exact same flow cells) (Bove et al., 2017a,b), and with the same flow cells (De Jong et al., 2018), and to study environmental dissolution (Pantano et al., 2018). To capture reactions of highly instable ENM-medium combinations on a time scale of minutes, it appears possible to eliminate fraction collection, and instead to hyphenate flow-cells directly to an ICP-MS; however, we adapted sampling times to physiological time scales (hours to days), guided by earlier evidence on other oxide materials. More specifically, flow-through systems have previously been used to study the pulmonary biodissolution of respirable man-made vitreous fibers (MMVF) (Nti, 2017). A large collection of abiotic dissolution rates and associated *in vivo* lung clearance rates has been made available for natural and man-made mineral fibers in a WHO report (IARC, 2002) which lists, among others, the following biodissolution rates of MMVF:

- MMVF34 “biosoluble stone wool” with a lung clearance half-life time of 6 days and  $k = 620 \text{ ng/cm}^2/\text{h}$  (at pH 4.5) and  $k = 59 \text{ ng/cm}^2/\text{h}$  (at pH 7.4);
- MMVF11 glass wool with a lung clearance half-life time of 9 days and  $k = 25 \text{ ng/cm}^2/\text{h}$  (at pH 4.5) and  $k = 100 \text{ ng/cm}^2/\text{h}$  (at pH 7.4);
- MMVF32 E-glass-wool with half-life time of 79 days and  $k = 9 \text{ ng/cm}^2/\text{h}$  (at pH 4.5) and  $k = 7 \text{ ng/cm}^2/\text{h}$  (at pH 7.4);
- crocidolite and amosite asbestos with half-life time of  $> 400$  days and  $k < 1 \text{ ng/cm}^2/\text{h}$  (at both pH).

It is interesting to note that many of the nanomaterials have dissolution rates ( $k$  values) at the lower end of the range spanned by the partially amorphous, partially crystalline aluminosilicates (stone wool, glass wool, asbestos). This is plausible considering the chemical composition. On the other hand, the BET surface of ENM is  $> 100 \times$  larger than that of typical glass or mineral fibers (which range around  $0.2 \text{ m}^2/\text{g}$ , due to several micrometer diameter) and this favors a low bio-persistence of ENM, because half-times are given by the inverse of  $k$  and lung-deposited specific surface area (Eq. SI.1).

#### 4.3. Discussion grouping and read-across

The results of the abiotic flow-through dissolution can be essential to substantiate a grouping hypothesis via the similarity of dissolution rates: The degree of biodissolution is similar for families of  $\text{Fe}_2\text{O}_3$  (nano)forms,  $\text{SiO}_2$  nanoforms,  $\text{CeO}_2$  nanoforms, ZnO nanoforms, thus primarily determined by the substance, but shows significant modulation by production routes and surface coatings. In contrast, the modulation by shape or size is limited. Nanoforms although different in shape ( $\text{Fe}_2\text{O}_3$ ), size ( $\text{CeO}_2$ ,  $\text{Fe}_2\text{O}_3$ ) or coatings ( $\text{SiO}_2$ , ZnO) can be grouped for pulmonary persistence, if their dissolution is sufficiently similar.

On the contrary, a dissimilarity of dissolution may be used to differentiate between ENM which are seemingly similar due to toxic components: Thus the four Cu-containing materials fall into different

groups as CuO and  $\text{Cu}_2(\text{OH})_2\text{CO}_3$  exhibit a significant or complete dissolution after 7 days, whereas both Cu-Phthalocyanine ENM do not show significant solubility. Accordingly, the *in vivo* potency (mediated by Cu ions) was high for CuO (Gosens et al., 2016) but low for Cu-Phthalocyanine (Arts et al., 2016). Similarly, a differential lung toxicity was observed for a set of NiO nanoparticles after intratracheal instillation. Also in this case there was a strong correlation of inflammation parameters with solubility in artificial lysosomal fluid (Shinohara et al., 2017).

Especially coatings or functionalization modulated the dissolution rate within an order of magnitude in our dataset. Stronger modulation is expected only for closed shells, such as oxide coatings on more soluble core particles. For those materials with a very low equilibrium solubility limit under lysosomal conditions, the local dose of the ENM is another important parameter affecting the dissolution rate. This was the case for  $\text{BaSO}_4$ , but not for the other materials. Accordingly, also *in vitro* the dissolution rate can depend on initial mass, and this needs to be considered in screening and grouping strategies, e.g. for implementation of the DF4nanoGrouping framework:

- **Tier 1 Solubility:** The method for Tier 1 should be stirring of the suspension in a beaker, followed by ultrafiltration and ICP-OES (or -MS) analysis, as established by (Avramescu et al., 2016) for their enhancement of the DF4nanoGrouping framework. A cutoff between soluble and non-soluble ENM should be defined as absolute concentration, e.g.  $100 \text{ mg/L}$ , as by the DF4nanoGrouping framework.
  - If already at Tier 1 the intended use and the critical route of exposure are known, then it is an option to perform the same test in the most relevant biological medium.
  - For environmental hazard assessment purposes, the same method with simple media ranging from pH 4 to pH 9, and a cutoff at  $9 \text{ mg/L}$  (at  $10 \text{ mg/mL}$  initial solids) is discussed in the OECD task group on dissolution (Rasmussen et al., 2018).
- **Tier 2 Dissolution:** For a more detailed measurement and a refinement in Tier 2 a flow-through dissolution setup is recommended. Dissolution rates are thus tested out of equilibrium using relevant media that are derived from the intended exposure scenario of the ENM, such as pH 4.5 PSF for mimicking the dissolution within alveolar macrophages. The flow-through setup (consisting of an ultrafiltration cell, subsequent ICP-MS analysis of the eluate, and TEM analysis of the remaining solids) has been standardized and benchmarked against inhalation results with the following parameters:  $1 \text{ mg}$  of ENM initial solids, relevant medium (for inhalation concern: PSF at pH 4.5) and a continuous flow-rate of  $2 \text{ mL/h}$  for 7 consecutive days. However, the dose of ENM, the medium and the flow-rate used for the flow-through dissolution can be adapted to the requirements of other exposure scenarios, such as investigation of the dissolution in the gastrointestinal tract, requiring independent validation.
- **Tier 2 Transformation:** The analysis of changes during dissolution can be integrated into this strategy by our medium-removing TEM sample preparation after completion of the flow-through dissolution test. In a companion paper, we show that also complex transformations of a borderline soluble material ( $\text{BaSO}_4$ ) are assessed correctly (Keller et al., 2018). The results presented here for 21 additional materials furthermore support the plausibility of transformation detection. No quantitative evaluation of crystallinity or composition can be proposed yet, but changes of the constituent particle size are quantified by automated image analysis ( $N > 300$ , e.g. using the NanoDefine tools).

Contrary to the hypothesis that AMs *in vitro* dissolution provides a more realistic model than the abiotic simulation of the AM lysosome alone, we found that macrophage-assisted dissolution *in vitro* is applicable only for a limited exposure period (1–2 days) and, therefore, may liberate comparatively low amounts of ions from ENM. Since the



method, as performed here, provided no further predictive value, we suggest that the Tier 2 “assessment of ENM similarity” can stick to abiotic flow-through dissolution at standardized conditions (initial mass of 1 mg, flow 2 mL/h) for grouping and read-across purposes. This experimental setup is in line with standards for evaluating biodissolution of mineral fibers. However, mechanistic investigations in Tier 3 may still require *in vivo* and cell-assisted studies.

The results of this study allow us to propose quantitative ranges to assign the tested nanomaterials in four distinct groups for the purpose of grouping of inhalation hazards.

1. The first group are non-persistent materials showing a high dissolution rate  $k > 100 \text{ ng/cm}^2/\text{h}$  and no remaining original particles in TEM, including CuO, Cu(OH)<sub>2</sub>CO<sub>3</sub>, SrCO<sub>3</sub>, ZnO NM-110 and coated ZnO NM-111. This cutoff corresponds to an abiotic dissolution ranging from 30% to 100% after 7 days. Materials in this group are cleared completely (down to LoD) during a STIS inhalation recovery period.
2. The second group are non-persistent materials showing a  $k$  ranging from  $1 \text{ ng/cm}^2/\text{h}$  to  $100 \text{ ng/cm}^2/\text{h}$  and also **significant transformation** or reprecipitation. The range corresponds to a significant dissolution above 10% per 7 days. This group comprises both (nano) forms nano-BaSO<sub>4</sub> NM-220 and non-nano BaSO<sub>4</sub> IRMM381. Chemical clearance (dissolution) dominates, but physical clearance (transport) and reprecipitation contribute to the processes in a relatively complex interplay.
3. The third group of nanomaterials shows a very low dissolution ( $k < 1 \text{ ng/cm}^2/\text{h}$  or below LoD) but a **significant transformation** during the test period. This corresponds to an abiotic dissolution  $\ll 30\%$  (or even no apparent dissolution). Examples are both nanoforms of Cu-Phthalocyanine and all tested silica materials, where differences may be related to the silica production process. For these materials the physical clearance from the lung (transport) is accompanied by aggregation and/or reprecipitation.
4. The fourth group contains all biopersistent materials that show very low or no dissolution ( $k < 1 \text{ ng/cm}^2/\text{h}$  or below LoD) and no significant transformation. All tested (nano)forms of Fe<sub>2</sub>O<sub>3</sub> (A, B, larger) as well as both CeO<sub>2</sub> (NM-211, NM-212) and both TiO<sub>2</sub> NM-104 and NM-105 belong to this group. Physical clearance (transport) dominates the pulmonary clearance.

Alternatively, group ranges might be defined by  $k$  values given in  $\text{ng/cm}^2/\text{h}$ , or by the more pragmatic “% dissolution per 7 days” which requires no BET measurement of the specific surface area of the ENM for evaluation of the flow-through raw data. The consideration of the specific surface area in case of the “ $k$  metric” is the major difference between the two metrics, and allows us to motivate the decadic group ranges with a rich body of mineral fiber literature (see discussion above). The  $k$  metric also favors the read-across between nanoform and non-nanoform, because it eliminates the dissimilarity of the specific surface and focuses on differences beyond size and surface area.

## 5. Conclusions

In this work, the flow-through dissolution system was used to investigate the out of equilibrium dissolution behavior of a broad set of ENM and compared to alveolar macrophage-assisted dissolution as well as the *in vivo* clearance in rats. A high degree of consistency of the abiotic dissolution and the *in vivo* clearance has been achieved for CeO<sub>2</sub> NM-212, two forms of colloidal SiO<sub>2</sub>, TiO<sub>2</sub> NM-105, CuO, nano BaSO<sub>4</sub> NM-220 and ZnO NM-111. This method and benchmark materials can be used to implement grouping frameworks such as those of ECHA (2017b) or ECETOC (Arts et al., 2015): For Tier 1 testing the investigation of the dissolution under static conditions is sufficient as proposed by (Avramescu et al., 2016). However, for Tier 2 testing the abiotic flow-through setup in relevant media is required, as proposed in

this work on the example of pulmonary biodissolution. Cultured alveolar macrophage-assisted dissolution is acknowledged as a potential method for very specific Tier 3 investigations but needs to be further explored to achieve sufficiently long exposure periods.

The flow-through dissolution setup and protocol used in this work combines an integrated quantification of dissolution by ICP-MS/-OES and detection of transformation through TEM. Using our 24 case studies, we proposed four groups based on decadic ranges of quantitative dissolution rates and on a qualitative analysis of transformation. The representatives of the four groups (benchmark materials) are ZnO NM-110 (complete dissolution), BaSO<sub>4</sub> NM-220 (slow dissolution, reprecipitation transformation), SiO<sub>2</sub> NM-203 (very low dissolution, reprecipitation/aggregation transformation), TiO<sub>2</sub> NM-105 or Fe<sub>2</sub>O<sub>3</sub> nano.B (very low dissolution, very low transformation). Finally, the method can be employed for testing of dissolution and transformation in environmental media.

## Acknowledgement

We thank Thorsten Wiczorek for excellent laboratory support on TEM imaging. We gratefully acknowledge helpful discussions with Alison Elder, Uschi Graham and Günter Oberdörster.

## Funding

This work was part of the project nanoGRAVUR supported by German Federal Ministry of Education and Research (BMBF), grant numbers 03XP0002B and 03XP0002J.

## Appendix A. Supplementary data

Supplementary data to this article can be found online at <https://doi.org/10.1016/j.impact.2018.08.005>.

## References

- Albrecht, C., et al., 2007. Surface-dependent quartz uptake by macrophages: potential role in pulmonary inflammation and lung clearance. *Inhal. Toxicol.* 19 (Suppl. 1), 39–48.
- Arts, J.H.E., et al., 2015. A decision-making framework for the grouping and testing of nanomaterials (DF4nanoGrouping). *Regul. Toxicol. Pharmacol.* 71 (2), S1–S27.
- Arts, J.H.E., et al., 2016. Case studies putting the decision-making framework for the grouping and testing of nanomaterials (DF4nanoGrouping) into practice. *Regul. Toxicol. Pharmacol.* 76, 234–261.
- Avramescu, M.-L., et al., 2016. Influence of pH, particle size and crystal form on dissolution behaviour of engineered nanomaterials. *Environ. Sci. Pollut. Res.* 1–12.
- Babick, F., et al., 2016. How reliably can a material be classified as a nanomaterial? Available particle-sizing techniques at work. *J. Nanopart. Res.* 18 (6), 1–40.
- Bhattacharjee, S., et al., 2012. Cytotoxicity and cellular uptake of tri-block copolymer nanoparticles with different size and surface characteristics. *Part. Fibre Toxicol.* 9, 11.
- Bhattacharjee, S., et al., 2013. Cytotoxicity of surface-functionalized silicon and germanium nanoparticles: the dominant role of surface charges. *Nanoscale* 5 (11), 4870–4883.
- Bove, P., et al., 2017a. Dissolution test for risk assessment of nanoparticles: a pilot study. *Nanoscale* 9 (19), 6315–6326.
- Bove, P., Malvindi, M.A., Sabella, S., 2017b. In Vitro Human Digestion Test to Monitor the Dissolution of Silver Nanoparticles. vol. 838. pp. 012003.
- Braakhuis, H.M., et al., 2014. Physicochemical characteristics of nanomaterials that affect pulmonary inflammation. *Part. Fibre Toxicol.* 11.
- Collier, Z.A., et al., 2015. Tiered guidance for risk-informed environmental health and safety testing of nanotechnologies. *J. Nanopart. Res.* 17 (3), 155.
- Dale, A.L., Lowry, G.V., Casman, E.A., 2015. Stream dynamics and chemical transformations control the environmental fate of silver and zinc oxide nanoparticles in a watershed-scale model. *Environ. Sci. Technol.* 49 (12), 7285–7293.
- De Jong, Wim H., De Rijk, Eveline, Bonetto, Alessandro, Wohlleben, Wendel, Stone, Vicki, Brunelli, Andrea, Badetti, Elena, Marcomini, Antonio, Gosens, Ilse, Cassee, Flemming R., 2018. Toxicity of copper oxide and basic copper carbonate nanoparticles after short-term oral exposure in rats. *Nanotoxicology* (revised June 2018).
- DeLoid, G.M., et al., 2017. An integrated methodology for assessing the impact of food matrix and gastrointestinal effects on the biokinetics and cellular toxicity of ingested engineered nanomaterials. *Part. Fibre Toxicol.* 14 (1), 40.
- Donaldson, K., Poland, C.A., 2013. Nanotoxicity: challenging the myth of nano-specific toxicity. *Curr. Opin. Biotechnol.* 24, 724–734.
- ECHA, 2017a. How to Prepare Registration Dossiers that Cover Nanoforms: Best



- Practices.
- ECHA, 2017b. Appendix R.6-1 for Nanomaterials Applicable to the Guidance on QSARs and Grouping of Chemicals.
- Eidi, H., et al., 2010. Cytotoxicity assessment of heparin nanoparticles in NR8383 macrophages. *Int. J. Pharm.* 396 (1–2), 156–165.
- Eidi, H., et al., 2012. Drug delivery by polymeric nanoparticles induces autophagy in macrophages. *Int. J. Pharm.* 422 (1–2), 495–503.
- Gao, X., Lowry, G.V., 2018. Progress towards standardized and validated characterizations for measuring physicochemical properties of manufactured nanomaterials relevant to nano health and safety risks. *Nanotoxicology* 9 (Supplement C), 14–30.
- Geiser, M., 2010. Update on macrophage clearance of inhaled micro- and nanoparticles. *J. Aerosol Med. Pulm. Drug Deliv.* 23 (4), 207–217.
- Godwin, H., et al., 2015. Nanomaterial categorization for assessing risk potential to facilitate regulatory decision-making. *ACS Nano* 9 (4), 3409–3417.
- Gosens, I., et al., 2016. Organ burden and pulmonary toxicity of nano-sized copper (II) oxide particles after short-term inhalation exposure. *Nanotoxicology* 10 (8), 1084–1095.
- Graham, U.M., et al., 2014. In vivo processing of ceria nanoparticles inside liver: impact on free-radical scavenging activity and oxidative stress. *ChemPlusChem* 79 (8), 1083–1088.
- Graham, U., et al., 2017a. Calcium Co-localization With In Vivo Cerium Phosphate Nanoparticle Formation After Intratracheal Instillation Dosing With CeCl<sub>3</sub> or CeO<sub>2</sub> NPs. vol. 23. pp. 1344–1345.
- Graham, U.M., et al., 2017b. From dose to response: in vivo nanoparticle processing and potential toxicity. In: Tran, L., Bafares, M.A., Rallo, R. (Eds.), *Modelling the Toxicity of Nanoparticles*. Springer International Publishing, Cham, pp. 71–100.
- Guldberg, M., et al., 1995. Method for determining in-vitro dissolution rates of man-made vitreous fibres. *Glas. Sci. Technol.* 68 (6), 181–187.
- Helmke, R.J., et al., 1987. From growth factor dependence to growth factor responsiveness: the genesis of an alveolar macrophage cell line. *In Vitro Cell. Dev. Biol.* 23 (8), 567–574.
- Helmke, R.J., German, V.F., Mangos, J.A., 1989. A continuous alveolar macrophage cell line: comparisons with freshly derived alveolar macrophages. *In Vitro Cell. Dev. Biol.* 25 (1), 44–48.
- Hofmann, T., et al., 2016. Comparative short-term inhalation toxicity of five organic diketopyrrolopyrrole pigments and two inorganic iron-oxide-based pigments. *Inhal. Toxicol.* 28 (10), 463–479.
- IARC, I.A.F.R.O.C., 2002. Man-made Vitreous Fibres. World Health Organization, pp. 1–433.
- Iler, R.K., 1979. The Chemistry of Silica Solubility, Polymerization, Colloid and Surface Properties, and Biochemistry of Silica. Wiley.
- Ivask, A., et al., 2017. Complete transformation of ZnO and CuO nanoparticles in culture medium and lymphocyte cells during toxicity testing. *Nanotoxicology* 1–16.
- Kass, E.H., 1964. The Role of the Alveolar Macrophage in the Clearance of Bacteria From the Lung \* (From the Channing Laboratory, Mallory Institute of Pathology, Thorndike Memorial Laboratory, and Second and Fourth (Harvard) Medical Semices, Boston City Hospital. Methods).
- Keller, J., et al., 2014. Time course of lung retention and toxicity of inhaled particles: short-term exposure to nano-Ceria. *Arch. Toxicol.* 88 (11), 2033–2059.
- Keller, J., Graham, U., Koltermann-Jilly, J., Gelein, R., Ma-Hock, L., Landsiedel, R., Wiemann, M., Oberdörster, G., Elder, A., Wohlleben, W., 2018. Predicting dissolution and transformation of inhaled nanoparticles in the lung using abiotic flow cells: the case of barium sulfate. (to be submitted).
- Kent, R.D., Vikesland, P.J., 2016. Dissolution and persistence of copper-based nanomaterials in undersaturated solutions with respect to cuprite solid phases. *Environ. Sci. Technol.* 50 (13), 6772–6781.
- Klaessig, F., 2018. Dissolution as a Paradigm in Regulating Nanomaterials. *Environ. Sci. Nano* 5, 1070–1077. <https://doi.org/10.1039/C7EN01130J>.
- Konduru, N., et al., 2014. Biokinetics and effects of barium sulfate nanoparticles. *Part. Fibre Toxicol.* 11 (1), 55.
- Koslowski, R., et al., 2003. Evidence for the involvement of TGF-beta and PDGF in the regulation of prolyl 4-hydroxylase and lysyloxidase in cultured rat lung fibroblasts. *Exp. Toxicol. Pathol.* 55 (4), 257–264.
- Kreyling, W., et al., 1979. In vitro dissolution of uniform cobalt oxide particles by human and canine alveolar macrophages. *Am. J. Respir. Cell Mol. Biol.* 2, 413–422.
- Kroll, A., et al., 2011. Cytotoxicity screening of 23 engineered nanomaterials using a test matrix of ten cell lines and three different assays. *Part. Fibre Toxicol.* 8 (1), 1.
- Kuempel, E., et al., 2012. Development of risk-based nanomaterial groups for occupational exposure control. *J. Nanopart. Res.* 14, 1029.
- Landsiedel, R., et al., 2010. Testing metal-oxide nanomaterials for human safety. *Adv. Mater.* 22 (24), 2601–2627.
- Landsiedel, R., et al., 2014. Application of short-term inhalation studies to assess the inhalation toxicity of nanomaterials. *Part. Fibre Toxicol.* 11 (1), 16.
- Landsiedel, R., Sauer, U.G., de Jong, W.H., 2017. Chapter 8: risk assessment and risk management. In: *Adverse Effects of Engineered Nanomaterials*, Second edition. Exposure, Toxicology, and Impact on Human Health Academic Press, pp. 189–222.
- Latvala, S., et al., 2016. Nickel release, ROS generation and toxicity of Ni and NiO micro- and nanoparticles. *PLoS One* 11 (7), e0159684.
- Lison, D., et al., 2008. Nominal and effective dosimetry of silica nanoparticles in cytotoxicity assays. *Toxicol. Sci.* 104 (1), 155–162.
- Lison, D., et al., 2009. Sintered indium-tin-oxide (ITO) particles: a new pneumotoxic entity. *Toxicol. Sci.* 108 (2), 472–481.
- Marques, M., Loebenberg, R., Almukainzi, M., 2011. Simulated biological fluids with possible application in dissolution testing. *Dissolut. Technol.* 8.
- Mehn, D., et al., 2018. Identification of nanomaterials: a validation report of two laboratories using analytical ultracentrifugation with fixed and ramped speed options. *Nanotoxicology* 10, 87–96.
- Mielke, J., et al., 2016. Evaluation of electron microscopy techniques for the purpose of classification of nanomaterials. In: *European Microscopy Congress 2016: Proceedings*. Wiley Online Library.
- Ministère de l'Environnement, d.l.É.e.d.l.M., 2015. Éléments issus des déclarations des substances à l'état nanoparticulaire: Exercice 2015.
- Mitrano, D.M., Nowack, B., 2017. The need for a life-cycle based aging paradigm for nanomaterials: importance of real-world test systems to identify realistic particle transformations. *Nanotechnology* 28 (7), 072001.
- Mitrano, D.M., et al., 2015. Review of nanomaterial aging and transformations through the life cycle of nano-enhanced products. *Environ. Int.* 77 (0), 132–147.
- Molina, R.M., et al., 2014. Bioavailability, distribution and clearance of tracheally instilled, gaged or injected cerium dioxide nanoparticles and ionic cerium. *Environ. Sci. Nano* 1 (6), 561–573.
- Muller, P., et al., 2015. Assessment of different electron microscopy techniques for particle size quantification of potential nanomaterials. *Microsc. Microanal.* 21 (Supplement S3), 2403–2404.
- Nel, A.E., et al., 2013. A multi-stakeholder perspective on the use of alternative test strategies for nanomaterial safety assessment. *ACS Nano* 7.
- Nti, 2017. PD ISO/TR 19057:2017 - nanotechnologies. Use and application of acellular in vitro tests and methodologies to assess nanomaterial biodegradability. *Nanotechnologies. Use and Application of Acellular In Vitro Tests and Methodologies to Assess Nanomaterial Biodegradability*.
- Oberdörster, G., Kuhlbusch, T.A.J., 2018. In vivo effects: methodologies and biokinetics of inhaled nanomaterials. *Nanotoxicology* 10 (Supplement C), 38–60.
- Oomen, A.G., et al., July 2017. Risk assessment frameworks for nanomaterials: scope, link to regulations, applicability, and outline for future directions in view of needed increase in efficiency. *Nanotoxicology* 10 (9), 1–13.
- Pantano, D., et al., 2018. Transformations of nanoenabled copper formulations govern release, antifungal effectiveness, and sustainability throughout the wood protection lifecycle. *Environ. Sci. Technol.* 52 (3), 1128–1138.
- Plakhova, T.V., et al., 2016. Solubility of nanocrystalline cerium dioxide: experimental data and thermodynamic modeling. *J. Phys. Chem. C* 120 (39), 22615–22626.
- Pulskamp, K., Diabate, S., Krug, H.F., 2007. Carbon nanotubes show no sign of acute toxicity but induce intracellular reactive oxygen species in dependence on contaminants. *Toxicol. Lett.* 168 (1), 58–74.
- Rasmussen, K., et al., 2018. Physico-chemical properties of manufactured nanomaterials - characterisation and relevant methods. An outlook based on the OECD Testing Programme. *Regul. Toxicol. Pharmacol.* 92 (Supplement C), 8–28.
- Rehn, B., et al., 1992. Recovery of rat alveolar macrophages by bronchoalveolar lavage under normal and activated conditions. *Environ. Health Perspect.* 97, 11–16.
- Scherbart, A.M., et al., 2011. Contrasting macrophage activation by fine and ultrafine titanium dioxide particles is associated with different uptake mechanisms. *Part. Fibre Toxicol.* 8 (1), 31.
- Shinozawa, N., et al., 2017. Kinetics and dissolution of intratracheally administered nickel oxide nanomaterials in rats. *Part. Fibre Toxicol.* 14 (1), 48.
- Stefaniak, A.B., et al., 2005. Characterization of phagolysosomal simulant fluid for study of beryllium aerosol particle dissolution. *Toxicol. in Vitro* 19 (1), 123–134.
- Steinhäuser, K.G., Sayre, P.G., 2017. Reliability of methods and data for regulatory assessment of nanomaterial risks. *Nanotoxicology* 7 (Supplement C), 66–74.
- Ullmann, C., Müller, P., 2017. SOP, Applicability Range and Method Performance Description for DLS & MiniTEM.
- Vencalek, B.E., et al., 2016. In situ measurement of CuO and Cu(OH)<sub>2</sub> nanoparticle dissolution rates in quiescent freshwater mesocosms. *Environ. Sci. Technol. Lett.* 3 (10), 375–380.
- Wagner, A.J., et al., 2007. Cellular interaction of different forms of aluminum nanoparticles in rat alveolar macrophages. *J. Phys. Chem. B* 111 (25), 7353–7359.
- Wang, Z., et al., 2016. Biological and environmental interactions of emerging two-dimensional nanomaterials. *Chem. Soc. Rev.* 45 (6), 1750–1780.
- Wiemann, M., et al., 2016. An in vitro alveolar macrophage assay for predicting the short-term inhalation toxicity of nanomaterials. *J. Nanobiotechnol.* 14 (1), 1–27.
- Wiemann, M., et al., 2018. In vitro and in vivo short-term pulmonary toxicity of differently sized colloidal amorphous SiO<sub>2</sub>. *Nanomaterials* 8 (3), 160.
- Wohlleben, W., et al., 2016. Influence of agglomeration and specific lung lining lipid/protein interaction on short-term inhalation toxicity. *Nanotoxicology* 1–11.
- Wohlleben, W., et al., 2017a. Nanoenabled products: categories, manufacture, and applications: protocols and industrial innovations. In: Mansfield, E. (Ed.), *Metrology and Standardization for Nanotechnology: Protocols and Industrial Innovations*. John Wiley & Sons, pp. 411–464.
- Wohlleben, W., et al., 2017b. Reliable nanomaterial classification of powders using the volume-specific surface area method. *J. Nanopart. Res.* 19 (2), 61.
- Wohlleben, W., et al., 2017c. Composition, respirable fraction and dissolution rate of 24 stone wool MMVF with their binder. *Part. Fibre Toxicol.* 14 (1), 29.

### 3.1.3 Addendum to “Abiotic dissolution rates of 24 (nano)forms of 6 substances compared to macrophage-assisted dissolution and in vivo pulmonary clearance: Grouping by biodissolution and transformation” [NanoImpact 12 (2018) 29-41]

Koltermann-Jüly J\*, **Keller JG\***, Vennemann A, Werle K, Müller P, Ma-Hock L, Landsiedel R, Wiemann M, Wohlleben W.

\*Equal contribution

NanoImpact, Volume 14, February 2019, 100154

<https://doi.org/10.1016/j.impact.2019.100154>

#### **Abstract:**

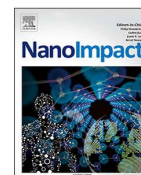
Numerous recent reviews have highlighted the urgent need for methods to determine the biodissolution of nanomaterials in relevant lung fluids, and to validate the results against the bioprocessing *in vivo*. Moreover, it is largely unknown to what extent (nano)forms of a substance that differ in size, shape, or coating also differ in biodissolution. Here we apply a previously optimized abiotic flow-through method to 24 (nano)forms of 6 substances and compare the results with alveolar macrophage-assisted biodissolution of a subset of these nanomaterials *in vitro* and short-term inhalation results *in vivo*. As a main result we found that the results obtained with the flow-through method for the lung were consistent to the results of *in vivo* studies and were not improved by measuring alveolar macrophage-assisted biodissolution for up to 48 h. Based on selected benchmark materials we propose four groups of materials according to quantitative biodissolution rates (1 ng/cm<sup>2</sup>/h to 100 ng/cm<sup>2</sup>/h cutoffs) and qualitative transformation parameters, as detected by TEM analysis. These groups were also reflected by different lung clearance rates, as previously determined in short term inhalation studies. Biodissolution was similar within substance (nano)forms of Fe<sub>2</sub>O<sub>3</sub>, SiO<sub>2</sub>, CeO<sub>2</sub>, ZnO, though slightly varied upon surface area/coating. But the difference of biodissolution between the substances was in some cases more than 1000-fold. In contrast, Cu-containing nanoforms behaved heterogeneously and require case-by-case testing of dissolution and transformation. Different production routes and/or surface coatings significantly modulated biodissolution, whereas effects of shape or size were limited. In summary, we refined a protocol for the abiotic determination of biodissolution along with an integrated assessment of nanomaterial transformation. The protocol is suggested as tier 2 methodology for grouping and read-across purposes.





Contents lists available at ScienceDirect

NanoImpact

journal homepage: [www.elsevier.com/locate/nanoimpact](http://www.elsevier.com/locate/nanoimpact)

## Addendum to “Abiotic dissolution rates of 24 (nano)forms of 6 substances compared to macrophage-assisted dissolution and in vivo pulmonary clearance: Grouping by biodissolution and transformation” [NanoImpact 12 (2018) 29–41]

Johanna Koltermann-Jüly<sup>a,b,1</sup>, Johannes G. Keller<sup>a,1</sup>, Antje Vennemann<sup>c</sup>, Kai Werle<sup>a</sup>, Philipp Müller<sup>a</sup>, Lan Ma-Hock<sup>a</sup>, Robert Landsiedel<sup>a</sup>, Martin Wiemann<sup>c</sup>, Wendel Wohlleben<sup>a,\*</sup>

<sup>a</sup> BASF SE, Dept. Experimental Toxicology and Ecology, and Dept. Material Physics, 67056 Ludwigshafen, Germany

<sup>b</sup> Biopharmaceutics and Pharmaceutical Technology, Saarland University, 66123 Saarbrücken, Germany

<sup>c</sup> IBE R&D Institute for Lung Health eGmbH, 48149 Münster, Germany

We recently refined a protocol for the abiotic determination of biodissolution along with an integrated assessment of nanomaterial transformations, and explored the level of similarity across 24 (nano) forms (Koltermann-Jüly et al., 2018). Based on benchmark materials we proposed four groups of materials according to quantitative biodissolution rates (1 ng/cm<sup>2</sup>/h to 100 ng/cm<sup>2</sup>/h cutoffs) and qualitative transformation parameters. The “continuous flow system” consists of a flow-cell with 5 kDa ultrafiltration membrane. The elemental concentration is determined in the eluate and is considered as dissolved ions.

In our original contribution, the limit of detection (LoD) of the inductively coupled plasma optical emission spectroscopy (ICP-OES) was not sufficiently sensitive to quantify the very low ion concentrations of several materials such as TiO<sub>2</sub>, CeO<sub>2</sub>, Fe<sub>2</sub>O<sub>3</sub> and CuPhthalocyanine. The lowest range of dissolution rates could thus not be explored. To close this gap, we repeated the flow-cell dissolution experiments under the same conditions as the original experiments, and quantified the dissolved ions by inductively coupled plasma mass-spectrometry (ICP-MS, Perkin Elmer Nexion 2000B). Furthermore, the ranking within the SiO<sub>2</sub> materials was not entirely identical if ranked by either the daily ion mass  $M_{\text{ion}}/d$  or by the dissolution constant  $k$ . This minor inconsistency was tracked to a mixed reporting of integral vs. interpolated dissolution. We have now made this entirely consistent by reporting values of integral dissolution both for  $k$  and  $M_{\text{ion}}/d$ . Apart from the ion detection technique, the protocol of the measurements was kept identical. The samples were diluted by a factor of 10 to 100 with 50 ms integration time on each mass. External calibration used concentrations of 0, 0.01, 0.1, 1, 10  $\mu\text{g L}^{-1}$  for Fe, Ti, Ce and Cu and 1, 10, 100,

1000  $\mu\text{g L}^{-1}$  for Si with matrix-matched standards. The ultra-high purity quartz nebulizer had an argon flow of 0.94 mL min<sup>-1</sup> and a sample flow rate of 0.29 mL min<sup>-1</sup>. With ICP-MS the limit of detection was 1.0  $\mu\text{g L}^{-1}$  for Si and below 0.01  $\mu\text{g L}^{-1}$  for the other elements. We therefore recommend using ICP-MS in further studies.

The corrected version of Table 2 of the original article is presented below. The results improve our understanding of slow or stagnant dissolution processes, and lend further support to the grouping scheme of the original article. Si is challenging in elemental analysis and the actual ion concentration detected by ICP-MS was above the nominal LoD by ICP-OES. Within the SiO<sub>2</sub> family, the differences between untreated and functionalized nanoforms are still observed with the enhanced detection, but at a reduced spread. We continue to observe that pyrogenic silica (NM-203) has a very similar, but slightly lower dissolution rate than the precipitated silica (NM-200) of roughly the same specific surface area, whereas an opposite trend is observed in dissolution without flow. (ECETOC, 2006) This does not prevent grouping of SiO<sub>2</sub> nanoforms. Due to the high surface area, clearance of SiO<sub>2</sub> nanoforms is mediated significantly by dissolution with up to 12% per 7 days (Table 2), despite low dissolution rates.

At even lower rates, the new results confirm the similarity within the CeO<sub>2</sub> nanoforms, within Fe<sub>2</sub>O<sub>3</sub> (nano)forms, within the TiO<sub>2</sub> nanoforms, and between CuPhthalo\_nano and CuPhthalo\_halogen: The comparison of rates does not exceed a factor of about two between different (nano)forms of the same substance, but varies between substances. All of the above materials remain below the 1 ng/cm<sup>2</sup>/h level, and the corresponding dissolution half-life values are always above 500 days. This indicates that dissolution might not significantly

DOI of original article: <https://doi.org/10.1016/j.impact.2018.08.005>

\* Corresponding author.

E-mail addresses: [johanna.koltermann-juelly@basf.com](mailto:johanna.koltermann-juelly@basf.com) (J. Koltermann-Jüly), [johannes-georg.keller@basf.com](mailto:johannes-georg.keller@basf.com) (J.G. Keller), [vennemann@ibe-ms.de](mailto:vennemann@ibe-ms.de) (A. Vennemann), [kai.werle@basf.com](mailto:kai.werle@basf.com) (K. Werle), [lan.ma-hock@basf.com](mailto:lan.ma-hock@basf.com) (L. Ma-Hock), [robert.landsiedel@basf.com](mailto:robert.landsiedel@basf.com) (R. Landsiedel), [martin.wiemann@ibe-ms.de](mailto:martin.wiemann@ibe-ms.de) (M. Wiemann), [wendel.wohlleben@basf.com](mailto:wendel.wohlleben@basf.com) (W. Wohlleben).

<sup>1</sup> Equal contribution.

<https://doi.org/10.1016/j.impact.2019.100154>

Available online 27 March 2019

2452-0748/ © 2018 The Author(s). Published by Elsevier B.V. All rights reserved.

**Table 2**

Cumulative evaluation of biodissolution of ENM in flow cells with pH 4.5 media at 2 mL h<sup>-1</sup> flow-through. New results of the present addendum (by ICP-MS analysis) are compared to original results (by ICP-OES analysis if not marked otherwise).

	M <sub>0</sub>	Max. ion concentration	Dissolved per 7 days	k	M <sub>ion</sub> /d
Unit	[mg]	[mg/L]	[%]	[ng/cm <sup>2</sup> /h]	[µg/day]
BaSO <sub>4</sub> NM-220 (nano)	1.05	1.3	58	10	51
BaSO <sub>4</sub> NM-220 (nano)	0.17	0.8	100	45	18
BaSO <sub>4</sub> IRMM381 (non-nano)	1.78	0.49	9	53	16
CeO <sub>2</sub> NM-211 (ICP-MS)	1.06	0.071	1.1	0.14	1.7
(ICP-OES)	1.1	< 0.1 (LoD)	< 3	< 0.28 (LoD)	< 3.9 (LoD)
CeO <sub>2</sub> NM-212 (ICP-MS)	1.03	0.0094	0.19	0.059	0.28
(ICP-OES)	1.02	< 0.1 (LoD)	< 3	< 0.73 (LoD)	< 3.6 (LoD)
Cu <sub>2</sub> (OH) <sub>2</sub> CO <sub>3</sub>	1.07	3.0	32	172	24
Cu_Phthalo_halogen (ICP-MS)	1.02	0.028	3.6	0.42	5.0
(ICP-OES)	1	< 0.1 (LoD)	< 35(LoD)	< 3.7(LoD)	< 2.4(LoD)
Cu_Phthalo_nano (ICP-MS)	1.06	0.07	4.9	0.76	7.4
(ICP-OES)	0.98	0.05	4.1	0.64	5.7
CuO	1.56	37	100	283	456
Fe <sub>2</sub> O <sub>3</sub> _larger (ICP-MS)	1.00	0.013	0.14	0.097	0.20
(ICP-OES)	1.09	< 0.1 (LoD)	< 3 (LoD)	< 1.56 (LoD)	< 3.7 (LoD)
Fe <sub>2</sub> O <sub>3</sub> _nano_A (ICP-MS)	1.00	0.049	0.53	0.041	0.76
(ICP-OES)	1.07	< 0.1 (LoD)	< 3 (LoD)	< 0.17 (LoD)	< 3.2 (LoD)
Fe <sub>2</sub> O <sub>3</sub> _nano_B (ICP-MS)	0.97	0.015	0.16	0.044	0.22
(ICP-OES)	0.99	< 0.1 (LoD)	< 3 (LoD)	< 0.65 (LoD)	< 3.6 (LoD)
SiO <sub>2</sub> NM-203 (ICP-MS)	1.00	0.58	10.1	0.39	14
(ICP-OES)	1.12	0.3	8	0.23	11
SiO <sub>2</sub> NM-200 (ICP-MS)	0.95	0.49	11.7	0.58	16
(ICP-OES)	1.01	0.45	11	0.38	7.76
SiO <sub>2</sub> _amino_200 (ICP-MS)	1.10	0.45	18.6	0.268	10.2
(ICP-OES)	1.06	0.28	7	0.22	4.8
SiO <sub>2</sub> _phosphonate_200 (ICP-MS)	1.10	0.27	10.8	0.45	16.9
(ICP-OES)	1.01	0.18	8	0.28	5.9
SiO <sub>2</sub> _untreated_50	1.17	0.03	0.5	0.088	1.6
SiO <sub>2</sub> _untreated_100	1.08	0.04	0.9	0.066	1.7
SiO <sub>2</sub> _untreated_200 (ICP-MS)	1.26	0.27	7.2	0.20	9.0
(ICP-OES)	1.0	0.05	1.2	0.044	2.1
SiO <sub>2</sub> _untreated_300	1.05	0.06	1.4	0.034	2.6
SrCO <sub>3</sub>	1.08	12.7	100	108	240
TiO <sub>2</sub> NM-104 (ICP-MS)	1.00	0.052	1.3	0.17	1.64
(ICP-OES)	1.09	< 0.1 (LoD)	< 0.03 (LoD)	< 0.031 (LoD)	< 2.4 (LoD)
TiO <sub>2</sub> NM-105 (ICP-MS)	1.01	0.011	0.35	0.056	0.50
(ICP-OES)	1.04	< 0.01 (LoD)	< 0.1 (LoD)	< 0.013 (LoD)	< 0.1 (LoD)
ZnO NM-110	1.12	18	100	204	217
ZnO NM-111	1.12	17	100	177	150

contribute to clearance from the lungs for any measured nanoform of the above substances, as confirmed by comparison to pulmonary clearance data of in vivo studies (Table 3 in the original contribution).

## References

ECETOC, 2006. Synthetic amorphous silica (CAS no. 7631-86-9). In: JACC, pp. 51.

Koltermann-Jilly, J., Keller, J.G., Vennemann, A., Werle, K., Müller, P., Ma-Hock, L., Landsiedel, R., Wiemann, M., Wohlleben, W., 2018. Abiotic dissolution rates of 24 (nano)forms of 6 substances compared to macrophage-assisted dissolution and in vivo pulmonary clearance: grouping by biodissolution and transformation. NanoImpact 12, 29–41.

### 3.1.4 Predicting dissolution and transformation of inhaled nanoparticles in the lung using abiotic flow cells: The case of barium sulfate

**Keller JG\***, Graham UM\*, Koltermann-Jülly J, Gelein R, Ma-Hock L, Landsiedel R, Wiemann M, Oberdörster G, Elder A, Wohlleben W.

\*Equal contribution

*Sci Rep* **10**, 458 (2020).

<https://doi.org/10.1038/s41598-019-56872-3>

#### **Abstract:**

Barium sulfate (BaSO<sub>4</sub>) was considered to be poorly soluble and toxicologically inert, but BaSO<sub>4</sub> NM-220 showed a surprisingly short retention after intratracheal instillation in rat lungs, and incorporation of Ba within the bones. Here we show that static abiotic dissolution cannot rationalize this result, whereas two dynamic abiotic dissolution systems (one flow-through and one flow-by) indicated 50 % dissolution after 5 to 6 days at non-saturating conditions regardless of flow orientation, which is close to the *in vivo* half-time of 9.6 days. Non-equilibrium conditions were thus essential to simulate *in vivo* biodissolution. Instead of shrinking from 32 nm to 23 nm (to match the mass loss to ions), TEM scans of particles retrieved from flow-cells showed an increase to 40 nm. Such transformation suggested either material transport through interfacial contact or Ostwald ripening at super-saturating conditions and was also observed *in vivo* inside macrophages by high-resolution TEM following 12 months inhalation exposure. The abiotic flow cells thus adequately predicted the overall pulmonary biopersistence of the particles that was mediated by non-equilibrium dissolution and recrystallization. The present methodology for dissolution and transformation fills a high priority gap in nanomaterial hazard assessment and is proposed for the implementation of grouping and read across by dissolution rates.

OPEN

# Predicting dissolution and transformation of inhaled nanoparticles in the lung using abiotic flow cells: The case of barium sulfate

Johannes G. Keller<sup>1,2,7</sup>, Uschi M. Graham<sup>3,7</sup>, Johanna Koltermann-Jüly<sup>1,4</sup>, Robert Gelein<sup>6</sup>, Lan Ma-Hock<sup>1</sup>, Robert Landsiedel<sup>1</sup>, Martin Wiemann<sup>5</sup>, Günter Oberdörster<sup>6</sup>, Alison Elder<sup>6\*</sup> & Wendel Wohlleben<sup>1\*</sup>

Barium sulfate ( $\text{BaSO}_4$ ) was considered to be poorly-soluble and of low toxicity, but  $\text{BaSO}_4$  NM-220 showed a surprisingly short retention after intratracheal instillation in rat lungs, and incorporation of Ba within the bones. Here we show that static abiotic dissolution cannot rationalize this result, whereas two dynamic abiotic dissolution systems (one flow-through and one flow-by) indicated 50% dissolution after 5 to 6 days at non-saturating conditions regardless of flow orientation, which is close to the *in vivo* half-time of 9.6 days. Non-equilibrium conditions were thus essential to simulate *in vivo* biodissolution. Instead of shrinking from 32 nm to 23 nm (to match the mass loss to ions), TEM scans of particles retrieved from flow-cells showed an increase to 40 nm. Such transformation suggested either material transport through interfacial contact or Ostwald ripening at super-saturating conditions and was also observed *in vivo* inside macrophages by high-resolution TEM following 12 months inhalation exposure. The abiotic flow cells thus adequately predicted the overall pulmonary biopersistence of the particles that was mediated by non-equilibrium dissolution and recrystallization. The present methodology for dissolution and transformation fills a high priority gap in nanomaterial hazard assessment and is proposed for the implementation of grouping and read-across by dissolution rates.

Knowledge about pulmonary retention kinetics of inhaled particles is an essential element of hazard assessment and of understanding the mechanisms by which adverse health outcomes may occur. Barium sulfate was generally assumed to be poorly-soluble and of low toxicity unless delivered at high concentrations over an extended period<sup>1,2</sup>. However, Konduru and colleagues reported that intratracheally instilled  $^{131}\text{BaSO}_4$  NM-220 exhibited a lung retention half-time of only 9.6 days in rats and that  $^{131}\text{Ba}$  was incorporated into the bones, suggesting nanoparticle dissolution and/or translocation to extrapulmonary sites<sup>3</sup>. A subsequent 90-day inhalation study in rats with a high concentration of aerosolized  $\text{BaSO}_4$  NM-220 ( $50 \text{ mg/m}^3$ )<sup>4</sup> revealed no signs of lung overload and a retention half-time of 56 days, which is close to the normal range for the rat lung<sup>4</sup>. A two-year rat inhalation study with  $\text{BaSO}_4$  NM-220 ( $50 \text{ mg/m}^3$ ), however, demonstrated an increase of retained Ba in the lung during the first year of exposure, after which a steady-state was achieved<sup>5</sup>. Since significant Ba accumulation in bone and bone marrow was also observed and, given that the measurements of Ba distribution [1–3] provide no information about its physicochemical characteristics, the complex *in vivo* dissolution and/or transformation of  $\text{BaSO}_4$  secondary to inhalation exposure require more detailed investigation.

<sup>1</sup>Department Experimental Toxicology and Ecology and Department Material Physics, BASF SE, 67056, Ludwigshafen, Germany. <sup>2</sup>Institute of Pharmacy, Faculty of Biology, Chemistry & Pharmacy, Freie Universität Berlin, 14195, Berlin, Germany. <sup>3</sup>National Institute of Occupational Safety and Health, Cincinnati, Ohio, 45226, USA. <sup>4</sup>Biopharmaceutics and Pharmaceutical Technology, Saarland University, 66123, Saarbrücken, Germany. <sup>5</sup>IBE R&D Institute for Lung Health gGmbH, Mendelstr. 11, 48149, Münster, Germany. <sup>6</sup>University of Rochester Medical Center, Rochester, New York, USA. <sup>7</sup>These authors contributed equally: Johannes G. Keller and Uschi M. Graham. \*email: [alison\\_elder@urmc.rochester.edu](mailto:alison_elder@urmc.rochester.edu); [wendel.wohlleben@basf.com](mailto:wendel.wohlleben@basf.com)



Particle clearance from the lung involves absorptive (dissolution) and non-absorptive (physical) mechanisms. For poorly-soluble particles, physical clearance mechanisms – involving macrophage engulfment, transport, and mucociliary propulsion towards the oropharynx – dominate the pattern of overall clearance. Kreyling<sup>6</sup> demonstrated a retention half-time of 70 days in the rat for poorly-soluble particles<sup>7</sup>. For metal or metal oxide nanoparticles that undergo *in vivo* dissolution, clearance may not be immediate due to biotransformation and binding events (proteins or other biomolecules) that prolong retention<sup>8–10</sup>. When dissolution starts at the oxidized surface layer of a metallic nanoparticle, there is a continuous process of ion-leaching and oxidation. After the original oxide layer was leached, a second-generation oxide layer forms on the shrinking particle. The binding events may slow down physical transport to compartments of more aggressive acidity, thus also slowing down the onset of dissolution after inhalation. Thus, the collective *in vivo* observations with lung-deposited BaSO<sub>4</sub> suggest that it is more biosoluble than assumed and, therefore, *in vivo* dissolution and processing must be considered.

The evaluation of particle solubility is a key element of many integrated testing strategies<sup>10–12</sup> and of frameworks for categorizing broad classes of materials, such as engineered nanomaterials (ENMs), in terms of their physicochemical properties<sup>13–19</sup>. Methods to assess the equilibrium (or quasi-dynamic) solubility of ENMs that are suspended in water or physiological buffers – as was done with BaSO<sub>4</sub> and supported the conclusion regarding its low solubility – are relatively well developed<sup>20,21</sup>. The OECD draft guideline under current discussion involves suspending particles in a medium, incubation, removal of remaining solids by centrifugation or ultrafiltration, and measurement of the analyte in solution<sup>22</sup>. These approaches could be adequately predictive of particle dissolution in a closed system, e.g., a cell culture well for *in vitro* exposure studies<sup>21</sup>. There are several drawbacks with these approaches, however, when the model in question is an *in vivo* one. First, the lung is not a static (equilibrium) system, as the ions that are liberated from the particles via dissolution are continuously removed from the compartment where deposition originally occurred, or they become bound to biomolecules or may form secondary nanoparticles via reprecipitation. Secondly, if the closed system reaches the solubility limit in the selected medium, the dissolution rate is easily underestimated and particles with some solubility may appear as very poorly-soluble. Thirdly, commonly-used methods generally lack a means for evaluating the structural transformation of remaining solids, i.e., physicochemical modifications that could impact clearance and particle disposition. Lastly, any abiotic system does not fully reflect disposition in lung because the lining and interstitial fluids throughout the respiratory tract are pH-balanced, complex mixtures of salts, serum proteins, and other biomolecules. Most importantly, phagocytosis by macrophages or other cell types introduces particles to the lysosomal microenvironment with an acidic pH. Thus, a dynamic (non-equilibrium) system with more realistic media composition that simulates extra- and intracellular lung environments with both fluid phase and solid phase product analysis may be better suited to an evaluation of the *in vivo* bioprocessing of deposited particles in the lung, particularly if both the intraphagolysosomal and lung surface microenvironments are considered.

Indeed, dynamic systems were developed and validated to estimate the biopersistence of mineral fibers<sup>23–25</sup>. In these systems, dissolved ions pass through a membrane with a pore size that excludes the parent particles. The ions on the other side of the membrane are continually removed from the system using flow-through or flow-by macrodialysis, thus achieving non-equilibrium conditions over the time course – hours to days – of the study. The dialysate is collected in discrete volumes, after which the target analyte is quantitated in the collected fractions and the waste that was not sampled. Adaptation to ENMs mainly requires the choice of appropriate separation membranes. Stefaniak and colleagues employed a membrane to separate the suspended particles from a larger volume of particle-free receptor medium, thus gaining size exclusion in addition to the flow-mediated concentration gradient that provided short-term disruption of equilibrium conditions<sup>21</sup>. Another quasi-dynamic system with relatively large volume was explored and a setup patented for oral exposure purposes<sup>26</sup>, demonstrating that dynamic setups can also be employed to study the structural transformations of remaining solids<sup>27</sup>. Transformation of nanoparticles by *in vivo* processing has been directly observed for the relatively biosoluble amorphous SiO<sub>2</sub> in the pulmonary compartment<sup>9</sup>. Transition metal oxides, specifically CeO<sub>2</sub>, have also demonstrated the potential to recrystallize in lysosomal conditions<sup>28</sup> or in extracellular medium<sup>9</sup>, and bioprocessing was observed to be organ-specific<sup>29</sup>. Such modulations of biopersistence by local physiological conditions could, thus, contribute significantly to the unusual biokinetics of nanoscale BaSO<sub>4</sub><sup>4,5,30</sup>.

We hypothesize that both the shedding of ions and *in vivo* biotransformation of remaining solids contribute to the biokinetics of nanoparticles. We describe here methodology to evaluate the abiotic dissolution of BaSO<sub>4</sub>, thought to be a poorly-soluble ENM, and explore the extent of agreement that can be reached in comparison to *in vivo* results.

## Materials

Previous *in vivo* studies on BaSO<sub>4</sub> NM-220 have already been conducted<sup>3,4</sup> and their physicochemical properties published in multiple reports<sup>31–33</sup>. BaSO<sub>4</sub> NM-220 is a benchmark material of the OECD sponsorship program. Table 1 lists physicochemical properties of NM-220 as relevant for ECHA nanoforms<sup>34</sup>.

## Methods

**Static solubility or quasi-dynamic abiotic dissolution.** Details for testing the solubility of BaSO<sub>4</sub> in phagolysosomal simulant fluid (PSF) under static conditions are provided in the *Supplementary Information*. In short, BaSO<sub>4</sub> was suspended in 200 mL PSF (composition described in<sup>21</sup>) at a concentration of 10 mg/mL, then incubated for 7 or 28 days at 37 °C with stirring. The remaining particulate matter was separated from the ions in solution using ultracentrifugation at 67,000 × g for 2 h, and the Ba concentration in the supernatant fraction was analyzed by inductively-coupled plasma mass spectrometry (ICP-MS). Particle dissolution under quasi-dynamic conditions was performed by suspending BaSO<sub>4</sub> in PSF (10 mg/mL) and injecting the suspension into a 2 mL dialysis cassette with a cut-off at 7 kDa (*Supplementary Information*). The dialysis cassette was placed horizontally



Property	BaSO <sub>4</sub> NM-220
Composition/crystallinity/impurities (XRD*)	purity > 93.8%; Na, Ca, Sr, F, Cl, organic compounds
Minimum external dimension (TEM**)	32 nm
Shape (TEM**)	Spheroidal
Specific surface area (BET***)	41 m <sup>2</sup> /g
Surface modification	None
Contact angle (water)	<10° (hydrophilic)

**Table 1.** Physicochemical properties of BaSO<sub>4</sub> NM-220. \*X-ray diffraction (XRD); \*\*Transmission electron microscopy (TEM); \*\*\*Brunauer-Emmett-Teller method (BET).

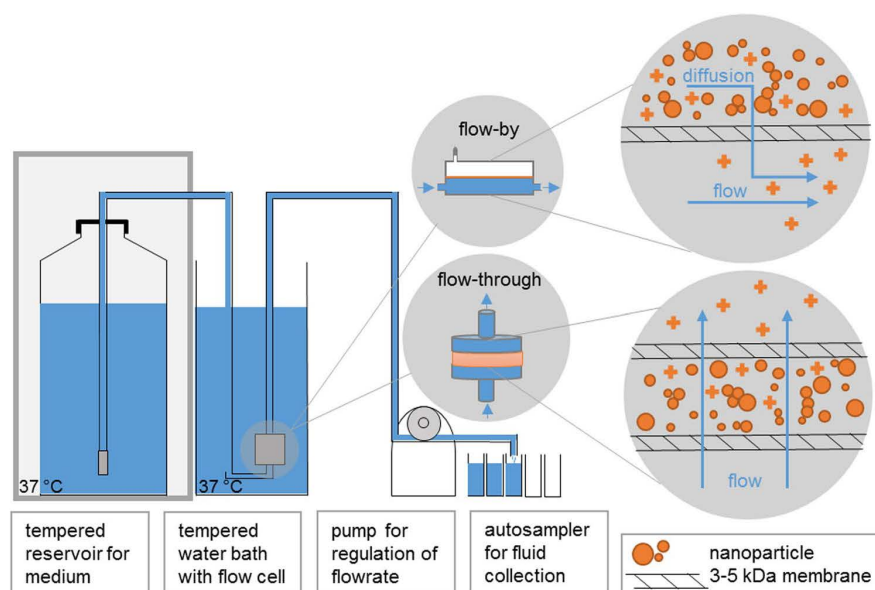


**Figure 1.** Dissolution method in abiotic flow cells (adapted from<sup>37</sup>). The medium was selected to match the conditions of either the phagolysosomal (pH 4.5) or lung lining fluid (pH 7.4) microenvironment. Particles are in direct contact with the membrane. The choice of the ultrafiltration membrane permeation cutoff is essential; a range 3 kDa to 5 kDa is recommended. This represents a size cut-off of ~1–2 nm (Ren *et al.*, 2006). Smaller cutoffs could induce excess pressure drops and are not recommended. Other options include (recommended): (1) especially for flow-through operation, anti-clogging filters on inlet tubing in the reservoir and elevation of the reservoir by roughly 30 cm, such that hydrostatic pressure compensates for the pressure drop by ultra-high molecular-weight polyethylene (UHMWPE) ultrafiltration membranes. (2) In one implementation, we operated five cells in parallel with a programmable autosampler. Each cell then has its own reservoir inlet tube, peristaltic pump tubing, and sampling.

in a glass vessel filled with 200 mL PSF as receptor medium at 37 °C with stirring. The receptor medium was exchanged daily and analyzed by ICP-MS. The methodological limit of detection for Ba was 0.1 mg/L.

**Flow-by abiotic dissolution.** The setup implements a Continuous Flow System (CFS) according to ISO TR 19057. A dynamic flow-by macrodialysis system<sup>23,24</sup> has been employed to estimate the *in vivo* dissolution of ENMs<sup>35</sup>. Here (Fig. 1), BaSO<sub>4</sub> (~1 mg/mL) was suspended in dissolution buffer before being injected into the upper chamber of a dialysis cell fitted with a 3.5 kDa cellulose ester symmetric membrane (Spectra/Pore®, Gardena, CA; effective pore size ~1.4 nm). The Ba-free dissolution buffers simulated extracellular lung lining fluid (pH maintained at 7.4 by bubbling 5% carbon dioxide into the buffer reservoir) or intraphagolysosomal fluid (pH adjusted to 4.5 with HCl). The latter of the two buffers is termed EU pH4.5 herein (see composition in *Supplementary Information*). The dialysis cells were submerged in a 37 °C water bath in a dark room. The buffers flowed by the dialysis cells at a rate of 60 μL/min, or ~3 mL/h. A fraction collector with metal-free, pre-weighed polypropylene tubes was used to collect the dialysates over the course of 7 days. For the first 24 h, two-hour fractions were collected (so, 12 fractions for Day 1); thereafter, the fractions were combined such that there were 6 daily fractions. The sample weight for each tube was recorded. After 7 days, the following additional samples were collected in ultra-clean polypropylene digestion tubes for analysis: the remaining solids in the upper chamber;

three rinses with 18 MΩ deionized water; and the dialysis membrane. The tubes were placed in a 90 °C heating block. Ultra-pure nitric acid was added to dissolve the membrane and the BaSO<sub>4</sub> nanoparticles. The Ba remaining in the upper cell after 7 days, the Ba left in the dialysis membrane, and the Ba found in each fraction was quantitated via atomic emission spectroscopy (Beckman Spectraspan V, Fullerton, CA; instrument limit of detection, ~10 μg/L).

**Flow-through abiotic dissolution and transformation.** The flow-through setup (Fig. 1) was recently described in detail as another implementation of a CFS according to ISO TR 19057<sup>36,37</sup>. CFS is established as a screening method of the dissolution kinetics of mineral fibers<sup>25,38,39</sup>. Unless otherwise mentioned, an ENM mass of M<sub>0</sub> = 1 mg was weighed onto a membrane (cellulose triacetate, Sartorius Stedim Biotech GmbH, Goettingen, Germany; 47 mm diameter, 5 kDa pore size), topped by another membrane, and enclosed in flow-through cells. The flow through cells were kept upright within a tempered water bath to ensure that emerging air bubbles can leave the system and do not accumulate within the cell. The initial surface area SA is M<sub>0</sub>\*BET (Table 1). The flow rate (V) was 48 mL/d, but was varied up to 100 mL/d. For the lower flow rate, this corresponds to a ratio, SA/V = 0.02 h/cm. The compositions of simulant fluids vary significantly in literature<sup>40</sup>. With the compositions documented in Table S1, the EU pH4.5 medium with a whole range of organic acids, or the simpler PSF medium –previously validated for the purpose of particle dissolution<sup>21</sup>– were employed at 37 ± 0.5 °C. The programmable sampler drew 10 mL eluates once per day from the total 100 mL collected. The Ba concentration in the eluates was determined by ICP optical emission spectrometry (ICP-OES, Agilent 5100). After the experiment, the cells were flushed with deionized water before opening them to rinse the remaining solids off the membrane. The resulting suspension was then pelleted onto a transmission electron microscopy (TEM) grid held at the bottom of a centrifuge vial within 30 min and then dried<sup>37</sup> so that the morphology of the remaining solids could be inspected with a reduction of interference from drying artifacts of PSF salts, which are removed by this preparation. Particle morphology was analyzed by TEM with a Tecnai G2-F20ST or Tecnai Osiris Microscope (FEI Company, Hillsboro, USA) at an acceleration voltage of 200 keV under bright-field conditions. X-ray photoelectron spectroscopy (XPS) was done using a Phi Versa Probe 5000 spectrometer using monochromatic Al Kα radiation.

**Derivation of dissolution rates.** For both of the flow-cell setups, we multiplied the measured Ba concentration of each eluate by the eluted volume to obtain a mass of dissolved Ba ions per sample and then stoichiometrically adjusted this value to obtain the dissolved mass of BaSO<sub>4</sub> at each sampling interval, Δt. We then analyzed the dissolution kinetics in three alternative ways:

- **Cumulative rate:** The amount of dissolved BaSO<sub>4</sub> at each time point M<sub>ion</sub>(T), is expressed as a fraction of the initial mass loading (M<sub>0</sub> = 100%) and cumulated from all samplings with concentration c<sub>i</sub>, flow V<sub>i</sub> and sampling interval Δt<sub>i</sub>, and includes the stoichiometry of BaSO<sub>4</sub>:

$$\frac{M_{ion}(T)}{M_0} = \frac{m(BaSO_4)}{m(Ba) * M_0} * \sum_{i=0}^T c_i(Ba) * V_i * \Delta t_i \tag{1a}$$

$$k = \frac{M_{ion}(T)}{M_0} \frac{1}{T * BET} \tag{1b}$$

The rate k incorporates the BET value in order to report results with a focus on composition or coating dependence, instead of size dependence. The conventional units of k are ng/cm<sup>2</sup>/h<sup>25,41</sup>. We typically determine k by the cumulated ions at the end of the test.

- **Curve fitting:** To verify first-order dissolution kinetics<sup>41</sup>, the cumulative dissolved BaSO<sub>4</sub> mass is expressed as an inverse relationship, i.e., decreasing solid retained BaSO<sub>4</sub> mass (M<sub>ion</sub>(T) – M<sub>0</sub>)/M<sub>0</sub>, and plotted against time on a semi-log scale. The dissolution rate – expressed as a fraction per hour – is calculated from the slope of this line and then converted to percent per day using the total system available starting mass. Dissolution rate and half-time (t'<sub>1/2</sub>, 50% dissolved) are inversely related and can be expressed in two alternative metrics (below) as given for first order modeling in ISO 19057:2017<sup>36,41</sup>. The BaSO<sub>4</sub> dissolution half-time allows direct extrapolation and comparison to the *in vivo* dissolution t<sub>1/2</sub> of inhaled BaSO<sub>4</sub>, which is derived from the total *in vivo* t<sub>1/2</sub>:

$$b_{diss} = \frac{\ln 2}{t'_{1/2}} \text{ or } t'_{1/2} = \frac{\ln 2}{b_{diss}} \tag{2a}$$

$$k_{diss} = \frac{\ln 2}{t'_{1/2} * BET} \text{ or } t'_{1/2} = \frac{\ln 2}{k_{diss} * BET} \tag{2b}$$

- **Instantaneous rates:** For each sampling interval Δt, the instantaneous dissolution rate k was constructed as:

$$k(t) = M_{ion}(t)/SA(t)/\Delta t. \tag{3}$$

We approximated the instantaneous surface area



$$SA(t) = BET(t = 0) * (M_0 - M_{ion}(t)) \quad (4)$$

and, thus, ignored changes of the size distribution and shape (see Discussion). Elsewhere<sup>37</sup> we explore modeling of SA(t) via the assumption of shrinking spheres<sup>36,41</sup>, which does not apply for particles with a tendency to transform, such as BaSO<sub>4</sub>.

It should be noted that the BET value that is used in Eq. (2b) for the determination of  $t_{1/2}$  cancels out with BET in Eq. (1b). Accordingly, the two evaluation approaches (fitting vs. cumulated rate) should coincide if the assumption of exponential decay (first order kinetics) is true. Also, the cumulative rate and the instantaneous rate should coincide in the absence of transformation during the test.

Expression of the rate as  $k_{diss}$  favors the read-across between nanoform and non-nanoform, because it eliminates the dissimilarity of the specific surface and focuses on modulation of the rate by different coatings or different crystallinities. The expression of the rate as  $b_{diss}$  avoids uncertainties regarding changes in particle surface area during the test and indicates a fraction of mass loss per unit time, which can readily be compared to *in vivo* dissolution rates – or to predict them – with the assumption of rapid clearance (no binding) of the dissolved ions.

**Evaluation of *in vivo* structural transformations via high-resolution analytical TEM.** Rat lung blocks from the 24-months inhalation study at 50 mg/m<sup>3</sup> of BaSO<sub>4</sub> NM-220<sup>5</sup> were cut to 50 to 70 nm thick sections and collected on 200 mesh Formvar/carbon coated copper grids. For ultrastructural and elemental characterization of selected lung sections high resolution scanning transmission microscopy (HRSTEM) was performed using a JEOL 2100F field emission TEM/STEM operated at 200 keV with an analytic pole piece. Tissue sections for HRSTEM were prepared without staining or osmication since OsO<sub>4</sub> nanoparticles form and can bind to select tissue regions, which makes it difficult to optically distinguish those from potentially inhaled BaSO<sub>4</sub> nanoparticles or second-generation particles from *in vivo* processing. Images were recorded with a Gatan Ultrascan 4kx 4k CCD camera and data analysis and processing used Gatan Digital Micrograph software (Gatan, Inc.). HRSTEM imaging and Energy-dispersive X-ray spectroscopy (EDS) were performed with a GATAN HAADF detector, Digiscan II, Gatan 2000 Image Filter (GIF), and an Oxford Aztec EDS system (Oxford Instruments, Oxfordshire, United Kingdom) respectively. All HRSTEM images were acquired using an analytical probe with 0.17 nm. A FEI Talos transmission and scanning electron microscope was used for fast EDS mapping with a high degree of sensitivity due to the wrap-around style EDS detector mounted on the objective lens. Maps generally took 1 to 2 min to acquire with a sensitivity great enough to detect elemental concentrations in 4-nm size particles. EDS provides the means to determine the relationship between elemental accumulation and tissue regions, particularly in a situation where dynamic processes may be in play such as *in vivo* processing<sup>9</sup>.

**Ethics approval and consent to participate.** All experiments were performed in accordance with relevant guidelines and regulations. The long-term two-year inhalation study with interim sacrificing after 12 months exposure was approved by the local authorizing agency for animal experiments (Landesuntersuchungsamt Koblenz, Germany) as referenced by the approval number G 12-3 028.

**Consent for publication.** All authors read and approved the final manuscript.

## Results

**Static abiotic solubility.** Data on the water solubility of BaSO<sub>4</sub> (2.45 ppm Ba ions at 20 °C<sup>42</sup>) cannot explain the *in vivo* observations. Even when solubility was measured in a medium that mimicked the intraphagolysosomal space, BaSO<sub>4</sub> was classified as insoluble with less than 0.1% dissolved (1000 ppm Ba ions)<sup>3</sup>. Here we replicated the static solubility measurements in different media and found 8 mg/L BaSO<sub>4</sub> (or 0.08%, nominal) dissolved in pH 4.5 phagolysosomal simulant fluid (PSF) over 7 days, stagnating at 5 mg/L (or 0.05%, nominal) after 28 days. We hypothesize it is not appropriate to express the data from a known static system as a rate but indicate nominal rates here to test the hypothesis. One sample of BaSO<sub>4</sub> was left to settle in PSF for nearly 2 years in a 200-mL beaker. The resulting ion concentration after nearly 2 years was identical to the concentration after 7 days. The addition of EDTA, to mimic alkaline earth metal-transporting proteins, only minimally increased BaSO<sub>4</sub> solubility to 9 mg/L within 28 days (or 0.09%). This is in contrast to recent investigations on Zn-ENM, for which adjustment of the relevant medium was sufficient to induce dissolution, thus better-matching the lack of *in vivo* biopersistence<sup>20</sup>.

We also evaluated the quasi-dynamic dissolution of BaSO<sub>4</sub> using dialysis<sup>43</sup>. The ion concentration in the receptor medium remained roughly constant in this system: 1.3 mg/L, 1.2 mg/L, 1.1 mg/L, 1.0 mg/L, and 2.0 mg/L on days 1, 2, 3, 4 and 7, respectively. The cumulative dissolution of 0.07% over 7 days and an apparent dissolution rate of  $k = 0.01 \text{ ng/cm}^2/\text{h}$  remained on the same level as the static solubility system, but below *in vivo* rates. This indicates that an equilibrium Ba concentration of about 1 to 2 mg/L in the pH 4.5 PSF medium is the limiting factor preventing further dissolution.

**Dynamic abiotic dissolution.** Motivated by a correlation between the *in vivo* biopersistence of mineral fibers and their abiotic dynamic dissolution rates, two laboratories independently evaluated the dissolution of BaSO<sub>4</sub> NM-220 using similar macrodialysis systems: one flow-by and one flow-through (Fig. 1). While a flow-by system with the EU pH4.5 medium (composition in Table S1) was used at the University of Rochester, a flow-through system with PSF medium (Table S1) was used at BASF SE. The initial mass (~1 mg BaSO<sub>4</sub>) was the same and the flow rates (2–3 mL/h) were similar. Both labs found that BaSO<sub>4</sub> NM-220 exhibited a significant dissolution (≥20% over 7 days) under dynamic conditions (Fig. 2A). The dissolution rates and half-times for the two setups do not agree quantitatively despite similar initial mass loadings and flow rates. Exponential fits (Fig. 2A) indicate dissolution  $t_{1/2}$  values of 5.9 days (flow-through, pH 4.5 PSF) and 28.9 days (flow-by, EU pH4.5), estimating about

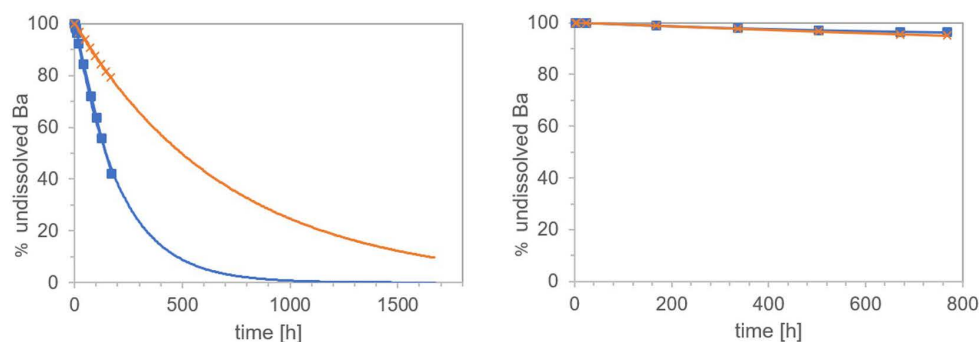


**Figure 2.** Dissolution kinetics of BaSO<sub>4</sub> (starting mass, ~1 mg) in pH 4.5 medium, tested by two dynamic dissolution methods: (A) flow-through (BASF, blue boxes) or flow-by (Rochester, orange crosses) macrodialysis. (B) comparison of both simulant fluids in the flow-through geometry (starting mass, 50 mg): PSF (blue boxes), EU pH4.5 (orange boxes). Note the different ranges of the y-axes.

	M <sub>0</sub>	M <sub>ion</sub> /T	t <sub>1/2</sub>	k <sub>diss</sub>	t' <sub>1/2</sub>	b <sub>diss</sub>
		[μg/d]	[d]	[ng/cm <sup>2</sup> /h]	[d]	[%/d]
Flow-through, PSF pH4.5	0.17 mg	17.5	2.6	44.7	1.6	43.3
	1 mg	51.1	5.9	10.3	6.8	10.2
	10 mg	53.6	72.1	0.9	78	0.89
	50 mg	58.0	247	0.2	346	0.2
Flow-by, EU pH4.5	0.08 mg	3.9	5	13.8	5.6	12.4
	0.8 mg	13.7	28.9	3.4	25.7	2.7
	8 mg	14.7	72.2	0.32	53.3	1.3

**Table 2.** Evaluation of cumulative dissolution of BaSO<sub>4</sub> in flow cells with pH 4.5 media using flow-through or flow-by methodology. The half-times t'<sub>1/2</sub> are obtained from b<sub>diss</sub> by direct fitting of the decay curve on a semi-log plot using Eq. (2a), whereas the half-times t<sub>1/2</sub> are derived via conversion of the cumulative rate k by Eq. (2b).

10% uncertainty due to extrapolation of surface areas for the flow-by data. Factors that could slightly impact the comparability of dissolution tests for partially-biosoluble materials such as BaSO<sub>4</sub> include temperature, different composition of pH4.5 media, flow geometry, membrane pore size, and initial loading. In flow-by geometry, the diffusion of ions from the sample compartment through the membrane into the flow (receptor) compartment could add another rate-limiting step that tends to reduce the apparent dissolution rate as observed from the ion concentrations in the flow compartment.

We replicated the experiment at BASF using EU pH4.5 and the flow-through system, keeping all other parameters unchanged except that the starting mass was increased to 50 mg. The dissolution kinetics in the flow-through setup were identical between the more complex EU pH4.5 and the simpler PSF pH4.5 media over the first few days (Fig. 2B). After 7 days, the dissolution rate in the PSF medium slowed down slightly as compared to the rates in the EU pH4.5 medium. Although it is possible that the phthalates in the PSF acted as ion scavengers – which would increase the solubility limit – PSF seems to slightly favor re-precipitation, thus reducing the apparent dissolution rate. To confirm this hypothesis, we changed the temperature during flow-through dissolution from 37 °C to 4 °C but started with the same initial mass of 1 mg. The apparent dissolution rate was reduced significantly by a factor of 2.5 (data not shown). Also, dissolution in neutral pH medium at 37 °C demonstrated significantly lower rates compared to media with pH 4.5 (Figs. S1 and S3), whereas an omission of organic acid and salts resulted in slight acceleration of apparent dissolution by 7% (data not shown).

Both labs observed that the dissolution kinetics depend on the initial mass of BaSO<sub>4</sub> (Table 2). Specifically, both labs observed that the Ba ion concentration was limited to a maximum of ~1 mg/L in the eluate from flow-through cells and to ~0.3 mg/L in the dialysate from flow-by cells. This limit is better reflected by the integral of the total mass of ions over the entire duration of the dissolution period, M<sub>ion</sub>/T (Eq. 1a), which turns out to be limited to about 60 μg/day in flow-through and about 15 μg/day in flow-by geometry (Table 2) at the specific flow rates used here. See also Figs. 2B and S2, demonstrating that higher M<sub>0</sub> leads to system saturation.

Although the mass loadings in abiotic dissolution experiments are not likely to mimic realistic *in vivo* exposure conditions, an observed solubility limit may be predictive of saturation-related events that occur *in vivo*. This is discussed further below, but first we rationalize the solubility limit by considering the ion sources (by particle dissolution) and ion losses (by flow<sup>36</sup>, flow cell geometries and reprecipitation).

The maximum observed ion concentration in flow-through geometry is close to the pH 4.5 solubility limit observed in the static and quasi-dynamic geometries but is about an order of magnitude higher than in flow-by



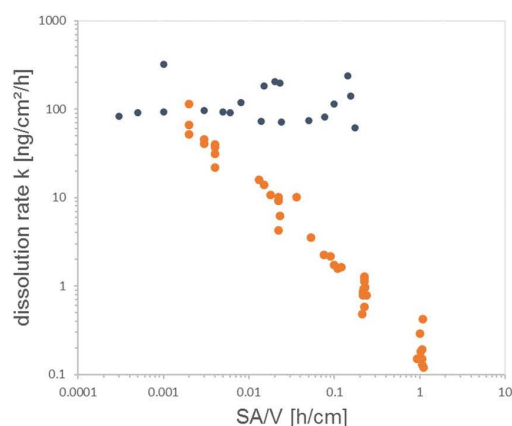


**Figure 3.** Instantaneous rate evaluation of biodissolution of  $\text{BaSO}_4$  in flow-through cells with pH 4.5 PSF media. Each cloud of stepwise rates stems from separate experiment of initial mass  $M_0$  and volume flow  $V$ . Five experiments for  $\text{BaSO}_4$  (orange) and two for  $\text{CuO}$  (black). See Table 2 for conventional evaluation (cumulative rates) of the same raw data.

geometry. The lower threshold of the flow-by system is attributed to the ion concentration in the local vicinity of the particles reaching the pH 4.5 solubility limit. We interpret the data to suggest that upon reaching the pH 4.5 solubility limit locally, ions reprecipitate before the flow removes them. Particle growth in the presence of dissolved ions under supersaturation conditions can lead to the growth of select NPs by the driving force of a lower-energy state of the overall system (Ostwald ripening process). The process matures further when the mobile ionic species (dissolved ions) are exchanged with and precipitated at immobile NPs surfaces and this process is driven by the difference in chemical potential at select NPs surfaces in confined spaces. The overall result can be a particle size increase and various structural and morphological changes (shape, size, crystallinity) of the affected NPs. This phenomenon can indeed be observed in both the flow-through and flow-by systems, i.e., only the measurements at lowest  $M_0$  (0.17 mg or 0.08 mg, respectively) remain below this limit. We also doubled the flow rate to  $V = 4 \text{ mL/h}$  for  $M_0 = 10 \text{ mg}$  and observed an increase in  $M_{\text{ion}}/T$  to  $102 \mu\text{g/day}$ , which is roughly twice the observed value at a flow rate of  $V = 2 \text{ mL/h}$  (Table 2). In summary, the cumulative apparent dissolution rates  $k$  and  $b$  (Table 2) scale roughly linearly with the  $\text{SA}/V$  ratio. Thus, to avoid reaching the solubility limit, either the initial mass can be reduced, or the flow can be increased.

We extensively tested both the reduction of initial mass or the increase of flow independently and in combination and analyzed both cumulative and instantaneous dissolution rates of the identical raw data. If we determine for each sampling interval the instantaneous rates  $k$  (in units of  $\text{ng}/\text{cm}^2/\text{h}$ , Eq. 3) and the instantaneous surface area per volume flow  $\text{SA}/V$  (in units of  $\text{h}/\text{cm}$ , Eq. 4), hundreds of instantaneous release rates collapse on a single linear relationship, regardless if  $\text{SA}/V$  was modulated by initial surface area or by flow rate or by gradual dissolution (Fig. 3). The best match of the predicted half-time with the *in vivo* half-time is obtained for  $\text{SA}/V$  ratios around 0.01 to 0.03  $\text{h}/\text{cm}$ . To ensure that this unusual observation is not an artifact of the experimental parameters, but truly a material-specific phenomenon, we tested another nanomaterial under identical conditions. We chose 10-nm  $\text{CuO}$  because it is a benchmark material in the draft OECD guideline on nanomaterial solubility and dissolution<sup>22</sup> and in the DF4nanoGrouping framework<sup>44</sup>. Like  $\text{BaSO}_4$ , no redox processes are involved in  $\text{CuO}$  dissolution, whereas other benchmark materials might differ by oxidative or reductive dissolution mechanisms<sup>12</sup>. If the  $\text{CuO}$  dissolution process is mediated by the ENM surface, re-precipitation remains irrelevant, and our calculation is correct, then  $k(t)$  of  $\text{CuO}$  should be constant for all  $t$  until full dissolution. Indeed, the instantaneous dissolution rates  $k$  of  $\text{CuO}$  were independent of  $\text{SA}/V$  across many orders of magnitude (Fig. 3), contrasting to the  $\text{BaSO}_4$  NM-220 behavior. Both  $\text{CuO}$  and  $\text{BaSO}_4$  do not change their redox state upon dissolution, and are thus non-reactive dissolution processes: in other cases, e.g. metallic  $\text{Cu}$ ,  $\text{Ag}$ ,  $\text{MoS}_2$ ,  $\text{CdS}$  etc., the electron exchange with a reaction partner from the surrounding medium may impose a rate-limiting step. In depth work on metal nanoparticles with a scope on the redox reaction forming the soluble product was done in by Gray *et al.* in 2018<sup>12</sup>.

Table 2 also highlights that the half-times  $t_{1/2}$  obtained by direct fitting on a semi-log plot are in close agreement with the half-times  $t'_{1/2}$  derived from conversion of the cumulative dissolution rate via Eq. 2a. Of note, the conversion assumes an exponential shape of the decay curve. Only for the highest initial loadings  $M_0 \geq 8 \text{ mg}$ , the values disagree significantly, because the saturation processes are reflected by linear (not exponential) kinetics (Fig. S3).

We also investigated the transformation of the shape and speciation of solids after abiotic testing: We flushed the flow-through cells with water, then opened the cells and rinsed off the remaining solids into a centrifuge vial with a TEM grid at the bottom as described in methodical detail in a recent paper and SI<sup>37</sup>. By centrifugation, all solid  $> 10 \text{ nm}$  was spun onto the TEM grid and the supernatant with its buffer salts was discarded. Compared to as-produced  $\text{BaSO}_4$  NM-220 (Fig. 4A), there was a shift towards larger particle diameters (Fig. 4B). Structural rearrangement towards a loss of small radii of curvature are observed (Fig. 4B), and occasionally, very large spherical structures were observed (Fig. 4D). Two different transformation processes are possible reasons for this

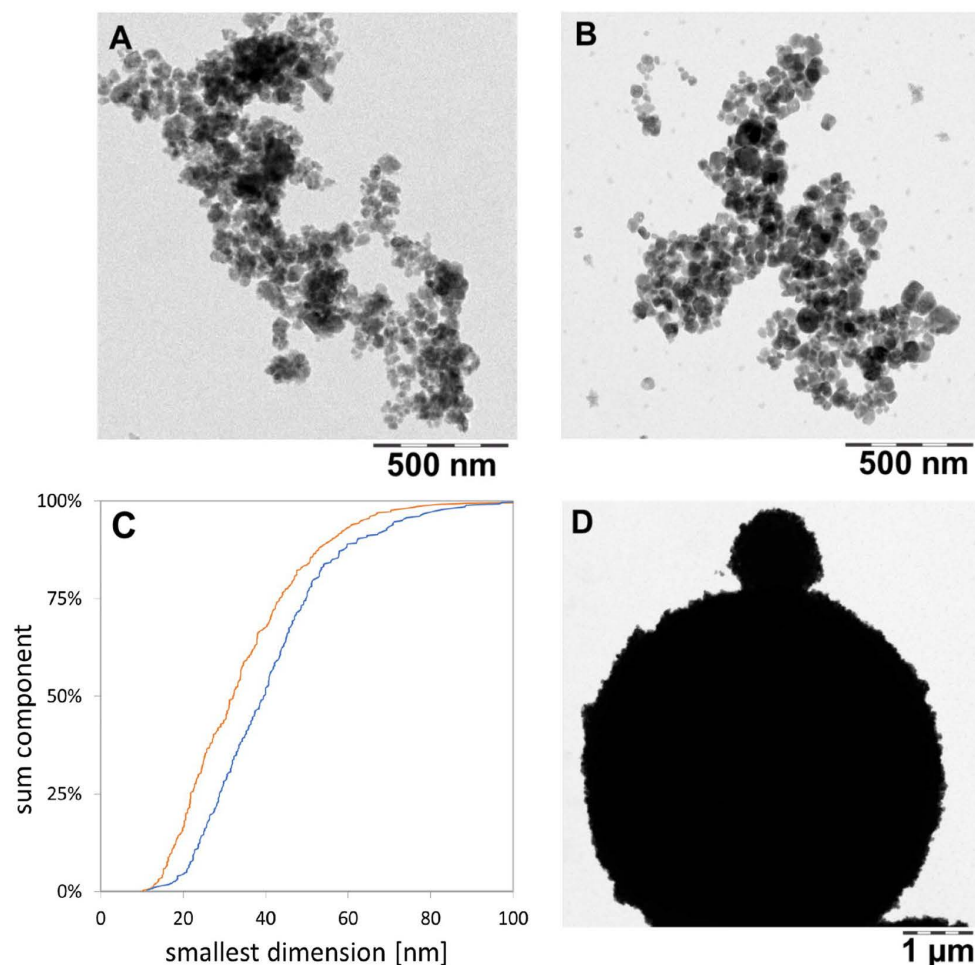


**Figure 4.** TEM images of  $\text{BaSO}_4$  transferred from remaining solids onto TEM grids (scale bar corresponds to 500 nm for (A,B) and 1  $\mu\text{m}$  for (D)). Panels: A as-produced particles; (B,D) after 72 hours of treatment in the flow-through cells with PSF. C shows the TEM particle size analysis of pristine  $\text{BaSO}_4$  particles (orange) and  $\text{BaSO}_4$  particles after treatment in PSF (blue) ( $N_A = 331$ ;  $N_B = 280$ ).

observation. Ostwald ripening, which is generally explained as a minimization of interfacial energy by an overall increase of the radii of curvature mediated by a minimal solubility of ions first described in<sup>45</sup>. Or secondly, competing intermolecular forces at the particle-particle interface inducing a material transport between particles of different sizes, as deduced from the study of perfluorocarbon blood substitutes<sup>46</sup>. Both processes are driven by the reduction of free energy. When comparing the TEM median particle size before and after continuous flow in PSF (Fig. 4C), a size shift from  $32.2 \pm 16$  nm to  $39.9 \pm 16.4$  nm was measured (by manual evaluation of approximately 300 particles). In contrast, the “shrinking sphere” model<sup>36</sup> would predict a diameter of 23 nm to match the 60% mass loss that is quantified as dissolved ions in the same experiment. XPS analysis confirmed that the preferred recrystallization species is  $\text{BaSO}_4$  (Figs. 5 and S4), in accord with the *in vivo* EDS observations (see next section).

With the present protocol, the flow conditions are highly controlled, but it is not possible to image the same nanoparticle over time. We also explored an alternative approach, where we repeatedly imaged the same ensemble of nanoparticle very far below the solubility limit at pH 4.5, but without controlling flow. The repeat scan shows that the sphericity of the remaining structures increases at the expense of structures with smaller radius of curvature (Fig. S5), consistent with either of the material transport mechanisms.

**Bioprocessing of  $\text{BaSO}_4$  particles in lung tissue: contributions to overall retention kinetics.** Long-term inhalation exposures (12–24 months) to  $\text{BaSO}_4$  NM-220 (Fig. 6a,b) at a high aerosol concentration ( $50 \text{ mg/m}^3$ ) resulted in significant accumulation of  $\text{BaSO}_4$  in lung macrophages (Fig. 6c,d). The retention of  $\text{BaSO}_4$  particles in the lung had reached a maximum at ~12 months of exposure. At 12 months of continued inhalation exposure, the retained dose of  $\text{BaSO}_4$  did not increase further, despite continued exposure. It appears that the continued pulmonary deposition of inhaled  $\text{BaSO}_4$  was counterbalanced by removal (dissolution of the nanoparticles



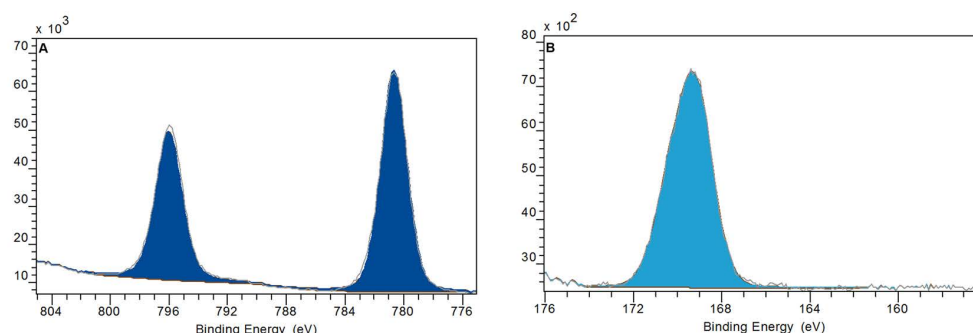


**Figure 5.** XPS results for BaSO<sub>4</sub> after flow-through testing in pH 4.5 PSF for 72 h. **(A)** Photoelectron energy line for Ba (3 days). **(B)** Photoelectron energy line for S (2p). The spectra can be fitted quantitatively with the benchmark chemical shifts of BaSO<sub>4</sub>. The elemental composition (Fig. S4) confirms a ratio Ba:S of 1:1.023, all consistent with an identification of the transformation product as BaSO<sub>4</sub>. Data was acquired and averaged on N = 5 measurements.

due to shedding of ions from the particle surfaces and elimination from the lung). The retained Ba in the lung was, thus, at an equilibrium between 12 and 24 months of exposure. The lung macrophages (Fig. 6c) contained nanoparticles that were identified with high resolution EDS to correspond to BaSO<sub>4</sub> (Fig. 6c). The spacing or relative distance between BaSO<sub>4</sub> particles inside the macrophages was rather small, with many particles seeded side-by-side (Fig. 6c–e). Surprisingly, the particle size distribution of BaSO<sub>4</sub> inside macrophages was significantly larger as compared with the parent material (Fig. 6a,b). This indicates that Ba and SO<sub>4</sub> ion concentrations inside the macrophage environment that contained many densely packed BaSO<sub>4</sub> particles, approached supersaturation conditions following the long-term inhalation exposure at a very high aerosol concentration (50 mg/m<sup>3</sup>). This resulted in the transformation and recrystallization of particles inside the lung macrophages. Material transport between particles had also occurred, whereby smaller particles dissolved faster, and the released ions were not removed, but rather deposited onto neighboring particle surfaces, allowing selective particle growth to take place (Fig. 6d,e). This is the first documentation of an inter-particle material transport mechanism of nanoparticles after uptake *in vivo*. In addition, BaSO<sub>4</sub> particles exhibited a greater size range (from sub-nano to micron scale) as compared with that of the starting materials which is in good agreement with observations from the abiotic flow through cells. Transformation of BaSO<sub>4</sub> involved a particle size effect and a recrystallization of the particles which was controlled by the saturation and supersaturation conditions in the macrophage microenvironment. The shedding of ions drove not only the *in vivo* dissolution kinetics, but also controlled the shape, morphology, and size distribution of retained BaSO<sub>4</sub> in the lung. This indicates that BaSO<sub>4</sub> undergoes transformation mediated by non-equilibrium dissolution (in line with the observed incorporation of Ba in bones within days after intratracheal instillation) and recrystallization, thus modulating the overall biopersistence of the particles. Not all macrophages contain copious amounts of densely packed BaSO<sub>4</sub> and it is important to point out that each macrophage represents a unique system where dissolution and supersaturation conditions are subject to the nanoparticle accumulation rate. Only when enough BaSO<sub>4</sub> nanoparticles collect inside a macrophage can transformation occur.

## Discussion

We posit that the measurement of dynamic particle dissolution should be an important element of predictive toxicity testing, i.e., the determination of dissolution *rates* in abiotic systems as opposed to static *solubility*. The *solubility* categorizes BaSO<sub>4</sub> (including the specific NM-220 grade) as poorly-soluble in water. However, solubility in water does not reflect *in vivo* reality in terms of 1) ongoing dynamic processes and 2) composition and pH of physiological fluids. The *dissolution rates* in physiological media better reflect an important component of *in vivo* particle clearance, considering that both absorptive chemical and physical clearance mechanisms are always working in tandem to affect total particle clearance (see below). Dissolution rates determined in appropriately-designed *abiotic* systems will be useful for grouping and classification of ENMs. From these predictive testing results, we also gain insight into the mechanisms that underlie biosolubility, which may explain experimental findings, e.g., the incorporation of Ba<sup>2+</sup> in bones (as Ca<sup>2+</sup> analogue).

Concerning the methodology, a solubility limit of ~100 mg/L has been proposed for testing strategies<sup>30,47</sup> and grouping frameworks<sup>13</sup> to define readily-soluble particles that would quickly lose their particulate nature. A currently developing OECD guideline describes a “screening test” that fulfills the requirements for Tier 1 grouping frameworks<sup>22</sup>. For purpose of initial screening of equilibrium *solubility*, the test could be performed in water, and then in the most relevant medium for exposure-specific testing<sup>20</sup>. For ENMs with solubility limits below 100 mg/L, for hazard assessment of innovative nanomaterials, or for endpoint-specific grouping and read-across between nanoforms, flow-by or flow-through dynamic dissolution (both are continuous flow systems<sup>36</sup>) in relevant media can offer predictivity of *in vivo* dissolution behavior<sup>10</sup>, but not necessarily total *in vivo* clearance rates.

In order to best model the contribution of dissolution to *in vivo* clearance, it makes good sense to focus on the intraphagolysosomal environment at pH 4.5 (although dissolution in extracellular fluid (at neutral pH) could also

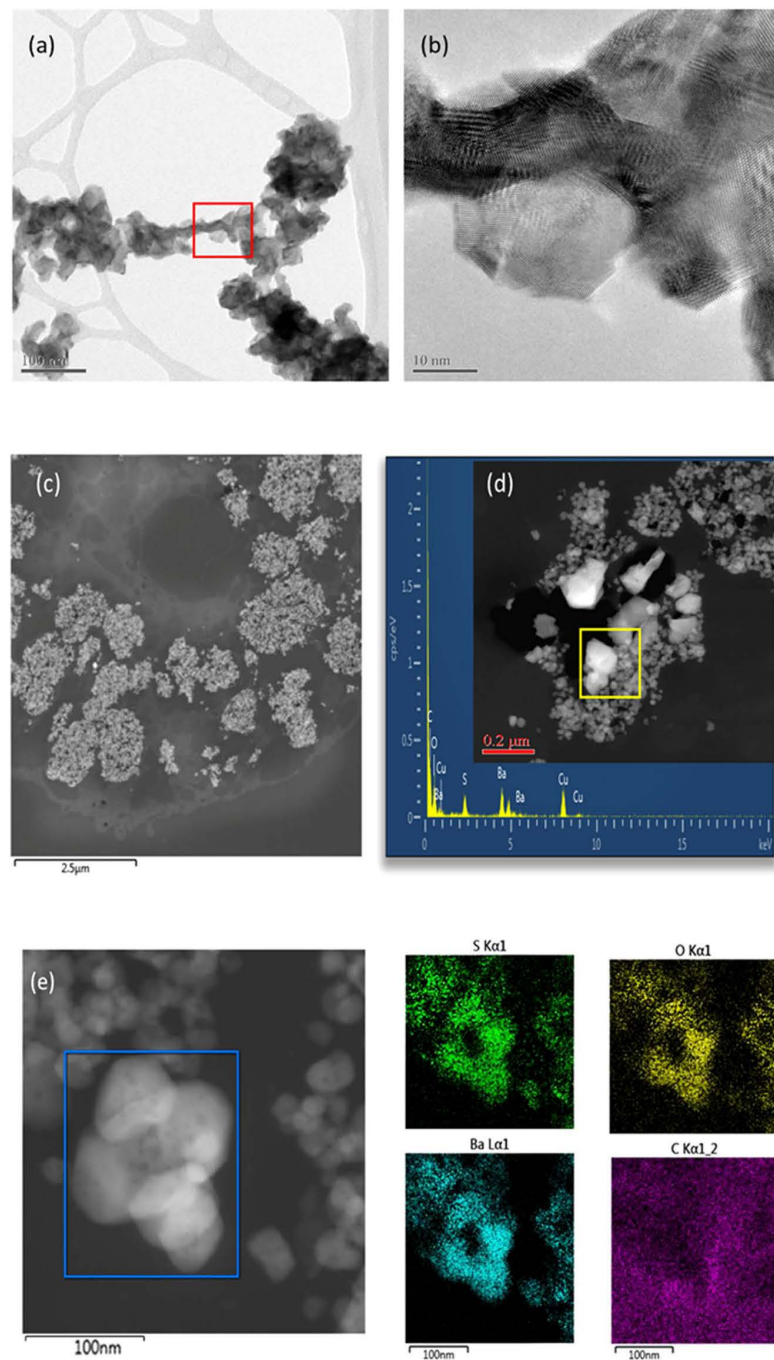


**Figure 6.** HRTEM/STEM structural characterization of as-produced  $\text{BaSO}_4$  nanoparticles and in rat lung sections. **(a,b)** pristine  $\text{BaSO}_4$  NM-220; **(c)**  $\text{BaSO}_4$  after 12 months inhalation exposure: accumulation in lung macrophage; **(d)** Transformation of  $\text{BaSO}_4$  in macrophage showing particle growth with crystalline facets. **(e)** HRSTEM of recrystallized  $\text{BaSO}_4$  in macrophage with corresponding high-resolution EDS mapping for S, Ba, O and C.

be considered and included in kinetic model equations). Additional information about the impact of different flow rates and starting masses would provide insight regarding saturation, which could be predictive of *in vivo* events. The selected methods for ion analysis should ideally have a limit of detection of  $10 \mu\text{g/L}$  or below for the target analyte. Methods for morphological analysis of remaining solids require sample preparation, which was



Exposure duration	Particle type and method of delivery	Total Retention $t_{1/2}$ (d)	$b_{tot}$ (d <sup>-1</sup> )	Dissolution Retention $t_{1/2}$ (d)	$b_{diss}$ (d <sup>-1</sup> )
---- <sup>(3)</sup>	<sup>131</sup> BaSO <sub>4</sub> NM-220 intratracheal instillation	9.6	7.23%	11.1	6.23%
90 days <sup>(4)</sup>	BaSO <sub>4</sub> NM-220 nose-only inhalation	56	1.24%	289	0.24%
2 years <sup>(5)</sup>	BaSO <sub>4</sub> NM-220 head-nose inhalation	45*	1.54%	128	0.54%

**Table 3.** Pulmonary dissolution rates and associated half-times for BaSO<sub>4</sub> derived from acute and repeated rat exposure studies. \*At steady-state.

developed here based on the NanoDefine D6.3 protocol for TEM analysis, using centrifugal pelleting of remaining solids onto a TEM grid (which inherently is a purification from dissolved species). To assess the extent of transformation, we recommend TEM-based morphological and size distribution analyses (N>100), with optional confirmation of chemical speciation, e.g., via SAD or XPS or XANES. For materials other than BaSO<sub>4</sub>, more complex re-speciations must be expected, e.g. Ag sulfidation, Cu oxidation<sup>48,49</sup>, CeO<sub>2</sub> re-speciation to CePO<sub>3</sub> needles<sup>29</sup>). Re-precipitation in flow-cells has been observed frequently during dissolution testing of stone wool mineral fibers, where especially Si tends to re-precipitate as gel on the surface of the fibers<sup>50–53</sup>. Most interestingly, a faster flow (lower SA/V ratio) is known to suppress gel formation and to increase the apparent stone wool dissolution rate<sup>54</sup>. These reports are analogous to our findings with BaSO<sub>4</sub>.

Dissolution should be expressed in terms of rate (e.g., k in units of ng/cm<sup>2</sup>/h or %/day) for which ample literature on dusts exists<sup>10</sup>. This approach challenges the cutoffs for categorization and grouping of ENMs, typically expressed in % dissolved or mg/L concentrations. BaSO<sub>4</sub> is clearly “insoluble” in mg/L metrics as determined using static systems but is correctly predicted to dissolve *in vivo* by the dynamic dissolution methods.

The findings from these studies could be used to propose alternative categories for grouping approaches of ENMs. For the rat, lung retention half-times ( $t_{1/2}$ ) for ‘poorly-soluble low-toxicity’ particles (PSLTs) are ~70 days and, by definition, reflect mechanical, macrophage-mediated clearance, generally following first-order kinetics<sup>10</sup>. Half-time and rate constants are inversely related to each other via Eq. (2). Using this equation to determine a rate constant for PSLTs yields ~0.01/day or roughly 1% of starting material – as expressed using any metric of choice – per day for the mechanical component of clearance. Knowing that total lung particle clearance reflects the sum of mechanical and dissolution clearance, one can derive groups of dissolution clearance rates such that faster rates would indicate readily- or partially-biosoluble particles. In a previous paper we applied the continuous flow system to 24 different ENMs, and suggested decadic ranges of the dissolution rates between <1 ng/cm<sup>2</sup>/h (insignificant dissolution – also asbestos falls into this group) and >100 ng/cm<sup>2</sup>/h (half-times on the order of 1 day)<sup>37</sup>. Expressing dissolution rates in percent per day enables comparisons to and predictions of *in vivo* clearance rates.

The preceding discussion is based on results from studies that were conducted in rats but could be adapted to human hazard characterization via the use of human-specific rate constants or retention half-times. While mechanical clearance rates exhibit species specificity and also be impacted by inflammatory responses, it is predicted that dissolution rates are similar between humans and rodents<sup>10</sup>. The method could be used to enhance the DF4nanoGrouping<sup>13</sup>, and to implement the ECHA grouping guidance<sup>55</sup> pending further validation by more varied case studies as proposed elsewhere<sup>37</sup>.

With regard specifically to BaSO<sub>4</sub> pulmonary clearance and transformation, Konduru and colleagues reported that intratracheally instilled <sup>131</sup>BaSO<sub>4</sub> NM-220 exhibited a lung retention half-time of 9.6 days in rats and that <sup>131</sup>Ba was incorporated into the bones, suggesting nanoparticle dissolution and/or extrapulmonary translocation<sup>3</sup>. A subsequent 90-day inhalation study in rats with aerosolized BaSO<sub>4</sub> of the same grade (50 mg/m<sup>3</sup>, full physicochemical equivalence to NM-220<sup>4</sup>) showed the gradual accumulation of Ba in lung tissue during exposure followed by steady clearance over a 90-day post-exposure period, with a reported retention half-time of 56 days, indicative of low *in vivo* solubility of BaSO<sub>4</sub> affecting its overall lung clearance. A two-year rat inhalation study in rats with BaSO<sub>4</sub> NM-220 (50 mg/m<sup>3</sup>) confirmed a steady increase of retained Ba in the lung up to one year of exposure, with no further increase during subsequent continued exposure up to two years<sup>5</sup>. The equilibrium lung burden of Ba over the exposure period (12–24 months) is explained by the fact that the daily deposited dose in the lung is equal to the amount being cleared daily, i.e., deposition and clearance rates are in equilibrium. Knowing the BaSO<sub>4</sub> aerosol characteristics (mass median aerodynamic diameter, geometric standard deviation, exposure concentration) and exposure duration, the daily deposition rate can be estimated using the MPPD model for rats with body weight-adjusted respiratory parameters, which results in a daily BaSO<sub>4</sub> lung clearance rate of 0.0154% of the daily deposited dose. This is equivalent to a retention half-time of 45 days (Eq. 2a). Since the lung clearance rate for biosoluble particles is the sum of mechanical and dissolution clearance rates, the difference between the normal rat clearance rate for PSLT particles (0.01/day) and the observed clearance rate in the equilibrium phase (0.0154/day) is the BaSO<sub>4</sub> *in vivo* dissolution clearance rate (0.0054/day;  $t_{1/2}$  = 128 d) (Table 3). The available data show that, for acute exposures, rapid clearance of BaSO<sub>4</sub> occurs and that dissolution contributes significantly to the total clearance. Following subchronic or chronic exposures, total lung clearance is slower, but is nevertheless faster than mechanical clearance alone. Of note is that the predicted dissolution rates and associated half-times for the 90-day and two-year studies are prolonged as compared to acute exposures, suggesting a saturation event. Both the fast, short-term *in vivo* dissolution at a lower ‘dose’ and the saturation at higher ‘doses’ were predicted by the abiotic assay (Table 2). The bioavailability of ionic Ba could predict secondary organ uptake with the caveat that there could be macromolecule binding events that might limit the clearance of Ba.

Depending on the initial loading, flow rate and flow cell geometry, the  $b_{\text{diss}}$  in the abiotic test ranges from 0.2% at strong saturation to 43% well below saturation, and abiotic dissolution half-times range from 350 days to 2 days (Table 2). The range of the half-time and rate values includes that which was found in the different *in vivo* studies. One might interpret that the intratracheal instillation study induced no or only mild saturation (locally), whereas the 90-day and two-year inhalation studies induced significant saturation, consistent with the morphological observations (Fig. 6).

The collective *in vivo* findings and those from the present dissolution studies suggest that Ba ions dissolved from lung-deposited particles – as opposed to the particles themselves – and were transported throughout the body and incorporated in bone epiphysi<sup>56–58</sup>. Furthermore, the long-term inhalation study results can be explained by a phenomenon whereby bone tissue – with its limited capacity and varying demand for bivalent cations over time – was saturated<sup>59</sup>, after which the net transport of Ba from lungs to bone decreased and, ultimately, the accumulation of Ba in the lungs increased. Within the (local) environment of the lungs, the ion removal rate depends on many factors, e.g., binding to biomolecules, that may affect the clearance rate.

Whether there is a specific or non-specific transport mechanism of Ba ions from the lung or a key trigger whose signaling results in the reduced removal of Ba from the lung remains to be elucidated. The measurement of Ba blood levels might help to shed light onto these questions. In addition, local clearance mechanisms in the lungs, such as mucociliary clearance and the clearance by alveolar macrophages, might be prolonged. We qualitatively observed significant accumulation of BaSO<sub>4</sub> in rat lung macrophages exposed for 12 months or longer to BaSO<sub>4</sub>. Of note, the acidic pH of the macrophage lysosome is essential to BaSO<sub>4</sub> dissolution, which is very significantly reduced at pH 7.4 (Fig. S1), by ~35% as compared to pH 4.5. Furthermore, removing the organics from the PSF pH 4.5 medium results in a significant decrease in dissolution (Fig. S3) and thus points to the ion scavenging effect of organic acids in lysosomal fluids. Taken together, uptake in macrophages and active transport of the ions are most likely steps in the clearance pathway, but dissolution in the neutral lining fluid may also contribute to total *in vivo* clearance.

Since the time-resolved abiotic dissolution shows that saturation conditions are reached, and furthermore crystalline particle growth was observed *in vivo* as well as in abiotic conditions, the structural transformation process are best described as Ostwald ripening. Once the net transport ceases, accumulation entails supersaturation conditions leading to the Ostwald ripening in macrophages that have accumulated BaSO<sub>4</sub> particles in phagolysosomes. Since each macrophage harbors unique concentrations of BaSO<sub>4</sub> particles, there are just as many systems (local supersaturation) to be considered. In this concept, the structure formation process is a self-catalyzing phenomenon: once the local ion concentration exceeds the solubility, triggering particle growth, the specific surface area of the deposited particles decreases, thus slowing dissolution until equilibrium is reached between removal via dissolution and addition by deposition. Further evidence for *in vivo* Ostwald ripening of inhaled BaSO<sub>4</sub> particles in lung tissue was recently presented<sup>60</sup>. Families of (nano)forms that share each one substance but differ in sizes, coatings or shapes, have been assessed by the same methodology for dissolution and transformation<sup>37</sup>. The BaSO<sub>4</sub> dissolution rate is intermediate in comparison, and materials such as amorphous silica show related reprecipitation phenomena, albeit at slower rate<sup>37</sup>.

Although the present study was designed to rationalize the clearance of BaSO<sub>4</sub> after inhalation, we note that the same concepts of local supersaturation (reaching the solubility limit of the specific ion in the lung medium) may be relevant to understand biokinetics after any other uptake routes. Accumulation of Ba in the lungs was reported after IV injection<sup>3,61</sup>. Giese 1934 and 1935 found after IV injection of BaSO<sub>4</sub> deposition in bone marrow, liver, spleen and lungs. Konduru *et al.* found 20% of the administered dose in lungs at 2 days post IV injection<sup>3</sup>. Ba ions are likely to have precipitated, similar to the observation via HRTEM of newly formed Ce-containing (nano)particles in the liver<sup>43,62</sup>. Huston *et al.* observed the formation of “refractile masses” after instillation of a Ba containing solution Veriopaque, which was accompanied by inhibited removal of Ba by macrophages.

Ba<sup>2+</sup> ions elicit systemic toxicity mainly via hypokalemia that is caused by the blocking of rectifying potassium channels in many cell types<sup>63</sup>. Although these effects do not necessarily require cellular uptake, it should be pointed out that Ba<sup>2+</sup> ions, similar to Sr<sup>2+</sup> ions, are capable of permeating specific Ca channels as well as non-selective cation channels of the cell membrane<sup>64–66</sup>, and some of these channels have been shown to be essential for macrophage function<sup>67–69</sup>. Ba<sup>2+</sup> ions may also be actively transported against an electrochemical gradient by Ca<sup>2+</sup> ATPases<sup>70</sup>. Once inside a cell, Ba<sup>2+</sup> ions may further pass to the different cell organelles such as endoplasmic reticulum, mitochondria, and lysosomes<sup>71</sup>. Thus, Ba<sup>2+</sup> ions dissolving from BaSO<sub>4</sub> nanoparticles may distribute across membranes between subcellular compartments with the net fluxes being determined by electrochemical driving forces: of note, phagolysosomes are acidified by an active transport of H<sup>+</sup> ions carried out by V-ATPases<sup>69</sup>, resulting in a positive potential of approximately 30 mV. This potential may act as an outward driving force for Ba<sup>2+</sup> ions, while at the same time creating an inward driving force for chloride ions, e.g., via CLC channels<sup>68,69</sup>. Although not yet proven it is tempting to speculate that these processes may be involved in fostering dissolution and/or recrystallization processes of BaSO<sub>4</sub> nanoparticles trapped in a macrophage's phagolysosome.

## Conclusion

Our results confirmed the previous findings that prediction of dissolution rates requires the use of relevant biological/physiological fluids rather than water<sup>20</sup>. The methodologies described herein for measuring abiotic dynamic particle dissolution and transformation involve a number of improvements:

- The use of continuous flow, rather than static incubation;
- The integrated assessment of residual solids with respect to transformations of shape, size distribution, and crystallinity by protocols for preparation, analysis and statistical image analysis, using TEM, optionally supported by XPS and EDX.



- The ready comparison, using the same experimental system, to compare to rapidly- and poorly-soluble benchmark particles, for grouping purposes as demonstrated elsewhere<sup>37</sup>;
- Ability to predict *in vivo* dissolution rates (with the acknowledged limitation that dissolved ions could be retained in tissues via binding to other molecules);
- The observation of dependence on initial loading mass could be useful for estimating *in vivo* solubility limits and, thus, provide insight regarding supersaturation that would impact total clearance rates.

Specifically, to BaSO<sub>4</sub> we propose that the unusual biokinetics of the long-term, high concentration BaSO<sub>4</sub> rat inhalation studies indicate a) the release of Ba ions via *in vivo* dissolution of phagocytosed particles, with transport to and uptake into the bone and b) recrystallization in lungs as additional transformation process that modifies ENM lung retention. The process is a self-catalyzing phenomenon as the specific surface area of the transforming particles decreases, thus slowing down dissolution. Especially the second year of the two-year inhalation study was, thus, conducted at significant saturation. Control measurements on CuO demonstrated that Ostwald ripening and supersaturation phenomena are not a methodical artifact, but characteristic of the BaSO<sub>4</sub> properties, and were reproducible in two labs and different lysosomal simulants. The rates and the transformation and the Ba speciation were verified *in vivo*, with the only limitation that *in vivo* processing resulted in less sphericity and more crystalline facets. The dynamic dissolution results thus qualitatively predicted the *in vivo* BaSO<sub>4</sub> dissolution, as well as the concentration-dependent Ostwald ripening process observed within the rat lung.

### Data availability

The test material BaSO<sub>4</sub> NM-220 is available from the OECD sponsorship repository at Fraunhofer Institute, Schmallenberg. The same-grade-later-batch used for the long-term inhalation study is available as JRCNM50001a in the frame of the PATROLS project from the JRC repository, Ispra.

Received: 28 January 2019; Accepted: 17 December 2019;

Published online: 16 January 2020

### References

1. Tran, C. L. *et al.* Inhalation of poorly soluble particles. II. Influence Of particle surface area on inflammation and clearance. *Inhal Toxicol* **12**, 1113–1126 (2000).
2. Cullen, R. T. *et al.* Inhalation of poorly soluble particles. I. Differences in inflammatory response and clearance during exposure. *Inhalation Toxicology* **12**, 1089–1111, <https://doi.org/10.1080/08958370050166787> (2000).
3. Konduru, N. *et al.* Biokinetics and effects of barium sulfate nanoparticles. *Particle and fibre toxicology* **11**, 55 (2014).
4. Schwotzer, D. *et al.* Effects from a 90-day inhalation toxicity study with cerium oxide and barium sulfate nanoparticles in rats. *Particle and Fibre Toxicology* **14**, 23, <https://doi.org/10.1186/s12989-017-0204-6> (2017).
5. Ma-Hock, L. *et al.* Long-term inhalation study with CeO<sub>2</sub>- and BaSO<sub>4</sub> nanomaterials – study design, in-life findings, and lung burden. In *Eurotox 2017* (2017).
6. Kreyling, W. G. Interspecies Comparison of Lung Clearance of “Insoluble” Particles. *Journal of Aerosol Medicine* **3**, S-93-S-110, [https://doi.org/10.1089/jam.1990.3.Suppl\\_1.S-93](https://doi.org/10.1089/jam.1990.3.Suppl_1.S-93) (1990).
7. Pauluhn, J. Pulmonary Toxicity and Fate of Agglomerated 10 and 40 nm Aluminum Oxyhydroxides following 4-Week Inhalation Exposure of Rats: Toxic Effects are Determined by Agglomerated, not Primary Particle Size. *Toxicological Sciences* **109**, 152–167 (2009).
8. Graham, U. *et al.* Calcium co-Localization with *in vivo* Cerium Phosphate Nanoparticle Formation after Intratracheal Instillation Dosing with CeCl<sub>3</sub> or CeO<sub>2</sub> NPs. Vol. 23 (2017).
9. Graham, U. M. *et al.* In *Modelling the Toxicity of Nanoparticles* (eds Lang Tran, Miguel A. Bañares, & Robert Rallo) 71–100 (Springer International Publishing, 2017).
10. Oberdörster, G. & Kuhlbusch, T. A. J. *In vivo* effects: Methodologies and biokinetics of inhaled nanomaterials. *NanoImpact* **10**, 38–60, <https://doi.org/10.1016/j.impact.2017.10.007> (2018).
11. Burden, N. *et al.* The 3Rs as a framework to support a 21st century approach for nanosafety assessment. *Nano Today* **12**, 10–13 (2017).
12. Gray, E. P. *et al.* Biodissolution and cellular response to MoO<sub>3</sub> nanoribbons and a new framework for early hazard screening for 2D materials. *Environmental Science: Nano* **5**, 2545–2559, <https://doi.org/10.1039/C8EN00362A> (2018).
13. Arts, J. H. E. *et al.* A decision-making framework for the grouping and testing of nanomaterials (DF4nanoGrouping). *Regulatory Toxicology and Pharmacology*, <https://doi.org/10.1016/j.yrtph.2015.03.007> (2015).
14. Collier, Z. A. *et al.* Tiered guidance for risk-informed environmental health and safety testing of nanotechnologies. *Journal of Nanoparticle Research* **17**, 155, <https://doi.org/10.1007/s11051-015-2943-3> (2015).
15. Drew, N. M., Kuempel, E. D., Pei, Y. & Yang, F. A quantitative framework to group nanoscale and microscale particles by hazard potency to derive occupational exposure limits: Proof of concept evaluation. *Regulatory Toxicology and Pharmacology* **89**, 253–267, <https://doi.org/10.1016/j.yrtph.2017.08.003> (2017).
16. Godwin, H. *et al.* Nanomaterial Categorization for Assessing Risk Potential To Facilitate Regulatory Decision-Making. *ACS Nano* **9**, 3409–3417, <https://doi.org/10.1021/acsnano.5b00941> (2015).
17. Kuempel, E., Castranova, V., Geraci, C. & Schulte, P. Development of risk-based nanomaterial groups for occupational exposure control. *J. Nanopart Res* **14**, 1029 (2012).
18. Oomen, A. G. *et al.* Grouping and read-across approaches for risk assessment of nanomaterials. *International journal of environmental research and public health* **12**, 13415–13434 (2015).
19. Oomen, A. G. *et al.* Risk assessment frameworks for nanomaterials: Scope, link to regulations, applicability, and outline for future directions in view of needed increase in efficiency. *NanoImpact* **9**, 1–13, <https://doi.org/10.1016/j.impact.2017.09.001> (2018).
20. Avramescu, M.-L., Rasmussen, P. E., Chénier, M. & Gardner, H. D. Influence of pH, particle size and crystal form on dissolution behaviour of engineered nanomaterials. *Environmental Science and Pollution Research*, 1–12, <https://doi.org/10.1007/s11356-016-7932-2> (2016).
21. Stefaniak, A. B. *et al.* Characterization of phagolysosomal simulant fluid for study of beryllium aerosol particle dissolution. *Toxicology in Vitro* **19**, 123–134, <https://doi.org/10.1016/j.tiv.2004.08.001> (2005).
22. Rasmussen, K. *et al.* Physico-chemical properties of manufactured nanomaterials - Characterisation and relevant methods. An outlook based on the OECD Testing Programme. *Regulatory Toxicology and Pharmacology* **92**, 8–28, <https://doi.org/10.1016/j.yrtph.2017.10.019> (2018).

23. Potter, R. M. & Mattson, S. M. Glass fiber dissolution in a physiological saline solution. *Glastechnische Berichte* **64**, 16–28 (1991).
24. Eastes, W., Potter, R. M. & Hadley, J. G. Estimating *In Vitro* Glass Fiber Dissolution Rate From Composition. *Inhalation Toxicology* **12**, 269–280, <https://doi.org/10.1080/089583700196149> (2000).
25. IARC, I. A. F. R. O. C. *Iarc Monographs on the Evaluation of Carcinogenic Risks to Humans* 1–433 (WORLD HEALTH ORGANIZATION, 2002).
26. Pompa, P. P., Sabella, S. & Cingolani, R.; Fondazione Istituto Italiano di Tecnologia. Device and method for determining the dissolution kinetics of colloidal nanoparticles. United States patent US20150233809A1 (2015).
27. Bove, P. *et al.* Dissolution test for risk assessment of nanoparticles: a pilot study. *Nanoscale* **9**, 6315–6326, <https://doi.org/10.1039/c6nr08131b> (2017).
28. Li, R. *et al.* Surface Interactions with Compartmentalized Cellular Phosphates Explain Rare Earth Oxide Nanoparticle Hazard and Provide Opportunities for Safer Design. *ACS Nano* **8**, 1771–1783, <https://doi.org/10.1021/nn406166n> (2014).
29. Graham, U. M. *et al.* Analytical High-resolution Electron Microscopy Reveals Organ-specific Nanoceria Bioprocessing. *Toxicologic Pathology* **46**, 47–61, <https://doi.org/10.1177/0192623317737254> (2018).
30. Laux, P. *et al.* Biokinetics of nanomaterials: The role of biopersistence. *NanoImpact* **6**, 69–80, <https://doi.org/10.1016/j.impact.2017.03.003> (2017).
31. Driessen, M. *et al.* Proteomic analysis of protein carbonylation: a useful tool to unravel nanoparticle toxicity mechanisms. *Particle and Fibre Toxicology* **12**, 36 (2015).
32. Hellack, B. *et al.* Characterization report for all nanoGEM materials. 1–41 (2013).
33. Landsiedel, R., Sauer, U. G., Ma-Hock, L., Schnekenburger, J. & Wiemann, M. Pulmonary toxicity of nanomaterials: a critical comparison of published *in vitro* assays with *in vivo* inhalation or instillation studies. *Nanomed* **9**, <https://doi.org/10.2217/nmm.14.149> (2014).
34. ECHA. How to prepare registration dossiers that cover nanoforms: best practices. *How to prepare registration dossiers that cover nanoforms: best practices*, <https://doi.org/10.2823/128306> (2017).
35. Elder, A. *et al.* Translocation of Inhaled Ultrafine Manganese Oxide Particles to the Central Nervous System. *Environmental Health Perspectives* **114**, 1172–1178, <https://doi.org/10.1289/ehp.9030> (2006).
36. Nti. In *Nanotechnologies. Use and application of acellular in vitro tests and methodologies to assess nanomaterial biodegradability* (2017).
37. Koltermann-Jully, J. *et al.* Abiotic dissolution rates of 24 (nano)forms of 6 substances compared to macrophage-assisted dissolution and *in vivo* pulmonary clearance: Grouping by biodissolution and transformation. *NanoImpact* **12**, 29–41, <https://doi.org/10.1016/j.impact.2018.08.005> (2018).
38. Wohlleben, W. *et al.* Composition, Respirable Fraction and Dissolution Rate of 24 Stone Wool MMVF with their Binder. *Particle and Fibre Toxicology* **14**, 29, <https://doi.org/10.1186/s12989-017-0210-8> (2017).
39. Guldberg, M., Christensen, V. R., Krøis, W. & Sebastian, K. Method for determining *in-vitro* dissolution rates of man-made vitreous fibres. *Glass science and technology* **68**, 181–187 (1995).
40. Kastury, E., Smith, E. & Juhasz, A. L. A critical review of approaches and limitations of inhalation bioavailability and bioaccessibility of metal(loid)s from ambient particulate matter or dust. *Science of The Total Environment* **574**, 1054–1074, <https://doi.org/10.1016/j.scitotenv.2016.09.056> (2017).
41. Utembe, W., Potgieter, K., Stefaniak, A. B. & Gulumian, M. Dissolution and biodegradability: Important parameters needed for risk assessment of nanomaterials. *Particle and Fibre Toxicology* **12**, 11 (2015).
42. McPherson, P. *Practical Volumetric Analysis*. (Royal Society of Chemistry, 2014).
43. Yokel, R. A., Hancock, M. L., Grulke, E. A., Unrine, J. M. & Graham, U. M. Nanoceria Dissolution and Carboxylic Acid Stabilization in Aqueous Dispersions. *The FASEB Journal* **31**, lb624 (2017).
44. Arts, J. H. E. *et al.* Case studies putting the decision-making framework for the grouping and testing of nanomaterials (DF4nanoGrouping) into practice. *Regulatory Toxicology and Pharmacology* **76**, 234–261, <https://doi.org/10.1016/j.yrtph.2015.11.020> (2016).
45. Lifshitz, I. & Slezov, V. Kinetics of diffusive decomposition of supersaturated solid solutions. *Soviet Physics JETP* **35**, 331 (1959).
46. Sommer, A. P., Röhlke, W. & Franke, R. P. Free Energy Reduction by Molecular Interface Crossing: Novel Mechanism for the Transport of Material Across the Interface of Nanoscale Droplets Induced by Competing Intermolecular Forces for Application in Perfluorocarbon Blood Substitutes. *Naturwissenschaften* **86**, 335–339, <https://doi.org/10.1007/s001140050629> (1999).
47. Hazardous, S. Committee on Announcement on Hazardous Substances 527. *BekGS* 527 (2013).
48. Vencalek, B. E. *et al.* *In Situ* Measurement of CuO and Cu(OH)<sub>2</sub> Nanoparticle Dissolution Rates in Quiescent Freshwater Mesocosms. *Environmental Science & Technology Letters* **3**, 375–380, <https://doi.org/10.1021/acs.estlett.6b00252> (2016).
49. Kent, R. D. & Vikesland, P. J. Dissolution and Persistence of Copper-Based Nanomaterials in Undersaturated Solutions with Respect to Cupric Solid Phases. *Environmental Science & Technology* **50**, 6772–6781, <https://doi.org/10.1021/acs.est.5b04719> (2016).
50. Guldberg, M. Method for determining *in-vitro* dissolution rates of man-made vitreous fibres. *Glass science and technology* **68** (1995).
51. Guldberg, M. *et al.* Measurement of *in-vitro* fibre dissolution rate at acidic pH. *Annals of Occupational Hygiene* **42**, 233–243 (1998).
52. Guldberg, M., Jensen, S. L., Knudsen, T., Steenberg, T. & Kamstrup, O. High-alumina low-silica HT stone wool fibers: A chemical compositional range with high biosolubility. *Regulatory Toxicology and Pharmacology* **35**, 217–226 (2002).
53. Zotos, B. K. *In vitro* measurement of fibre dissolution rate relevant to biopersistence at neutral pH: An interlaboratory round robin. *Inhalation toxicology* **9**, <https://doi.org/10.1080/089583797198051> (1997).
54. Thelohan, S. & De Meringo, A. *In vitro* dynamic solubility test: influence of various parameters. *Environmental health perspectives* **102**, 91 (1994).
55. ECHA. Appendix R.6-1 for nanomaterials applicable to the Guidance on QSARs and Grouping of Chemicals. *Appendix R.6-1 for nanomaterials applicable to the Guidance on QSARs and Grouping of Chemicals*, <https://doi.org/10.2823/884050> (2017).
56. Bligh, P. H. & Taylor, D. M. Comparative studies of the metabolism of strontium and barium in the rat. *The Biochemical journal* **87**, 612–618 (1963).
57. Panahifar, A. *et al.* Three-dimensional labeling of newly formed bone using synchrotron radiation barium K-edge subtraction imaging. *Phys Med Biol* **61**, 5077–5088, <https://doi.org/10.1088/0031-9155/61/13/5077> (2016).
58. Moore, W. Jr Comparative metabolism of barium-133 and calcium-45 by embryonic bone grown *in vitro*. *Radiation research* **21**, 376–382 (1964).
59. Misawa, Y. *et al.* Effect of age on alveolar bone turnover adjacent to maxillary molar roots in male rats: A histomorphometric study. *Archives of Oral Biology* **52**, 44–50, <https://doi.org/10.1016/j.archoralbio.2006.06.012> (2007).
60. Graham, U. *et al.* In *9th International Conference on Nanotoxicology* Vol. P15.37 (Neuss, Germany, 2018).
61. Giese, W. Experimentelle Untersuchungen zur Staublungenfrage. *Beitr. path. Anat* **94**, 35 (1934).
62. Yokel, R. A., Unrine, J. M., Wu, P., Wang, B. & Grulke, E. A. Nanoceria biodistribution and retention in the rat after its intravenous administration are not greatly influenced by dosing schedule, dose, or particle shape. *Environmental Science: Nano* **1**, 549–560, <https://doi.org/10.1039/C4EN00035H> (2014).
63. Hille, B. *Ion channels of excitable membranes*. Vol. 507 (Sinauer Sunderland, MA, 2001).
64. Mörk, A.-C. *et al.* Effects of particulate and soluble (1–3)- $\beta$ -glucans on Ca<sup>2+</sup> influx in NR8383 alveolar macrophages. *Immunopharmacology* **40**, 77–89 (1998).
65. Campo, B., Surprenant, A. & North, R. A. Sustained depolarization and ADP-ribose activate a common ionic current in rat peritoneal macrophages. *The Journal of Immunology* **170**, 1167–1173 (2003).



66. Dernison, M. *et al.* Growth-dependent modulation of capacitative calcium entry in normal rat kidney fibroblasts. *Cellular signalling* **22**, 1044–1053 (2010).
67. Vaeth, M. *et al.* Ca<sup>2+</sup> signaling but not store-operated Ca<sup>2+</sup> entry is required for the function of macrophages and dendritic cells. *The Journal of Immunology* **195**, 1202–1217 (2015).
68. Link, T. M. *et al.* TRPV2 has a pivotal role in macrophage particle binding and phagocytosis. *Nature immunology* **11**, 232 (2010).
69. Riazanski, V. *et al.* TRPC6 channel translocation into phagosomal membrane augments phagosomal function. *Proceedings of the National Academy of Sciences* **112**, E6486–E6495 (2015).
70. Ohsumi, Y. & Anraku, Y. Calcium transport driven by a proton motive force in vacuolar membrane vesicles of *Saccharomyces cerevisiae*. *Journal of Biological Chemistry* **258**, 5614–5617 (1983).
71. Xu, H., Martinoia, E. & Szabo, I. Organellar channels and transporters. *Cell Calcium* **58**, 1–10 (2015).

### Acknowledgements

We thank Kai Werle for excellent technical support. We thank Philipp Müller who supervised the TEM analyses, and Sabine Hirth who supervised the XPS analyses. This work was partially supported by project nanoGRAVUR (BMBF, FKZ 03XP0002B) and NIH P30 ES001247.

### Author contributions

J.G.K. performed the flow-through testing; UG performed the HRTEM study; R.G. performed, and A.E. supervised the flow-by testing; J.K.J. performed the static solubility and quasi-dynamic abiotic dissolution testing; R.L., L.M.H., G.O., M.W. contributed to the interpretation of results; W.W. conceived and supervised the project. All authors contributed to the writing of the manuscript.

### Competing interests

J.G.K., J.K.J., L.M.H., R.L., W.W. are employees of BASF SE, a company producing nanomaterials. All other authors declare that they have no competing interests.

### Additional information

**Supplementary information** is available for this paper at <https://doi.org/10.1038/s41598-019-56872-3>.

**Correspondence** and requests for materials should be addressed to A.E. or W.W.

**Reprints and permissions information** is available at [www.nature.com/reprints](http://www.nature.com/reprints).

**Publisher's note** Springer Nature remains neutral with regard to jurisdictional claims in published maps and institutional affiliations.



**Open Access** This article is licensed under a Creative Commons Attribution 4.0 International License, which permits use, sharing, adaptation, distribution and reproduction in any medium or format, as long as you give appropriate credit to the original author(s) and the source, provide a link to the Creative Commons license, and indicate if changes were made. The images or other third party material in this article are included in the article's Creative Commons license, unless indicated otherwise in a credit line to the material. If material is not included in the article's Creative Commons license and your intended use is not permitted by statutory regulation or exceeds the permitted use, you will need to obtain permission directly from the copyright holder. To view a copy of this license, visit <http://creativecommons.org/licenses/by/4.0/>.

© The Author(s) 2020

### 3.1.5 Understanding Dissolution Rates via Continuous Flow Systems with Physiologically Relevant Metal Ion Saturation in Lysosome

**Keller JG**, Peijnenburg W, Werle K, Landsiedel R, Wohlleben W.

*Nanomaterials* 2020, 10(2), 311

<https://doi.org/10.3390/nano10020311>

#### **Abstract:**

Dissolution rates of nanomaterials can be decisive for acute in vivo toxicity (via the released ions) and for biopersistence (of the remaining particles). Continuous flow systems (CFSs) can screen for both aspects, but operational parameters need to be adjusted to the specific physiological compartment, including local metal ion saturation. CFSs have two adjustable parameters: the volume flowrate and the initial particle loading. Here we explore the pulmonary lysosomal dissolution of nanomaterials containing the metals Al, Ba, Zn, Cu over a wide range of volume flowrates in a single experiment. We identify the ratio of particle surface area (SA) per volume flowrate (SA/V) as critical parameter that superimposes all dissolution rates of the same material. Three complementary benchmark materials—ZnO (quick dissolution), TiO<sub>2</sub> (very slow dissolution), and BaSO<sub>4</sub> (partial dissolution)—consistently identify the SA/V range of 0.01 to 0.03 h/μm as predictive for lysosomal pulmonary biodissolution. We then apply the identified method to compare against non-nanoforms of the same substances and test aluminosilicates. For BaSO<sub>4</sub> and TiO<sub>2</sub>, we find high similarity of the dissolution rates of their respective nanoform and non-nanoform, governed by the local ion solubility limit at relevant SA/V ranges. For aluminosilicates, we find high similarity of the dissolution rates of two Kaolin nanoforms but significant dissimilarity against Bentonite despite the similar composition.





Article

# Understanding Dissolution Rates via Continuous Flow Systems with Physiologically Relevant Metal Ion Saturation in Lysosome

Johannes G. Keller <sup>1,2</sup> , Willie Peijnenburg <sup>3,4</sup> , Kai Werle <sup>1</sup>, Robert Landsiedel <sup>1</sup> and Wendel Wohlleben <sup>1,\*</sup>

<sup>1</sup> BASF SE, Dept. Experimental Toxicology and Ecology and Dept. Advanced Materials Research, 67056 Ludwigshafen, Germany; johannes-georg.keller@basf.com (J.G.K.); kai.werle@basf.com (K.W.); robert.landsiedel@basf.com (R.L.)

<sup>2</sup> Institute of Pharmacy, Faculty of Biology, Chemistry & Pharmacy, Freie Universität Berlin, 14195 Berlin, Germany

<sup>3</sup> National Institute of Public Health and the Environment RIVM, 3721 Bilthoven, The Netherlands; willie.peijnenburg@rivm.nl

<sup>4</sup> Institute of Environmental Sciences (CML), Leiden University, 2333 Leiden, The Netherlands

\* Correspondence: wendel.wohlleben@basf.com; Tel.: +49-621-609-5339

Received: 20 December 2019; Accepted: 7 February 2020; Published: 12 February 2020



**Abstract:** Dissolution rates of nanomaterials can be decisive for acute in vivo toxicity (via the released ions) and for biopersistence (of the remaining particles). Continuous flow systems (CFSs) can screen for both aspects, but operational parameters need to be adjusted to the specific physiological compartment, including local metal ion saturation. CFSs have two adjustable parameters: the volume flow-rate and the initial particle loading. Here we explore the pulmonary lysosomal dissolution of nanomaterials containing the metals Al, Ba, Zn, Cu over a wide range of volume flow-rates in a single experiment. We identify the ratio of particle surface area (SA) per volume flow-rate (SA/V) as critical parameter that superimposes all dissolution rates of the same material. Three complementary benchmark materials—ZnO (quick dissolution), TiO<sub>2</sub> (very slow dissolution), and BaSO<sub>4</sub> (partial dissolution)—consistently identify the SA/V range of 0.01 to 0.03 h/μm as predictive for lysosomal pulmonary biodissolution. We then apply the identified method to compare against non-nanoforms of the same substances and test aluminosilicates. For BaSO<sub>4</sub> and TiO<sub>2</sub>, we find high similarity of the dissolution rates of their respective nanoform and non-nanoform, governed by the local ion solubility limit at relevant SA/V ranges. For aluminosilicates, we find high similarity of the dissolution rates of two Kaolin nanoforms but significant dissimilarity against Bentonite despite the similar composition.

**Keywords:** dissolution; dissolution rate; nanomaterial grouping; risk assessment; 3R method; regulatory hazard assessment

## 1. Introduction

With a steadily increasing demand for engineered nanomaterials (ENMs) for industrial applications, the ENM production volumes reported by industry are a significant share of the total particle production [1]. The properties of the nanomaterials are specifically designed for their different intended uses and are therefore varied in surface treatment, composition, size, and morphology. Often one substance exists in many different nanoforms. The vast amount of nanoforms makes it impossible to investigate the risk potential of each individual nanoform [1,2]; therefore, grouping and read across approaches are urgently needed to reduce the uncertainty related to the risk of nanomaterials [3–5]. The nanoform is described through chemical composition, surface properties, size, and shape [6].

However, these properties are insufficient to forecast potential environmental and human health-related hazards and do not take into account the complex mechanism of pulmonary retention, clearance, and translocation that particles are exposed to upon inhalation [7–10]. Thus, the European Chemicals Agency (ECHA) as well as the Environmental Protection Agency (EPA) are prioritizing the dissolution rate as a key criterion for the assessment of the risk potential of nanomaterials [11]. This criterion can then be used to compare different nanoforms of a substance. Nevertheless, it is not sufficient to group the nanomaterials into soluble and insoluble [12] as the dissolution kinetic spans over many orders of magnitude from fast dissolving ENMs such as our benchmark materials ZnO and CuO to poorly soluble materials such as TiO<sub>2</sub> and Fe<sub>2</sub>O<sub>3</sub> [13]. The dissolution rate is measured in ion mass per solid particle surface per time and is designated as  $k$  [ng/cm<sup>2</sup>/h] [14]. In contrast, the solubility is measured in equilibrium saturated suspensions to yield the conventional solubility limit [4]. Low solubility should not be interpreted as a sufficient indication of biopersistence, because the static setup does not represent the conditions that particles are exposed to when being taken up into a physiological system. In comparison to the static system, the physiological system is an open system with both passive and active transport away from the remaining particles. The continuous flow-through system for nanomaterials is currently used for quantifying environmental [15] as well as oral dissolution [14,16] and was adapted from a system used for man-made vitreous fibers (MMVF) [17–19]. One might anticipate that the testing has to be done with a range of initial ENM mass concentrations at the same flow-rate in order to verify that the results are truly not limited by local concentrations reaching the solubility limit. Otherwise, a false negative result of apparently low dissolution rate might occur. The results on MMVF have highlighted that the solubility limit can be avoided by increasing the flow-rate at the same initial mass [20]. However, false positive results of overestimating the physiological ion transport and, hence, overestimating the biodissolution are also imaginable. Continuous flow systems (CFSs) have two adjustable parameters that can be used to prevent false predictions: the volume flow-rate and the initial particle loading. The decisive parameter in MMVF testing was the ratio SA/V of surface area per flow-rate, but this has not been explored yet for nanomaterials.

Here we propose and demonstrate a more efficient alternative to verify predictive conditions by ramping the fluid flow of the continuous flow system at the same initial ENM mass. The ramped flow-rates are applied to a set of nanoforms and non-nanoforms containing the critical metals Al, Ba, Zn, Cu with existing *in vivo* inhalation clearance results [12,21,22] to validate the dissolution results with three different benchmark materials for quickly soluble, soluble, and insoluble with ZnO, BaSO<sub>4</sub>, and TiO<sub>2</sub>, respectively.

## 2. Materials and Methods

The assessment of the dissolution rate of ENMs through flow-rate ramping is a complimenting technique to the current dissolution setup as described in Koltermann-Jüly et al. 2018 and Keller et al. 2020 [14,23]. The continuous flow-system was developed to assess the dissolution far from equilibrium. However, the solubility limit of the tested ENMs requires the tester to run multiple tests with varying initial masses in order to verify that the dissolution is not limited by local concentrations reaching the solubility limit. Therefore, the technique of flow-rate ramping is presented as an advanced technique that can be transferred to all materials and cannot fully be described by measuring at a single initial mass. The fundamentals of this testing methods are described in the next section.

Ten different materials were selected with high industrial relevance. Their basic nanoform descriptors and other properties have been published recently [24] and are reproduced in Table S1. These materials consist of two different kinds of BaSO<sub>4</sub>, one nanosized material provided by the Organization for Economic Co-operation and Development (OECD) sponsorship program and the non-nanosized BaSO<sub>4</sub> IRMM381 as a non-nanosized form provided by the Institute for Reference Materials and Measurement (IRMM), with permission of Solvay [25,26]. CuO was produced by PlasmaChem GmbH, Germany [22]. Furthermore, two kinds of Kaolin IRMM-385 (JRC-IRMM, Geel) and Kaolin (BASF SE, Ludwigshafen) were used, which both differ in size and form and were provided



by the OECD sponsorship program. Additionally, Bentonite NM600 was provided by the OECD sponsorship program. ZnO NM110 and NM111 were kindly provided by the Joint Research Center (JRC) repository of the OECD sponsorship program and differed in their surface coating. ZnO NM111 is used as a benchmark material for a quickly dissolving nanomaterial as per the available inhalation *in vivo* results and has a hydrophobic triethoxycaprylsilane coating [27,28].

### 2.1. Continuous Flow System with Programmable Sampling, ICP-OES or ICP-MS Analysis

The setup (Figure 1) implements a “continuous flow system” described in ISO 19057:2017 [29]. It is essentially a replication of the established flow-through testing of the dissolution kinetics of mineral fibers [19,30], was described for this purpose [31], and was used here with minor adaptations to match the specifics of ENMs: The ENM mass of 1 mg was weighed onto a membrane (cellulose triacetate, Sartorius Stedim Biotech GmbH, Goettingen, Germany): 47 mm diameter, 5 kDa, and a pore size of ~1 nm, topped by another membrane, and enclosed in flow-through cells. Standard conditions are 1 mg initial solid mass in the flow-through cell, and 2 mL/h flow. The phagolysosomal simulant fluid (PSF) pH 4.5 (composition in Table S2), which is an acidic buffer simulating the phagolysosomal compartment of macrophages [31,32], and which was previously validated for the purpose of inhaled beryllium dissolution by National Institute of Standards and Technology (NIST) laboratories [32], was employed at  $37 \pm 0.5$  °C. In contrast to the larger volume flow cells used by Bove et al. for oral dissolution testing [16], in our setup the ENMs were in direct contact with the ultrafiltration membrane. In contrast to the flow cells used by Kent et al., our cells held industrially produced ENMs, not lab-grown arrays of similar chemical composition [15]. The core idea of separating ions from remaining solids was shared by all three setups. The programmable sampler drew 4–10 mL of the eluate once to two times per day for seven days. Depending on the flow-rate (Table 1) the samples were drawn for 3–44 h per sample in order to fill the vials. The rest of the eluate was collected in a container. The ion concentrations of the eluates from different time points were determined by inductively coupled plasma–optical emission spectrometry (ICP-OES Agilent 5100 and Varian 725 ES) with a limit of detection of 0.1 mg/L, or alternatively by inductively coupled plasma–mass spectrometry (ICP-MS Perkin Elmer Nexion 2000b, Perkin Elmer Inc., Waltham, USA) with a limit of detection of 0.1 ppb. Prior to taking the measurement, the instrument was optimized in accordance with the manufacturer’s specification. Duplicate measurements were taken and averaged. We measured with 10 s integration time, and the dilution factors were between 1 and 10. External calibration used concentrations of 0/1/5 mg/L with matrix-matched standards. The nebulizer (Meinhard 1 mL) had a flow of 0.7 L/min at a pump rate of 15 rpm. For ICP-MS, duplicate measurements were taken and averaged. The eluate was diluted with a factor in between 100 and 1000 and the external calibration used concentrations of 0.1/1/10 ppb. The nebulizer had a flow of 0.92 L/min at a pump rate of 35 rpm.

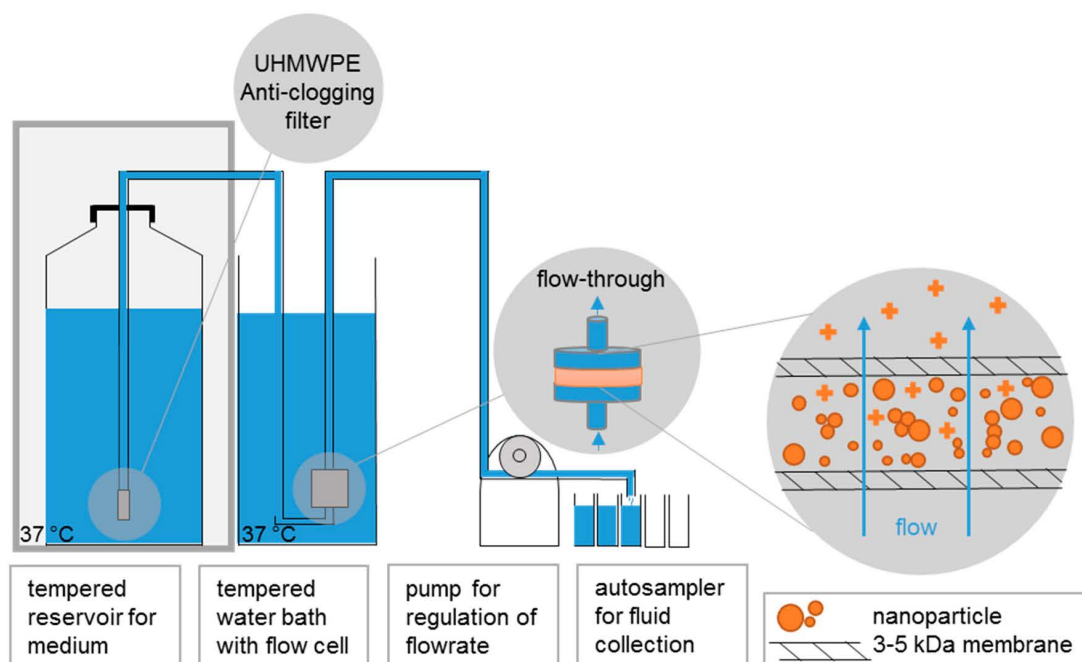


**Figure 1.** Dissolution setup. The reservoir for the physiological fluid was controlled at 37 °C, as well as the flow-through cells. The peristaltic pump regulated the flow-rate of up to eight cells in parallel, with a programmable autosampler for fluid collection. The flow-through cell was equipped with 5 kDa membranes to hold back particles and only allow the flow of ions. The meniscus of the reservoir was elevated approx. 0.5 m above the cells such that the hydrostatic pressure balanced the pressure drop by the 5 kDa membrane.

**Table 1.** Ramped flow-rates in dependence of time. Ramp up describes an increasing flow-rate from 0.1 to 3 mL/h, and ramp down describes a decreasing flow-rate from 3 to 0.1 mL/h.

Sampling Time [h]	Flow-Rate [mL/h]	
	Ramp Up ↑	Ramp Down ↓
24	0.1	3.0
48	0.1	3.0
72	0.2	2.0
84	0.5	2.0
96	0.5	1.0
106	1.0	1.0
120	1.0	0.5
125	2.0	0.5
135	2.0	0.2
147	3.0	0.1
168	3.0	0.1

## 2.2. Continuous Flow System with Ramped Flow-Rates to Ensure Out-Of-Equilibrium Conditions

To further understand the dissolution behavior of nanomaterials, the dissolution conditions were varied in order to ensure non-equilibrium conditions. This was done by varying the flow-rate drastically between 0.1 and 3 mL/h within a single measurement. The precise flow-rates can be seen in Table 1. The flow-rate was gradually changed after either each or every second filled vial. Therefore, the sampling time of a single time point was varied between 3 and 24 h. Besides the varying flow-rate, adjusted through the flow-regulating pump, the measurements were done in accordance to the continuous flow-through system with constant flow-rate. After each run, the ion content was determined through ICP-MS.

There are three ways to express the dissolution rate of the nanoparticles. These three ways have been described in our previous contribution [23], each working best to describe the dissolution mechanism of a certain set of materials and are reproduced here for completeness of methodology. For this purpose, we multiplied the amount of eluate with the ion concentration to determine the total ion mass dissolved, as illustrated for BaSO<sub>4</sub>:

- Cumulative rate: The amount of dissolved BaSO<sub>4</sub> at each time point  $M_{ion}(T)$  is expressed as a fraction of the initial mass loading ( $M_0 = 100\%$ ) and cumulated from all samplings with concentration  $c_i$ , flow  $V_i$ , and sampling interval  $\Delta t_i$ , and includes the stoichiometry of BaSO<sub>4</sub>:

$$\frac{M_{ion}(T)}{M_0} = \frac{m(BaSO_4)}{m(Ba) * M_0} \sum_{i=0}^T c_i(Ba) V_i \Delta t_i, \quad (1)$$

$$k = \frac{M_{ion}(t)}{M_0} \frac{1}{t_{BET}}. \quad (2)$$

The rate  $k$  incorporates the Brunauer–Emmett–Teller (BET) value [33]. The BET method uses adsorption of gases at constant temperature to determine the surface area of particles, in order to report results with a focus on composition or coating dependence, instead of size dependence. The conventional units of  $k$  are ng/cm<sup>2</sup>/h [30,34]. We typically determine  $k$  by the number of cumulated ions during a specific time interval at the end of the test.

- Curve fitting: To verify first-order dissolution kinetics [34], the cumulative dissolved BaSO<sub>4</sub> mass is expressed as an inverse relationship, i.e., decreasing solid retained BaSO<sub>4</sub> mass ( $(M_{ion}(T) - M_0)/M_0$ ), and plotted against time on a semi-log scale. The dissolution rate—expressed as a fraction per hour—is calculated from the slope of this line and then converted to percent per day using the total system's available starting mass. Dissolution rate and half-time ( $t'_{1/2}$ , 50% dissolved) are inversely related and can be expressed in two alternative metrics (below) as given for first-order modeling in ISO 19057:2017 [29,34]. The BaSO<sub>4</sub> dissolution half-time allows direct extrapolation and comparison to the in vivo dissolution  $t_{1/2}$  of inhaled BaSO<sub>4</sub>, which is derived from the total in vivo  $t_{1/2}$ :

$$b_{diss} = \frac{\ln 2}{t'_{1/2}}, \quad (3)$$

$$t'_{1/2} = \frac{\ln 2}{b_{diss}}. \quad (4)$$

- Instantaneous rates: For each sampling interval  $\Delta t$ , the instantaneous dissolution rate  $k$  was constructed as:

$$k(t) = \frac{M_{ion}(t)}{SA(t) \Delta t}, \quad (5)$$

$$SA(t) = BET(t_0)(M_{ion}(t)). \quad (6)$$

We approximated the instantaneous surface area and, thus, ignored changes of the size distribution and shape (see Discussion). Elsewhere [14] we explored modeling of  $SA(t)$  via the assumption of shrinking spheres [29,34], which does not apply for particles with a tendency to undergo morphological transformation processes, such as BaSO<sub>4</sub>.

### 2.3. Terminology of Modeling Nanomaterial Dissolution

In this section, we recapitulate the relationship between the ENM, assumed to be a spherical particle, and the ion concentration. For this, we introduce the following notation:

- $R(T)$ : radius of a particle in cm with  $R_0 = R(0)$
- $v(t) = \frac{4}{3}\pi R^3$ : volume of a particle



- $A(t) = 4\pi R^2$ : area of a particle
- $k$ : rate constant at which particle dissolves in  $\text{ng}/\text{cm}^2/\text{h}$
- $\rho$ : density of particle  $\text{g}/\text{cm}^3$
- $t$ : time in h
- $I(t)$ : ions present in the solution in g
- $m$ : mass of fluid in the flow cell, in g
- $\dot{m}$ : flow of fluid per time, in  $\text{g}/\text{h}$ .

Then when extending the model to a suspension of particles we use

- $C_{NP}(t)$ : concentration of particles at time  $t$  in  $\text{g}/\text{L}$
- $C_{ion}(t)$ : concentration of ions at time  $t$  in  $\text{g}/\text{L}$
- $N_0$ : number of NPs present in the solution per liter at  $t = 0$  in  $1/\text{L}$ .

In this notation, the concentration of particles (NP) and ions are given by

$$C_{NP}(t) = N_0 v(t), \quad (7)$$

$$C_{ion}(t) = N_0 I(t). \quad (8)$$

Due to dissolution, the well-established “shrinking sphere” model [35] links the generation of ions to a reduction of the particle volume:

$$\frac{dC_{NP}}{dt} = N_0 \rho \frac{dv}{dt} = -kAN_0 = -k4\pi R^2 N_0, \quad (9)$$

$$\frac{dC_{ion}}{dt} = N_0 \frac{dI}{dt} = kAN_0 = k4\pi R^2 N_0. \quad (10)$$

### 3. Results

Nine nanomaterials and one particle of bigger size were tested within the flow-through dissolution system with ramped flow-rates. The dissolution of the nanomaterials in phagolysosomal simulant fluid at pH 4.5 with increasing flow-rate was compared against a run with decreasing flow-rate as shown in Figure 2. The blue data points display the ascending flow-rate ramp from 0.1 to 3 mL, whereas orange dots indicate the descending flow-rate from 3 to 0.1 mL/h. Similar time-resolved dissolution curves were obtained for the nanomaterials ZnO NM111 and CuO. Both materials dissolve completely after a time period of 7 days either with the ramp up or the ramp down, considering that the acidic conditions of pH 4.5 are the driving force of this complete dissolution. Both materials could easily be measured with the He kinetic energy discrimination (KED) mode [35,36] of the ICP-MS since their limit of detection (LoD) is rather low, even traces up to 0.01 ppb could be measured. However, despite their similarity, the difference between the ascending and descending curve is significant. Interestingly, the ascending flow-rate forms an S-shaped curve while the descending flow-rate describes a rapid decrease of nanomaterial and after less than 50 h 100% of the nanomaterial is already dissolved. Thus, the descending flow-rate ramp cannot be used to better describe the dissolution for quickly dissolving nanomaterials. At the beginning phase of the ascending flow-through measurement, a high initial mass, which goes along with high surface area is exposed to a low flow-rate, resulting in a slower dissolution. The data points for the ascending flow-rate ramping are spread over a broader distribution of surface area to flow-rate (Figure 3). These graphs also prove that the measurement was done under out-of-equilibrium conditions and the saturation limit of the ions was not reached. Upon reaching saturation, data points are expected to be in a straight line.

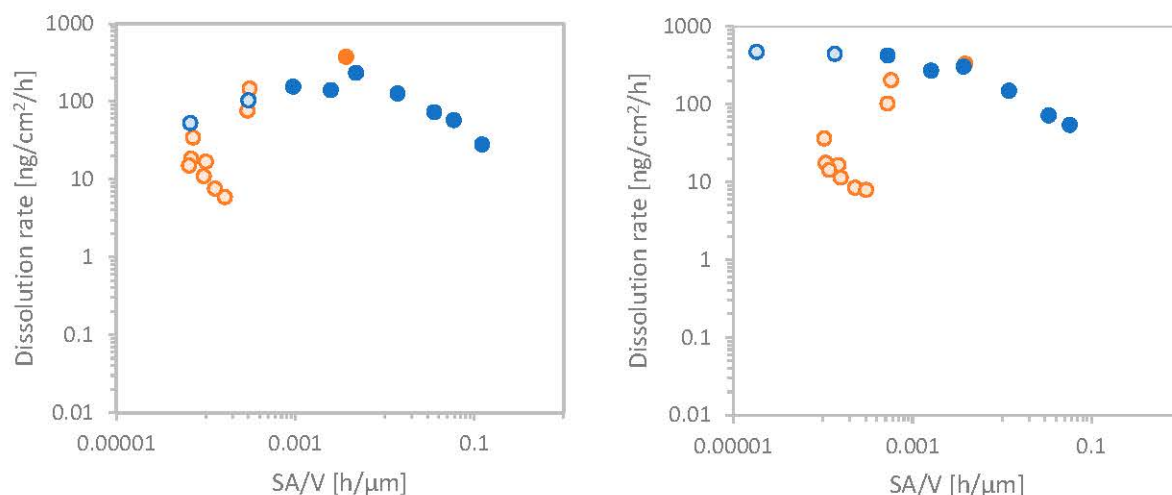


**Figure 2.** Time-resolved dissolution kinetics of CuO (left) and ZnO NM 111 (right). The blue curve indicates the ascending flow-rate ramping, whereas the orange curve indicates a descending flow-rate ramping. Unfilled circles indicate points with remaining mass calculated to be <10%; the corresponding instantaneous rates are equally marked not sufficiently reliable in Figure 3.

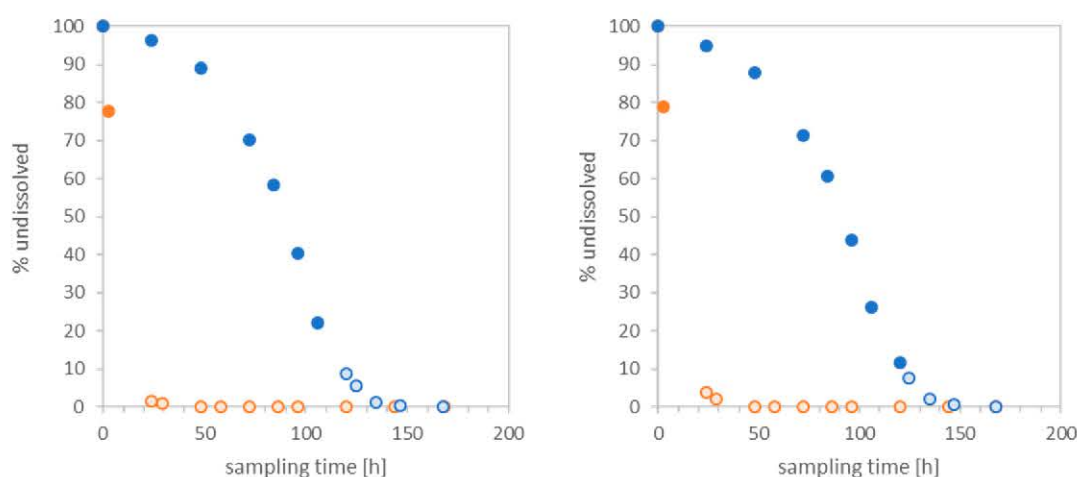


**Figure 3.** Dissolution rate depending on surface area and flow-rate. CuO (left) and ZnO NM111 (right). Blue curve indicates ascending and orange curve descending flow-rate ramping. Unfilled circles indicate points with low reliability due to remaining mass <10%. Note the superimposed orange and blue dots.

The results on the dissolution with ramped flow-rate on two different BaSO<sub>4</sub> particles, BaSO<sub>4</sub> NM220 and BaSO<sub>4</sub> non-nano are displayed in Figure 4. Two initial masses for the ramp down (dashed line) of BaSO<sub>4</sub> NM220 (green) and one for BaSO<sub>4</sub> IRMM381 (yellow) were compared to the ramp up (solid line) for one initial mass of BaSO<sub>4</sub> NM220 and two initial masses of BaSO<sub>4</sub> IRMM381. The graph shows the plot of SA/V versus the dissolution rate  $k$  with dissolution rates that differ by a few orders of magnitude. This difference can be due to the difference in BET, as for instance the nano BaSO<sub>4</sub> possess a 16-fold higher surface area than the non-nano form. Furthermore, this observation is confirmed by the time-resolved dissolution curve as seen on the left-hand side of Figure 4. However, when normalizing the surface area with different initial masses for the ramp up (BaSO<sub>4</sub> NM220 0.11 mg PSF vs. BaSO<sub>4</sub> IRMM381 1.42 mg PSF) as well as for the ramp down (BaSO<sub>4</sub> NM220 0.14 mg PSF vs. BaSO<sub>4</sub> IRMM381 0.86 mg), similar values for the dissolution rate can be observed for the two different nanoforms. Therefore, the results for the increasing flow-rate as well as the results for the static flow-rate do achieve a good predictability for dissolution rates between 0.01 and 0.03 h/μm; whereas the decreasing flow-rate as seen in Figure 4 cannot be applied.

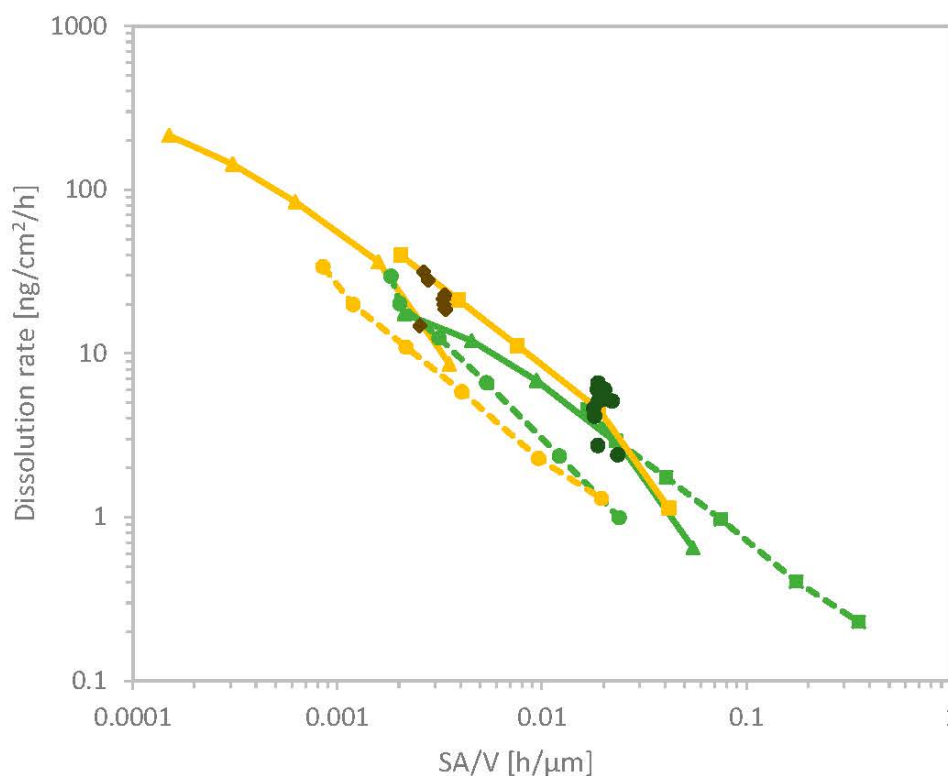


**Figure 4.** Dissolution rate of BaSO<sub>4</sub> NM220 (green) and BaSO<sub>4</sub> IRMM381 (yellow). The SA/V is plotted against the dissolution rate  $k$  [ng/cm<sup>2</sup>/h]. The dashed line indicates the ramp down with decreasing flow-rate 3–0.1 mL/h and the solid line represents the ramp up with increasing flow-rate from 0.1 to 3 mL/h. The two different dashed green curves vary in initial mass. The dashed green curve with the square has an initial mass of 1.01 mg, whereas the curve with the round symbol has an initial mass of 0.14 mg. The two yellow solid curves vary from 1.42 mg initial mass for the square to 0.12 mg for the triangle. Both darker spots represent the dissolution rate for the dynamic dissolution with constant flow-rate for nano BaSO<sub>4</sub> NM220 yellow and BaSO<sub>4</sub> IRMM381 dark green.

The consistency between the instantaneous dissolution rates determined with fixed flow vs. ramped (increasing) flow has been assessed for BaSO<sub>4</sub> NM220, CuO, ZnO NM110, and ZnO NM111, and the results in the SI (Figure S4) demonstrate a) that the rule of 10% remaining mass successfully removes unreliable data and b) that the ramped flow enlarges the range of SA/V that is accessible in a single measurement. Data below 10% remaining mass are considered unreliable since weighing in 1 mg of ENM into the flow-through cell always induces uncertainties. Furthermore, by calculating the dissolved fraction for quickly dissolving materials, often no ions can be detected anymore even though dissolution has not reached 100% yet.

The apparent inverse linear relationship between the dissolution rate and SA/V was found for BaSO<sub>4</sub> NM220 before [23], but the new finding that this behavior extends to the non-nanoform and across a wide range of volume flow-rates (Figure 4) deserves a mechanistic understanding. Here we develop a model of partial and very slow dissolution in the continuous flow system, where a fraction of the fluid mass  $\dot{m}/m$  is exchanged during each time interval. To represent the influence of saturation,  $f(C_{ion})$  is a function that decays to zero at the ion solubility limit, and  $f(0) = 1$ :

$$\frac{dC_{ion}}{dt} = N_0 \frac{dI}{dt} = 4k\pi R(t)^2 N_0 f(C_{ion}). \quad (11)$$

Compared to Equation (9), the saturation term in Equation (11) limits the ion concentration, where the curve shape of  $f(C_{ion})$  of course depends on substance and medium. Importantly, the flow



introduces an additional loss term to the ions (not to the particles, due to the ultrafiltration membrane!), leading from Equation (11) to Equation (12):

$$\frac{dC_{ion}}{dt} = N_0 \frac{dI}{dt} - N_0 I \frac{\dot{m}}{m} = 4k\pi R(t)^2 N_0 f(C_{ion}) - N_0 I \frac{\dot{m}}{m}. \quad (12)$$

This assumes that the ion concentration is homogeneous in the volume of the flow cell. We can now introduce the experimental observation that, for partial and very slow dissolution, the concentration of ions  $C_{ion}$  does not change over time:  $\frac{dC_{ion}}{dt} = 0$ , and obtain:

$$I \frac{\dot{m}}{m} N_0 = 4k\pi R(t)^2 N_0 f(C_{ion}). \quad (13)$$

Using the notation from MMVF literature  $SA(t) := 4\pi R(t)^2$  and the volume flow-rate  $V_{fluid} := \dot{m} / \rho_{fluid}$  this expression transforms to

$$I \frac{\rho_{fluid} V}{m} = k SA(t) f(C_{ion}). \quad (14)$$

Solving for  $k$ , and simplifying  $C_{ion} = I \frac{\rho_{fluid}}{m}$ , we obtain

$$k = \frac{C_{ion}}{f(C_{ion})} \frac{V}{SA(t)}. \quad (15)$$

Hence the measured  $k$  is reduced by saturation and is inversely proportional to the SA/V ratio with:

$$k \propto \frac{1}{SA/V}. \quad (16)$$

As a next step, we explored whether this universal relationship applies to partial and very slow dissolution of substances other than  $BaSO_4$ . In total, 15 different flow-through dissolution measurements with an increasing flow-rate were conducted and combined within Figure 5. The dissolution rate of the quickly dissolving benchmark materials, CuO as well as three different kinds of ZnO were compared with moderately soluble Kaolin, Bentonite,  $BaSO_4$ , and insoluble nanoforms of  $TiO_2$  NM105 and food grade non-nano  $TiO_2$  E171. This graph especially shows that there is a significant difference of the dissolution rate between the quickly dissolving nanoforms of ZnO and CuO and the moderately soluble nanomaterials. All quickly dissolving materials exhibited an almost horizontal line in the graph which represents a continuous dissolution rate, which is not dependent on the surface area of the nanomaterial. Nevertheless, ZnO NM110 shows a significantly slower dissolution for certain flow-rates and therefore high SA/V values must be excluded. The graph shows that even quickly dissolving materials such as ZnO can show dissolution rates below  $100 \text{ ng/cm}^2/\text{h}$  if the dissolution is tested at SA/V values below  $0.1 \text{ h}/\mu\text{m}$ . However, the plot additionally shows diagonal curves for  $BaSO_4$  NM220,  $BaSO_4$  IRMM381, Kaolin JRC-IRMM385, Kaolin, and Bentonite.



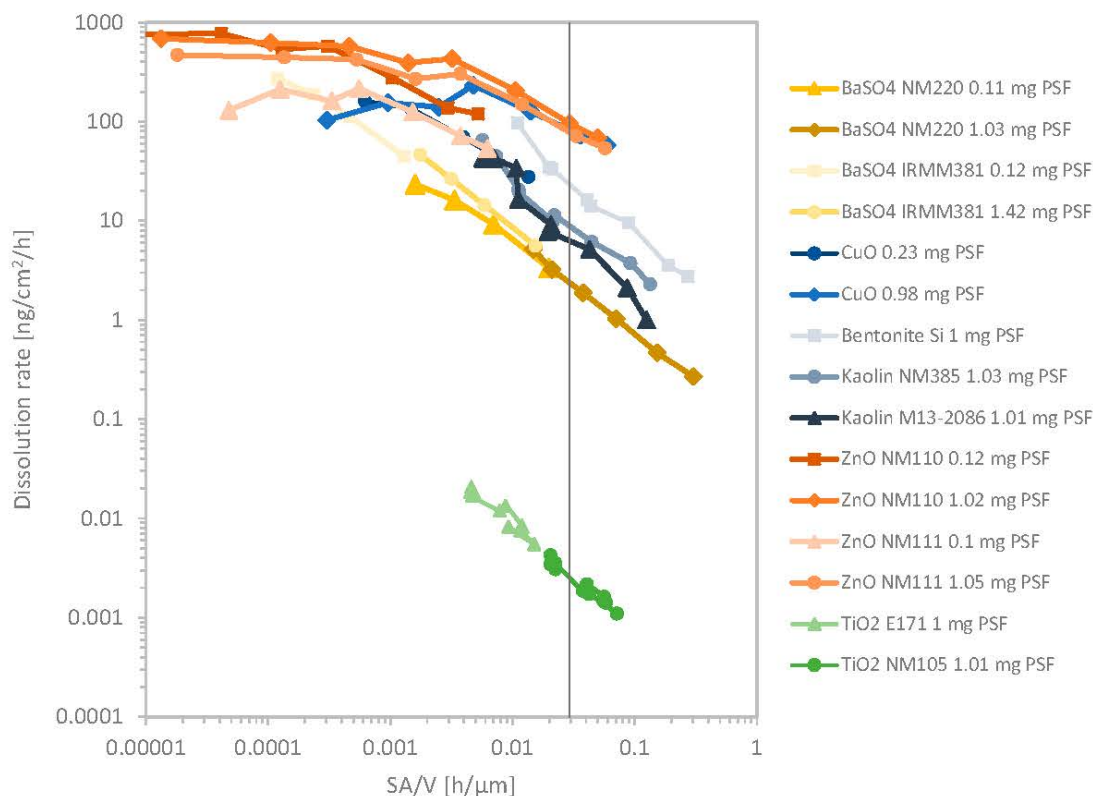


**Figure 5.** Cumulated SA/V plot vs. dissolution rate  $k$  [ $\text{ng}/\text{cm}^2/\text{h}$ ] of 10 different tested nanomaterials in 15 different runs with varying initial masses. The dots of each run are connected through a line with each other for visualization purpose only. The family of  $\text{TiO}_2$  (nano)forms is displayed in green,  $\text{BaSO}_4$  (nano)forms in yellow,  $\text{CuO}$  in blue,  $\text{ZnO}$  in shades of orange, and aluminosilicates Bentonite and Kaolin in grey. The vertical line displays the optimum SA/V.

Both materials,  $\text{ZnO}$  NM110 and the surface-treated  $\text{ZnO}$  NM111 exhibited a similar dissolution process. Therefore, a significant impact of the hydrophobic triethoxycaprylsilane coating could not be observed. Furthermore, Bentonite as well as both Kaolin materials showed a similar dissolution behavior with a diagonal line in the SA/V vs.  $k$  plot. The comparison of different dissolution rates of aluminosilicates depending on the analyzed ion is shown in Figure S3. The graphs S3A–C confirm the hypothesis that Si dissolves more readily than Al, with a factor of 100 between the respective dissolution rates. Therefore, the dissolution of Al is the rate-limiting step in the dissolution kinetics of aluminosilicates.

The two insoluble materials,  $\text{TiO}_2$  E171 and  $\text{TiO}_2$  NM105, furthermore show a diagonal slope in Figure 5 just like the other partially soluble materials. This behavior is understood and explained in the previous mentioned equations. However, when both  $\text{TiO}_2$  particles were tested at low SA/V values below  $0.001 \text{ h}/\mu\text{m}$  false positive predictivities were observed which are not in agreement with observations made in *in vivo* studies [37], nor other previous dissolution experiments. Therefore, for the test, the flow-rate must be adjusted to keep SA/V above  $0.001 \text{ h}/\mu\text{m}$ . The quickly soluble ENMs,  $\text{CuO}$  and  $\text{ZnO}$ , exhibited horizontal lines within the SA/V against  $k$  plot at low SA/V ratios below  $0.001 \text{ h}/\mu\text{m}$ .

Both flow-rate operation modes (fixed and ramped) are compared against each (Figure S4). Here similar initial masses of  $\text{BaSO}_4$  NM220,  $\text{CuO}$ ,  $\text{ZnO}$  NM110, and  $\text{ZnO}$  NM111 were measured for both models. The flow-rate ramp with increasing flow increases the spread of the data points more than done by the fixed flow. This results in better spread data points of the dissolution. This characteristic can be best observed for  $\text{BaSO}_4$  NM220 in Figure S4A, where a cloud of data points is achieved through fixed flow-rate dissolution.

#### 4.2. Method

The modeling was based on the well-known “shrinking sphere” assumption [34], but added a loss term of ion transport through the ultrafiltration membrane of the flow cell, and added a saturation limit of ion concentration. The model provided an analytical basis (Equation 16) for the inverse linear relationship between  $k$  and  $SA/V$  that was observed for all materials ( $BaSO_4$  (nano and non-nano),  $TiO_2$  (nano and non-nano), Bentonite, Kaolin) as soon as saturation contributes:

- The model confirms that the prefactor is specific to the solubility limit of the ions in the medium, but independent of the size  $R$  of the particles.
- The model confirms that the slope of the inverse relationship to  $SA/V$  is universal for all substances, all sizes thereof, and all medium compositions. This aspect is proven here with experimental data on pulmonary lysosomal dissolution but is predicted as well for gastro-intestinal dissolution.

The screening of the different flow-rates within the dynamic flow-through dissolution setup with ramped flow-rates shows that flow-rates can be adapted in order to optimize the predictivity of the dissolution of nanomaterials. The advancements of the ramped flow-rate compared to the fixed flow-rate are clearly visible for  $BaSO_4$  NM220 (Figure S4A). Here the fixed flow-rate leads to a cloud of datapoints, whereas through the ramped flow the datapoints are more widespread, which leads to a better understanding of the dissolution mechanism. This observation was also made for both ZnO NM110 and NM111. Especially for these two quickly dissolving materials, an improvement of the datapoints could be achieved. Nevertheless, this increase is not as significant for the fast dissolving ENM CuO (Figure S4B).

The aim of this setup was to match the dissolution rate of nanomaterials with the clearance measured within in vivo systems. Thus, through increasing or decreasing the flow-rate by a factor of 100 the dissolution kinetics can be matched with the clearance in the rat lung. Though we observed false predictivities for some flow-rates (Figure 5), there were some flow-rates which led to a slower dissolution for ZnO nanoparticles but furthermore also to an increased dissolution of  $TiO_2$ . These false predictivities can be excluded by sticking to a certain  $SA/V$  range between 0.01 and 0.03  $h/\mu m$ . Within this  $SA/V$  range (Figure 5), the predicted biodissolution matches existing in vivo expectations: ZnO is cleared from lungs within days, whereas clearance of  $TiO_2$  is dominated by physical transport, not by dissolution [14,22,28]. For  $BaSO_4$  NM220, the relatively fast in vivo clearance with half-time of 9.6 days was attributed to partial dissolution with 11.1 days half-time [23,50]. With the BET of NM220, this half-time corresponds to  $k = 6.3 \text{ ng/cm}^2/\text{h}$ , which is obtained at  $SA/V = 0.02 \text{ h}/\mu m$  (Figure 5). We thus recommend the  $SA/V$  range of 0.01–0.03  $h/\mu m$  for optimal predictivity of biopersistence under pulmonary lysosomal conditions. This value is consistent with all benchmark materials.

However, based on the results seen in Figure 2, the ramp with decreasing flow-rate is not suitable for quickly dissolving materials and of limited reliability for the case of partially dissolving materials such as both  $BaSO_4$  (nano)forms.

Even though the flow-through system is an advanced system for the analysis of the dissolution of nanomaterials there are still some drawbacks which could not be fixed until now. One of the major reasons of measurement uncertainties of quickly dissolving ENMs is the void volume of the flow-through cell. The cell consists of three different stages which are separated from each other through two 5 kDa membranes, the dissolution happens in stage two, where the medium interacts with the ENM. After dissolution the ions penetrate the membrane into stage three and are then transported away and sampled into vials. However, the first 3 mL of the measurement that are sampled into the vials are part of the void volume of the system and did not interacted with the nanomaterials yet. Therefore, these measurements can be discarded. Thus, in order to minimize errors, only samples after at least a volume exchange by a factor of two are used for calculations.

Another reason for uncertainty arises from the interpolation of the remaining solids. Even though we created two different calculation systems for the dissolution process (“shrinking spheres” and “vanishing particles”) the dissolution of an ENM cannot fully be described by either one of



#### 4.2. Method

The modeling was based on the well-known “shrinking sphere” assumption [34], but added a loss term of ion transport through the ultrafiltration membrane of the flow cell, and added a saturation limit of ion concentration. The model provided an analytical basis (Equation 16) for the inverse linear relationship between  $k$  and  $SA/V$  that was observed for all materials ( $BaSO_4$  (nano and non-nano),  $TiO_2$  (nano and non-nano), Bentonite, Kaolin) as soon as saturation contributes:

- The model confirms that the prefactor is specific to the solubility limit of the ions in the medium, but independent of the size  $R$  of the particles.
- The model confirms that the slope of the inverse relationship to  $SA/V$  is universal for all substances, all sizes thereof, and all medium compositions. This aspect is proven here with experimental data on pulmonary lysosomal dissolution but is predicted as well for gastro-intestinal dissolution.

The screening of the different flow-rates within the dynamic flow-through dissolution setup with ramped flow-rates shows that flow-rates can be adapted in order to optimize the predictivity of the dissolution of nanomaterials. The advancements of the ramped flow-rate compared to the fixed flow-rate are clearly visible for  $BaSO_4$  NM220 (Figure S4A). Here the fixed flow-rate leads to a cloud of datapoints, whereas through the ramped flow the datapoints are more widespread, which leads to a better understanding of the dissolution mechanism. This observation was also made for both  $ZnO$  NM110 and NM111. Especially for these two quickly dissolving materials, an improvement of the datapoints could be achieved. Nevertheless, this increase is not as significant for the fast dissolving ENM  $CuO$  (Figure S4B).

The aim of this setup was to match the dissolution rate of nanomaterials with the clearance measured within *in vivo* systems. Thus, through increasing or decreasing the flow-rate by a factor of 100 the dissolution kinetics can be matched with the clearance in the rat lung. Though we observed false predictivities for some flow-rates (Figure 5), there were some flow-rates which led to a slower dissolution for  $ZnO$  nanoparticles but furthermore also to an increased dissolution of  $TiO_2$ . These false predictivities can be excluded by sticking to a certain  $SA/V$  range between 0.01 and 0.03  $h/\mu m$ . Within this  $SA/V$  range (Figure 5), the predicted biodissolution matches existing *in vivo* expectations:  $ZnO$  is cleared from lungs within days, whereas clearance of  $TiO_2$  is dominated by physical transport, not by dissolution [14,22,28]. For  $BaSO_4$  NM220, the relatively fast *in vivo* clearance with half-time of 9.6 days was attributed to partial dissolution with 11.1 days half-time [23,50]. With the BET of NM220, this half-time corresponds to  $k = 6.3$   $ng/cm^2/h$ , which is obtained at  $SA/V = 0.02$   $h/\mu m$  (Figure 5). We thus recommend the  $SA/V$  range of 0.01–0.03  $h/\mu m$  for optimal predictivity of biopersistence under pulmonary lysosomal conditions. This value is consistent with all benchmark materials.

However, based on the results seen in Figure 2, the ramp with decreasing flow-rate is not suitable for quickly dissolving materials and of limited reliability for the case of partially dissolving materials such as both  $BaSO_4$  (nano)forms.

Even though the flow-through system is an advanced system for the analysis of the dissolution of nanomaterials there are still some drawbacks which could not be fixed until now. One of the major reasons of measurement uncertainties of quickly dissolving ENMs is the void volume of the flow-through cell. The cell consists of three different stages which are separated from each other through two 5 kDa membranes, the dissolution happens in stage two, where the medium interacts with the ENM. After dissolution the ions penetrate the membrane into stage three and are then transported away and sampled into vials. However, the first 3 mL of the measurement that are sampled into the vials are part of the void volume of the system and did not interacted with the nanomaterials yet. Therefore, these measurements can be discarded. Thus, in order to minimize errors, only samples after at least a volume exchange by a factor of two are used for calculations.

Another reason for uncertainty arises from the interpolation of the remaining solids. Even though we created two different calculation systems for the dissolution process (“shrinking spheres” and “vanishing particles”) the dissolution of an ENM cannot fully be described by either one of

these processes but might also be influenced by a combination of both scenarios. This calculation influences both the dissolution rate as well as the remaining mass. With decreasing remaining solid and increasing flow-rate the dissolution-rate,  $k$  increases significantly. This increase does not represent the median dissolution-rate and is often 2–4 times higher. Therefore, values with soluble ENMs with less than 10% remaining solid at any point in time were discarded and neither used for plots nor for further calculations.

## 5. Conclusions

Ramping the flow-rate is a promising approach to expand the range of regular out-of-equilibrium flow-through dissolution to nearly five orders of magnitude of the decisive parameter  $SA/V$ , which is the ratio of surface area and volume flow. This is especially relevant for slowly or partially dissolving ENM where the dissolution can be limited by saturation conditions. A model predicted a universal scaling of dissolution rates with  $SA/V$  and was confirmed by data on ENM dissolving to Al, Zn, Cu, Ba, Ti ions. The ramping allows the operator to investigate the dissolution properties within one single run and one initial mass which usually needs two to three different masses to fully describe the dissolution. The ramp with *increasing* flow-rate is useful as a screening tool for quickly dissolving ENMs because the wide range of flow-rates produces more relevant data points before complete dissolution compared to flow-through dissolution with fixed flow. The proposed benchmark materials for quick dissolution under acidic conditions—CuO, ZnO NM110—and the benchmark for very slow dissolution—TiO<sub>2</sub> E171 and NM105—are confirmed as suitable benchmark materials, and are decisive to identify appropriate ranges of fluid flow velocities ( $V$ ) and  $SA/V$  ratios: Extremes of  $SA/V$  below 0.001 h/ $\mu\text{m}$  or above 0.1 h/ $\mu\text{m}$  are excluded by the calibration of the predicted biopersistence against the in vivo observed pulmonary biopersistence. The additional case of the partially dissolving material, BaSO<sub>4</sub>, allowed us to recommend the range 0.01–0.03 h/ $\mu\text{m}$  for optimal predictivity of biopersistence under pulmonary lysosomal conditions.

For the cases studied here, TiO<sub>2</sub> and BaSO<sub>4</sub>, the nanoform and the non-nanoform had the same dissolution rate normalized to the specific surface area. For Kaolin, different nanoforms of the same substance had the same dissolution rate. For all aluminosilicates, significantly faster leaching of Si than of Al was observed, leading to the prediction of crystalline structure transformation, and faster release of ions from Bentonite than from Kaolin. The diagonal, in the  $k$  vs ( $SA/V$ ) plot, as reported earlier for BaSO<sub>4</sub> NM220 [50], is not a unique phenomenon but is observed for all materials with partial dissolution limited by local ion solubility limits, even for (nano)forms of TiO<sub>2</sub>. The specific rates of the BaSO<sub>4</sub> NM220 nanoform were also observed for the non-nanoform BaSO<sub>4</sub> IRMM381. The dissolution of both materials is therefore governed by the same mechanism and by the same solubility limit.

**Supplementary Materials:** The following materials are available online at <http://www.mdpi.com/2079-4991/10/2/311/s1>: Table S1: Descriptors and properties of tested engineered nanomaterials. Reproduced from Wohleben et al. (Nanoscale, 2019). Table S2: Chemical composition of phagolysosomal simulant fluid (PSF) as reproduced from Keller et al. (Sci. Rep., 2020). Figure S3: Dissolution kinetic of three different Aluminosilicates. Grey indicates the dissolution of Si ions, whereas red indicates the dissolution kinetic of Al ions. Bentonite NM600, Kaolin JRC-IRMM385, and Kaolin 1 in Figure S3A–C respectively. Figure S4: Comparison of  $SA/V$  vs. dissolution rate  $k$  between the fixed flow-rate dissolution setup (orange) and the ramped flow-rate dissolution setup (blue) for **A** BaSO<sub>4</sub> NM220, **B** CuO, **C** ZnO NM110, and **D** ZnO NM111. Unfilled circles indicate points with low reliability due to remaining mass <10%.

**Author Contributions:** K.W. and J.G.K. performed ramped flow-through dissolution; J.G.K. performed ICP-MS measurements; W.P. created the Peijnenburg model; R.L. contributed to the interpretation of results; for W.W. excogitated and supervised the project, furthermore he contributed to the interpretation of the results. All authors have read and agreed to the published version of the manuscript.

**Funding:** This project has received funding from the European Union's Horizon 2020 research and innovation program under grant agreement no. 760840.

**Conflicts of Interest:** J.G.K., W.W., R.L., and K.W. are employees of BASF SE, a company manufacturing nanomaterials.



## References

1. Ministère de l'Environnement. *Éléments Issus des Déclarations des Substances à L'état Nanoparticulaire*; Exercice 2015; Ministère de l'Environnement: Paris, France, 2015.
2. Wohlleben, W.; Punckt, C.; Aghassi-Hagmann, J.; Siebers, F.; Menzel, F.; Esken, D.; Drexel, C.P.; Zoz, H.; Benz, H.U.; Weier, A. Nanoenabled Products: Categories, Manufacture, and Applications. *Metrolog. Stand. Nanotechnol. Protoc. Ind. Innov.* **2017**, *409–464*. [[CrossRef](#)]
3. Arts, J.H.; Hadi, M.; Keene, A.M.; Kreiling, R.; Lyon, D.; Maier, M.; Michel, K.; Petry, T.; Sauer, U.G.; Warheit, D.; et al. A critical appraisal of existing concepts for the grouping of nanomaterials. *Regul. Toxicol. Pharm.* **2014**, *70*, 492–506. [[CrossRef](#)] [[PubMed](#)]
4. Arts, J.H.E.; Hadi, M.; Irfan, M.-A.; Keene, A.M.; Kreiling, R.; Lyon, D.; Maier, M.; Michel, K.; Petry, T.; Sauer, U.G.; et al. A decision-making framework for the grouping and testing of nanomaterials (DF4nanoGrouping). *Regul. Toxicol. Pharmacol.* **2015**, *71*, S1–S27. [[CrossRef](#)] [[PubMed](#)]
5. Oomen, A.G.; Bleeker, E.A.; Bos, P.M.; van Broekhuizen, F.; Gottardo, S.; Groenewold, M.; Hristozov, D.; Hund-Rinke, K.; Irfan, M.-A.; Marcomini, A. Grouping and read-across approaches for risk assessment of nanomaterials. *Int. J. Environ. Res. Public Health* **2015**, *12*, 13415–13434. [[CrossRef](#)] [[PubMed](#)]
6. Commission, E. Commission Regulation (EU) 2018/1881 of 3 December 2018 amending Regulation (EC) No 1907/2006 of the European Parliament and of the Council on the Registration, Evaluation, Authorisation and Restriction of Chemicals (REACH) as regards Annexes I, III, VI, VII, VIII, IX, X, XI, and XII to address nanoforms of substances. *Comm. Regul. (EU) 2018/1881* **2018**, *308*, 1–20.
7. Oberdörster, G. Lung clearance of inhaled insoluble and soluble particles. *J. Aerosol Med.* **1988**, *1*, 289–330. [[CrossRef](#)]
8. Ferin, J. Pulmonary retention and clearance of particles. *Toxicol. Lett.* **1994**, *72*, 121–125. [[CrossRef](#)]
9. Oberdörster, G.; Ferin, J.; Gelein, R.; Soderholm, S.C.; Finkelstein, J. Role of the Alveolar Macrophage in Lung Injury—Studies with Ultrafine Particles. *Environ. Health Perspect.* **1992**, *97*, 193–199.
10. Ferin, J.; Oberdörster, G.; Penney, D.P. Pulmonary retention of ultrafine and fine particles in rats. *Am. J. Respir. Cell Mol. Biol.* **1992**, *6*, 535–542. [[CrossRef](#)]
11. ECHA. *Appendix for Nanoforms Applicable to the Guidance on Registration and Substance Identification*; ECHA: Helsinki, Finland, 2019.
12. Oberdörster, G.; Kuhlbusch, T.A.J. In vivo effects: Methodologies and biokinetics of inhaled nanomaterials. *NanoImpact* **2018**, *10*, 38–60. [[CrossRef](#)]
13. Koltermann-Jüly, J.; Keller, J.G.; Vennemann, A.; Werle, K.; Müller, P.; Ma-Hock, L.; Landsiedel, R.; Wiemann, M.; Wohlleben, W. Addendum to “Abiotic dissolution rates of 24 (nano)forms of 6 substances compared to macrophage-assisted dissolution and in vivo pulmonary clearance: Grouping by biodissolution and transformation” [NanoImpact 2018, 12, 29–41]. *NanoImpact* **2019**, 100154. [[CrossRef](#)]
14. Koltermann-Jüly, J.; Keller, J.G.; Vennemann, A.; Werle, K.; Müller, P.; Ma-Hock, L.; Landsiedel, R.; Wiemann, M.; Wohlleben, W. Abiotic dissolution rates of 24 (nano)forms of 6 substances compared to macrophage-assisted dissolution and in vivo pulmonary clearance: Grouping by biodissolution and transformation. *NanoImpact* **2018**, *12*, 29–41. [[CrossRef](#)]
15. Kent, R.D.; Vikesland, P.J. Dissolution and Persistence of Copper-Based Nanomaterials in Undersaturated Solutions with Respect to Cupric Solid Phases. *Environ. Sci. Technol.* **2016**, *50*, 6772–6781. [[CrossRef](#)] [[PubMed](#)]
16. Bove, P.; Malvindi, M.A.; Kote, S.S.; Bertorelli, R.; Summa, M.; Sabella, S. Dissolution test for risk assessment of nanoparticles: A pilot study. *Nanoscale* **2017**, *9*, 6315–6326. [[CrossRef](#)]
17. International Agency for Research on Cancer (IARC). *Man-made Mineral Fibres and Radon*; World Health Organization: Lyon, France, 1988.
18. Donaldson, K. Biological activity of respirable industrial fibres treated to mimic residence in the lung. *Toxicol. Lett.* **1994**, *72*, 299–305. [[CrossRef](#)]
19. Guldberg, M.; Christensen, V.R.; Krøis, W.; Sebastian, K. Method for determining in-vitro dissolution rates of man-made vitreous fibres. *Glass Sci. Technol.* **1995**, *68*, 181–187.
20. Thelohan, S.; De Meringo, A. In vitro dynamic solubility test: Influence of various parameters. *Environ. Health Perspect.* **1994**, *102*, 91.

21. Landsiedel, R.; Sauer, U.G.; Ma-Hock, L.; Schnekenburger, J.; Wiemann, M. Pulmonary toxicity of nanomaterials: A critical comparison of published *in vitro* assays with *in vivo* inhalation or instillation studies. *Nanomedicine* **2014**, *9*, 2557–2585. [[CrossRef](#)]
22. Gosens, I.; Cassee, F.R.; Zanella, M.; Manodori, L.; Brunelli, A.; Costa, A.L.; Bokkers, B.G.H.; de Jong, W.H.; Brown, D.; Hristozov, D.; et al. Organ burden and pulmonary toxicity of nano-sized copper (II) oxide particles after short-term inhalation exposure. *Nanotoxicology* **2016**, *10*, 1084–1095. [[CrossRef](#)]
23. Keller, J.G.; Graham, U.M.; Koltermann-Jüly, J.; Gelein, R.; Ma-Hock, L.; Landsiedel, R.; Wiemann, M.; Oberdörster, G.; Elder, A.; Wohlleben, W. Predicting dissolution and transformation of inhaled nanoparticles in the lung using abiotic flow cells: The case of barium sulfate. *Sci. Rep.* **2020**, *10*, 458. [[CrossRef](#)]
24. Wohlleben, W.; Hellack, B.; Nickel, C.; Herrchen, M.; Hund-Rinke, K.; Kettler, K.; Riebeling, C.; Haase, A.; Funk, B.; Kühnel, D. The nanoGRAVUR framework to group (nano) materials for their occupational, consumer, environmental risks based on a harmonized set of material properties, applied to 34 case studies. *Nanoscale* **2019**, *11*, 17637–17654. [[CrossRef](#)] [[PubMed](#)]
25. Babick, F.; Mielke, J.; Wohlleben, W.; Weigel, S.; Hodoroaba, V.-D. How reliably can a material be classified as a nanomaterial? Available particle-sizing techniques at work. *J. Nanoparticle Res.* **2016**, *18*, 158. [[CrossRef](#)] [[PubMed](#)]
26. Wohlleben, W.; Mielke, J.; Bianchin, A.; Ghanem, A.; Freiberger, H.; Rauscher, H.; Gemeinert, M.; Hodoroaba, V.-D. Reliable nanomaterial classification of powders using the volume-specific surface area method. *J. Nanoparticle Res.* **2017**, *19*, 61. [[CrossRef](#)] [[PubMed](#)]
27. Arts, J.H.; Irfan, M.-A.; Keene, A.M.; Kreiling, R.; Lyon, D.; Maier, M.; Michel, K.; Neubauer, N.; Petry, T.; Sauer, U.G. Case studies putting the decision-making framework for the grouping and testing of nanomaterials (DF4nanoGrouping) into practice. *Regul. Toxicol. Pharmacol.* **2016**, *76*, 234–261. [[CrossRef](#)] [[PubMed](#)]
28. Landsiedel, R.; Ma-Hock, L.; van Ravenzwaay, B.; Schulz, M.; Wiench, K.; Champ, S.; Schulte, S.; Wohlleben, W.; Oesch, F. Gene toxicity studies on titanium dioxide and zinc oxide nanomaterials used for UV-protection in cosmetic formulations. *Nanotoxicology* **2010**, *4*, 364–381. [[CrossRef](#)]
29. ISO/TR19057. *Nanotechnologies—Use and Application of Acellular in Vitro Tests and Methodologies to Assess Nanomaterial Biodurability*; ISO/TR, 19057; International Organisation for Standardization: Geneva, Switzerland, 2007.
30. International Agency for Research on Cancer (IARC). *Man-Made Vitreous Fibres*; World Health Organization: Lyon France, 2002; pp. 1–433.
31. Wohlleben, W.; Waindok, H.; Daumann, B.; Werle, K.; Drum, M.; Egenolf, H. Composition, Respirable Fraction and Dissolution Rate of 24 Stone Wool MMVF with their Binder. *Part. Fibre Toxicol.* **2017**, *14*, 29. [[CrossRef](#)]
32. Stefaniak, A.B.; Guilmette, R.A.; Day, G.A.; Hoover, M.D.; Breyse, P.N.; Scripsick, R.C. Characterization of phagolysosomal simulant fluid for study of beryllium aerosol particle dissolution. *Toxicol. In Vitro* **2005**, *19*, 123–134. [[CrossRef](#)]
33. Naderi, M. Surface Area: Brunauer–Emmett–Teller (BET). In *Progress in Filtration and Separation*; Elsevier: London, UK, 2015; pp. 585–608.
34. Utembe, W.; Potgieter, K.; Stefaniak, A.B.; Gulumian, M. Dissolution and biodurability: Important parameters needed for risk assessment of nanomaterials. *Part. Fibre Toxicol.* **2015**, *12*, 11. [[CrossRef](#)]
35. Yamada, N. Kinetic energy discrimination in collision/reaction cell ICP-MS: Theoretical review of principles and limitations. *Spectrochim. Acta Part B At. Spectrosc.* **2015**, *110*, 31–44. [[CrossRef](#)]
36. Hattendorf, B.; Günther, D. Suppression of in-cell generated interferences in a reaction cell ICP-MS by bandpass tuning and kinetic energy discrimination. *J. Anal. At. Spectrom.* **2004**, *19*, 600–606. [[CrossRef](#)]
37. Cullen, R.T.; Tran, C.L.; Buchanan, D.; Davis, J.M.G.; Searl, A.; Jones, A.D.; Donaldson, K. Inhalation of Poorly Soluble Particles. I. Differences In Inflammatory Response and Clearance During Exposure. *Inhal. Toxicol.* **2000**, *12*, 1089–1111. [[CrossRef](#)] [[PubMed](#)]
38. Landsiedel, R.; Ma-Hock, L.; Kroll, A.; Hahn, D.; Schnekenburger, J.; Wiench, K.; Wohlleben, W. Testing metal-oxide nanomaterials for human safety. *Adv.Mater.* **2010**, *22*, 2601–2627. [[CrossRef](#)] [[PubMed](#)]
39. Warheit, D.B.; Donner, E.M. Risk assessment strategies for nanoscale and fine-sized titanium dioxide particles: Recognizing hazard and exposure issues. *Food Chem. Toxicol.* **2015**, *85*, 138–147. [[CrossRef](#)] [[PubMed](#)]



- study of titanium dioxide nanoparticles with a primary particle size of 2 to 5 nm. *Environ. Health Perspect.* **2007**, *115*, 397–402. [[CrossRef](#)]
43. Warheit, D.B.; Brock, W.J.; Lee, K.P.; Webb, T.R.; Reed, K.L. Comparative pulmonary toxicity inhalation and instillation studies with different TiO<sub>2</sub> particle formulations: Impact of surface treatments on particle toxicity. *Toxicol. Sci.* **2005**, *88*, 514–524. [[CrossRef](#)]
  44. Bermudez, E.; Mangum, J.B.; Wong, B.A.; Asgharian, B.; Hext, P.M.; Warheit, D.B.; Everitt, J.I. Pulmonary responses of mice, rats, and hamsters to subchronic inhalation of ultrafine titanium dioxide particles. *Toxicol. Sci.* **2004**, *77*, 347–357. [[CrossRef](#)]
  45. Guldberg, M.; Jensen, S.L.; Knudsen, T.; Steenberg, T.; Kamstrup, O. High-alumina low-silica HT stone wool fibers: A chemical compositional range with high biosolubility. *Regul. Toxicol. Pharmacol.* **2002**, *35*, 217–226. [[CrossRef](#)]
  46. Scientific Committee of Consumer Safety. Guidance on the safety assessment of nanomaterials in cosmetics. Brussels, Belgium. *SCCS* **2019**, *1611*, 19.
  47. Scientific Committee of Consumer Safety. The SCCS notes of guidance for the testing of cosmetic ingredients and their safety evaluation. Brussels, Belgium. *SCCS* **2015**, *1564*, 15.
  48. Vela, E.; Hernández-Orte, P.; Castro, E.; Ferreira, V.; Lopez, R. Effect of bentonite fining on polyfunctional mercaptans and other volatile compounds in Sauvignon Blanc wines. *Am. J. Enol. Vitic.* **2017**, *68*, 30–38. [[CrossRef](#)]
  49. Gualtieri, A.F.; Lusvardi, G.; Zoboli, A.; Di Giuseppe, D.; Lassinantti Gualtieri, M. Biodurability and release of metals during the dissolution of chrysotile, crocidolite and fibrous erionite. *Environ. Res.* **2019**, *171*, 550–557. [[CrossRef](#)] [[PubMed](#)]
  50. Konduru, N.; Keller, J.; Ma-Hock, L.; Gröters, S.; Landsiedel, R.; Donaghey, T.C.; Brain, J.D.; Wohlleben, W.; Molina, R.M. Biokinetics and effects of barium sulfate nanoparticles. *Part. Fibre Toxicol.* **2014**, *11*, 55. [[CrossRef](#)]



© 2020 by the authors. Licensee MDPI, Basel, Switzerland. This article is an open access article distributed under the terms and conditions of the Creative Commons Attribution (CC BY) license (<http://creativecommons.org/licenses/by/4.0/>).

### 3.1.6 Dosimetry in vitro – exploring the sensitivity of deposited dose predictions vs. affinity, polydispersity, freeze-thawing, and analytical methods.

**Keller JG**, Quevedo DF, Faccani L, Costa AL, Landsiedel R, Werle K, Wohlleben W.

Nanotoxicology, 15:1, 21-34,  
<https://doi.org/10.1080/17435390.2020.1836281>

**Abstract:**

Dose-response by in vitro testing is only valid if the fraction of the particle dose that deposits onto adherent cells is known. Modeling tools such as the ‘distorted grid’ (DG) code are common practices to predict that fraction. As another challenge, workflow efficiency depends on parallelized sample preparation, for which freeze-thaw protocols have been explored earlier, but not their implications on dosimetry. Here we assess the sensitivity of the DG code toward freeze thaw protocols and variations in user-defined parameters, including the estimation of particle cell affinity and determination of agglomerate size, which we measure by DLS or AUC. We challenge the sensitivity by materials of varying composition, surface functionalization, and size (TiO<sub>2</sub>, CeO<sub>2</sub>, BaSO<sub>4</sub>, 2x Ag, 3x SiO<sub>2</sub>). We found that the average effective density is robust, but the dose predictions by different approaches varied typically 2-fold and up to 10-fold; this uncertainty translates directly into the uncertainty of no-effect-concentrations. The use of standardized dispersion protocols increases the uncertainty in doses. The choice of a measurement method and minor details of the particle size distribution strongly influence the modeled dosimetry. Uncertainty is high for very well dispersed nanomaterials; since then, the assumed affinity of particles to cells has a decisive influence. Against this background, the modulation of deposited dose by freeze-thaw protocols is a minor factor that can be controlled by aligning the protocols of sample preparation. However, even then, the uncertainty of deposited doses must be considered when comparing the in vitro toxicity of different nanomaterials.



## Dosimetry *in vitro* – exploring the sensitivity of deposited dose predictions vs. affinity, polydispersity, freeze-thawing, and analytical methods

Johannes G. Keller<sup>a\*</sup> , Daniel F. Quevedo<sup>b\*</sup> , Lara Faccani<sup>c,d</sup>, Anna L. Costa<sup>c</sup>, Robert Landsiedel<sup>a</sup> , Kai Werle<sup>a</sup> and Wendel Wohlleben<sup>a</sup>

<sup>a</sup>Department of Material Physics and Department of Experimental Toxicology and Ecology, BASF SE, Ludwigshafen, Germany;

<sup>b</sup>Department of Biomedical Engineering, University of Michigan, Ann Arbor, MI, USA; <sup>c</sup>Institute of Science and Technology for Ceramics, CNR-ISTEC-National Research Council of Italy, Faenza, Italy; <sup>d</sup>University of Parma, Parma, Italy

### ABSTRACT

Dose-response by *in vitro* testing is only valid if the fraction of the particle dose that deposits onto adherent cells is known. Modeling tools such as the 'distorted grid' (DG) code are common practices to predict that fraction. As another challenge, workflow efficiency depends on parallelized sample preparation, for which freeze-thaw protocols have been explored earlier, but not their implications on dosimetry. Here we assess the sensitivity of the DG code toward freeze-thaw protocols and variations in user-defined parameters, including the estimation of particle-cell affinity and determination of agglomerate size, which we measure by DLS or AUC. We challenge the sensitivity by materials of varying composition, surface functionalization, and size (TiO<sub>2</sub>, CeO<sub>2</sub>, BaSO<sub>4</sub>, 2x Ag, 3x SiO<sub>2</sub>). We found that the average effective density is robust, but the dose predictions by different approaches varied typically 2-fold and up to 10-fold; this uncertainty translates directly into the uncertainty of no-effect-concentrations. The use of standardized dispersion protocols increases the uncertainty in doses. The choice of a measurement method and minor details of the particle size distribution strongly influence the modeled dosimetry. Uncertainty is high for very well dispersed nanomaterials; since then, the assumed affinity of particles to cells has a decisive influence. Against this background, the modulation of deposited dose by freeze-thaw protocols is a minor factor that can be controlled by aligning the protocols of sample preparation. However, even then, the uncertainty of deposited doses must be considered when comparing the *in vitro* toxicity of different nanomaterials.

### ARTICLE HISTORY

Received 22 May 2020  
Revised 18 September 2020  
Accepted 9 October 2020



### KEYWORDS

dosimetry; deposited dose; nanomaterials; effective density; affinity


### Introduction

As the demand for consumer products for daily life increases, the need for materials with advanced functionalities has continuously been growing. These functionalities have resulted in improvements in a plethora of sectors, whether better color contrast in TV screens through core-shell quantum dots, sunscreens that use titanium oxide nanoparticles to be effective and yet transparent longer-lasting coatings (Stark et al. 2015; Wohlleben, Kingston, et al. 2017). These advances hold the use of nanomaterials at their core, and the production volumes of these engineered nanomaterials (ENM) represent a substantial share of the total production volume (Ministère de l'Environnement 2015; Wigger,

Wohlleben, and Nowack 2018). Until recently, risk assessment of nanomaterials has been based on the risk assessment of the bulk material in question, whereas adapted methods are required to ensure that potential unique behaviors of nanoforms do not occur unnoticed (Donaldson and Poland 2013). Furthermore, traditional methods of regulatory toxicology testing have heavily relied on *in vivo* experiments. The sheer number of nanoforms makes *in vivo* testing of every material an untenable prospect, logistically and ethically. Recent REACH regulation, which was enacted in the European Union from January 2020, mandates that all entities producing nanomaterials register these as nanoforms of the substance and demonstrate their safe use

**CONTACT** Wendel Wohlleben  wendel.wohlleben@basf.com  Department of Material Physics and Department of Experimental Toxicology and Ecology, BASF SE, Ludwigshafen 67056, Germany

\*Equal contributing authors.

 Supplemental data for this article can be accessed [here](#).

© 2020 Informa UK Limited, trading as Taylor & Francis Group

(ECHA 2017; European Commission 2018). Thus, advances in the standardization of *in vitro* testing methods for the hazard assessment of ENM are needed to support grouping and read-across and thus build efficient regulatory frameworks (Oomen et al. 2018; Oomen et al. 2015; Arts et al. 2016; Arts et al. 2015; Wohlleben, Coleman, et al. 2019).

Alternative testing methods to investigate the hazard potential of ENMs are currently under development, based on several design requirements. First, they must be valid and robust. Second, they should be more straightforward and less expensive than current methods. Third, due to the large number of ENMs that need to be tested, it should be possible to test samples in parallel and thus increase the throughput.

A freeze-thaw protocol addresses the second and third requirements. Freeze-thawing would enable samples prepared by the NANoREG sample preparation protocol with extended sonication to be run in parallel, which is more efficient than running multiple sonications, dynamic light scattering (DLS), and effective dose setups in parallel. In a recent publication by Vila et al., a freeze-thaw protocol to enable the parallel testing of different nanomaterials (NMs) was introduced. However, research needs were identified regarding potential variations in the effective density and dosimetry with the new freeze-thaw protocol (Vila et al. 2017).

The goal of dosimetry modeling is to use physicochemical characteristics to predict the fraction of total dosed particles seen by cells. Only particles that accumulate at the cell's surface contribute to the effective dose. When ENMs or their agglomerates come into spatial vicinity to the cell's surface, they may be repelled, in which case they are not likely to induce a cellular response, or they may stick to the cell's surface, which builds up the dose that reaches the cells, and as such is a prerequisite of internalization (Liu et al. 2012). The surface affinity and stickiness can be calculated in principle (Wohlleben, Punckt, et al. 2017; Chen et al. 2014; Xia, Monteiro-Riviere, and Riviere 2010), but in *in vitro* settings, ENMs can have significant interactions with biological media, unlike what is observed in small molecule-based systems. Unique ENM behaviors include the formation of a protein corona as well as particle dissolution, leading to changing settling and diffusion profiles. The properties of

these ENM behaviors are dependent on environmental factors such as temperature, media composition, media viscosity, and pH. A model which considers the different physical theories that govern diffusion and sedimentation, and allows for complex data inputs such as size distributions and effective densities, would give a toxicologist with access to a characterization library the ability to consider ENM complexity allowing them to design experiments that produce relevant, accurate and translatable results. These type of *in vitro* dosimetry models have been under development for the past decade, with the field advanced significantly by the work of the Teeguarden and the Demokritou groups, who developed the *In vitro* Sedimentation, Diffusion and Dosimetry (ISSD) and Distorted Grid (DG) models of *in vitro* nanomaterial dosimetry, respectively (Teeguarden et al. 2007; Lison et al. 2008; DeLoid et al. 2015; DeLoid, Cohen, et al. 2017; DeLoid et al. 2014). However, the relevance of particle transport has also been questioned since fluid movement might dominate the transport in reality (Lison et al. 2008). Specifically, the DG model is an advanced MATLAB-based model that considers additional variables, such as size distribution, as well as different behaviors and boundary conditions, such as diffusion, sticky and non-sticky bottoms, particle size distributions, and effective density.

Here we assess the sensitivity of the distorted grid (DG) code toward freeze-thaw protocols and variations in user-defined parameters, including an estimation of particle affinity and an approximation of the polydisperse colloidal properties, for which we employ either DLS or AUC measurements. We challenge the sensitivity by materials of varying composition, surface functionalization, and size ( $\text{TiO}_2$ ,  $\text{CeO}_2$ ,  $\text{BaSO}_4$ , 2x Ag, 3x  $\text{SiO}_2$ ). Our results shall support modeling *in silico* how the materials will behave *in vitro*. These results can ultimately guide the decision of whether a particular ENM needs additional testing *in vivo*.

## Materials and methods

In total, eight different engineered nanomaterials were selected, which represent a variety of industrial applied ENMs. These ENMs are used as pigments, polishing agents for silicon wafers, catalytic additives in fuels, and fillers in the paint.  $\text{TiO}_2$



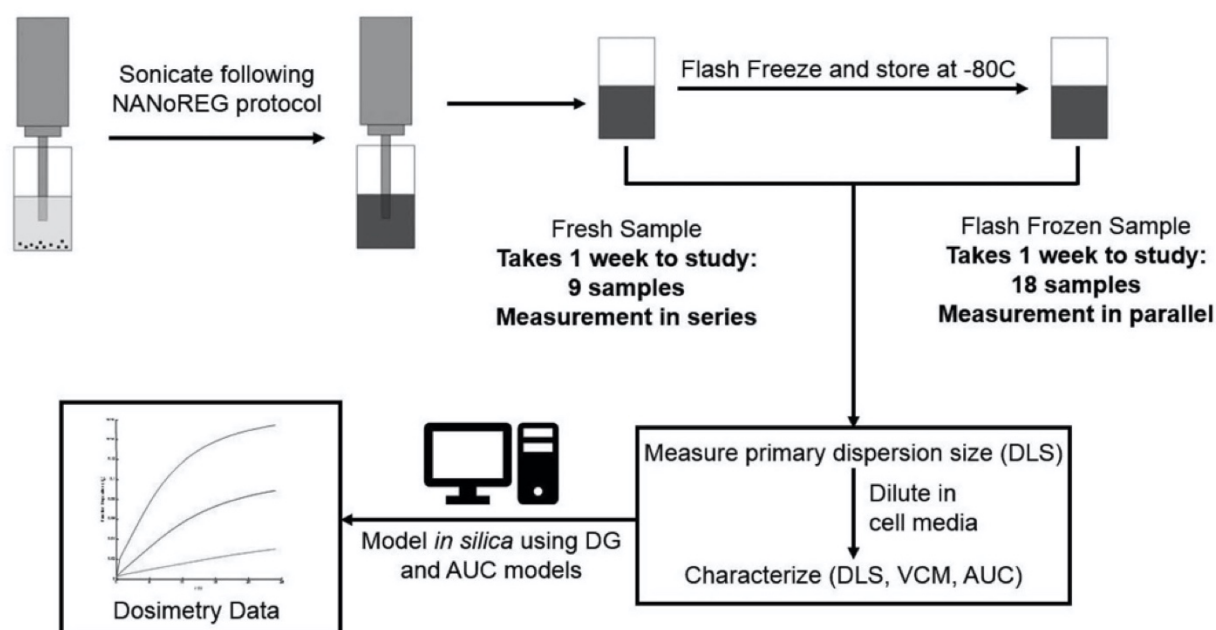


**Figure 1.** Schematic summary of the workflow design. Including sample dispersion in the first step, with the sonication following the NANoREG protocol followed by either direct DLS, VCM, and AUC measurement or after flash freezing at  $-80^{\circ}\text{C}$ . With a consecutive analysis of the dosimetry data.

NM-105 (21 nm),  $\text{CeO}_2$  NM-212 (40 nm),  $\text{BaSO}_4$  NM-220 (32 nm), Ag NM-300k, and Ag NM-302 were provided as part of the OECD sponsorship program by the Joint Research Center (JRC) with the pristine median diameter given in brackets (Rasmussen et al. 2014). Amorphous  $\text{SiO}_2$  (8.8 nm) was provided by the Leibniz Research Institute for Environmental Medicine (IUF), Düsseldorf, Germany. Sigma\_Ag (27.6 nm) was purchased from Sigma-Aldrich Inc. 576832-5 G (Sigma Aldrich Inc., St. Louis, MO).  $\text{SiO}_2$  DQ12 (111.6 nm) was produced for the PATROLS project and provided by the Institute for Occupational Medicine (IOM, Edinburgh, United Kingdom). All median diameters given in brackets were determined through transmission electron microscopy (TEM) with an FEI Tecnai F20 at an acceleration voltage of 200 kV (Figures S3).

The approach taken in this set of experiments almost entirely relied on the Standard Operating Procedures (SOPs) optimized by the NANoREG project (Jensen et al. 2011), along with selected recommendations on settings for the DG model given by DeLoid, Wang, et al. (2017) for the preparation of stock suspensions, followed by flash freezing treatment (Figure 1; Vila et al. 2017).

The goal was to use the SOP as a basis to build a workflow easy to replicate, providing reproducible

results, and easy for partners to replicate (Figure 1). Any deviations from the SOP were noted.

In summary, each material was weighed out to make 6 mL of a stock dispersion with a concentration of 2.56 mg/mL in 99.5 vol% sterile-filtered BSA-water (0.05% w/v), 0.5 vol% EtOH (96% pure; Jensen et al. 2011). BSA works as stabilization and dispersing agent and helps to increase the dispersibility of the stock dispersion. EtOH enables the handling of hydrophobic materials. Each ENM was weighed out to be as close as possible to a total mass of 15.36 mg and placed in 30 mL Scint-Burk glass vials. The vials had the same diameter as those recommended by the NANoREG protocol and differed only in height, leading to an increased volume capacity. Subsequently, the material was prewetted by the appropriate EtOH volume, followed by the addition of BSA-water, taking care to wash down the sides of the vial for material recovery. The BSA-water was prepared by first creating a 1% BSA-stock solution and then further dilute it with Millipore water to a total concentration of 0.05% (Jensen et al. 2011).

NM-300K, NM-302, and Sigma Ag were all weighed out under argon atmosphere and stored under argon. NM-402 was weighed out using additional precautions: the weighing out was

conducted in a hood specialized for Carbon NanoTube (CNT) use, using gloves and a 3M Aura Disposable Respirator (3M ID GT500073132, 3M Maplewood, NJ). All other materials were weighed out using a separate calibrated scale.

A Branson 550 probe sonicator equipped with a 3 mm tip was used for dispersion. The sonicator was calibrated following the SOP to deliver 7.35 W of critical sonication energy to each sample. All materials were sonicated for 16 min to create 6 mL of nanoparticle stock dispersion with a concentration of 2.56 mg/mL. For dispersions, care was taken to ensure that the tip of the sonicator was consistently submerged to a similar depth across samples, between the upper quarter and upper half of the volume. All dispersions were submerged in an ice-water bath during sonication. Between samples, the tip of the sonicator was washed by sonication for 5 min in a 50:50 EtOH:DI H<sub>2</sub>O solution, followed by rinsing by EtOH and air drying to prevent cross-contamination.

Within 5 min following sonication, the particle dispersion was aliquoted into 1.5 mL microcentrifuge tubes (Eppendorf, 0030 120.191, Eppendorf AG, Hamburg, Germany) and flash-frozen in liquid nitrogen (LN<sub>2</sub>; Vila et al. 2017). The tubes were prepared by puncturing the cap with a small hole to prevent decompression at low temperatures. Cryo-protective gear, namely gloves and long tweezers were used to protect the user, and all work was done in a chemical hood. The tubes were kept in LN<sub>2</sub> for at least 2 min and then placed in long term storage at  $-80^{\circ}\text{C}$ . Our facilities did not have the standard  $-80^{\circ}\text{C}$  freezers, and thus, we stored samples in dry ice ( $-78.5^{\circ}\text{C}$ ), which is considered an insignificant difference against the original protocol by Vila et al.

After flash freezing, each aliquot was thawed as needed. This was done by placing each aliquot in a hot ( $\sim 65^{\circ}\text{C}$ ) bath sonicator for 1 min, or until a small ice core was left in the tube. Immediately following thawing, the ENM suspensions were diluted 10x in water (primary particles) and in cell media, with either Dulbecco Modified Eagle Medium (31053028, Gibco<sup>TM</sup>, Thermo Fisher Scientific, Waltham, USA) +10% Fetal Bovine Serum, (10500056, Gibco<sup>TM</sup>, Thermo Fisher Scientific, Waltham, MA) +1% Minimal Essential Medium (11140068, Gibco<sup>TM</sup>, Thermo Fisher Scientific,

Waltham, MA) + 1% Penicillin/Streptomycin 100x (15140122, Gibco<sup>TM</sup>, Thermo Fisher Scientific, Waltham, USA) or RPMI (Rosewell Park Memorial Institute) (11835030, Gibco<sup>TM</sup>, Thermo Fisher Scientific, Waltham, MA), once incubated for one hour at  $37^{\circ}\text{C}$ . After the incubation, the samples were characterized using one of three techniques: dynamic light scattering (DLS), volumetric centrifugation method (VCM,) or analytical ultracentrifugation (AUC); each particle type was processed and characterized in independent triplicates.

### ***Volumetric centrifugation method (VCM)***

The effective densities of the ENMs dispersed in cell media were measured as previously described by DeLoid et al. (2014). Briefly, after incubation at  $37^{\circ}\text{C}$ , 1 mL of sample was loaded into VCM tubes (87007, TPP Techno Plastic Products AG, Trasadingen, Switzerland) and centrifuged for one hour at 3000-G, unless otherwise detailed. After centrifugation, the volume of the pelleted ENMs was measured using a VCM 'easy read' measuring device (87010, TPP Techno Plastic Products AG, Trasadingen, Switzerland). The effective densities were then calculated using the equations described by DeLoid et al. (2014).

### ***Dynamic light scattering (DLS)***

Flash-frozen samples are rapidly thawed in a  $65^{\circ}\text{C}$  bath sonicator until no ice crystals were left in the sample and diluted 10x in the testing medium. Hydrodynamic size distributions of pristine and cell media dispersions were measured using Dynamic Light Scattering (DLS) using a Malvern Zetasizer ZEN1600 (Malvern Panalytical Ltd. Malvern, UK). Instrument settings were set as dictated by the NANoREG SOP.

### ***Analytical ultracentrifugation (AUC)***

AUC implements an optical system synchronized with the centrifugal frequency to monitor the radial concentration profile during centrifugal separation. The samples were directly loaded in AUC cells without further preparation. All measurements were done on a Beckman Coulter XLI Proteome Lab (Beckman Coulter Inc., Brea, CA). The cells were all



mounted on a 4-sample or 8-sample titanium rotor at 1000 rpm for 30 min, followed by 3000 rpm for 30 min and 12,000 rpm for two hours. The samples were measured using either interference or absorbance optics to detect sedimentation, as described by the NanoDefine project (Mehn et al. 2018). Both types of sedimentation data were evaluated with sedfit v15.0 software.

### Dosimetry by AUC sedimentation driven transport

The raw sedimentation coefficients measured by AUC, as fitted by sedfit software, do not require any assumptions about particle size, density, or composition. Instead, the measured distribution of sedimentation coefficients can be directly used to calculate the deposited dose. The AUC sedimentation coefficients are converted into delivered doses by integrating the sedimentation-driven transport to this model the deposited dose by a method that was already described in the literature (Sauer et al. 2015; Wohlleben, Coleman, et al. 2019). The delivered doses measured by AUC and calculated by sedimentation-driven transport model were compared with those calculated by the Distorted Grid *in silico* model.

### Dosimetry by DG in silico model

The principle of DG modeling relies on successive modeling of diffusion and sedimentation based on the media height, with variable heights of the sub-compartment from run to run, and the particle size distribution. The iterative modeling also accounts for the stickiness of the bottom of the wells, which can be tuned accordingly. The model results are given as delivered ENM mass. The particle number dictates the probability of particle-particle collisions but is not a conserved metric when particles agglomerate.

If using AUC as an input of size distributions, the AUC sedimentation coefficient was first converted to size distribution using (a) the skeletal density of each material, (b) the fractal dimension, or (c) the effective density, for use as input data for the Distorted Grid model. This procedure is described in Wohlleben (2012). If using DLS as an input of size distributions, triplicate DLS measurements were averaged. In either case, VCM triplicate data were

**Table 1.** DLS hydrodynamic diameter size (z-average) and effective density of primary dispersion (H<sub>2</sub>O) and after 1-h incubation in the medium after freeze-thawing. The medium was DMEM/FBS as specified in methods.

ENM	z-Average (nm ± σ)		Effective Density (g/cm <sup>3</sup> ± σ)
	Water	Medium	Medium
TiO <sub>2</sub> NM-105	274.9 ± 46.4	287.7 ± 42.8	1.408 ± 0.009
CeO <sub>2</sub> NM-212	281.0 ± 18.9	242.6 ± 2.6	2.214 ± 0.029
BaSO <sub>4</sub> NM-220	176.4 ± 37.9	151.1 ± 27.5	2.034 ± 0.049
Ag NM-300K	135.1 ± 3.8	92.7 ± 14.7	2.004 ± 0.153
Ag NM-302	1104.0 ± 114.6	1027.4 ± 44.0	8.617 ± 0.181
Amorphous SiO <sub>2</sub>	230.8 ± 26.8	1169.1 ± 155.2	1.156 ± 0.013
Sigma Ag	195.1 ± 5.5	163.0 ± 2.7	2.465 ± 0.093
DQ12	471.0 ± 19.7	402.4 ± 44.1	1.787 ± 0.000

averaged and used as input data for the Distorted Grid (DG) model developed by (DeLoid et al. 2015; DeLoid, Wang, et al. 2017). The model provided by DeLoid et al. was run using an auxiliary MATLAB macro written to allow for data input using Microsoft Excel and batch processing multiple materials and conditions. The modified MATLAB code, auxiliary macro, and associated templates are available by request. The adjustable parameters used for the modeling are listed in Table S1, and the resulting effective densities are reported in Table 1.

## Results

### Effects of flash freezing of ENM characteristics on dosimetry prediction by DG compared to freshly prepared samples

To see how flash-freezing would affect dosimetry modeling, we compared fresh and flash-frozen dispersions of three ENMS: CeO<sub>2</sub> NM-212, BaSO<sub>4</sub> NM-220, and Amorphous SiO<sub>2</sub>. The particles were dispersed and then either immediately characterized or flash-frozen. Flash-frozen samples were thawed out after one week of storage at -78.5 °C and then characterized.

As seen in Figure 2, we found that while there were no large differences in the z-averages between the fresh samples and the flash-frozen samples (both for primary and 1-h media incubation samples, Table 1, there were differences in the hydrodynamic diameter size distributions. As shown in Figure 3, while the main effect seen in some materials, such as CeO<sub>2</sub> NM-212, was a small increase in the overall diameter, other materials developed a

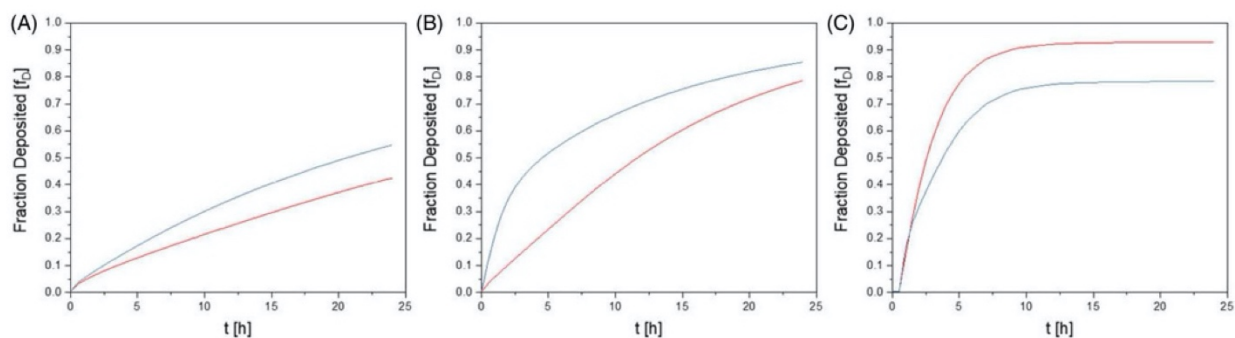


**Figure 2.** Effect of fresh sample vs. flash freeze-thawing on the deposited dose of samples on A BaSO<sub>4</sub> NM220, B CeO<sub>2</sub> NM212, and C Amorphous SiO<sub>2</sub>. For A and B the lower curve indicates the fresh sample, whereas the upper curve indicates the sample prepared after the freeze-thawing protocol. For C the upper curve is the fresh sample, whereas the lower curve represents the sample prepared after the freeze-thawing protocol.

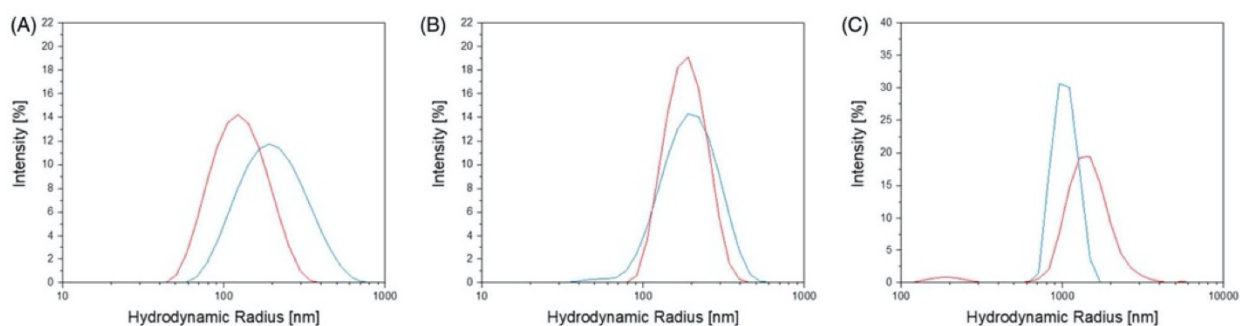


**Figure 3.** Effect of fresh sample vs. flash freeze-thawing on the hydrodynamic diameter on A BaSO<sub>4</sub> NM-220, B CeO<sub>2</sub> NM-212, and C Amorphous SiO<sub>2</sub>. Compared to the freeze-thawing protocol (blue in the online pdf), the fresh sample (red in the online pdf) has lower deposited fraction in (A,B), but higher deposited fraction in (C).

multimodal size distribution due to agglomeration. As shown in Table S2, the change in particle size distributions translated to large differences in some of the materials, with increases of 61.7, 50.3, and 82.5 nm for CeO<sub>2</sub> NM-212, BaSO<sub>4</sub> NM-220, and Amorphous SiO<sub>2</sub>, respectively. Surprisingly, we found that effective density was much more resistant to freezing-induced changes and found no differences between fresh and flash-frozen samples. We compared the z-average after flash freezing in different media such as DMEM and RPMI media (Table S2). The data clearly shows that the difference between fresh and flash-freezing was more significant for RPMI than for DMEM/FBS.

To investigate how the observed physicochemical changes would affect dosimetry, the deposition of particles with and without flash freezing was modeled using the DG model as described in the methods section. The deposited dose after 24 h was modeled for specific nanomaterials at a

concentration of 0.256 mg/mL with reflective boundary conditions.

#### **Variability between triplicates**

Variability between different dispersions of the same material affected the DG modeling results in different magnitudes, depending on the material analyzed. Certain materials, such as NM-212, showed considerable variability in percent-deposited after 24 h (Figure 4(B)). Other materials, such as NM-220 and Sigma Ag, showed much less variability in the range of 7–14% (Figure 4(A, C)).

#### **Quantitative differences between different thermodynamic boundary conditions**

The DG model has built into its capability to simulate different levels of ‘stickiness’ between nanoparticles and the bottom of the well. Only exceptional



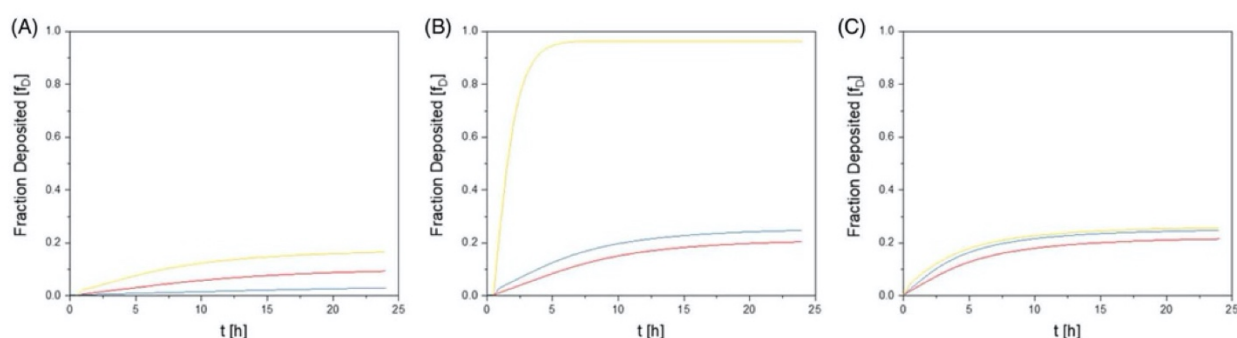


**Figure 4.** Variability of triplicate sample preparation affects dosimetry modeling. DG model over 24 h for three materials: A BaSO<sub>4</sub> NM-220, B CeO<sub>2</sub> NM-212, and C Sigma Ag. The model was set up to use the appropriate variables for each material, with the only difference between each simulation being a different nanoparticle size distribution, as acquired by DLS, and different effective densities, measured using VCM.

**Table 2.** The fraction of deposited dose after 24 h (%).

	DG prediction			Measured (sedimentation transport only) AUC integration of sedimentation coefficients	x-Fold spread of all approaches to determine the deposited dose
	DLS input, Reflective Boundary	DLS input, Adhesive Boundary ( $K_d = 1 \times 10^{-9}$ M)	AUC input, Adhesive Boundary ( $K_d = 1 \times 10^{-9}$ M)		
	[% deposited dose after 24 h]				
Amorphous SiO <sub>2</sub>	73.57	74.77	56.0	60.50	1.3
DQ12	49.02	60.64	30.88	68.67	2.2
TiO <sub>2</sub> NM-105	18.53	25.69	20.80	42.67	2.3
CeO <sub>2</sub> NM-212	44.33	54.97	40.98	42.00	1.3
BaSO <sub>4</sub> NM-220	9.05	23.67	1.9	15.33	12
Ag NM-300K	31.93	41.81	17.02		2.5
Ag Sigma	22.17	38.25	3.74	14.67	10

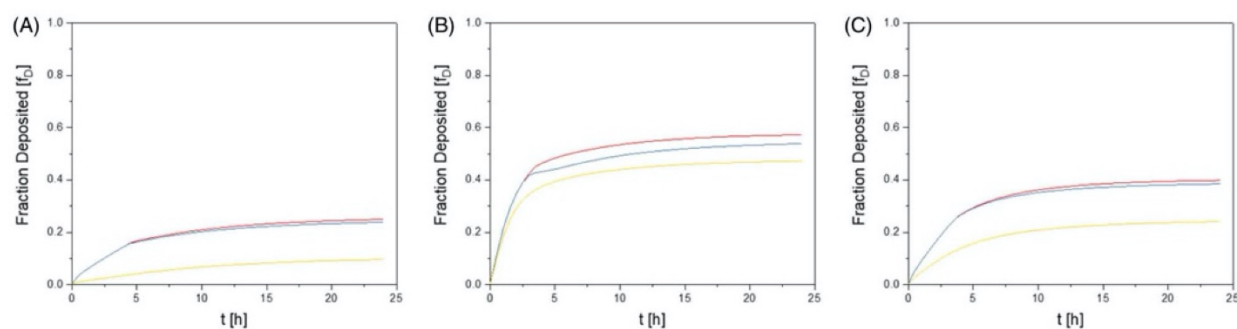


**Figure 5.** Assumptions on boundary condition simulations into the DG model can affect the predictions. We examined this by modeling deposition over 24 h in three materials: A BaSO<sub>4</sub> NM-220, B, CeO<sub>2</sub> NM-212 and C Sigma Ag, and varying the boundary conditions. Here, the red curves correspond to a  $K_d$  (M) =  $1 \times 10^9$ , blue corresponds to  $K_d$  (M) =  $1 \times 10^8$ , and the yellow curve corresponds to no boundary conditions, resulting in a reflective bottom.

cases of nano-pharmaceutical carriers have well-defined, targeted cellular interaction (Brenner et al. 2018). Varying stickiness allows the model to account for the different ENM uptake rates based upon cell type. The method used to model this stickiness is described in the original publication for the DG model (DeLoid et al. 2015; DeLoid, Wang, et al. 2017). Briefly, stickiness is simulated using a Langmuir-isotherm adsorption process, where the

particles are adsorbed and desorbed to the bottom of the well. Once adsorbed, the particles are removed from the system until desorbed. Once the stickiness is included, it is defined by ascribing an association constant,  $K_d$ , to the nanoparticles.  $K_d$  is assumed to be specific to each experimental condition and is not well understood, but it is thought to be cell-, ENM-, and media-dependent. Decreasing  $K_d$  will lead to higher particle adsorption to the



bottom of the well. We studied how significantly stickiness would affect dosimetry based upon experimental data (Table 2). We simulated dosimetry in the DG model over a 24-h period using three different materials. Each material was simulated as described previously, with the boundary being either reflective (adsorption turned off), low-adhesion ( $K_d = 1 \times 10^{-8}$ ), or high-adhesion ( $K_d = 1 \times 10^{-9}$ ). The  $K_d$  values were chosen following the work done initially by (DeLoid et al. 2015). Specific values (Figure 5 and Table 2) highlight that simulations can differ by as much as 29.52% for Ag NM-302, 14% for BaSO<sub>4</sub> NM220, or as low as 1.2% for Amorphous SiO<sub>2</sub>.

### Quantitative differences between different methods used to provide a size distribution for modeling

Since the measured polydispersity of the size distribution was critical for the DG predictions, we explored the model's sensitivity to different methods of determining the size distribution. DLS is very reliable on the z-average diameter, but less so on the complete distribution. Fractionating methods instead have the advantage of quantification of few-percentage fractions of agglomerates or individual constituent particles. Here we compare DLS to AUC size distributions, evaluated with the independently measured effective density, and find that the parity plot between AUC and DLS has a slope far below parity, indicating that the DLS differentiates the median size between different ENMs less than AUC (Figure 6).

The particle size distribution (PSD) from DLS vs. AUC with  $D_f$  can be seen in Figure 7. Here the PSD is shown for both silica-based materials, SiO<sub>2</sub> amorphous and crystalline B DQ12. The figure demonstrates the different particle size assumptions, based on the measurement method, which would strongly affect the deposited dose (Figure S2). We then employed the size distributions from AUC in the DG model and found (Table 2) significant differences in a deposited dose, which can be related to the differences in PSD.

## Discussion

### Flash freezing vs. fresh dosimetry measurements

The NANoREG Protocol was developed as a standard operating procedure to produce consistent and

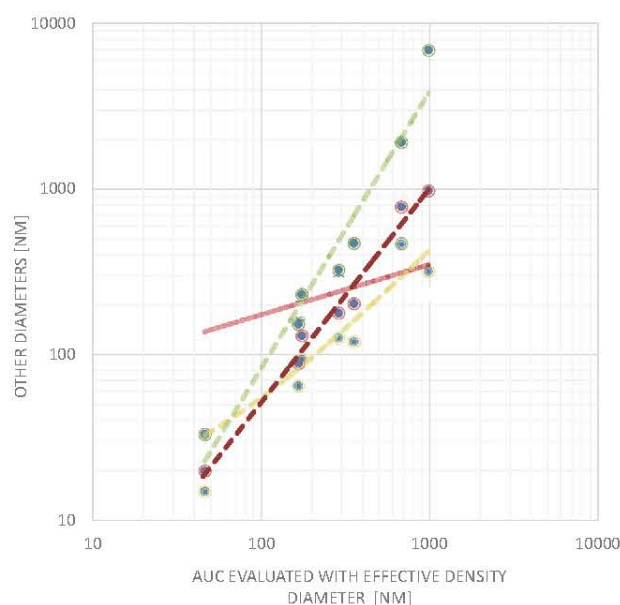


**Figure 6.** Parity plot of the mass median particle diameter with different density assumptions for AUC and DLS measurements for Amorphous SiO<sub>2</sub>, DQ12, TiO<sub>2</sub> NM105, CeO<sub>2</sub> NM212, BaSO<sub>4</sub> NM220, Ag NM300K, and Ag Sigma. The solid red line corresponds to the DLS measurement. The red dashed line connecting the blue dots with a red outer shell corresponds to the AUC fractal dimension evaluation with  $D=2.54$ . The green dashed line connecting the blue dots with a green outer shell corresponds to the AUC fractal dimension evaluation with  $D=2.1$ . The yellow dashed line connects the blue points with the yellow sphere and describes the AUC solid sphere evaluation with  $D=3$ . Linear regression was used for the fits in the double log plot.

repeatable nanoparticle dispersions of ENMs for nanotoxicological studies (Gao and Lowry 2018). While the protocol is straightforward and the required equipment is standard across most nanotoxicology labs, it is time-consuming, taking approximately 10 min per dispersion and 5 min between samples. Additionally, it can be wasteful if a fresh dispersion is made for every experiment. The protocol produces 6 mL of particle dispersion at a concentration 100x more concentrated than the highest commonly used in toxicological *in vitro* assays, making approximately enough samples for 30 96-well microwell plates with each dispersion. Flash freezing is more time-efficient, which is key for large scale batch characterizations (Vila et al. 2017). While prior studies suggest the stability of ENM dispersions during flash-freezing (Vila et al. 2017), all dosimetry models are based upon data collected from dispersions followed by immediate dosimetry measurements (Teeguarden et al. 2007; DeLoid, Cohen, et al. 2017), which begs the

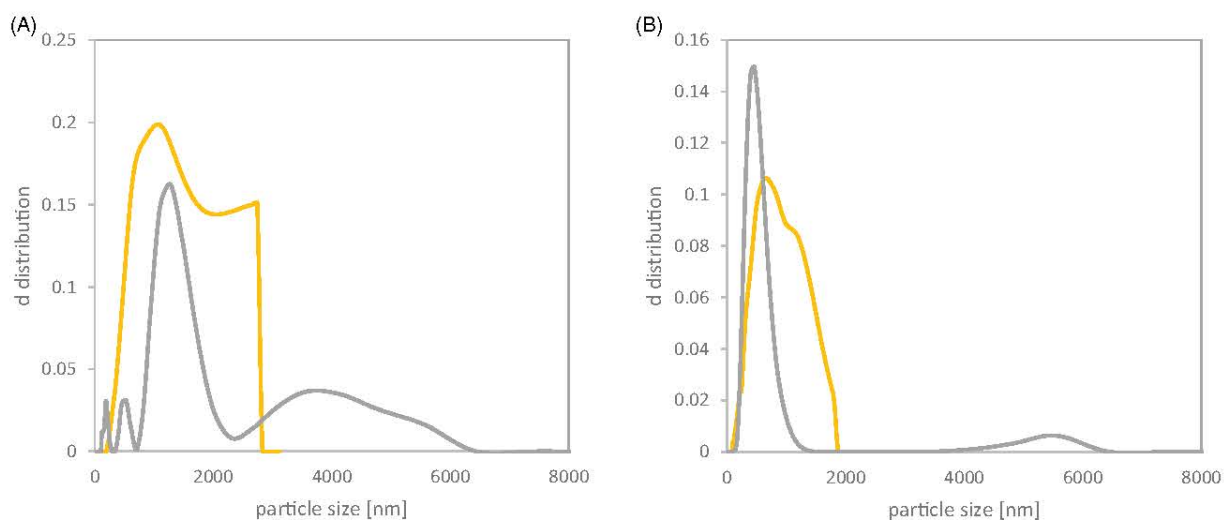


**Figure 7.** Particle size distribution for A SiO<sub>2</sub> Amorphous and B DQ12. The yellow curve indicates the PSD as measured by AUC, whereas the gray curve was measured through DLS.

question of the potential biases of using similar models on flash-frozen samples.

Therefore, we decided to test the flash freezing method for characterization and modeling. Here we observe only small differences in z-averages as seen in Table S2, from  $219.3 \pm 2.3$  nm to  $281.0 \pm 18.9$  nm for CeO<sub>2</sub> NM-212 fresh vs. freeze-thaw and  $126.1 \pm 1.0$  nm to  $176.4 \pm 37.85$  nm for BaSO<sub>4</sub> NM-220. This results in an effective density of  $2.200 \pm 0.067$  g/cm<sup>3</sup> and  $2.214 \pm 0.029$  g/cm<sup>3</sup> for CeO<sub>2</sub> NM-212 and  $2.174 \pm 0.000$  g/cm<sup>3</sup> and  $2.034 \pm 0.049$  g/cm<sup>3</sup> for BaSO<sub>4</sub> NM220 for fresh and flash-frozen, respectively. These discrepancies have a negligible effect on transport properties, but they are a correction to the finding by Vila et al. (2017), which reported no differences between flash-frozen and fresh samples. While their investigation found differences in z-average, which agree with our findings, they did not report their particle size distributions. The flash freezing process seems to have promoted the aggregation of the ENMs, and as large ENM aggregates sediment at faster rates, this increases the effective delivered doses.

We also evaluated the differences in z-average in two different media, DMEM/FBS and RPMI. The results are shown in Table S2 highlight significant differences between fresh and flash-frozen samples for CeO<sub>2</sub> NM-212 and Amorphous SiO<sub>2</sub> in RPMI, whereas BaSO<sub>4</sub> NM-220 does not exhibit differences by more than 10%. This can be attributed to the more vital protein interaction of the positively

charged CeO<sub>2</sub> (Chen et al. 2014; Wohlleben et al. 2016; Schaefer et al. 2012).

It is highly probable that flash-freezing methods will continue to be used within industrial and regulatory applications, enabling comparative toxicology by parallel testing. Our results clarified that even with identical standardized dispersion methods, flash freezing changes the dosimetry behavior of the materials. Thus the key for relevant results in toxicology experiments is that methods must be consistent between characterization, *in silico* modeling, and *in vitro* toxicology.

#### DLS ENM replication explorations

As measured through DLS, the particle size distribution is prone to be affected by small numbers of large agglomerates within the dispersion (Gollwitzer et al. 2016). Sigma\_Ag was the only material to give a good reproducibility among three triplicates (Figure 4). The differences between triplicate one and triplicates two and three for CeO<sub>2</sub> NM-212 are most likely due to poor dispersion of triplicate one with a z-average of 660 nm compared to 294 nm and 267 nm for triplicate 2 and 3 with an effective density only differing slightly from  $2.24$  g/cm<sup>3</sup> for triplicate one to  $2.19$  g/cm<sup>3</sup> for triplicates two and three. A sample that is not correctly dispersed can result in a different deposition profile after modeling. While sample to sample variability is expected, these simulations highlight the concern that variability may be



propagated and multiplied during experiments that rely on multiple dependent measurements. This type of error propagation can be calculated using accepted statistical tools. Thus, it is crucial for future experiments to investigate whether averaging  $n$  number of dispersions and subsequent characterization will result in sufficiently accurate dosimetry data for biological experiments. These future experiments may focus on quantitatively measuring deposition in a controlled environment and comparing the measured deposited fraction to that predicted by simulations using averaged characterization data. The experiment itself might look like those conducted by (DeLoid et al. 2015) or an alternative method. Ideally, these experiments will reveal the required number of replicates for materials to result in an average that, when modeled, will reflect the average dose that reaches the cells.

#### **Particle size distribution measurement methods**

If the ENM has a high tendency to agglomerate, DLS is not the most suitable method for determining the particle size distribution (Gollwitzer et al. 2016) since this experimental variance has a strong influence on the prediction of the deposited dose. We found that DLS tends to underestimate the differentiation between ENMs in its size distribution measurements (Table 1), leading to possible false predictions of the deposited dose. Specifically, DLS shows tested materials having similar agglomerations, whereas AUC indicates significant differences. Comparing the deposited dose (Figure 4) after six hours with the dose after 24 h, it is evident that after six hours, the largest fraction is already deposited and that there is only a small change in deposited dose after 24 h. We, therefore, suggest benchmarking modeling predictions through AUC, where available, especially for agglomerated particles. Agglomeration is most sensitively detected in mass metrics, which should be preferred over number metrics in the ENM dispersion characterization in the cell culture medium. For DLS and AUC, it also requires the least conversions.

#### **DG stickiness conditions and compartment height**

DG modeling shows a strong dependency on adjustable parameters, such as boundary conditions

for sticky, non-sticky, and reflective bottoms, and the simulation of the height of the sub-compartment. When using 0.01 mm, the suggested height of the sub-compartment, we interestingly observed some significant dips within the deposited dose curve over time, as seen in Figure S1. When adjusting this height of the sub-compartment to 0.0005 mm, the dips vanish – however, the computing time for modeling the dosimetry changes from a few hours to several days.

Furthermore, the adjustment of the adhesive boundary has a significant effect on the deposited dose, with the boundary being either reflective (adsorption turned off), with low-adhesion ( $K_d = 1 \times 10^{-8}$ ), or high-adhesion ( $K_d = 1 \times 10^{-9}$ ). Affinities cannot be independently determined with certainty due to the modification of the surface by corona formation and unknown interaction with cellular epitopes (Liu et al. 2012; Chen and Riviere 2017). As expected, the resulting dosimetry curves (Figure 5) showed a higher deposited dose in high-adhesion conditions, with a factor of up to 2.5 (23 vs. 9% deposited) compared to the other conditions with otherwise identical input parameters, and a factor of 12 (23 vs. 1.9% deposited) if also the size input is varied. The results obtained by choosing the adhesive boundary emphasize the contribution of diffusion-driven transport but are dependent on an unsupported assumption of particle-cell adhesion.

Considering further that convection adds to particle transport but is not modeled (Lison et al. 2008), one might accelerate the delivery of the entire dose onto the cells by minimizing the fluid's height above the cells. Alternatively, one might consider the use of non-adherent cell lines, working in suspension with agitation.

#### **Varying PSD input parameters**

The significant impact of using the particle size distribution from two different characterization techniques to model the deposited dose was previously described by (Petersen et al. 2019). Petersen et al. described that using the mean diameter instead of the PSD only shows a change in the deposited dose of about 10%. Using substantially different analytical techniques for the PSD determination causes more considerable differences due to the



agglomeration of the tested ENMs. The two different methods used here to determine the deposited dose differ in their principle of particle transport. AUC only takes sedimentation into account (by direct measurement), whereas DG uses both diffusion and sedimentation (by calculation).

Table 2 shows that the deposited dose, as modeled by the DG model with DLS as input data for the particle size distribution, matches the deposited dose as determined directly by AUC quite well, whereas the DG model using AUC size distribution data differs overall by more than 30%. The spread of deposited dose predictions is about 10-fold for BaSO<sub>4</sub> NM220 and Ag<sub>sigma</sub> materials and about 2-fold for the six others; this uncertainty translates directly into the uncertainty of no-effect-concentrations.

Furthermore, when comparing the modeled deposited dose to the sedimented dose measured directly from the  $S_{ved}$  values as received by AUC-measurements, the direct comparison of predicted deposited dose to AUC measurements (under accelerated gravitational forces, thus suppressing the diffusional contribution) shows good agreement for Amorphous SiO<sub>2</sub> and DQ12, for which sedimentation is the dominant transport. In contrast, the discrepancy is significant for BaSO<sub>4</sub> NM-220 and Ag NM-300K, for which diffusion dominates the transport. This is consistent with the relatively narrow size distribution of BaSO<sub>4</sub> NM-220 and Ag NM-300K at smaller sizes. We had expected that the deposited dose for DG modeling should be as high as the deposited dose directly obtained by measuring the sedimentation by AUC but did not find that to be the case, even when using AUC size distributions as DG input (Table 2).

In the previous modeling with the *in vitro* sedimentation, diffusion, and dosimetry (ISDD) model, it was observed that for agglomerated particles, the robustness of predictions of the deposited dose was low. In contrast, well-dispersed single particles tended to have a high deposited dose by the ISDD model, in significant contrast to AUC measurement (Sauer et al. 2015). Based on the systematic variation of stickiness that we performed here (albeit in the analogous DG model), we can now attribute the earlier erroneous ISDD predictions to the assumption of the high affinity of the particles to

cells, which is assumed to be 'sticky' in the ISDD model.

### **The fractal dimension of ENM-protein agglomerates**

Our complementary data by hydrodynamic characterization with VCM, DLS, or AUC input can finally be interpreted in terms of the hydrodynamic properties of ENM-protein structures. DeLoid et al. highlighted that the concept of effective density is related via the Stirling formula to the fractal dimension of ENM agglomerate (DeLoid et al. 2014). An existing implementation of fractal dimensions in AUC (Wohlleben 2012) can be used to match the fractal dimension in the Stirling formula such that the median diameters agree with the evaluation by the effective measured density (Figure 6). Evaluation with  $D_f = 3$  (corresponding to solid spheres) remains *below* parity, but also the results using the theory of reaction-limited colloidal aggregation (RLCA; Lin et al. 1990) does not fit because the evaluation with  $D_f = 2.1$  remains *above* parity. The best approximation to parity is reached by  $D_f = 2.54$ . This value is nearly identical to the theoretical expectation for diffusion-limited colloidal aggregation (DLCA; Lin et al. 1990). Thus, we can interpret that the ENM-protein agglomerates assemble with a high ENM-ENM stickiness (hence DLCA) upon each collision of protein-decorated ENMs.

### **Conclusions**

We explored the sample preparation and the dosimetry of ENM *in vitro* testing. Knowing the mass fraction of the dose that accumulates at the cells allows re-calculating dose-response curves (Teegarden et al. 2007) and thus enhances the predictivity of *in-vitro* toxicology (DeLoid, Cohen, et al. 2017; DeLoid et al. 2014). Regarding the sample preparation, the freeze-thaw protocol enabled parallel testing by flash freezing the samples after sonication (Vila et al. 2017); this altered the presence of agglomerates in the particle size distribution of fresh dispersions up to 35% however, after 1-h incubation, the difference was below 25%. The effective density was only minimally altered by  $+0.15 \text{ g/cm}^3$ . Thus, overall it

modulated the dosimetry of the particles. The modulation tended to be lower in DMEM/FBS than in RPMI without serum. Nevertheless, characterization and *in silico* modeling that reflected the actual colloidal properties during *in vitro* toxicology can be obtained by matching the freeze-thaw protocols, which are reproducible.

Regarding dosimetry, the fundamental notion that the deposited dose is lower than the total administered dose can be easily supported by simple measurements (DLS, VCM) and DG modeling. With a deposited dose ranging between 9–73% for the different nanomaterials with reflective boundary conditions, we observed that the prediction of deposited dose varied significantly. Especially for well-dispersed ENMs, uncertainty was introduced by choosing an arbitrary value of the affinity of particles to cells ('reflective' vs. 'adhesive' bottom). Additionally, for polydisperse ENMs, minor details of the particle size distribution strongly influence the modeled dosimetry, such that the choice of the measurement technique, for example, DLS or AUC introduces further uncertainties to the dosimetry modeling. For any polydisperse ENM, we found it necessary to increase the DG model computing resources by reducing the output compartment height to 0.0005 mm; otherwise, dips in the particle settling traces lead to erroneous predictions.

However, even with optimized computing resources, the uncertainty of the actual deposited dose was considerable. Especially when using standardized dispersion protocols (NANoREG) and polydisperse industrially relevant materials, the predictions of the model incurred an uncertainty of the deposited dose due to uncertainty in the inputs. The dose-response that is obtained by the modeled prediction of the deposited dose can thus shift significantly: If the *in vitro* reactivity of different nanoforms differs by a factor of 2.5, one cannot conclude if the results are from a dissimilarity of biological interactions or the methodical uncertainty of dosimetry modeling. For very well dispersed nanoforms, the range of uncertainty extends to a factor of 10.

### Acknowledgments

Daniel Quevedo thanks Phil Demokritou for a research stay at Harvard TH Chan School of Public Health that highlighted

the need to minimize compartment height. We thank Florian Niederhöfer for enabling calculations on the Curiosity supercomputer.

### Disclosure statement


JGK, RL, KW, WW are employees of BASF SE, a company producing nanomaterials. All other authors declare that they have no competing interests.

### Funding

This project has received funding from the European Union's Horizon 2020 Research and Innovation Program under grant agreement No. [760813] PATROLS project.

### ORCID

Johannes G. Keller  <http://orcid.org/0000-0002-4292-2471>

Daniel F. Quevedo  <http://orcid.org/0000-0001-5892-364X>

Robert Landsiedel  <http://orcid.org/0000-0003-3756-1904>

### References

- Arts, J. H. E., M. Hadi, M.-A. Irfan, A. M. Keene, R. Kreiling, D. Lyon, M. Maier, et al. 2015. "A Decision-Making Framework for the Grouping and Testing of Nanomaterials (DF4nanoGrouping)." *Regulatory Toxicology and Pharmacology* 71 (2): S1–S27. doi:10.1016/j.yrtph.2015.03.007.
- Arts, J. H. E., M.-A. Irfan, A. M. Keene, R. Kreiling, D. Lyon, M. Maier, K. Michel, et al. 2016. "Case Studies Putting the Decision-Making Framework for the Grouping and Testing of Nanomaterials (DF4nanoGrouping) into Practice." *Regulatory Toxicology and Pharmacology* 76: 234–261. doi:10.1016/j.yrtph.2015.11.020.
- Brenner, J. S., D. C. Pan, J. W. Myerson, O. A. Marcos-Contreras, C. H. Villa, P. Patel, H. Hekierski, et al. 2018. "Red Blood Cell-Hitchhiking Boosts Delivery of Nanocarriers to Chosen Organs by Orders of Magnitude." *Nature Communications* 9 (1): 1–14. doi:10.1038/s41467-018-05079-7.
- Chen, R., and J. E. Riviere. 2017. "Biological and Environmental Surface Interactions of Nanomaterials: Characterization, Modeling, and Prediction." *Wiley Interdisciplinary Reviews: Nanomedicine and Nanobiotechnology* 9: e1440.
- Chen, R., Y. Zhang, F. Darabi Sahneh, C. M. Scoglio, W. Wohlleben, A. Haase, N. A. Monteiro-Riviere, and J. E. Riviere. 2014. "Nanoparticle Surface Characterization and Clustering through Concentration-Dependent Surface Adsorption Modeling." *ACS Nano* 8 (9): 9446–9456. doi:10.1021/nn503573s.
- DeLoid, G., J. M. Cohen, T. Darrah, R. Derk, L. Rojanasakul, G. Pyrgiotakis, W. Wohlleben, and P. Demokritou. 2014.



- "Estimating the Effective Density of Engineered Nanomaterials for in Vitro Dosimetry." *Nature Communications* 5: 3514. doi:10.1038/ncomms4514.
- DeLoid, G. M., J. M. Cohen, G. Pyrgiotakis, and P. Demokritou. 2017. "Preparation, Characterization, and in Vitro Dosimetry of Dispersed, Engineered Nanomaterials." *Nature Protocols* 12 (2): 355–371. doi:10.1038/nprot.2016.172.
- DeLoid, G. M., J. M. Cohen, G. Pyrgiotakis, S. V. Pirela, A. Pal, J. Liu, J. Srebric, and P. Demokritou. 2015. "Advanced Computational Modeling for in Vitro Nanomaterial Dosimetry." *Particle and Fibre Toxicology* 12: 32. doi:10.1186/s12989-015-0109-1.
- DeLoid, G. M., Y. Wang, K. Kapronezai, L. R. Lorente, R. Zhang, G. Pyrgiotakis, N. V. Konduru, et al. 2017. "An Integrated Methodology for Assessing the Impact of Food Matrix and Gastrointestinal Effects on the Biokinetics and Cellular Toxicity of Ingested Engineered Nanomaterials." *Particle and Fibre Toxicology* 14 (1): 40. doi:10.1186/s12989-017-0221-5.
- Donaldson, K., and C. A. Poland. 2013. "Nanotoxicity: challenging the Myth of Nano-Specific Toxicity." *Current Opinion in Biotechnology* 24 (4): 724–734. doi:10.1016/j.copbio.2013.05.003.
- ECHA. 2017. "How to Prepare Registration Dossiers That Cover Nanoforms: Best Practices." *European Chemical Agency*, May. [https://enuveprod-universitatpolit.netdna-ssl.com/php\\_preencionintegral/sites/default/files/noticia/38091/field\\_adjuntos/howtoregisternanoen.pdf](https://enuveprod-universitatpolit.netdna-ssl.com/php_preencionintegral/sites/default/files/noticia/38091/field_adjuntos/howtoregisternanoen.pdf)
- European Commission. 2018. "Commission Regulation (EU) 2018/1881 of 3 December 2018 amending Regulation (EC) No 1907/2006 of the European Parliament and of the Council on the Registration, Evaluation, Authorisation and Restriction of Chemicals (REACH) as regards Annexes I, III, VI, VII, VIII, IX, X, XI, and XII to address nanoforms of substances (Text with EEA relevance)." *Official Journal of the European Union*, December 4. <https://eur-lex.europa.eu/legal-content/EN/TXT/PDF/?uri=CELEX:32018R1881>
- Gao, X., and G. V. Lowry. 2018. "Progress towards Standardized and Validated Characterizations for Measuring Physicochemical Properties of Manufactured Nanomaterials Relevant to Nano Health and Safety Risks." *NanoImpact* 9: 14–30. doi:10.1016/j.impact.2017.09.002.
- Gollwitzer, C., D. Bartczak, H. Goenaga-Infante, V. Kestens, M. Krumrey, C. Minelli, M. Palmi, et al. 2016. "A Comparison of Techniques for Size Measurement of Nanoparticles in Cell Culture Medium." *Analytical Methods* 8 (26): 5272–5282. doi:10.1039/C6AY00419A.
- Jensen, K., Y. Kembouche, E. Christiansen, N. Jacobsen, H. Wallin, C. Guiot, O. Spalla, and O. Witschger. 2011. *The Generic NANOGENOTOX Dispersion Protocol—Standard Operation Procedure (SOP)*. NANOGENOTOX Deliverable Report 3. Copenhagen, Denmark: National Research Centre for the Working Environment.
- Lin, M. Y., H. M. Lindsay, D. A. Weitz, R. C. Ball, R. Klein, and P. Meakin. 1990. "Universal reaction-limited colloid aggregation." *Physical Review A, Atomic, Molecular, and Optical Physics* 41 (4): 2005–2020. doi:10.1103/physrev.41.2005.
- Lison, D., L. C. Thomassen, V. Rabolli, L. Gonzalez, D. Napierska, J. W. Seo, M. Kirsch-Volders, P. Hoet, C. E. Kirschhock, and J. A. Martens. 2008. "Nominal and Effective Dosimetry of Silica Nanoparticles in Cytotoxicity Assays." *Toxicological Sciences* 104 (1): 155–162. doi:10.1093/toxsci/kfn072.
- Liu, J., J. Katahara, G. Li, S. Coe-Sullivan, and R. H. Hurt. 2012. "Degradation Products From Consumer Nanocomposites: A Case Study on Quantum Dot Lighting." *Environmental Science & Technology* 46 (6): 3220–3227. doi:10.1021/es204430f.
- Mehn, D., I. M. Rio-Echevarria, D. Gilliland, M. Kaiser, K. Vilsmeier, P. Schuck, and W. Wohlleben. 2018. "Identification of Nanomaterials: A Validation Report of Two Laboratories Using Analytical Ultracentrifugation with Fixed and Ramped Speed Options." *NanoImpact* 10: 87–96. doi:10.1016/j.impact.2017.12.005.
- Ministère de l'Environnement. 2015. *Éléments issus des déclarations des substances à l'état nanoparticulaire: Exercice 2015*. Lyon, France: Ministère de l'Environnement.
- Oomen, A. G., E. A. Bleeker, P. M. Bos, F. van Broekhuizen, S. Gottardo, M. Groenewold, D. Hristozov, et al. 2015. "Grouping and Read-across Approaches for Risk Assessment of Nanomaterials." *International Journal of Environmental Research and Public Health* 12 (10): 13415–13434. doi:10.3390/ijerph121013415.
- Oomen, A. G., K. G. Steinhäuser, E. A. J. Bleeker, F. van Broekhuizen, A. Sips, S. Dekkers, S. W. P. Wijnhoven, and P. G. Sayre. 2018. "Risk Assessment Frameworks for Nanomaterials: Scope, Link to Regulations, Applicability, and Outline for Future Directions in View of Needed Increase in Efficiency." *NanoImpact* 9: 1–13. doi:10.1016/j.impact.2017.09.001.
- Petersen, E. J., A. R. M. Bustos, B. Toman, M. Johnson, M. Ellefson, C. G. C. A. L. Neuer, Q. Chan, et al. 2019. "Determining What Really Counts: Modeling and Measuring Nanoparticle Number Concentrations." *Environmental Science: Nano* 6 (9): 2876–2896.
- Rasmussen, K., J. Mast, P.-J. De Temmerman, E. Verleysen, N. Waegeneers, F. Van Steen, J. C. Pizzolon, L. De Temmerman, E. Van Doren, and K. A. Jensen. 2014. "Titanium Dioxide, NM-100, NM-101, NM-102, NM-103, NM-104, NM-105: Characterisation and Physico-Chemical Properties." *JRC Science and Policy Reports*.
- Sauer, U. G., A. Aumann, L. Ma-Hock, R. Landsiedel, and W. Wohlleben. 2015. "Influence of Dispersive Agent on Nanomaterial Agglomeration and Implications for Biological Effects in Vivo or in vitro." *Toxicology in Vitro* 29 (1): 182–186. doi:10.1016/j.tiv.2014.10.011.
- Schaefer, J., C. Schulze, E. E. J. Marxer, U. F. Schaefer, W. Wohlleben, U. Bakowsky, and C. M. Lehr. 2012. "Atomic Force Microscopy and Analytical Ultracentrifugation for Probing Nanomaterial Protein Interactions." *ACS Nano* 6 (6): 4603–4614. doi:10.1021/nn202657q.



- Stark, W., P. Stoessel, W. Wohlleben, and A. Hafner. 2015. "Industrial Applications of Nanoparticles." *Chemical Society Reviews* 44 (16): 5793–5805. doi:10.1039/c4cs00362d.
- Teeguarden, J. G., P. M. Hinderliter, G. Orr, B. D. Thrall, and J. G. Pounds. 2007. "Particokinetics in Vitro: dosimetry Considerations for in Vitro Nanoparticle Toxicity Assessments." *Toxicological Sciences* 95 (2): 300–312.
- Vila, L., L. Rubio, B. Annangi, A. García-Rodríguez, R. Marcos, and A. Hernández. 2017. "Frozen Dispersions of Nanomaterials Are a Useful Operational Procedure in Nanotoxicology." *Nanotoxicology* 11 (1): 31–40. doi:10.1080/17435390.2016.1262918.
- Wigger, H., W. Wohlleben, and B. Nowack. 2018. "Redefining Environmental Nanomaterial Flows: Consequences of the Regulatory Nanomaterial Definition on the Results of Environmental Exposure Models." *Environmental Science: Nano* 5 (6): 1372–1385.
- Wohlleben, W. 2012. "Validity Range of Centrifuges for the Regulation of Nanomaterials: From Classification to as-Tested Coronas." *Journal of Nanoparticle Research : An Interdisciplinary Forum for Nanoscale Science and Technology* 14 (12): 1300. doi:10.1007/s11051-012-1300-z.
- Wohlleben, W., V. Coleman, and D. Gilliland. 2019. "Analytical Centrifugation." In *Characterization of Nanoparticles: Measurement Processes for Nanoparticles*, edited by W. Unger, I. V.-D. Hodoroaba and A. Shard. Amsterdam, The Netherlands: Elsevier.
- Wohlleben, W., M. D. Driessen, S. Raesch, U. F. Schaefer, C. Schulze, B. Vacano, A. Vennemann, et al. 2016. "Influence of Agglomeration and Specific Lung Lining Lipid/Protein Interaction on Short-Term Inhalation Toxicity." *Nanotoxicology* 10 (7): 970–911. doi:10.3109/17435390.2016.1155671.
- Wohlleben, W., B. Hellack, C. Nickel, M. Herrchen, K. Hund-Rinke, K. Kettler, C. Riebeling, et al. 2019. "The nanoGRAVUR Framework to Group (nano)materials for their occupational, consumer, environmental risks based on a harmonized set of material properties, applied to 34 case studies." *Nanoscale* 11 (38): 17637–17654. doi:10.1039/c9nr03306h.
- Wohlleben, W., C. Kingston, J. Carter, E. Sahle-Demessie, S. Vázquez-Campos, B. Acrey, C.-Y. Chen, et al. 2017. "NanoRelease: Pilot Interlaboratory Comparison of a Weathering Protocol Applied to Resilient and Labile Polymers with and without Embedded Carbon Nanotubes." *Carbon* 113: 346–360. doi:10.1016/j.carbon.2016.11.011.
- Wohlleben, W., C. Punckt, J. Aghassi-Hagmann, F. Siebers, F. Menzel, D. Esken, C.-P. Drexel, et al. 2017. "Nanoenabled Products: Categories, Manufacture, and Applications: Protocols and Industrial Innovations." In *Metrology and Standardization for Nanotechnology: Protocols and Industrial Innovations*, edited by E. Mansfield, D. L. Kaiser, D. Fujita, and M. Van de Voorde, 411–464. Hoboken, NJ: John Wiley & Sons.
- Xia, X. R., N. A. Monteiro-Riviere, and J. E. Riviere. 2010. "An Index for Characterization of Nanomaterials in Biological Systems." *Nature Nanotechnology* 5 (9): 671–675. doi:10.1038/nnano.2010.164.

### 3.2 MANUSCRIPTS SUBMITTED OR UNDER PEER REVIEW

Biodissolution in cascaded simulants of the gastro-intestinal tract: towards robust screening methods and nanomaterial grouping.

**Keller JG<sup>a,b\*</sup>**, Cristo LD<sup>c\*</sup>, Seleci DA<sup>b</sup>, Landsiedel R<sup>a</sup>, Werle K<sup>b</sup>, Sabella S<sup>c</sup>, Wohlleben W<sup>b\*</sup>

\* equal contribution

<sup>a</sup>BASF SE, Dept. Of Experimental Toxicology and Ecology, 67056 Ludwigshafen, Germany

<sup>b</sup>BASF SE, Dept. of Material Physics, 67056 Ludwigshafen, Germany

<sup>c</sup>Instituto Italiano di Tecnologia, Nanoregulatory Platform, Drug Discovery and Development Department, 16163 Genova, Italy

#### Introduction

Ingested ENM pass through at least three clearly differentiated compartments: mouth (saliva), stomach, intestine. Especially pharmacological applications of targeted release particles often consider separately the sub compartments of small vs. large intestine vs. colon.[137] Substances in nanoform may become bioavailable by dissolution of the particles,[138] or, to a smaller extent, may be internalized as particles.[139] Ions that were dissolved in one compartment may be complexed and may re-precipitate in the next compartment.[140, 141] Reactive processes in the relatively aggressive compartments may induce transformation of the crystallinity, surface chemistry, particle size and state of agglomeration, to name the descriptors that are most important next to the dissolution rate. The transformed particles may induce local effects during the GIT passage[142] or after internalization and systemic availability to the liver and beyond.[143] The food-grade TiO<sub>2</sub> E171 with only >36% of the particles being below the size of 100 nm accumulated in the body to some extent[99] and a spurious signal was detected in placenta perfusates and in meconium (the first stool of newborns), the size distribution of which differed significantly with 70% to 100% of particles below 100nm.[144] The in-vivo study alone cannot decide if the particles that became systemically available are a *fraction* of the pristine material, or a *transformation* thereof. Physical-chemical investigation is needed. When the specific ENM is susceptible[145] to the reaction partners in GIT conditions, it is important to assess transformation not only with regard to biokinetics, but also as element of a realistic hazard assessment: before dosing in-vitro experiments one must design the exposure identity by pre-treatments of ENM to mimic the in-vivo transformation.[146]

Several implementations of cascaded GIT dissolution testing have been published.[141, 147-151] On that basis, two ongoing OECD projects are developing guidance and guidelines to simulate and assess the GIT dissolution and transformation; both are targeting a cascaded incubation in saliva, stomach and intestine simulants. However, the exact composition of simulant fluids, the most appropriate methods of sampling, of separation of ions from remaining particles, and analytics of both fractions, are a matter of debate.

E.g., studies on Ag NM300 have shown that ions are complexed by enzymes acting as ion scavenger, thus shifting the dissolution towards ions and accelerating the kinetics rate of particle dissolution.[147] However, complex fluids with high concentrations of enzymes are challenging in fractionation and analytics. Food component may further increase realism but may not increase robustness of results. The guidance by EFSA does not require complex fluids, and it only indicates an assessment criterion for quickly dissolving ENM

(88% in 30 minutes), meaning that particles dissolve already during the diffusion through the mucus layer and do not even get in touch with any tissue. This can be considered as the *upper* limit of the biologically relevant range of dissolved fraction, and it triggers an exemption from the need to perform nano-specific risk assessment (i.e., read-across to the ionic form).

Here we assess the relevance of the enzymes via their impact a) on ion dissolution and b) on particle transformation. We then apply a robust medium in a screening of case studies of different nanoforms and non-nanoforms of oxides of Zn, Si, Ce, Ti, and of organic pigments of DPP, ML2A, Isoindolinone substance classes. Our results can inform the assessment of GIT biodissolution by screening methods as required for grouping of different nanoforms and can be considered as more robust option for the OECD round robin that is planned in the frame of the NanoHarmony project. As corollary, we aim to explore if one can, be comparison between dissolution experiments and in-vivo literature, propose a practical *lower* limit of the biologically relevant range of dissolution.

## Methods

The in-vitro setup consists of a stirred beaker with cascaded addition of simulants for saliva, stomach, intestine. The setup and its adaptation to nanomaterials adheres to ISO TS 19057. The chosen concentration matches the max daily intake of nanomaterials through food, as proposed by EFSA.

The saliva dispersions were stirred for 5 min at a temperature of 37 °C. After removing a sample, gastric juice was added and set to a pH 2.0 to 2.5. During two hours of stirring at 37 °C, samples were collected, and finally intestinal fluid was added, and set to a pH of 6.4. Again, during two hours of stirring at 37 °C, samples were collected. Immediately after drawing the samples, they were split by ultrafiltration for analysis of dissolved components and of remaining particles.

The simulant fluids are standardized in DIN 19738 [152] and currently being harmonized by the OECD project for a new TG “Determination of solubility and dissolution rate of nanomaterials in water and relevant synthetic biologically mediums” (lead by Denmark and Germany). The ENM were dispersed with a BRANSON Sonifier 450D at an amplitude of 30% for 16 minutes within an inverted cup-horn sonicator to deliver an energy output of 7.35 W. A 50 mL Nalgene® bottle was used to reduce inorganic impurities. For fluids with enzymes, the enzymes were added after the sonication process. The saliva dispersions were stirred for 5 min at a temperature of 37 °C. After removing 5 mL of the dispersion for ion and transformation analysis, 21 mL of gastric juice was added and adjusted to a pH 2.0. After two hours of stirring at 37 °C, the next 5 mL sample was drawn and analyzed, and 25 mL of intestinal fluid was added, and the pH was adjusted to 6.4. Again, after two hours of stirring, the last sample was drawn and analyzed. Immediately after drawing the samples, they were split for analysis of dissolved components and of remaining particles.

For dissolution analysis, the dispersion was filtered through a 0.02 µm Al-Si syringe filter to remove particles and stop them from further dissolving. For inorganics, the filtrate was diluted by a factor of 10 with 0.1N HNO<sub>3</sub> and was analyzed by ICPMS (Nexion 2000b, Perkin Elmer,) with a Meinhardt nebulizer and Argon gas flow of 0.92 L/min and a pump rate of 18 rpm. The external calibration used concentrations of 0.1/1/10/100/1000/1000 ppb depending on the analyzed ion. For Si the detection limit was at 10 ppb.



## RESULTS

The filtrate of organics was analyzed by UV-Vis spectroscopy (Cary 5000, Agilent Technologies, Santa Clara, CA, US) in 5-cm-cuvettes with calibration by the extinction coefficient as described above. For constituent particle analysis, we employed a SAXS, XRD and TEM with SAD. The benchmark materials were analyzed via TEM with SAD at an acceleration voltage of 200 keV under bright-field conditions. (Tecnai G2-F20ST. FEI Company, Hillsboro, USA). Therefore, the final particle dispersion was diluted by factor of 100.000 and centrifuged onto TEM grids at 5000 g.

For both benchmark materials and organic pigments (which are crystalline), the sample was dried, spread on glass and subjected to XRD analysis of the crystalline identity (by the characteristic diffraction peaks) and analysis of the crystallite size (by fitting the broadening of the peaks via EVA). The instrument D8 Advance Serie 2 employed a Cu-Anode with 0.1° collimation; the diffracted X-rays were selected at 8 mm with Ni 0.5 mm aperture (Soller 4°; Lynx-Eye 3°). The particle size of amorphous silica was in the detection interval of our local SAXS instrument. Here an analog detector was used.

The agglomerate size analysis was employed through spICPMS. Here, spICPMS was not applicable or not valuable for some particles: we did not analyze materials that dissolve quickly (ZnO), very small particles (SiO<sub>2</sub>), organics (pigments). We did analyze TiO<sub>2</sub>, CeO<sub>2</sub>, BaSO<sub>4</sub> with and without enzymes. We are aware, however, that the incubation is (by EFSA requirements) and concentrations far higher than admitted for spICPMS analysis. The dilution of samples invariably changes adsorbates (“soft corona”), such that only agglomerates induced by “hard coronas” are detectable.

The initial concentration of pigments was aligned with the BfR publication. [141] We chose the “high” starting concentration of 6 mg/ml, which is successively diluted to 1mg/mL in intestine, because only in this approach the total mass is sufficient for XRD analysis. The same approach had to be taken for SAXS and XRD analysis of metal containing ENM.

*Table 2 Composition of GIT simulant media according to DIN ISO 19738 media*

Composition DIN ISO 19738		[mg/L]
Saliva	NaCl	1667
	NaSCN	500
	Na <sub>2</sub> SO <sub>4</sub>	1833
	NaHCO <sub>3</sub>	500
	KCL	1500
	KH <sub>2</sub> PO <sub>4</sub>	2000
	CaCl <sub>2</sub> *2H <sub>2</sub> O	500
	Uric acid	333
	Urea	33
Not always included	Mucin	2500
	α-Amylase	833
Stomach	NaCl	4143
	KCl	1000
	KH <sub>2</sub> PO <sub>4</sub>	386
Not always included	Mucin	4286
	Pepsin	1429
	conc. HCl	20 µl

Intestine	KCl	300
	CaCl <sub>2</sub> *2H <sub>2</sub> O	500
	MgCl <sub>2</sub> *6H <sub>2</sub> O	200
	NaHCO <sub>3</sub>	1000
	Urea	300
Not always included	Pancreatin	9000
	Trypsin	300
always in intestine	Bile	9000

For other analytical approaches, especially with regard to the quantification of dissolved ions, and for substances with known daily intake, we approximated the relevant test concentration by referencing the maximum daily intake to the 4 to 5 L of human GIT secretions as recommended by EFSA.[153] With an approximate uptake of 1.1-2.2 mg/kg body-weight/day by humans, TiO<sub>2</sub> is one of the most relevant food additives.[99] For SiO<sub>2</sub>, the European Food Safety Authority (EFSA) estimates an even higher daily intake of between 20-50 mg for a 60 kg person.[102] This estimate would translate to a maximum relevant concentration of 50 mg/4 L=12.5 mg/L. Considering finally the limits of analytical methods and a margin of uncertainty, we finally decided to compare all metal-based materials primarily at a concentration of 50 mg/L in the intestine compartment, which is about half of the “low” dose of Sieg et al. but still above the maximum relevant concentration.

## Results and Discussion

### Optimization of methodology on benchmark materials

In order to optimize the methodology of cascaded GI treatment the relevance and the impact of enzymes on both the ion dissolution as well as the particle transformation was assessed on a selection of benchmark materials. Here, ZnO NM110 was used as a benchmark material for quickly dissolving ENM under acidic conditions within both labs. SiO<sub>2</sub> NM200 was chosen as a partial dissolving material and tested in the lab of BASF, and TiO<sub>2</sub> E171 was used as a benchmark material with very slow dissolution in both labs.

**TiO<sub>2</sub> E171**

The dissolution and transformation behavior of TiO<sub>2</sub> E171 was assessed in both type 1 and type 3 media. Within the TEM comparison of TiO<sub>2</sub> E171 (Figure XB) with and without enzymes, no significant difference can be observed. Furthermore, this is confirmed through SAD. TiO<sub>2</sub> NM105 which was used as a benchmark material behaved similar and thus showed no significant transformation after cascaded GI treatment. The biopersistence in both media was also confirmed through XRD evaluation. Here the data showed no new peaks and no significant change in peak with. Remarkably however, the interaction of enzymes with the

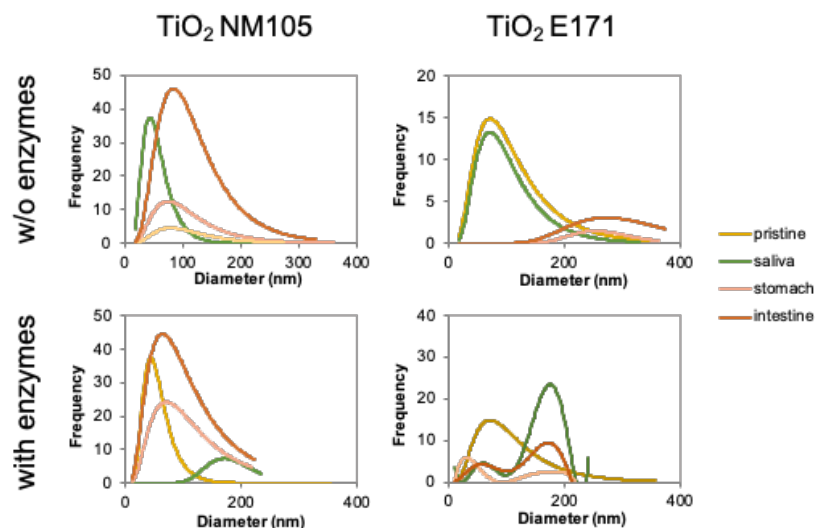


Figure 5: Particle size distribution as determined through spICP-MS for TiO<sub>2</sub> NM105 and TiO<sub>2</sub> E171 with and without enzymes.

particles (DIN type 1) increased the ion concentration after filtration with 0.02  $\mu\text{m}$  as detected via ICP-MS within the intestinal fluid vs. the enzyme-free intestinal fluid (DIN type 3). This detectable increase in Ti-ion concentration up to a very low level of <0.05% (Figure 6) was observed for both TiO<sub>2</sub> materials, E171 and NM105. This is explicable through the complexation of ions with the enzymes, shifting the dissolution kinetics. spICP-MS showed that an agglomeration through enzymes can induce a bimodal size distribution of E171 but keeping within the same size range of 40-400 nm (Figure 5). NM105 only differed within the saliva medium. Within the other two fluids, no modulation by enzymes was detected.



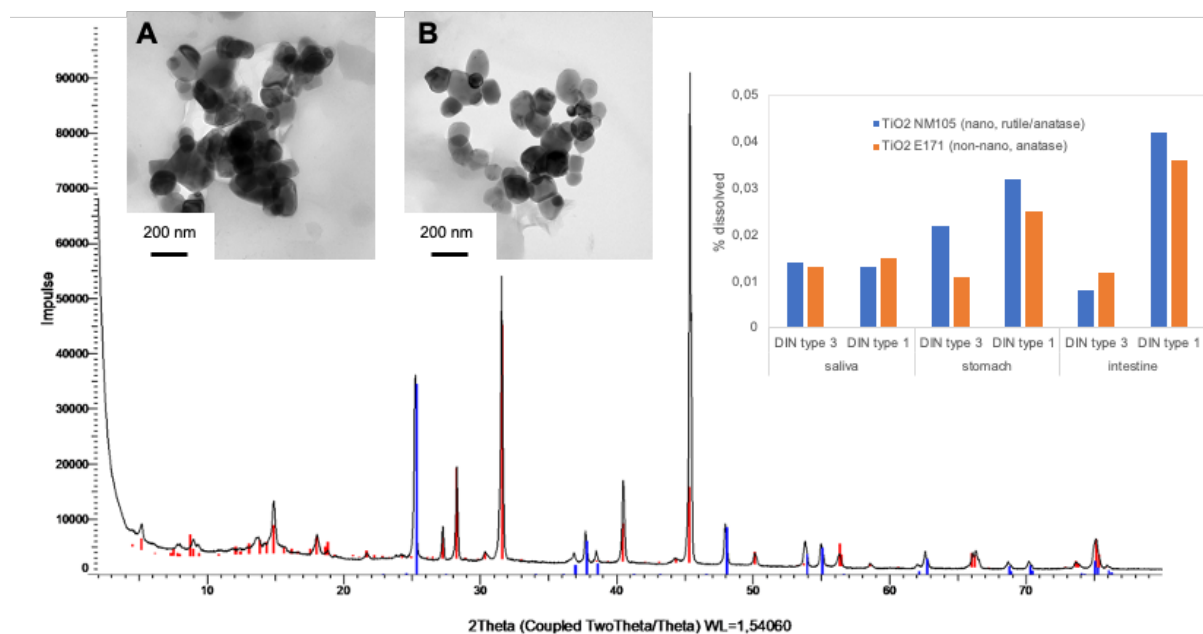


Figure 6: XRD Graph of pristine  $\text{TiO}_2$  E171 particles (blue),  $\text{TiO}_2$  after dissolution in cascaded GI fluids (black) and the media background (red). TEM images after type 1 media (A) and type 3 media (B).  $\text{TiO}_2$  dissolution concentration in different compartments in dependence on media composition.

### $\text{SiO}_2$ NM200

Based on the TEM images for the comparison for  $\text{SiO}_2$  NM200 a better dispersion was observed with enzymes after the cascaded GI treatment (Figure 7) when compared to the results without enzymes.

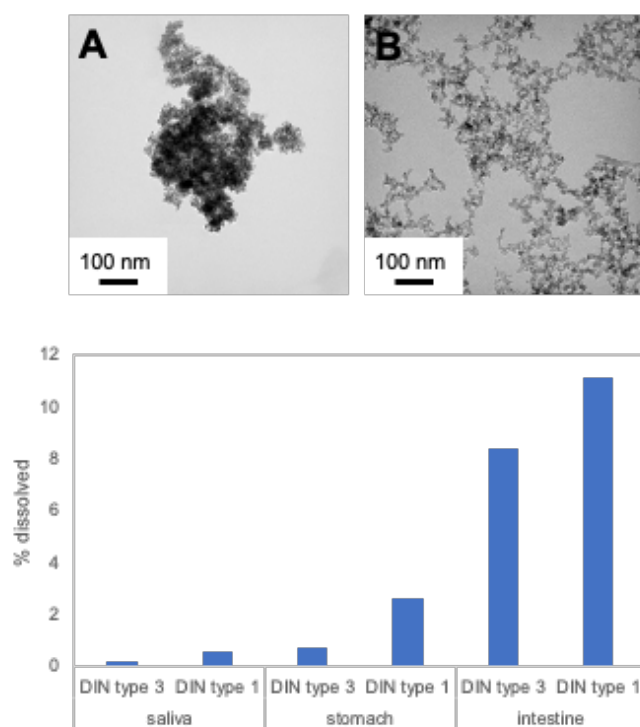


Figure 7: TEM images after type 1 media (A) and type 3 media (B).  $\text{SiO}_2$  NM200 dissolved percentage in different compartments in dependence on media composition.

Also, for the case of  $\text{SiO}_2$  NM200, the filtration of the sample with enzymes increased the ion concentration within the intestinal juice vs. the enzyme-free type 3 to a certain extent. This observation was made in all three compartments. All of the resulting dissolved percentages remain far below the daily uptake of  $\text{SiO}_2$  ENM as proposed by EFSA cutoffs and so the enzymes are not critical to the assessment of this material.

### ZnO NM110

Finally, we needed to check that our quickly dissolving benchmark is correctly detected without enzymes. Extensive work on the dissolution behavior of ZnO NM110 was done

within the lab of IIT, here a dissolution in the range of 80-100% was detected after 30 min of incubation

## RESULTS

within intestinal juice. Which resembles the time point of 150 min from start point as relevant for EFSA regulatory purposes. The concentration remained rather constant for initial concentrations of 25 mg/L and 50 mg/L but showed an inferior dissolved content for the concentration of 100 mg/L over time at the end of the digestion process (240 min). At concentrations of 25 mg/L and 50 mg/L ZnO NM110 shows the behavior of an instantaneous dissolving NF. However, this test showed that the dissolution process appears to be concentration dependent. Though, an interaction of the ions with the media composition resulting in aggregation processes may occur.

Furthermore, the data showed, that the dissolution rate is dependent on the enzyme composition with protein components accelerating the dissolution rate. Since no aminoacidic substrates are within the media and no biochemical mechanisms are present, this acceleration may be induced through improving the colloidal stability. The ion concentration of ZnO in juice 3 without enzymes was reduced to 50% within intestinal fluid at the end of the digestion process after 240 mins.

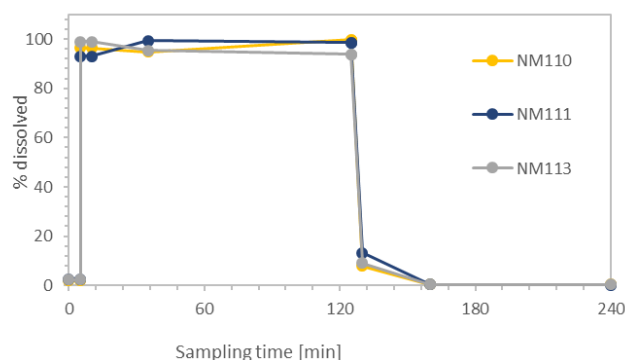


Figure 8: % dissolved Zn in dependence of time in the three different compartments for ZnO NM110 (yellow), ZnO NM111 (blue) and ZnO NM113 (gray).

These observations made at IIT were furthermore supported by results obtained within the labs at BASF for the gastric juice. Here the exposure of ZnO to two more versions of Juice 3 with inorganic and organic components but without enzymes resulted in a fast dissolution effect. ZnO NM110 here showed a half-time <5 min but as soon as the intestinal media was added, a reprecipitation was induced and the dissolved Zn content dropped close to zero with low dissolution. The behavior within the intestinal

fluid as measured at BASF is in contrast to the results obtained at IIT. The significant differences between 0% dissolution at BASF and 50% dissolution at IIT after 240 mins may be related to the initial concentration of the material.

When testing three different ZnO ENM differing in particle size, surface coating, and hydrophobicity, NM110, NM111, NM113 with the enzyme free DIN 19738 media (type 3) similar dissolution behavior was observed within all three different media. With an instantaneous dissolution of nearly 100% after changing from saliva to gastric juice and a sudden drop as soon as the intestinal juice was added, and the pH adjusted to 7.4 (Figure 8)

Tests done within the commercially available pre-mixed FaSSIF V2 simulants were not taken into account, since the exact composition is not known and can therefore not help to understand potential dissolution effects on the media composition.

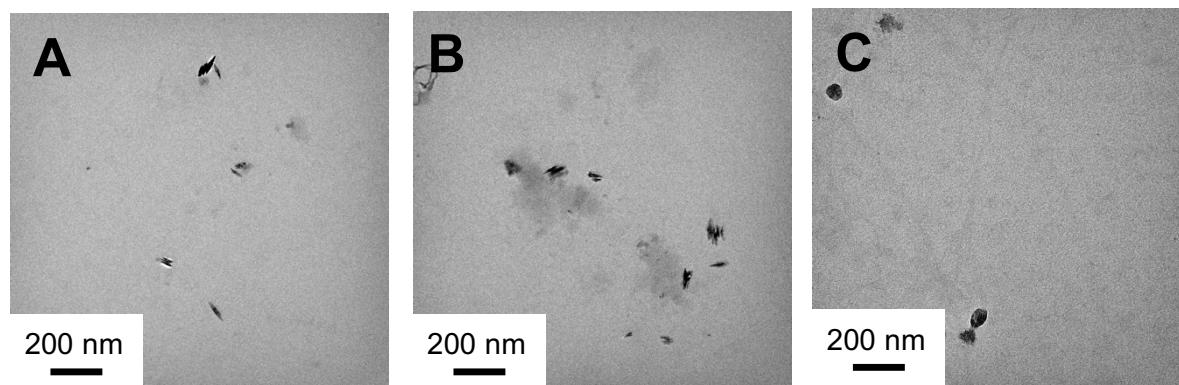


Figure 9: TEM images after dissolution in the three different compartments for ZnO NM110 (A), ZnO NM111 (B) and ZnO NM113 (C)

The TEM image analysis showed that small particles were found after the exposure to the cascaded simulated GI conditions, however these particles could not be identified as Zn by EDX. Figure 9 shows the residues for the three tested ZnO particles.

#### **Interim conclusion on optimization of methodology on benchmark materials:**

The methodology to assess the dissolution and transformation of ENMs within the gastrointestinal tract in a simulated cascaded system with the three relevant juices including all relevant components such as inorganics, enzymes, organics is regarded as gold standard. However, frequently observed a clogging of filters in the presence of the enzymes. This is not a mere technical issue, since ions that are complexed by the enzymes will then not pass the membranes and will not be detected as dissolved component. The counts before and after filtration were identical for Ag in saliva (SS1) and FaSSGF media with triplicate reproducibility of 0.48% to 0.94% (1 SD). In contrast, the counts after filtration in FaSSIF medium scattered by 39% (1 SD) and were 60% lower than before filtration. This is strong indication of complexation of Ag in the FaSSIF medium, leading to false negative conclusions on dissolution of the Ag ENM. On Cu in saliva, scatter increased from 0.952% to 2.59% at reduction of count rate by 15% before and after filtration. On Ti in FaSSIF, scatter increased from 0.14% to 9.1% at reduction of count rate by 31% before and after filtration. In all of the three cases (Cu@saliva, Ti@FaSSIF, Ag@FaSSIF), the effects are attributed to complexation of ions, leading to filtration losses and false negatives. Analogue experiments in the DIN media of Table 1 are ongoing and will be published elsewhere. In some cases, enzymes induce inhomogeneities that do not allow representative sampling of digested ENM.

Using simplified versions of these fluids (without enzymes) resolves such practical issues separation of ions from particles, and on sampling and the homogeneity. By the above data, we have demonstrated that the morphology of remaining particles is not influenced by the enzymes.



## RESULTS

---

We therefore propose that screening with simplified juices by removing the enzymes or organic components is possible, if the ion dissolution results on benchmark materials match the results obtained by full juices, both for quickly dissolving benchmark (ZnO NM110) and very slowly dissolving benchmark (TiO<sub>2</sub> E171). For the specific case of the DIN 19738 media without enzymes, the above data demonstrates such validity.

### Screening of dissolution and transformation

Across all case studies, and across the three GIT compartments, the dissolved concentration spans an enormous range of values from 20 mg/L (fully dissolved ZnO in stomach), down to 0.02 µg/L (DPP pigment in stomach). These are six orders of magnitude. In the following we present and discuss case studies in order of decreasing dissolution

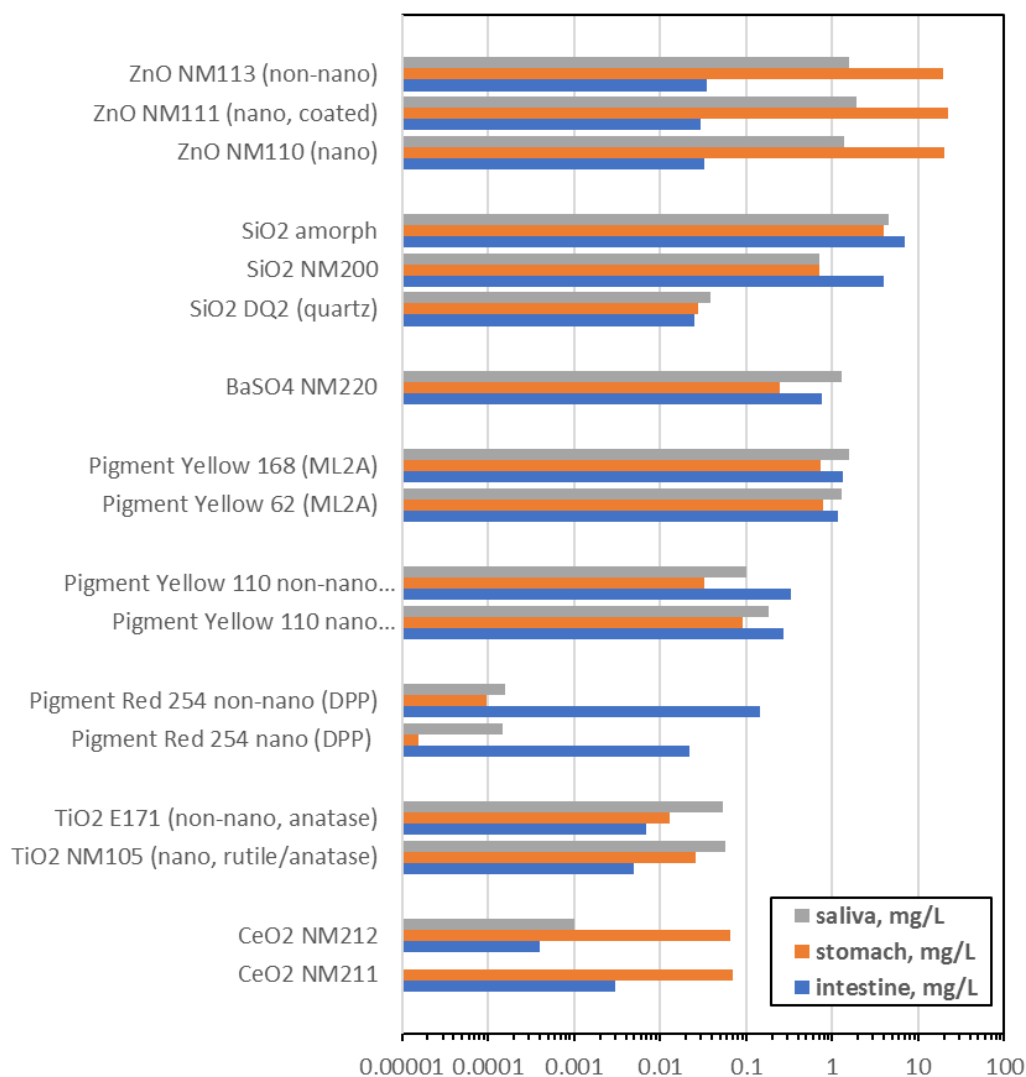


Figure 10: Dissolved concentration in each of the three compartments, with DINI9738 type 3 juices.

### ZnO comparison of NFs

The dissolved ion concentrations of the three ZnO forms, thereof one NF (NM110), one coated NF (NM111), one non-nano-form (NM113) are strikingly similar in all three cascaded compartments. What's more, also the kinetics with 5-minute time resolution is not significantly different: All ZnO materials remain undissolved in saliva, then dissolve more than 90% in less than 5 minutes in stomach. This is sufficient to fulfill the EFSA guidance that a nano-specific assessment is not required.

Immediately after switching to the intestinal simulant, the free Zn ions are reduced to less than 20% of the total Zn content, and within 30 minutes, less than 1% remains as free Zn ions. This behavior is a

## RESULTS

---

transformation that starts from Zn ions and is linked to the limited solubility of Zn ions at the near-neutral pH of the intestinal fluid. We note that enzymes are not required to dissolve ZnO. They can modulate the complexation of ions, but this could only accelerate dissolution. However, as shown by IIT in GRACIOUS, the complexation of Zn ions by enzymes can interfere with the separation by ultrafiltration or ultracentrifugation, thus inducing false negatives of apparently limited dissolution, whereas the Zn ions have actually been released, but were not accessible to detection.

### **SiO<sub>2</sub>**

The dissolution experiments on the different silicate materials, confirm the trend on solubility in dependency on the crystal structure. Where amorphous silicate materials dissolve whereas crystalline silicate material persists. Here we explored that SiO<sub>2</sub>\_amorphous quicker than SiO<sub>2</sub> NM200, which again dissolves much quicker than the crystalline DQ12. For the silicate materials we expect a higher dissolution within the neutral pH of saliva and intestinal fluid, which is in line Sohal et al. However, the observed dissolution kinetic also confirms the fact that NaCl favors the dissolution of SiO<sub>2</sub>. Within a GRACIOUS case study, BASF investigated the transformation of small silicate particles through SAXS. Here we had trouble separating the particles, due to their small size below 10 nm. Furthermore, for biological scenarios unrealistically high concentration had to be used. (See SI)

### **CeO<sub>2</sub>**

For both CeO<sub>2</sub>, spICPMS shows similar trends: low agglomeration in saliva and intestine, higher agglomeration of the pristine material than as well as in the in the gastric juice. This phenomenon seems to be dictated by the substance primarily, and is not explicable by pH changes, especially not after the dilution for spICPMS measurement. The XRD evaluation did not show any significant change of crystallite size with 11 nm before and after the digestion process. Furthermore, no new XRD diffraction peaks were found, confirming no transformation before and after. The TEM image (Figure 11 A and B) as well as the SAD shows no deviation from the TEM and SAD of the pristine material.



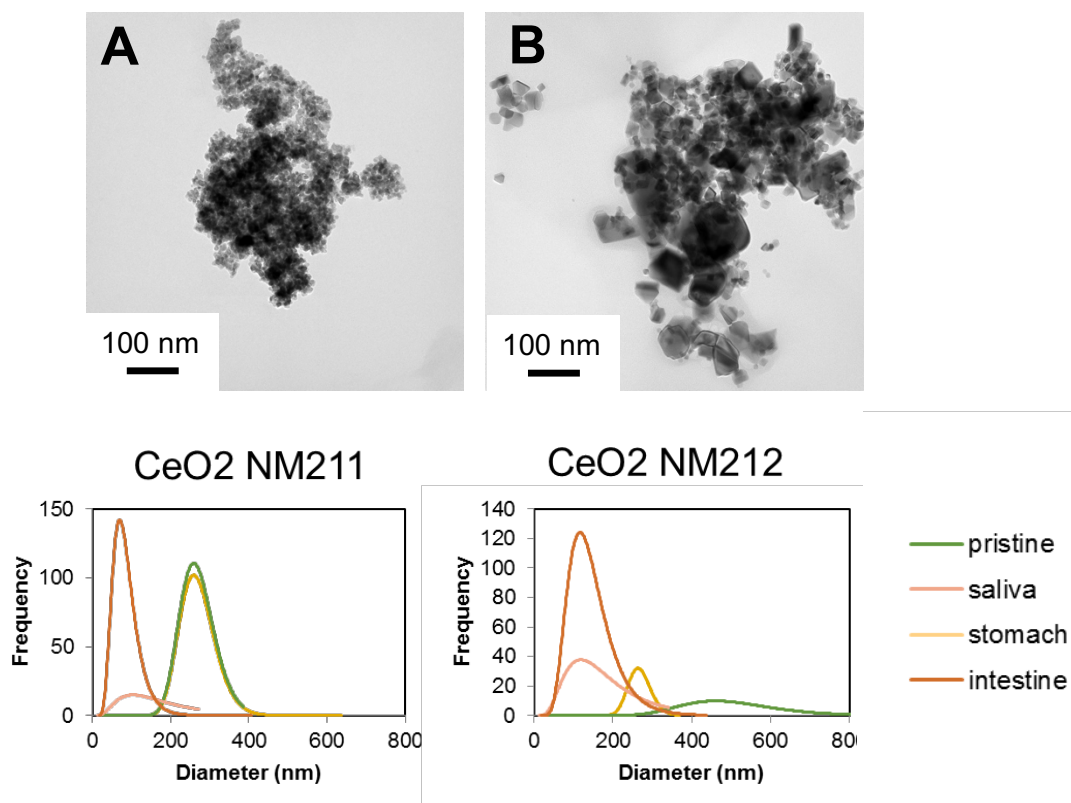


Figure 11: TEM images of (A)  $\text{CeO}_2$  NM211 and (B)  $\text{CeO}_2$  NM212 after exposure to the cascaded GI conditions. And spICP-MS particle size distribution for both materials.

## TiO<sub>2</sub>

Additionally, to the food-grade E171, NM105 was used as a benchmark material. Here we also did not observe any significant changes of crystallite size nor new XRD diffraction peaks after exposure to the three different compartments. Moreover, the comparison of the TEM images confirms this for NM105.

Sample	Crystallite size in nm	Uncertainty	Difference relevant?	Evaluated diffraction peak angle
[5] TiO <sub>2</sub> NM105 after GI	17	2	no	48,0 °
[6] TiO <sub>2</sub> NM105 pristine	18	2		48,0 °
[7] TiO <sub>2</sub> E171 after GI	46	5	no	25,4 °
[8] TiO <sub>2</sub> E171 pristine	56	6		25,4 °
[9] CeO <sub>2</sub> NM211 after GI	11	1	no	47,5 °
[10] CeO <sub>2</sub> NM211 pristine	11	1		47,5 °
[11] CeO <sub>2</sub> NM212 after GI	22	2	no	47,5 °
[12] CeO <sub>2</sub> NM212 pristine	26	3		47,5 °
[13] Background GIT	/			/

### **Organic Pigments**

Each two forms were investigated, and showed that organic pigments were as insoluble as  $\text{TiO}_2$  or  $\text{CeO}_2$ , with the exception of metal-lake pigments, which showed weak dissolution. Isoindolinone substance were stable in stomach with a comparable dissolved concentration as  $\text{TiO}_2$  or  $\text{CeO}_2$ . However, within the intestine an about 5-fold higher concentration was found than within the stomach. The tests furthermore showed that in terms of biopersistence there was no significant difference between the NF and non-nano-form

The NFs of metal-lake pigments (ML2A class) was unstable under GI conditions, comparable dissolved concentration as  $\text{SiO}_2$ . The overall dissolved content was about 20-to-50-fold higher than for  $\text{TiO}_2$  and 20-to-50-fold lower than for  $\text{ZnO}$ . The substance (classes) of laked (metal-precipitated) pigments were previously found to dissociate under physiological conditions.[154]

The DPP pigments were insoluble, in two compartments with a 100-fold lower dissolved concentration than  $\text{TiO}_2$ . However, in intestine the concentration was within the order of  $\text{TiO}_2$  stomach concentration. At an extremely low level, the highest measurable dissolved content of maximally 0.024 %, with 0.143 mg/L dissolved concentration is found in the intestine simulat with bile salts and nearly neutral pH6.5. There is no significant difference between the NF and non-nano-form

The observed lack of bioavailability of purely organic pigments is in accord with in vivo findings of oral gavage experiments and the current REACH data,[155, 156] and sets them apart from partially dissolving metals and metal oxides.[141, 157, 158] The metal-laked pigments might require a separate assessment.

## Conclusion

When assessing the ion dissolution of metal-oxide ENMs, enzymes might have a relevant effect on the kinetic as they can act as ions scavengers. The formation of enzyme-ion complexes shifts the equilibrium to dissolution as observed in the case of TiO<sub>2</sub> E171, where a 0.05% higher dissolved content was observed within the enzyme containing media. If the test is intended for prediction of the bio accessibility of the generated ions, then it is important to include enzymes and only consider the complete medium composition as the gold standard. However, for solubility considerations, screening and ranking NFs in simplified juices is possible. The EFSA guidance only provides a fixed criterion for quickly soluble materials, but no criterion for insoluble materials.[153, 159] For dissolution analysis, the material is considered as *quickly soluble* if more than 88% are dissolved after 30 minutes in either stomach compartment or intestine compartment. Based on data obtained on TiO<sub>2</sub>, we propose that the material is considered as *insoluble* if less than 0.1 mg/L are dissolved in any of the three cascaded compartments. No bioavailability of organic pigments, as compared to the partial degradation of some oxides (ZnO, SiO<sub>2</sub>, CuO) is predicted by the current abiotic screening and is in accord with in vivo findings of oral gavage experiments. [140, 155-158, 160-162] Future studies need to also consider alternative metrics such as a “% dissolved” cutoff or k-rate cut-off (which is not easily calculated in a cascaded model with re-precipitation), and limits of acceptable dissimilarity between NFs. On the primary particle transformation and agglomeration though, enzymes only have limited effects. The use of the whole juice including enzymes might be considered as a gold standard, however it can influence the sampling by clogging the filters and effect the homogeneity during sampling. Screening with simplified juices, without organics or enzymes can be applied to benchmark materials which match the results obtained within full juices both for quickly dissolving (ZnO NM110) and very slowly dissolving benchmark (TiO<sub>2</sub> E171). For particle analysis, the particles are considered as *transforming* if the XRD diffractogram shows the emergence of new peaks or the loss of peaks compared to the pristine materials. methods that do not require concentrations far above the expected daily intake (XRD, SAXS), and not far below (spICPMS) would be preferred. As a supporting criterion, a change of crystallite size that exceeds that the combined uncertainty of crystallite size analysis of 10% on both the pristine and GIT-aged material, is taken as indication of transformation. TEM is unique on morphology changes, and also widely available. We tend to not propose spICPMS as criterion due to dilution concerns, and limited added value from case studies. To the best of our knowledge this is the first contribution where cascaded GIT screening media were validated and then applied on different NFs per substance for grouping and read across purposes. When using the benchmark materials to compare the dissolution behavior to the testing materials, no difference was found between the NFs in terms of their dissolution and transformation behavior despite substantial differences between substances (nano & non-nano).



## References

- Bettini, S., E. Boutet-Robinet, C. Cartier, C. Coméra, E. Gaultier, J. Dupuy, N. Naud, S. Taché, P. Gysan, S. Reguer, N. Thieriet, M. Réfrégiers, D. Thiaudière, J.-P. Cravedi, M. Carrière, J.-N. Audinot, F. H. Pierre, L. Guzylack-Piriou and E. Houdeau (2017). "Food-grade TiO<sub>2</sub> impairs intestinal and systemic immune homeostasis, initiates preneoplastic lesions and promotes aberrant crypt development in the rat colon." *Scientific Reports* **7**: 40373.
- Bove, P., M. A. Malvindi and S. Sabella (2017). *In vitro* human digestion test to monitor the dissolution of silver nanoparticles.
- Bove, P., M. A. Malvindi, S. S. Kote, R. Bertorelli, M. Summa and S. Sabella (2017). "Dissolution test for risk assessment of nanoparticles: a pilot study." *Nanoscale* **9**(19): 6315-6326.
- Bove, P., M. A. Malvindi and S. Sabella (2017). "In vitro human digestion test to monitor the dissolution of silver nanoparticles." *Journal of Physics: Conference Series* **838**(1): 012003.
- Buesen, R., R. Landsiedel, U. G. Sauer, W. Wohlleben, S. Groeters, V. Strauss, H. Kamp and B. van Ravenzwaay (2014). "Effects of SiO<sub>2</sub>, ZrO<sub>2</sub>, and BaSO<sub>4</sub> nanomaterials with or without surface functionalization upon 28-day oral exposure to rats." *Archives of toxicology* **88**(10): 1881-1906.
- De Jong, W. H., E. De Rijk, A. Bonetto, W. Wohlleben, V. Stone, A. Brunelli, E. Badetti, A. Marcomini, I. Gosens and F. R. Cassee (2019). "Toxicity of copper oxide and basic copper carbonate nanoparticles after short-term oral exposure in rats." *Nanotoxicology* **13**(1): 50-72.
- EC (2003). "Scientific Committee on Toxicity, Ecotoxicity and the Environment (CSTEE)."
- Graham, U. M., M. T. Tseng, J. B. Jasinski, R. A. Yokel, J. M. Unrine, B. H. Davis, A. K. Dozier, S. S. Hardas, R. Sultana and E. A. Grulke (2014). "In vivo processing of ceria nanoparticles inside liver: impact on free-radical scavenging activity and oxidative stress." *ChemPlusChem* **79**(8): 1083-1088.
- Gray, E. P., C. L. Browning, M. Wang, K. D. Gion, E. Y. Chao, K. J. Koski, A. B. Kane and R. H. Hurt (2018). "Biodissolution and cellular response to MoO<sub>3</sub> nanoribbons and a new framework for early hazard screening for 2D materials." *Environmental Science: Nano* **5**(11): 2545-2559.
- Guillard, A., E. Gaultier, C. Cartier, L. Devoille, J. Noireaux, L. Chevalier, M. Morin, F. Grandin, M. Z. Lacroix, C. Coméra, A. Cazanave, A. de Place, V. Gayrard, V. Bach, K. Chardon, N. Bekhti, K. Adel-Patient, C. Vayssière, P. Fisicaro, N. Feltin, F. de la Farge, N. Picard-Hagen, B. Lamas and E. Houdeau (2020). "Basal Ti level in the human placenta and meconium and evidence of a materno-foetal transfer of food-grade TiO<sub>2</sub> nanoparticles in an ex vivo placental perfusion model." *Particle and Fibre Toxicology* **17**(1): 51.
- Hardy, A., D. Benford, T. Halldorsson, M. J. Jeger, H. K. Knutsen, S. More, H. Naegeli, H. Noteborn, C. Ockleford and A. Ricci (2018). "Guidance on risk assessment of the application of nanoscience and nanotechnologies in the food and feed chain: Part 1, human and animal health." *EFSA Journal* **16**(7).
- Krause, B. C., F. L. Kriegel, D. Rosenkranz, N. Dreijack, J. Tentschert, H. Jungnickel, P. Jalili, V. Fessard, P. Laux and A. Luch (2020). "Aluminum and aluminum oxide nanomaterials uptake after oral exposure—a comparative study." *Scientific reports* **10**(1): 1-10.
- Laux, P., T. Tralau, J. Tentschert, A. Blume, S. Al Dahouk, W. Bäuml, E. Bernstein, B. Bocca, A. Alimonti and H. Colebrook (2016). "A medical-toxicological view of tattooing." *The Lancet* **387**(10016): 395-402.
- Marques, M., R. Loeberberg and M. Almukainzi (2011). "Simulated Biological Fluids with Possible Application in Dissolution Testing." *Dissolution Technologies* **8**: 15-29.
- Molina, R. M., N. V. Konduru, R. J. Jimenez, G. Pyrgiotakis, P. Demokritou, W. Wohlleben and J. D. Brain (2014). "Bioavailability, distribution and clearance of tracheally instilled, gavaged or injected cerium dioxide nanoparticles and ionic cerium." *Environmental Science: Nano* **1**(6): 561-573.
- Pavan, C., M. Delle Piane, M. Gullo, F. Filippi, B. Fubini, P. Hoet, C. J. Horwell, F. Huaux, D. Lison, C. Lo Giudice, G. Martra, E. Montfort, R. Schins, M. Sulpizi, K. Wegner, M. Wyart-Remy, C. Ziemann and F. Turci (2019). "The puzzling issue of silica toxicity: are silanols bridging the gaps between surface states and pathogenicity?" *Particle and Fibre Toxicology* **16**(1): 32.
- Poças, F. and R. Franz (2018). overview on European regulatory issues, legislation, and EFSA evaluations of nanomaterials. *Nanomaterials for Food Packaging*, Elsevier: 277-300.
- Sauer, U. G. and R. Kreiling (2019). "The grouping and assessment strategy for organic pigments (GRAPE): Scientific evidence to facilitate regulatory decision-making." *Regulatory Toxicology and Pharmacology*: 104501.
- Schneider, S., R. Landsiedel, W. Wohlleben, A. Wolterbeek, I. Waalkens-Berendsen and H. van de Sandt (2011). "Oral prenatal developmental toxicity study with NM-200 synthetic amorphous silica in Wistar rats." *Reproductive Toxicology* **32**(2): 173-174.
- Sieg, H., C. Kästner, B. Krause, T. Meyer, A. Burel, L. Böhmert, D. Lichtenstein, H. Jungnickel, J. Tentschert and P. Laux (2017). "Impact of an artificial digestion procedure on aluminum-containing nanomaterials." *Langmuir* **33**(40): 10726-10735.

- Sohal, I. S., Y. K. Cho, K. S. O'Fallon, P. Gaines, P. Demokritou and D. Bello (2018). "Dissolution Behavior and Biodurability of Ingested Engineered Nanomaterials in the Gastrointestinal Environment." ACS Nano **12**(8): 8115-8128.
- Stock, V., L. Böhmert, E. Lisicki, R. Block, J. Cara-Carmona, L. K. Pack, R. Selb, D. Lichtenstein, L. Voss, C. J. Henderson, E. Zabinsky, H. Sieg, A. Braeuning and A. Lampen (2019). "Uptake and effects of orally ingested polystyrene microplastic particles in vitro and in vivo." Archives of Toxicology **93**(7): 1817-1833.
- Stratmann, H., M. Hellmund, U. Veith, N. End and W. Teubner (2020). "Indicators for lack of systemic availability of organic pigments." Regulatory Toxicology and Pharmacology: 104719.
- Walczak, A. P. (2015). Development of an integrated in vitro model for the prediction of oral bioavailability of nanoparticles, Wageningen University.
- Walczak, A. P., R. Fokkink, R. Peters, P. Tromp, Z. E. Herrera Rivera, I. M. Rietjens, P. J. Hendriksen and H. Bouwmeester (2012). "Behaviour of silver nanoparticles and silver ions in an in vitro human gastrointestinal digestion model." Nanotoxicology **7**(7): 1198-1210.
- Warheit, D. B., S. C. Brown and E. M. Donner (2015). "Acute and subchronic oral toxicity studies in rats with nanoscale and pigment grade titanium dioxide particles." Food and Chemical Toxicology **84**: 208-224.
- Weir, A., P. Westerhoff, L. Fabricius, K. Hristovski and N. Von Goetz (2012). "Titanium dioxide nanoparticles in food and personal care products." Environmental science & technology **46**(4): 2242-2250.

---



---

## **5 SUMMARY AND CONCLUSION**

**Dissolution and Transformation (after inhalation)**

In this work, the continuous flow system, which was previously developed to assess the persistence of man-made vitreous fibres (MMVF), was adapted and used to assess the dissolution rate and transformation of a broad set of nanomaterials in relevant physiological media. The nanomaterials were chosen based on the production volume as well as industrial relevance (Figure 1). The adapted continuous flow system with an integrated quantification of ions by ICP-MS and detection of transformation through TEM advantages over a static dissolution approach was shown. This was further confirmed by exemplarily comparing BaSO<sub>4</sub> NM220 dissolution results with alveolar macrophage-assisted dissolution and existing *in vivo* clearance data in rats. The flow-through assessment of BaSO<sub>4</sub> NM220 did not only predict the persistence correctly but also led to the same Ostwald ripening observed in *in vivo* studies. Control measurements on CuO demonstrated that this effect was not a methodological artifact.

A high degree of consistency of the abiotic dissolution and the *in vivo* clearance has been achieved for CeO<sub>2</sub> NM211, CeO<sub>2</sub> NM212 CuO, nano BaSO<sub>4</sub> NM220 and ZnO NM111 (Table 3). Within this material selection, the measured half-times span four orders of magnitude from less than one day (ZnO, quickly dissolving) to about 10 days (BaSO<sub>4</sub>, partially dissolving, partially transforming) to more than 1000 (TiO<sub>2</sub>, very slowly dissolving). This confirmed the predictive value of our adapted CFS. We then assessed in comparative testing the modulation of dissolution by the particle's structure: The dissolution is a surface-controlled process. Nanomaterials were measured to have the same dissolution rate as their non-nano analogues of the same substance. Of course, at identical dissolution *rates* the *halftimes* of the nanomaterial is shorter than that of larger-sized particles due to its higher specific surface area. We finally also confirmed the expectation that coatings can modulate dissolution, but for a quickly dissolving material as ZnO this transient retardation only lasts a few hours.

Table 3 Comparison abiotic dynamic dissolution in PSF after 7 days vs. *in vivo* pulmonary clearance in % after 21 days.

	<b>Abiotic dynamic dissolution PSF % dissolved per 7 days</b>	<b>In vivo pulmonary % cleared per 21 days</b>
CeO <sub>2</sub> NM212	3	5
CeO <sub>2</sub> NM211	3	7
BaSO <sub>4</sub> NM220	58 *	52 *
CuO	100	>85 (LoD)
ZnO NM111	99	93

We confirmed the expectation that the composition of the physiological media has a profound effect on the dissolution and transformation of nanomaterials: Already within the pulmonary compartment, the lung lining fluid with pH7.4 was compared against the lysosomal fluid with pH 4.5 and different organic acids. Materials

such as ZnO, BaSO<sub>4</sub>, CuO, Fe<sub>2</sub>O<sub>3</sub>, and CuPhthalocyanines exerted a higher dissolution within the more acidic lysosomal fluid; all SiO<sub>2</sub> based materials dissolved significantly quicker within the neutral lung lining fluid. Based on the intra-lab validation of the CFS for pulmonary dissolution, we advanced the robustness of the method by standardisation. While the routine setup worked satisfactorily with low initial masses of ENM and subsequent elemental electron microscopy analysis, it was essential to further refine the setup for slowly and partially dissolving nanomaterials, for which we developed a model to show that dissolution is limited by saturation conditions dictated by the ratio of total surface area (SA) over fluid flow (V). When assessing these materials, a ramping of the flow rate led to an expansion of the measurable SA/V ratio by five orders of magnitude. It further enabled the assessment of the dissolution behaviour in more detail. By choosing a SA/V between 0.03 h/μm and 0.01 h/μm, the measured dissolution correctly predicted the observations made *in vivo* (Table 2). Outside of this SA/V range, false prediction invalidated the test conditions, e.g., TiO<sub>2</sub> would have been predicted as partially dissolving, or, on the opposite end, ZnO would have been predicted as only partially dissolving. Therefore, it is mandatory to exclude all SA/V values above 0.03 h/μm and below 0.01 h/μm. The same experimental setup for different materials ranging in chemical composition, size, shape, surface functionalization, and crystallinity was used to enable grouping of different nanoforms.

The SOP describing the dissolution setup was transferred to other labs for inter-lab comparison and harmonization. Based on ZnO data in PSF, KRIS was able to reproduce and confirm the quick dissolution that we had measured. We standardised this method and drafted an SOP which is currently the basis of an OECD test guideline development (lead by Denmark and Germany). One of the publications was highlighted by ECHA in their recent guidance on “information requirements and chemical safety assessment “.[108]

### **Dissolution and Transformation (after ingestion)**

For the biodissolution after ingestion, in the successive GIT compartments, we implemented a setup that allowed the cascaded incubation in complex fluids that simulate saliva, stomach, intestine. When assessing the ions released by dissolution of metal-oxide ENMs, enzymes (and other proteins) might have a relevant effect on the kinetic as they can act as ions scavengers. The formation of enzyme-ion complexes shifts the equilibrium to dissolution as observed in the case of TiO<sub>2</sub> E171, where a 0.05% higher dissolved content was observed within the enzyme containing media. If the test is intended to predict unbound ions released from the ENM, then including enzymes in the simulation fluid can be useful. However, for solubility considerations only, more simple fluids are sufficient. Moreover, the use of simulation fluids including enzymes might influence the sampling by clogging the filters and effect the homogeneity during sampling.

For regulatory purposes, the EFSA provides a fixed criterion to define quickly soluble materials, but no criterion for less soluble materials.[153, 159] For dissolution analysis, the material is considered as *quickly soluble* if more than 88% are dissolved after 30 minutes in either stomach compartment or intestine compartment. Based on data obtained on TiO<sub>2</sub>, we propose that the material is considered *insoluble* if less than 0.1 mg/L are dissolved in any of the three cascaded compartments. In contrast to partially degrading of some inorganic oxides (ZnO, SiO<sub>2</sub>, CuO) For organic pigments no release of dissolved, bioavailable is

expected based on the abiotic dissolution screening. This is in accord with *in vivo* findings in oral gavage studies. [140, 155-158, 160-162] Future studies need to also consider alternative metrics such as a “% dissolved” or k-rate (which is not easily calculated in a cascaded model with re-precipitation) and criteria to define if different nanoforms are sufficiently similar dissolving after ingestion.

To the best of our knowledge this is the first contribution where cascaded GIT screening media were validated and then applied to different nanoforms for grouping and read across purposes. When using the benchmark materials to compare the dissolution behavior to the testing materials, no difference was found between the nanoforms in terms of their dissolution and transformation behavior despite substantial differences (nano & non-nano, particle size, coating). Among three different ZnO nanoforms we found a similarity in both the dissolution as well as transformation behavior. The same observation was made for two different TiO<sub>2</sub> nanoforms. Here similar dissolution and the absence of transformation was detected for both materials. Eventually this setup will allow grouping of nanoforms based on their biopersistence within a cascaded GIT setup.

Via the PATROLS and NanoHarmony projects, the results contribute to the robustness of two OECD projects focusing on integrated testing of oral uptake and toxicity.

### **Dosimetry in *in vitro* toxicity studies**

The sample preparation and the dosimetry of ENM *in vitro* testing was explored. Through analysis of the mass fraction of the dose accumulating at the cells, the predictivity of results obtained in *in vitro* toxicity studies could be enhanced through relevant dose-response curves. [124, 163] By furthermore exploring the possibilities and limitations of a freeze-thaw protocol for sample preparation, parallel testing through flash freezing the samples after sonication was enabled. [164] The freeze-thaw sample preparation altered the fraction of agglomerates by 35% compared to freshly prepared dispersions. After one-hour incubation, however, the difference was below 25%. Thus, overall, it modulated the dosimetry of the particles. Nevertheless, characterization and *in silico* modelling that reflected the actual colloidal properties during *in vitro* toxicology could be obtained by freeze-thawing.

Regarding dosimetry, the fundamental notion that the deposited dose is lower than the total administered dose can be easily supported by simple measurements (DLS, VCM) and DG modelling. The deposited dose prediction varied significantly, ranging between 9 to 73% for the different nanomaterials with reflective boundary conditions. Especially for well-dispersed ENMs, uncertainty was introduced by choosing an arbitrary value of the affinity of particles to stick to cell surfaces (“reflective” vs. “adhesive” bottom). Additionally, for polydisperse ENMs, minor details of the particle size distribution strongly influenced the modelled dosimetry, such that the choice of the measurement technique - e.g., DLS or AUC - introduced further uncertainties to the dosimetry modelling. For any polydisperse ENM, reducing the output compartment height to 0.0005 mm helped to remove dips in the particle settling traces and the generation of erroneous predictions, but tremendously increased the DG model computing resources. Therefore, with optimized computing resources, the uncertainty of the actual deposited dose was considerable. When using



standardized dispersion protocols (NANoREG) and polydisperse industrially relevant materials, the model's predictions incurred an uncertainty of the deposited dose due to uncertainty in the inputs. The dose-response obtained by the modelled prediction of the deposited dose can thus shift significantly: If the *in vitro* reactivity of different nanoforms differs by a factor of 2.5, one cannot conclude if the results are from a dissimilarity of biological interactions or the methodical uncertainty of dosimetry modelling. For very well dispersed nanoforms, the range of uncertainty extends to a factor of 10.

In current grouping frameworks, the uncertainty within the dosimetry predictions is not adequately taken into account. Therefore, AUC data, which was previously shown to act as a reliable source for dosimetry predictions, can be used as a basis for *in-vitro* toxicology assessment by also including systematic uncertainties.



---

## **6 OUTLOOK**

Methods developed in this thesis project provide data on extrinsic material properties which are relevant for the risk assessment of ENMs. A coherent ranking scheme needs to be developed to bring the data obtained by these methods into use for hazard and risk assessment of ENMs. Furthermore, the extrinsic reactivity of an ENM, needs to be included in this scheme next to the dissolution, transformation, and dosimetry of ENMs. Such a comprehensive grouping framework is currently developed within the GRACIOUS project. [165]

The relevant properties describing nanomaterials' hazard potential are also playing an essential role in advanced materials. Some of these materials are not captured by the REACH definition of a nanomaterials in terms of their external dimensions. However, due to a nano-porous structure they still retain unique properties. As a first example, the dissolution and reactivity of a set of organic and inorganic aerogels, was assessed. Overall, these results showed a very low inherent toxicity of aerogels and supported a grouping based on similarities in physicochemical properties. The validity of the concept and methods developed for particles needs to be further verified for advanced materials that contain or release nanostructures.

The current frameworks are being developed to address the risk assessment of monoconstituent nanomaterials. These are relatively simple in terms of their chemical composition as well as surface functionalization. However, with increasing applications, the complexity of nanomaterials may increase as well. These next-generation nanomaterials with a more complex composition, may have different and more difficult to understand toxicological properties. Examples include the active centers in battery electrodes, catalysts, or photovoltaic modules. Therefore, the validity of these frameworks must be checked. The HARMLESS project - which will start in 2021, aims to provide novel tools, guidance, and decision support for balancing functionality versus risk for next-generation nanomaterials.



---

## **7 ZUSAMMENFASSUNG**

Während die Anwendungsgebiete von technisch hergestellten Nanomaterialien aufgrund ihrer einzigartigen Eigenschaften ständig zunehmen, müssen wir auch bedenken, dass sie auch potenzielle Risiken bergen. Es gibt zahlreiche Wege, wie Menschen sowohl natürlich vorkommende Nanomaterialien als auch technische hergestellte Nanomaterialien aufnehmen können, entweder durch Einatmen, Verschlucken oder durch dermale Aufnahme und Injektionen für medizinische Anwendungen. Daher ist es von größtem Interesse deren Gefährdungspotenzial zu berücksichtigen. Alle Nanomaterialien, die auf den europäischen Markt kommen, müssen daher auf ihre Sicherheit für Mensch und Umwelt getestet werden. Die bisher etablierten Richtlinien zur Bestimmung des Gefährdungspotenzials von Bulkmaterialien müssen jedoch angepasst werden, um auf Nanomaterialien angewandt werden zu können. Insbesondere für Inhalationsstudien müssen die physikalisch-chemischen Eigenschaften von Nanomaterialien bewertet werden. Die Dispergierbarkeit, die Form, die Partikelgröße, die Auflösung, die Reaktivität und einige weitere intrinsische und extrinsische Eigenschaften haben einen direkten Einfluss auf die Ablagerung, den Transport sowie das Entzündungspotential in der Lunge.

Im Rahmen dieser Arbeit wurde eine Auswahl an Metall-, Metalloxid- und organischen Nanomaterialien auf der Grundlage industrieller Relevanz und verfügbarer *in-vivo* Toxizitätsdaten ausgewählt, um ihre extrinsischen Eigenschaften hinsichtlich ihres Risikopotentials zu bewerten.

Um den Verbleib und das Gefährdungspotenzial eines Nanomaterials im menschlichen Organismus oder in der Umwelt zu bestimmen, ist es zwingend notwendig zu verstehen, wie ein Nanomaterial mit physiologischen Medien interagiert. Wesentlich für das Verständnis des Verhaltens, ist die Bestimmung der Auflösung und der Transformation von ihnen in relevanten Medien. Von Mineralfasern ist bekannt, dass mit dem „Continuous Flow System“ (CFS) die Persistenz in der Lunge vorhergesagt werden kann.

Das eine Ziel der hier beschriebenen Arbeit war es, Methoden zur Untersuchung der Auflösung von Nanomaterialien zu entwickeln und zu standardisieren, um deren Verbleib im menschlichen Körper vorherzusagen. Hier wurde gezeigt, dass durch Anpassung des bereits für Mineralfasern etablierten Durchflusssystems sowie einer Quantifizierung der Ionen durch ICP-MS und Detektion der Transformation durch TEM deutliche Vorteile gegenüber einem statischen Auflösungsansatz erreicht wurden. Dies wurde durch den Vergleich der BaSO<sub>4</sub> NM220-Auflösungsergebnisse mit Daten aus Versuchen mit alveolaren Makrophagen-unterstützten Auflösung sowie bestehenden *in-vivo*-Daten in Ratten weiter gefestigt. Das angepasste Durchflusssystem war nicht nur im Stande die Persistenz des Nanomaterials im Tierversuch vorherzusagen, sondern zeigte auch die gleiche Ostwald-Reifung der BaSO<sub>4</sub> Partikeln, wie zuvor in Tierversuchen beobachtet wurde. Kontrollmessungen an CuO zeigten, dass dieser Effekt kein methodisches Artefakt war.

Ein hohes Maß an Übereinstimmung der abiotischen Auflösung und der *in vivo*-Clearance wurde für CeO<sub>2</sub> NM211, CeO<sub>2</sub> NM212 CuO, nano BaSO<sub>4</sub> NM220 und ZnO NM111 erreicht.

Zusätzlich konnte mit dieser Arbeit die Erwartung bestätigt werden, dass die Zusammensetzung des physiologischen Mediums einen tiefgreifenden Einfluss auf die Auflösung und Transformation von Nanomaterialien hat.

Während der Aufbau des CFS bei dem Großteil der Messungen die erwarteten Ergebnisse darstellen konnte, so war es unerlässlich, das Setup für sich langsam und nur teilweise auflösende Nanomaterialien weiter zu verfeinern, da die Auflösung durch Sättigungsbedingungen begrenzt wird. Hier führte eine zeitabhängige Steigerung der Flussrate zu einer Erweiterung des messbaren Bereichs um fünf Größenordnungen. Zudem wurde eine detailliertere Beurteilung des Auflösungsverhaltens für ebendiese Materialien ermöglicht.

Die Anleitung, die den Auflösungsaufbau sowie die Durchführung beschreibt, wurde an andere Labore zum Vergleich und zur Harmonisierung übertragen. Basierend auf ZnO-Daten in PSF konnte KRISS die in dieser Arbeit bestimmte, schnelle Auflösung, reproduzieren und bestätigen. Zusätzlich wurde diese Methode standardisiert und dient derzeit als Grundlage für die Entwicklung einer OECD-Prüfrichtlinie (unter Federführung von Dänemark und Deutschland). Eine der Veröffentlichungen wurde von der ECHA in ihrem jüngsten Leitfaden hervorgehoben. Die hieraus gewonnenen Daten können helfen, Gruppen von Nanoformen mit ähnlichen Gefahrenpotenzial zu identifizieren.

Für die Simulation der oralen Aufnahme wurde während dieser Arbeit ein Aufbau entwickelt, der die aufeinanderfolgende Inkubation in komplexen Flüssigkeiten erlaubt; Speichel, Magen und Darm. Bei der Auflösung von Nanomaterialien könnten Enzyme (und andere Proteine) einen relevanten Einfluss auf die Kinetik freigesetzter Ionen haben, da sie als Ionenfänger wirken können.

Basierend auf den für TiO<sub>2</sub> gewonnenen Daten kann die Aussage getroffen werden, dass das Material als unlöslich gilt, wenn weniger als 0,1 mg/L in einem der drei simulierten physiologischen Flüssigkeiten aufgelöst werden. Im Gegensatz zum teilweisen Abbau einiger anorganischer Oxide (ZnO, SiO<sub>2</sub>, CuO) wird für organische Pigmente auf der Grundlage des abiotischen Auflösungsscreenings keine Freisetzung von gelöstem, bioverfügbarem Material erwartet. Dies steht im Einklang mit *in-vivo*-Befunden oraler Studien. Zukünftige Studien sollten auch alternative Metriken in Betracht ziehen, wie z. B. den prozentualen aufgelösten Anteil oder die Auflösungsrate  $k$ , welche durch die Auflösung in aufeinanderfolgenden Medien deutlich komplexer zu berechnen ist. Bei der Verwendung von Benchmark-Materialien zum Vergleich des Auflösungsverhaltens wurde trotz erheblicher Unterschiede (nano & nicht-nano, Partikelgröße, Beschichtung) kein Unterschied zwischen den Nanoformen in Bezug auf ihr Auflösungs- und Transformationsverhalten gefunden. Unter drei verschiedenen ZnO-Nanoformen wurden Ähnlichkeiten sowohl im Auflösungs- als auch im Transformationsverhalten beobachtet.

Dieser Aufbau kann in Zukunft dazu dienen eine Gruppierung von Nanoformen basierend auf ihrer Biopersistenz innerhalb der verschiedenen oralen Medien zu ermöglichen. Die Daten finden Anwendung in den beiden Projekten, PATROLS und NanoHarmony, zwei OECD-Projekten, die sich unter anderem mit dem toxikologischen Potential der oralen Aufnahme beschäftigen.

Das andere Ziel der Arbeit war es, sowohl die Probenvorbereitung und Dosimetrie von Nanomaterialien als auch deren Beitrag zur Vorhersagekraft für *in-vitro*-Tests zu untersuchen. Durch die Analyse des sedimentierten Anteils in Abhängigkeit der Zeit, konnte die Vorhersagekraft durch entsprechende Dosis-Wirkungs-Kurven verbessert werden. Darüber hinaus wurden die Möglichkeiten und Grenzen eines Gefrier- und Auftau-Zyklus in der Probenvorbereitung untersucht. Wässrige Nanomaterial Dispersionen wurden

nach Behandlung im Ultraschallbad, schockgefrostet und erneut aufgetaut. Die Probenvorbereitung veränderte den Anteil der Agglomerate um 35 % im Vergleich zu frisch hergestellten Dispersionen. Nach einstündiger Inkubation lag der Unterschied jedoch unterhalb von 25 %. Obwohl der Gefrier-Auftau-Prozess die Partikel stärker agglomerieren ließ, konnten sowohl Charakterisierungen als auch Modellierungen durchgeführt werden, die die tatsächlichen kolloidalen Eigenschaften während *in-vitro* Versuche widerspiegeln.

Die Vorhersage der deponierten Dosis variierte erheblich und lag zwischen 9 und 73 % für die verschiedenen Nanomaterialien mit reflektierenden Randbedingungen. Dies konnte die Beobachtung erklären, dass die deponierte Dosis meist deutlich geringer ausfiel als die Gesamtdosis des Testsystems. Diese Beobachtung wurde zusätzlich unterstützt durch simple gravimetrische Messungen sowie Lichtstreuungsmethoden zur Bestimmung der Partikel- und Agglomeratgröße.

Im Modellierungsansatz wurde besonders für gut dispergierte Nanomaterialien die Unsicherheit des Testsystems durch die Wahl eines willkürlichen Wertes für die Affinität der Partikel, an Zelloberflächen eingeführt. Die Wahl zwischen "reflektierendem" vs. "adhäsivem" Boden, führte zur starken Beeinflussung polydisperser Nanomaterialien. Hier konnten bereits sehr kleine Abweichungen der Partikelgrößenverteilung die modellierte Dosimetrie stark beeinflussen. Durch die Verringerung des Abstands der Berechnungsabschnitte auf 0,0005mm von 0,015mm konnten fehlerhafte Vorhersagen beseitigt werden. Dies führte jedoch zu einem nahezu exponentiell gesteigerten Rechenaufwand. Bei Verwendung von standardisierten Protokollen (NANoREG) sowie polydispersen Materialien war die Vorhersage des Modells mit großer Unsicherheit der deponierten Dosis behaftet. Im Falle der Differenz in *in-vitro*-Reaktivität verschiedener Nanoformen um den Faktor 2,5 konnte bereits keine Aussage mehr getroffen werden, ob die Ergebnisse auf eine Ungleichheit der biologischen Wechselwirkungen oder auf die methodische Unsicherheit der Dosimetrie-Modellierung zurückzuführen sind. Im Falle von sehr gut dispergierten Nanoformen hat man hier Spielraum bis zu einer zehnfachen Unsicherheit.

Im aktuellen Gruppierungsrahmen wird die Unsicherheit innerhalb der Dosimetrie-Vorhersagen nicht angemessen berücksichtigt. Daher können die Daten - welche durch Analytische Ultrazentrifugen erzeugt wurden - von denen zuvor gezeigt wurde, dass sie als zuverlässige Quelle für Dosimetrie-Vorhersagen dienen, als Grundlage für die Bewertung der In-vitro-Toxikologie verwendet werden. Hier müssen lediglich systematische Unsicherheiten einbezogen werden.



---

## **8 REFERENCES**

1. Feynman, R.P., *There's plenty of room at the bottom*. California Institute of Technology, Engineering and Science magazine, 1960.
2. Binnig, G., et al., *Surface studies by scanning tunneling microscopy*. Physical review letters, 1982. **49**(1): p. 57.
3. Taniguchi, N., *On the basic concept of nanotechnology*. Proceeding of the ICPE, 1974.
4. Meetoo, D. and M. Lappin, *Nanotechnology and the future of diabetes management*. Journal of Diabetes Nursing, 2009. **13**(8): p. 288-297.
5. Marie, H.A. *Examples of Nanoscale Objects*. 2020 26.08.2020]; Available from: [thoughtco.com/examples-of-nanoscale-608575](http://thoughtco.com/examples-of-nanoscale-608575).
6. ISO, *ISO/TS 80004-2: 2015. Nanotechnologies-Vocabulary-Part 2: Nano-objects*. 2015.
7. Horikoshi, S. and N. Serpone, *Microwaves in nanoparticle synthesis: fundamentals and applications*. 2013: John Wiley & Sons.
8. Krug, H.F. and P. Wick, *Nanotoxicology: an interdisciplinary challenge*. Angewandte Chemie International Edition, 2011. **50**(6): p. 1260-1278.
9. EC, *Commission recommendation of 18 October 2011 on the definition of nanomaterial*. Commission recommendation of 18 October 2011 on the definition of nanomaterial, Official Journal of the European Union, 2011.
10. Testing, A.S.f. and Materials., *Standard terminology relating to nanotechnology*. Annual Book of ASTM Standards, 2006: p. 1085-1089.
11. Strambeanu, N., L. Demetrovici, and D. Dragos, *Natural sources of nanoparticles*, in *Nanoparticles' Promises and Risks*. 2015, Springer. p. 9-19.
12. Moghimi, S.M., A.C. Hunter, and J.C. Murray, *Nanomedicine: current status and future prospects*. The FASEB journal, 2005. **19**(3): p. 311-330.
13. Nel, A., et al., *Toxic potential of materials at the nanolevel*. science, 2006. **311**(5761): p. 622-627.
14. Karakoti, A., L. Hench, and S. Seal, *The potential toxicity of nanomaterials—the role of surfaces*. Jom, 2006. **58**(7): p. 77-82.
15. Daniel, M.-C. and D. Astruc, *Gold nanoparticles: assembly, supramolecular chemistry, quantum-size-related properties, and applications toward biology, catalysis, and nanotechnology*. Chemical reviews, 2004. **104**(1): p. 293-346.
16. Klabunde, K.J. and R.M. Richards, *Nanoscale materials in chemistry*. 2009: John Wiley & Sons.
17. Whitesides, G.M., *Nanoscience, nanotechnology, and chemistry*. Small, 2005. **1**(2): p. 172-179.
18. Whitesides, G.M., *Reinventing Chemistry*. Angewandte Chemie International Edition, 2015. **54**(11): p. 3196-3209.
19. Zhu, W., P.J. Bartos, and A. Porro, *Application of nanotechnology in construction*. Materials and Structures, 2004. **37**(9): p. 649-658.
20. Sanchez, F. and K. Sobolev, *Nanotechnology in concrete—a review*. Construction and building materials, 2010. **24**(11): p. 2060-2071.
21. Abdussalam-Mohammed, W., *Review of Therapeutic Applications of Nanotechnology in Medicine Field and its Side Effects*. Journal of Chemical Reviews, 2019. **1**(3. pp. 154-251): p. 243-251.
22. Bhattacharyya, D., et al., *Nanotechnology, big things from a tiny world: a review*. International Journal of u-and e-Service, Science and Technology, 2009. **2**(3): p. 29-38.
23. Koo, O.M., I. Rubinstein, and H. Onyuksel, *Role of nanotechnology in targeted drug delivery and imaging: a concise review*. Nanomedicine: Nanotechnology, Biology and Medicine, 2005. **1**(3): p. 193-212.
24. West, J.L. and N.J. Halas, *Applications of nanotechnology to biotechnology: Commentary*. Current opinion in Biotechnology, 2000. **11**(2): p. 215-217.
25. Webster, T.J., et al., *Nano-biotechnology: carbon nanofibres as improved neural and orthopaedic implants*. Nanotechnology, 2003. **15**(1): p. 48.
26. Roco, M.C. and W.S. Bainbridge, *Converging technologies for improving human performance: Nanotechnology, biotechnology, information technology and cognitive science*. 2013: Springer Science & Business Media.
27. Kumar, A. and M. Jee, *Nanotechnology: a review of applications and issues*. International Journal of Innovative Technology and Exploring Engineering (IJITEE), 2013. **3**(4): p. 1-2.
28. Korkin, A., P.S. Krstić, and J.C. Wells, *Nanotechnology for electronics, photonics, and renewable energy*. Vol. 78. 2010: Springer.

29. Malani, A.S., A.D. Chaudhari, and R.U. Sambhe, *A review on applications of nanotechnology in automotive industry*. International Journal of Mechanical, Aerospace, Industrial, Mechatronic and Manufacturing Engineering, 2016. **10**(1).
30. Asmatulu, R., P. Nguyen, and E. Asmatulu, *Nanotechnology safety in the automotive industry*, in *Nanotechnology safety*. 2013, Elsevier. p. 57-72.
31. Lohani, A., et al., *Nanotechnology-based cosmeceuticals*. International Scholarly Research Notices, 2014. **2014**.
32. Raj, S., et al., *Nanotechnology in cosmetics: Opportunities and challenges*. Journal of pharmacy & bioallied sciences, 2012. **4**(3): p. 186.
33. Duncan, T.V., *Applications of nanotechnology in food packaging and food safety: Barrier materials, antimicrobials and sensors*. Journal of Colloid and Interface Science, 2011. **363**(1): p. 1-24.
34. Sozer, N. and J.L. Kokini, *Nanotechnology and its applications in the food sector*. Trends in biotechnology, 2009. **27**(2): p. 82-89.
35. Lauterwasser, C., *Small sizes that matter: opportunities and risks of nanotechnologies. Report in Cooperation with the OECD International Futures Programme*. Allianz Center for Technology, Munich. <http://www.oecd.org/chemicalsafety/nanosafety/44108334.pdf>. Accessed, 2005.
36. Communities, C.o.t.E., *Preparing for our future: Developing a common strategy for key enabling technologies in the EU*. 2009.
37. Navya, P. and H.K. Daima, *Rational engineering of physicochemical properties of nanomaterials for biomedical applications with nanotoxicological perspectives*. Nano Convergence, 2016. **3**(1): p. 1.
38. Oomen, A.G., et al., *Concern-driven integrated approaches to nanomaterial testing and assessment - report of the NanoSafety Cluster Working Group 10*. Nanotoxicology., 2013.
39. Stone, V., et al., *ITS-NANO - Prioritising nanosafety research to develop a stakeholder driven intelligent testing strategy*. Particle and Fibre Toxicology, 2014. **11**(1): p. 9.
40. Colognato, R., et al., *Interactions with the Human Body*. 2012.
41. Buzea, C., I.I. Pacheco Blandino, and K. Robbie, *Nanomaterials and nanoparticles: Sources and toxicity*. Biointerphases, 2008. **2**: p. MR17-MR172.
42. Wang, J., et al., *Detection and analysis of reactive oxygen species (ROS) generated by nano-sized TiO<sub>2</sub> powder under ultrasonic irradiation and application in sonocatalytic degradation of organic dyes*. Ultrasonics Sonochemistry, 2011. **18**(1): p. 177-183.
43. Landsiedel, R., et al., *Testing metal-oxide nanomaterials for human safety*. Adv.Mater., 2010. **22**: p. 2601-2627.
44. Schanen, B.C., et al., *Exposure to titanium dioxide nanomaterials provokes inflammation of an in vitro human immune construct*. Acs Nano, 2009. **3**(9): p. 2523-2532.
45. Oberdorster, G., E. Oberdorster, and J. Oberdorster, *Nanotoxicology: an emerging discipline evolving from studies of ultrafine particles*. Environ Health Perspect, 2005. **113**: p. 823-839.
46. Singer, N. *New Products Bring Side Effect: Nanophobia*. 2008. **533**.
47. Alleyne, R. *Food manufacturers fear nanotechnology backlash*. 2010.
48. Fadeel, B., et al., *There's plenty of room at the forum: Potential risks and safety assessment of engineered nanomaterials*. Nanotoxicology, 2007. **1**(2): p. 73-84.
49. Grieger, K.D., S.F. Hansen, and A. Baun, *The known unknowns of nanomaterials: describing and characterizing uncertainty within environmental, health and safety risks*. Nanotoxicology, 2009. **3**(3): p. 222-233.
50. Woskie, S.R., et al., *Understanding Workplace Processes and Factors that Influence Exposures to Engineered Nanomaterials*. International Journal of Occupational and Environmental Health, 2010. **16**(4): p. 365-377.
51. Fadeel, B., A. Pietroiusti, and A.A. Shvedova, *Adverse effects of engineered nanomaterials: exposure, toxicology, and impact on human health*. 2017: Academic Press.
52. Nohynek, G.J. and E.K. Dufour, *Nano-sized cosmetic formulations or solid nanoparticles in sunscreens: a risk to human health?* Archives of toxicology, 2012. **86**(7): p. 1063-1075.
53. Ministère de la transition écologique et solidaire, *Éléments issus des déclarations des substances à l'état nanoparticulaire exercice 2019 : rapport d'étude*. 2020.
54. European Union Observatory for Nanomaterials. *Nanomaterial database*. 2020 [cited 2020 16.09]; Available from: [https://euon.echa.europa.eu/search-for-nanomaterials?p\\_p\\_id=nanosearch\\_WAR\\_dissnanoinventoriesportlet](https://euon.echa.europa.eu/search-for-nanomaterials?p_p_id=nanosearch_WAR_dissnanoinventoriesportlet).
55. Danish Consumer Council and Danish Technical University. *The Nanodatabase*. 2012 26.08.2020]; Available from: <http://nanodb.dk/>.
56. Seaton, A. and K. Donaldson, *Nanoscience, nanotoxicology, and the need to think small*. The Lancet, 2005. **365**(9463): p. 923-924.

## REFERENCES

---

57. Elder, A., et al., *Translocation of Inhaled Ultrafine Manganese Oxide Particles to the Central Nervous System*. Environmental Health Perspectives, 2006. **114**(8): p. 1172-1178.
58. Oberdörster, G. and T.A.J. Kuhlbusch, *In vivo effects: Methodologies and biokinetics of inhaled nanomaterials*. NanoImpact, 2018. **10**(Supplement C): p. 38-60.
59. Bouwmeester, H., M. van der Zande, and M.A. Jepson, *Effects of food-borne nanomaterials on gastrointestinal tissues and microbiota*. Wiley Interdisciplinary Reviews: Nanomedicine and Nanobiotechnology, 2018. **10**(1): p. e1481.
60. Katz, L.M., K. Dewan, and R.L. Bronaugh, *Nanotechnology in cosmetics*. Food and Chemical Toxicology, 2015. **85**: p. 127-137.
61. Monteiro-Riviere, N.A., et al., *Safety evaluation of sunscreen formulations containing titanium dioxide and zinc oxide nanoparticles in UVB sunburned skin: an in vitro and in vivo study*. Toxicological Sciences, 2011. **123**(1): p. 264-280.
62. Wagner, S., et al., *Spot the difference: engineered and natural nanoparticles in the environment—release, behavior, and fate*. Angewandte Chemie International Edition, 2014. **53**(46): p. 12398-12419.
63. LaDou, J., *The asbestos cancer epidemic*. Environmental health perspectives, 2004. **112**(3): p. 285-290.
64. Donaldson, K., et al., *Asbestos, carbon nanotubes and the pleural mesothelium: a review of the hypothesis regarding the role of long fibre retention in the parietal pleura, inflammation and mesothelioma*, in *Particle and Fibre Toxicology*. 2010.
65. Jaurand, M.-C.F., A. Renier, and J. Daubriac, *Mesothelioma: Do asbestos and carbon nanotubes pose the same health risk?* Particle and Fibre Toxicology, 2009. **6**(1): p. 16.
66. Palomaki, J., et al., *Long, needle-like carbon nanotubes and asbestos activate the NLRP3 inflammasome through a similar mechanism*. ACS nano, 2011. **5**(9): p. 6861-6870.
67. Stone, V. and R. Tantra, *An outline scoping study to determine whether high aspect ratio nanoparticles (HARN) should raise the same concerns as do asbestos fibres*. IOM Report on Project CB0406, Edinburgh, UKUpton A, Barrett J, Becklake MR, Burdett G, Chatfield E, Davis JMG, 2008.
68. IARC Working Group on the Evaluation of Carcinogenic Risks to Humans, *Arsenic, metals, fibres, and dusts*. IARC monographs on the evaluation of carcinogenic risks to humans, 2012. **100**(PT C): p. 11.
69. Maynard, A.D., et al., *Safe handling of nanotechnology*. Nature, 2006. **444**: p. 267-269.
70. Burden, N., et al., *The 3Rs as a framework to support a 21st century approach for nanosafety assessment*. Nano Today, 2017. **12**: p. 10-13.
71. Burden, N., et al., *Aligning nanotoxicology with the 3Rs: What is needed to realise the short, medium and long-term opportunities?* Regulatory Toxicology and Pharmacology, 2017. **91**: p. 257-266.
72. Schrage, A., et al., *Refinement and reduction of acute oral toxicity testing: a critical review of the use of cytotoxicity data*. Alternatives to laboratory animals, 2011. **39**(3): p. 273-295.
73. Pan, Y., et al., *Nano-QSAR modeling for predicting the cytotoxicity of metal oxide nanoparticles using novel descriptors*. RSC advances, 2016. **6**(31): p. 25766-25775.
74. Fadeel, B., et al., *Advanced tools for the safety assessment of nanomaterials*. Nature Nanotechnology, 2018. **13**(7): p. 537-543.
75. Brunauer, S., P.H. Emmett, and E. Teller, *Adsorption of gases in multimolecular layers*. Journal of the American chemical society, 1938. **60**(2): p. 309-319.
76. Standardization, I.O.f., *ISO/TS 17200:2013: Nanotechnology - Nanoparticles in powder form - Characteristics and measurements*. 2013: ISO.
77. Standardization, I.O.f., *ISO/TR 13014: 2012: Nanotechnologies: Guidance on Physico-chemical Characterization of Engineered Nanoscale Materials for Toxicologic Assessment*. 2012: ISO.
78. Stefaniak, A.B., *Principal Metrics and Instrumentation for Characterization of Engineered Nanomaterials*. Metrology and Standardization of Nanotechnology: Protocols and Industrial Innovations, 2017: p. 151-174.
79. Oberdorster, G., V. Stone, and K. Donaldson, *Toxicology of nanoparticles: A historical perspective*. Nanotoxicology, 2007. **1**.
80. Moreno-Horn, M. and T. Gebel, *Granular biodurable nanomaterials: no convincing evidence for systemic toxicity*. Crit Rev Toxicol, 2014. **44**.
81. Council, N.R., *Comparative dosimetry of radon in mines and homes*. 1991: National Academies Press.
82. Beyersmann, D. and A. Hartwig, *Carcinogenic metal compounds: recent insight into molecular and cellular mechanisms*. Archives of toxicology, 2008. **82**(8): p. 493.



83. Conner, S.D. and S.L. Schmid, *Regulated portals of entry into the cell*. Nature, 2003. **422**(6927): p. 37-44.
84. OECD, *413: Subchronic Inhalation Toxicity: 90-day Study*. OECD Guidelines for the Testing of Chemicals, Section, 2009. **4**.
85. Wiench, K. and L. Ma-Hock, *The Short-Term Inhalation Study (STIS) as a Range Finder and Screening Tool in a Tiered Grouping Strategy*, in *In Vivo Inhalation Toxicity Screening Methods for Manufactured Nanomaterials*. 2019, Springer. p. 25-65.
86. Elder, A., et al., *Effects of Subchronically Inhaled Carbon Black in Three Species. I. Retention Kinetics, Lung Inflammation, and Histopathology*. Toxicological Sciences, 2005. **88**(2): p. 614-629.
87. Landsiedel, R., et al., *Application of short-term inhalation studies to assess the inhalation toxicity of nanomaterials*. Particle and fibre toxicology, 2014. **11**(1): p. 16.
88. Möhner, M., A. Pohrt, and J. Gellissen, *Occupational exposure to respirable crystalline silica and chronic non-malignant renal disease: systematic review and meta-analysis*. International archives of occupational and environmental health, 2017. **90**(7): p. 555-574.
89. NIOSH, *Health effects of occupational exposure to respirable crystalline silica*. 2002, NIOSH; Center for Disease Control and Prevention Publication Atlanta.
90. Konduru, N., et al., *Biokinetics and effects of barium sulfate nanoparticles*. Particle and fibre toxicology, 2014. **11**(1): p. 55.
91. McClements, D.J. and H. Xiao, *Is nano safe in foods? Establishing the factors impacting the gastrointestinal fate and toxicity of organic and inorganic food-grade nanoparticles*. npj Science of Food, 2017. **1**(1): p. 1-13.
92. Yokel, R.A. and R.C. MacPhail, *Engineered nanomaterials: exposures, hazards, and risk prevention*. Journal of Occupational Medicine and Toxicology, 2011. **6**(1): p. 1-27.
93. Dekkers, S., et al., *Presence and risks of nanosilica in food products*. Nanotoxicology, 2011. **5**(3): p. 393-405.
94. Fröhlich, E.E. and E. Fröhlich, *Cytotoxicity of nanoparticles contained in food on intestinal cells and the gut microbiota*. International journal of molecular sciences, 2016. **17**(4): p. 509.
95. Landsiedel, R., et al., *Gut microbiome and plasma metabolome changes in rats after repeated oral gavage of SiO<sub>2</sub> and Ag nanoparticles*. Particle Fibre Toxicology, submitted to PFT.
96. Brand, W., P. van Kesteren, and A. Oomen, *Potential health risks of nanomaterials in food: a methodology to identify signals and prioritise risks*. 2020.
97. Sirelkhatim, A., et al., *Review on zinc oxide nanoparticles: antibacterial activity and toxicity mechanism*. Nano-micro letters, 2015. **7**(3): p. 219-242.
98. Esmaeillou, M., et al., *Toxicity of ZnO nanoparticles in healthy adult mice*. Environmental toxicology and pharmacology, 2013. **35**(1): p. 67-71.
99. Weir, A., et al., *Titanium dioxide nanoparticles in food and personal care products*. Environmental science & technology, 2012. **46**(4): p. 2242-2250.
100. Jovanović, B., *Critical review of public health regulations of titanium dioxide, a human food additive*. Integrated environmental assessment and management, 2015. **11**(1): p. 10-20.
101. Wang, J., et al., *Acute toxicity and biodistribution of different sized titanium dioxide particles in mice after oral administration*. Toxicology letters, 2007. **168**(2): p. 176-185.
102. EC, *Scientific Committee on Toxicity, Ecotoxicity and the Environment (CSTEE)*. 2003.
103. So, S.J., I.S. Jang, and C.S. Han, *Effect of micro/nano silica particle feeding for mice*. Journal of nanoscience and nanotechnology, 2008. **8**(10): p. 5367-5371.
104. EFSA Scientific Committee, *Guidance on the risk assessment of the application of nanoscience and nanotechnologies in the food and feed chain*. EFSA Journal, 2011. **9**(5): p. 2140.
105. EC, *No 1907/2006 of the European Parliament and of the Council of 18 December 2006 concerning the Registration Evaluation, Authorisation and Restriction of Chemicals (REACH), establishing a European Chemicals Agency, amending Directive*. 2006. **45**: p. 1-849.
106. Commission, E., *Commission Regulation (EU) 2018/1881 of 3 December 2018 amending Regulation (EC) No 1907/2006 of the European Parliament and of the Council on the Registration, Evaluation, Authorisation and Restriction of Chemicals (REACH) as regards Annexes I, III, VI, VII, VIII, IX, X, XI, and XII to address nanoforms of substances*. Commission Regulation (EU) 2018/1881, 2018.
107. The European Chemicals Agency, *Chemical safety assessment 2009*.
108. ECHA, *Guidance on information requirements and chemical safety assessment: Appendix R7-1 for nanoforms applicable to Chapter R7a and R7c Endpoint specific guidance*. ECHA, 2020.
109. European Chemicals Agency, *Read-Across Assessment Framework (RAAF)*. 2017, ECHA Helsinki, Finland.

## REFERENCES

---

110. ECHA, *Appendix R.6-1 for nanomaterials applicable to the Guidance on QSARs and Grouping of Chemicals*. Appendix R.6-1 for nanomaterials applicable to the Guidance on QSARs and Grouping of Chemicals, 2017.
111. Teubner, W. and R. Landsiedel, *Read-across for hazard assessment: The ugly duckling is growing up*. *Alternatives to Laboratory Animals*, 2015. **43**(6): p. P67-P71.
112. Arts, J.H.E., et al., *A decision-making framework for the grouping and testing of nanomaterials (DF4nanoGrouping)*. *Regulatory Toxicology and Pharmacology*, 2015(0).
113. Arts, J.H., et al., *Case studies putting the decision-making framework for the grouping and testing of nanomaterials (DF4nanoGrouping) into practice*. *Regulatory Toxicology and Pharmacology*, 2016. **76**: p. 234-261.
114. Wohlleben, W., et al., *The nanoGRAVUR framework to group (nano) materials for their occupational, consumer, environmental risks based on a harmonized set of material properties, applied to 34 case studies*. *Nanoscale*, 2019. **11**(38): p. 17637-17654.
115. Kuempel, E., et al., *Development of risk-based nanomaterial groups for occupational exposure control*. *J. Nanopart Res*, 2012. **14**: p. 1029.
116. ISO, *Nanotechnologies — Electron spin resonance (ESR) as a method for measuring reactive oxygen species (ROS) generated by metal oxide nanomaterials*. 2017.
117. Landsiedel, R., et al., *Pulmonary toxicity of nanomaterials: a critical comparison of published in vitro assays and in vivo inhalation or instillation studies*. *Nanomedicine*, 2014. **9**(16): p. 2557-2585.
118. Ojha, P.K., et al., *Toward comprehension of multiple human cells uptake of engineered nano metal oxides: quantitative inter cell line uptake specificity (QICLUS) modeling*. *Nanotoxicology*, 2019. **13**(1): p. 14-34.
119. Epa, V.C., et al., *Modeling Biological Activities of Nanoparticles*. *Nano Letters*, 2012.
120. Chau, Y.T. and C.W. Yap, *Quantitative nanostructure–activity relationship modelling of nanoparticles*. *Rsc Advances*, 2012. **2**(22): p. 8489-8496.
121. Hinderliter, P.M., et al., *ISDD: a computational model of particle sedimentation, diffusion and target cell dosimetry for in vitro toxicity studies*. *Particle and fibre toxicology*, 2010. **7**(1): p. 1-20.
122. Cohen, J.M., J.G. Teeguarden, and P. Demokritou, *An integrated approach for the in vitro dosimetry of engineered nanomaterials*. *Particle and fibre toxicology*, 2014. **11**(1): p. 20.
123. DeLoid, G.M., et al., *Advanced computational modeling for in vitro nanomaterial dosimetry*. *Particle and Fibre Toxicology*, 2015. **12**(1): p. 32.
124. DeLoid, G.M., et al., *Preparation, characterization, and in vitro dosimetry of dispersed, engineered nanomaterials*. *Nature Protocols*, 2017. **12**(2): p. 355-371.
125. Ministère de l'Environnement, d.l.É.e.d.l.M., *Éléments issus des déclarations des substances à l'état nanoparticulaire: Exercice 2015*. 2015: Lyon.
126. Totaro, S., et al., *The JRC nanomaterials repository: a unique facility providing representative test materials for nanoEHS research*. *Regulatory Toxicology and Pharmacology*, 2016. **81**: p. 334-340.
127. Ma-Hock, L., et al., *Long-term inhalation study with CeO<sub>2</sub>- and BaSO<sub>4</sub> nanomaterials – study design, in-life findings, and lung burden*, in *Eurotox 2017*. 2017.
128. Keller, J., et al., *Time course of lung retention and toxicity of inhaled particles: short-term exposure to nano-Ceria*. *Archives of toxicology*, 2014. **88**(11): p. 2033-2059.
129. Molina, R.M., et al., *Bioavailability, distribution and clearance of tracheally instilled, gavaged or injected cerium dioxide nanoparticles and ionic cerium*. *Environmental Science: Nano*, 2014.
130. Babick, F., et al., *How reliably can a material be classified as a nanomaterial? Available particle-sizing techniques at work*. *Journal of Nanoparticle Research*, 2016. **18**(6): p. 1-40.
131. Wohlleben, W., et al., *Reliable nanomaterial classification of powders using the volume-specific surface area method*. *Journal of Nanoparticle Research*, 2017. **19**(2): p. 61.
132. Wiemann, M., et al., *In Vitro and In Vivo Short-Term Pulmonary Toxicity of Differently Sized Colloidal Amorphous SiO<sub>2</sub>*. *Nanomaterials*, 2018. **8**(3): p. 160.
133. Landsiedel, R., et al., *Application of short-term inhalation studies to assess the inhalation toxicity of nanomaterials*. *Part Fibre Toxicol*, 2014. **11**.
134. Arts, J.H.E., et al., *Case studies putting the decision-making framework for the grouping and testing of nanomaterials (DF4nanoGrouping) into practice*. *Regulatory Toxicology and Pharmacology*, 2016. **76**: p. 234-261.
135. Hofmann, T., et al., *Comparative short-term inhalation toxicity of five organic diketopyrrolopyrrole pigments and two inorganic iron-oxide-based pigments*. *Inhalation Toxicology*, 2016. **28**(10): p. 463-479.
136. Gosens, I., et al., *Organ burden and pulmonary toxicity of nano-sized copper (II) oxide particles after short-term inhalation exposure*. *Nanotoxicology*, 2016. **10**(8): p. 1084-1095.

137. Marques, M., R. Loebenberg, and M. Almukainzi, *Simulated Biological Fluids with Possible Application in Dissolution Testing*. Dissolution Technologies, 2011. **8**: p. 15-29.
138. Stock, V., et al., *Uptake and effects of orally ingested polystyrene microplastic particles in vitro and in vivo*. Archives of Toxicology, 2019. **93**(7): p. 1817-1833.
139. Molina, R.M., et al., *Bioavailability, distribution and clearance of tracheally instilled, gavaged or injected cerium dioxide nanoparticles and ionic cerium*. Environmental Science: Nano, 2014. **1**(6): p. 561-573.
140. Bove, P., M. A Malvindi, and S. Sabella, *In vitro human digestion test to monitor the dissolution of silver nanoparticles*. Vol. 838. 2017. 012003.
141. Sieg, H., et al., *Impact of an artificial digestion procedure on aluminum-containing nanomaterials*. Langmuir, 2017. **33**(40): p. 10726-10735.
142. Bettini, S., et al., *Food-grade TiO<sub>2</sub> impairs intestinal and systemic immune homeostasis, initiates preneoplastic lesions and promotes aberrant crypt development in the rat colon*. Scientific Reports, 2017. **7**: p. 40373.
143. Graham, U.M., et al., *In vivo processing of ceria nanoparticles inside liver: impact on free-radical scavenging activity and oxidative stress*. ChemPlusChem, 2014. **79**(8): p. 1083-1088.
144. Guillard, A., et al., *Basal Ti level in the human placenta and meconium and evidence of a materno-foetal transfer of food-grade TiO<sub>2</sub> nanoparticles in an ex vivo placental perfusion model*. Particle and Fibre Toxicology, 2020. **17**(1): p. 51.
145. Gray, E.P., et al., *Biodissolution and cellular response to MoO<sub>3</sub> nanoribbons and a new framework for early hazard screening for 2D materials*. Environmental Science: Nano, 2018. **5**(11): p. 2545-2559.
146. Pavan, C., et al., *The puzzling issue of silica toxicity: are silanols bridging the gaps between surface states and pathogenicity?* Particle and Fibre Toxicology, 2019. **16**(1): p. 32.
147. Bove, P., et al., *Dissolution test for risk assessment of nanoparticles: a pilot study*. Nanoscale, 2017. **9**(19): p. 6315-6326.
148. Bove, P., M.A. Malvindi, and S. Sabella, *In vitro human digestion test to monitor the dissolution of silver nanoparticles*. Journal of Physics: Conference Series, 2017. **838**(1): p. 012003.
149. Sohal, I.S., et al., *Dissolution Behavior and Biodurability of Ingested Engineered Nanomaterials in the Gastrointestinal Environment*. ACS Nano, 2018. **12**(8): p. 8115-8128.
150. Walczak, A.P., *Development of an integrated in vitro model for the prediction of oral bioavailability of nanoparticles*. 2015, Wageningen University.
151. Walczak, A.P., et al., *Behaviour of silver nanoparticles and silver ions in an in vitro human gastrointestinal digestion model*. Nanotoxicology, 2012. **7**(7): p. 1198-1210.
152. Paetz, A., *New DIN 19738: 2000-05 (draft): Soil structure-availability for resorption of organic and inorganic pollutants from contaminated soils; Neue DIN 19738: 2000-05 (Entwurf): Bodenbeschaffenheit-Resorptionsverfuegbarkeit von organischen und anorganischen Schadstoffen aus kontaminiertem Bodenmaterial*. 2000.
153. Hardy, A., et al., *Guidance on risk assessment of the application of nanoscience and nanotechnologies in the food and feed chain: Part 1, human and animal health*. EFSA Journal, 2018. **16**(7).
154. Laux, P., et al., *A medical-toxicological view of tattooing*. The Lancet, 2016. **387**(10016): p. 395-402.
155. Sauer, U.G. and R. Kreiling, *The grouping and assessment strategy for organic pigments (GRAPE): Scientific evidence to facilitate regulatory decision-making*. Regulatory Toxicology and Pharmacology, 2019: p. 104501.
156. Stratmann, H., et al., *Indicators for lack of systemic availability of organic pigments*. Regulatory Toxicology and Pharmacology, 2020: p. 104719.
157. De Jong, W.H., et al., *Toxicity of copper oxide and basic copper carbonate nanoparticles after short-term oral exposure in rats*. Nanotoxicology, 2019. **13**(1): p. 50-72.
158. Krause, B.C., et al., *Aluminum and aluminum oxide nanomaterials uptake after oral exposure-a comparative study*. Scientific reports, 2020. **10**(1): p. 1-10.
159. Poças, F. and R. Franz, *overview on European regulatory issues, legislation, and EFSA evaluations of nanomaterials*, in *Nanomaterials for Food Packaging*. 2018, Elsevier. p. 277-300.
160. Warheit, D.B., S.C. Brown, and E.M. Donner, *Acute and subchronic oral toxicity studies in rats with nanoscale and pigment grade titanium dioxide particles*. Food and Chemical Toxicology, 2015. **84**: p. 208-224.
161. Buesen, R., et al., *Effects of SiO<sub>2</sub>, ZrO<sub>2</sub>, and BaSO<sub>4</sub> nanomaterials with or without surface functionalization upon 28-day oral exposure to rats*. Archives of toxicology, 2014. **88**(10): p. 1881-1906.

## REFERENCES

---

162. Schneider, S., et al., *Oral prenatal developmental toxicity study with NM-200 synthetic amorphous silica in Wistar rats*. *Reproductive Toxicology*, 2011. **32**(2): p. 173-174.
163. DeLoid, G., et al., *Estimating the effective density of engineered nanomaterials for in vitro dosimetry*. *Nat Commun*, 2014. **5**: p. 3514.
164. Vila, L., et al., *Frozen dispersions of nanomaterials are a useful operational procedure in nanotoxicology*. *Nanotoxicology*, 2017. **11**(1): p. 31-40.
165. Stone, V., et al., *A framework for grouping and read-across of nanomaterials-supporting innovation and risk assessment*. *Nano Today*, 2020. **35**: p. 100941.